



The University of Manchester

DOCTORAL THESIS

Compressive Faraday Imaging for Next-Generation Radio Telescopes

Author:

Miguel Angel Carcamo Vasquez

Supervisor:

Anna M. M. Scaife

*A thesis submitted to the University of Manchester
for the degree of Doctor of Philosophy
in the*

Department of Physics and Astronomy in the School of Natural Sciences
Faculty of Science and Engineering

2023

Contents

| | |
|--|-----------|
| Contents | 2 |
| List of Figures | 12 |
| List of Tables | 14 |
| Abbreviations | 15 |
| Abstract | 16 |
| Declaration of Authorship | 17 |
| Copyright Statement | 18 |
| Acknowledgements | 20 |
| Dedication | 21 |
| 1 Introduction | 22 |
| 1.1 Context | 22 |
| 1.2 Plasma effects | 24 |
| 1.2.1 Review of Maxwell's Equations for Electromagnetism | 24 |
| 1.3 Radio Emission Mechanisms | 28 |
| 1.3.1 Synchrotron Emission | 28 |
| 1.3.2 Polarisation of Synchrotron Emission | 32 |
| 1.4 Astronomical Faraday Rotation | 33 |
| 1.5 The RM Synthesis Method | 37 |
| 2 Interferometry | 41 |
| 2.1 Radio Interferometers | 41 |
| 2.1.1 Visibility Weighting | 44 |
| 2.1.2 Anti-aliasing Considerations | 46 |
| 2.2 RFI Excision | 48 |
| 2.3 Parallel-hand calibration | 49 |
| 2.3.1 Delay calibration | 51 |
| 2.3.2 Bandpass calibration | 51 |

| | | |
|----------|--|-----------|
| 2.3.3 | Complex gain calibration | 51 |
| 2.4 | Polarisation calibration | 52 |
| 2.4.1 | Cross-hand delay calibration | 53 |
| 2.4.2 | Leakage calibration | 53 |
| 2.4.3 | Polarisation angle calibration | 55 |
| 2.5 | Interferometric Imaging | 56 |
| 2.5.1 | Model Image Representations and Multi-Frequency Synthesis . . . | 57 |
| 2.5.2 | Self-Calibration | 59 |
| 3 | Compressed Sensing Faraday Reconstruction | 61 |
| 3.1 | Compressed Sensing | 61 |
| 3.1.1 | Sparsity, incoherence and RIP | 63 |
| 3.1.2 | Regularization | 63 |
| 3.1.3 | CS Optimization methods | 64 |
| 3.2 | Applications of Compressive Sensing to radio astronomy | 67 |
| 3.3 | Applications of Compressive Sensing to 1D data | 70 |
| 3.4 | Faraday Spectra Reconstruction | 72 |
| 3.5 | Application to Simulated Data | 75 |
| 3.5.1 | Evaluation Metrics | 77 |
| | Peak-signal-to-noise ratio (PSNR) | 77 |
| | Root Mean Squared Error (RMSE) | 78 |
| | Sparsity | 79 |
| | Model selection criterion: AIC and BIC | 79 |
| 3.5.2 | Comparison with RM-CLEAN | 82 |
| 4 | JVLA Abell 1314 | 90 |
| 4.1 | Abell 1314 Case Study | 90 |
| 4.2 | JVLA Data Reduction | 91 |
| 4.2.1 | RFI Excision | 92 |
| 4.2.2 | Calibration models | 93 |
| 4.2.3 | Cross-hand delay calibration | 94 |
| 4.2.4 | Leakage calibration | 94 |
| 4.2.5 | Polarisation angle calibration | 96 |
| 4.2.6 | Calibration checks | 98 |
| 4.2.7 | Imaging | 98 |
| 4.3 | Faraday Imaging | 98 |
| 4.4 | Polarised radio galaxies | 103 |
| 4.4.1 | IC 708 | 103 |
| 4.4.2 | IC 711 | 104 |
| 4.4.3 | IC 712 | 105 |
| 4.5 | Galactic contribution | 106 |
| 4.6 | X-ray data analysis | 107 |
| 4.7 | Radio RM profiles | 109 |

| | | |
|----------|---|------------|
| 5 | eMERLIN Cluster Sample | 114 |
| 5.1 | Abell 1314 | 114 |
| 5.2 | eMERLIN Data Reduction | 115 |
| 5.2.1 | RFI Excision | 115 |
| 5.2.2 | Parallel-hand Calibration | 115 |
| 5.2.3 | Self-Calibration | 117 |
| 5.2.4 | Total Intensity Images | 118 |
| 5.3 | eMERLIN Polarisation Calibration | 119 |
| 5.3.1 | Cross-hand problems in CASA | 119 |
| 5.3.2 | Cross-hand Calibration | 121 |
| | Cross-hand delay calibration | 121 |
| | Leakage calibration | 130 |
| | Polarisation angle calibration | 131 |
| 5.3.3 | Polarisation Images | 131 |
| 6 | MeerKAT Deep Field | 135 |
| 6.1 | MeerKAT MIGHTEE-POL Data Reduction | 136 |
| 6.2 | MeerKAT Deep Field optimal wavelet selection | 138 |
| 6.3 | Rotation Measure extraction on the MIGHTEE-POL survey | 140 |
| 6.3.1 | COSMOS | 142 |
| 7 | Future work and conclusions | 147 |
| 7.1 | Future work | 147 |
| 7.2 | Conclusions | 149 |
| | Bibliography | 151 |

List of Figures

| | | |
|-----|--|----|
| 1.1 | Presence of an induction B on closed circuit C formed by a conducting wire. | 26 |
| 1.2 | Diagram of synchrotron emission, arising from a charged particle moving along a helical path around an ordered magnetic field. The Lorentz force causing the acceleration a is perpendicular to the magnetic field vector \mathbf{B} , and both are also perpendicular to the circular component of the charge velocity \mathbf{v} . The radiation is concentrated in a beamwidth of $\sim 1/\gamma$ radians. (Obtained from Emma Alexander at https://emmaalexander.github.io/resources.html). | 29 |
| 1.3 | Flux densities of sources 3C 123, 3C 196, 3C 286 and 3C 295 for frequencies between 1 and 50 GHz. Derived flux densities from Perley and Butler, 2013 values are depicted as black dots. The red lines are the result of a power-law fitting on the flux density data. | 32 |
| 1.4 | Representation of astronomical Faraday rotation. Two electromagnetic waves coming from an astronomical source and passing through magneto-ionic plasma (grey background) are shown. The waves pass through plasma with opposite orientations of magnetic field, therefore, the polarisation angles of the waves at the top and bottom are rotated clockwise and anti-clockwise, respectively. (Obtained from Emma Alexander at https://emmaalexander.github.io/resources.html). | 37 |
| 2.1 | Diagram to show the two-element interferometer and to illustrate the principles of aperture synthesis. Two receiver dishes are pointed at an angle θ from the zenith towards a single far-field point source. The antennas are at a distance D apart (the baseline between them). There is a timing offset of τg , due to the light travel distance offset of $D \sin \theta$, which is used to combine the signals of the two dishes. (Obtained from Emma Alexander at https://emmaalexander.github.io/resources.html). | 42 |
| 2.2 | Dirty images (top) and dirty beams (bottom) of HL Tauri Band 6 ALMA data. Weighting schemes from left to right: Natural weighting, Briggs with robust parameter equal 0.0 (a balance between natural and uniform) and uniform weighting. | 46 |

| | | |
|-----|---|----|
| 2.3 | (a) True model image with a hyperbolic secant at the center. (b) Visibility sampling | 47 |
| 2.4 | (a) Dirty image of one hyperbolic secant. (b) Dirty image of two hyperbolic secants but one has been moved outside the field of view. (c) Dirty image of (b) using a Gaussian kernel. | 48 |
| 2.5 | From left to right: CLEAN, MEM model and restored MEM images from Cárcamo et al., 2018 using HL Tauri Band 6 ALMA data. | 57 |
| 3.1 | Example of optimisation of delta basis function coefficients using a L2 (on top) and L1 (on bottom) minimization. | 65 |
| 3.2 | Scenario 1. On the left we show the simulated polarisation data as a function of λ^2 . In the center, the dirty Faraday depth spectrum of the same data. On the right, the reconstructed Faraday depth spectrum from a noisy and incomplete realisation of these data with $\sigma_{QU} = 0.7$ mJy/beam with a 30% removal fraction, using the delta basis function. The theoretical $\pm 5\sigma_\phi$ noise boundary for complex Faraday depth is shown as red lines. | 76 |
| 3.3 | Scenario 2. On the left we show the simulated polarisation data as a function of λ^2 . In the center, the dirty Faraday depth spectrum of the same data. On the right, the reconstructed Faraday depth spectrum from a noisy and incomplete realisation of these data with $\sigma_{QU} = 0.7$ mJy/beam with a 30% removal fraction, using the delta basis function. The theoretical $\pm 5\sigma_\phi$ noise boundary for complex Faraday depth is shown as red lines. | 76 |
| 3.4 | Scenario 3. On the left we show the simulated polarisation data as a function of λ^2 . In the center, the dirty Faraday depth spectrum of the same data. On the right, the reconstructed Faraday depth spectrum from a noisy and incomplete realisation of these data with $\sigma_{QU} = 0.7$ mJy/beam with a 30% removal fraction, using the delta basis function. The theoretical $\pm 5\sigma_\phi$ noise boundary for complex Faraday depth is shown as red lines. | 77 |
| 3.5 | Scenario 1 with different amounts of noise and removal fractions. First row has a noise fraction of 0.2 of the peak, second row 0.5 and third row 0.8. First column has a removal fraction of 0.2, second column 0.5 and last column 0.8. | 78 |
| 3.6 | PSNR, RMSE, AIC and BIC using all discrete wavelet families for reconstruction using the discrete wavelet transform. First row shows scenario 1, second row for scenario 2 and third row for scenario 3. | 80 |
| 3.7 | PSNR, RMSE, AIC and BIC using all discrete wavelet families for reconstruction using the undecimated wavelet transform. First row shows scenario 1, second row for scenario 2 and third row for scenario 3. | 81 |
| 3.8 | PSNR, RMSE, AIC and BIC for delta function basis reconstruction. First row shows scenario 1, second row for scenario 2 and third row for scenario 3. | 83 |

| | | |
|------|---|----|
| 3.9 | PSNR, RMSE, AIC and BIC using a discrete wavelet basis reconstruction. The first row shows Scenario 1, the second row shows Scenario 2 and the third row shows Scenario 3. We have used wavelets dmey, haar and sym9, respectively. | 84 |
| 3.10 | PSNR, RMSE, AIC and BIC using an undecimated wavelet basis reconstruction. First row shows scenario 1, second row for scenario 2 and third row for scenario 3. We have used wavelets coif3, haar and haar, respectively. | 85 |
| 3.11 | Faraday depth reconstructions of a simulated thin source (Scenario 1). From top to bottom: reconstructions using the delta basis function, the delta basis function combined with the discrete wavelet db7, the delta basis function combined with the undecimated wavelet db34, and RM-CLEAN. In each plot, the top panel displays the amplitude values of the restored (black), model (red), and dirty Faraday depth spectrum (dotted grey). The vertical dashed grey line indicates the position at the peak in Faraday depth. The horizontal dashed blue line represents the theoretical 5σ boundary on the amplitude of polarized intensity. The bottom panel illustrates the amplitude, real, and imaginary parts of the residuals. Red and blue dashed lines represent the theoretical $\pm 5\sigma$ and $\pm 3\sigma$ noise boundaries, respectively. | 86 |
| 3.12 | Faraday depth reconstructions of a simulated thick source (modified Scenario 2). The source polarised intensity has been increased to $0.11 \text{ mJy beam}^{-1}$ to ensure its visibility in the plots. From top to bottom: reconstructions using the delta basis function, the delta basis function combined with the discrete wavelet dmey, the undecimated wavelet haar, and RM-CLEAN. In each plot, the top panel displays the amplitude values of the restored (black), model (red), and dirty Faraday depth spectrum (dotted grey). The vertical dashed grey line indicates the position at the peak in Faraday depth. The horizontal dashed blue line represents the theoretical 5σ boundary on the amplitude of polarized intensity. The bottom panel illustrates the amplitude, real, and imaginary parts of the residuals. Red and blue dashed lines represent the theoretical $\pm 5\sigma$ and $\pm 3\sigma$ noise boundaries, respectively. | 87 |

| | | |
|------|---|-----|
| 3.13 | Faraday depth reconstructions of a simulated thin and thick source (modified Scenario 3). The source polarised intensity has been increased to $0.11 \text{ mJy beam}^{-1}$ to ensure its visibility in the plots. From top to bottom: reconstructions using the delta basis function, the delta basis function combined with the discrete wavelet <code>dmey</code> , the delta basis function combined with the undecimated wavelet <code>db38</code> , and RM-CLEAN. In each plot, the top panel displays the amplitude values of the restored (black), model (red), and dirty Faraday depth spectrum (dotted grey). The vertical dashed grey line indicates the position at the peak in Faraday depth. The horizontal dashed blue line represents the theoretical 5σ boundary on the amplitude of polarized intensity. The bottom panel illustrates the amplitude, real, and imaginary parts of the residuals. Red and blue dashed lines represent the theoretical $\pm 5\sigma$ and $\pm 3\sigma$ noise boundaries, respectively. | 88 |
| 4.1 | 3C 286 and 3C 147 flux densities from Perley and Butler, 2017 (black lines) and their respective fitted flux densities using Equation (4.2) (red lines). . | 95 |
| 4.2 | Polarisation angle fit for 3C 286. Each black marker represent a datum taken from the VLA polarimetry webpage. The red line represents the fit along the wavelength squared axis. The shade on cyan color represent the frequency bandwidth used for this JVLA dataset. | 96 |
| 4.3 | Polarisation fraction fit for 3C 286. Each black marker represent a datum taken from the VLA polarimetry webpage. The red line represents the fit along the wavelength squared axis. The shade on cyan color represent the frequency bandwidth used for this JVLA dataset. | 97 |
| 4.4 | Overlay image of cluster Abell 1314. Image of the SDSS optical spectral with three overlaid contours. Purple contours represent the X-ray XMM-Newton point-source subtracted surface brightness. Blue contours represent the WISE $3.4 \mu\text{m}$ infrared emission. Finally, red contours represent the VLA C-configuration total intensity radio emission at 1.5 GHz. The contours start at 3.75σ , 50σ and 5.0σ , respectively and all of them are spaced by a factor of 2. σ value for radio contours is listed in Table 4.3. The eleven detected radio galaxies are marked with numbers and the cluster center is marked with a yellow cross. See Table 4.2 for further information about each source. | 99 |
| 4.5 | Total intensity images of 3C 286 (left) and 3C 147 (right). The vector lines show the polarisation angle and their magnitudes show their polarisation fraction. | 100 |
| 4.6 | On top: Full field total intensity and polarisation fraction maps. On bottom: Zoom in on polarisation fraction maps of IC708 (left) and IC711 (right). Polarisation angles is represented as cyan vectors on bottom figures. . . . | 101 |
| 4.7 | RMTF for the VLA Abell 1314 data. | 102 |

- 4.8 IC 708. Contours show radio total intensity in increments of 1σ from 5σ . Greyscale shows: (left) the observed peak rotation measure; (centre) the uncertainty on the observed rotation measure, σ_ϕ ; and (right) the polarisation fraction, P/I ; all for the region where $P > 6\sigma_{QU}$. The regions of the image are used to define the core, the north and south lobes of this galaxy. as described in Section 4.4.1, this is indicated by yellow, blue and cyan circles, respectively. 104
- 4.9 Line of sight at the core of IC 708. The upper panel shows the dirty and the restored Faraday depths with a peak at $109.34 \text{ rad m}^{-2}$. The lower panel shows the amplitude, the real and imaginary parts of the residual signal. Light and dark grey dashed lines show 5σ and 3σ boundaries, respectively. 104
- 4.10 IC 711. Contours show radio total intensity in increments of 1σ from 5σ . Greyscale shows: (left) the observed peak rotation measure; (centre) the uncertainty on the observed rotation measure, σ_ϕ ; and (right) the polarisation fraction, P/I ; all for the region where $P > 6\sigma_{QU}$ 105
- 4.11 Line of sight at the core of IC 711. The upper panel shows the dirty and the restored Faraday depths with a peak at $-34.17 \text{ rad m}^{-2}$. The lower panel shows the amplitude, the real and imaginary parts of the residual signal. Light and dark grey dashed lines show 5σ and 3σ boundaries, respectively. 105
- 4.12 IC 712. Contours show radio total intensity in increments of 1σ from 5σ . Greyscale shows: (left) the observed peak rotation measure; (centre) the uncertainty on the observed rotation measure, σ_ϕ ; and (right) the polarisation fraction, P/I ; all for the region where $P > 6\sigma_{QU}$ 106
- 4.13 Line of sight at the core of IC 712. The upper panel shows the dirty and the restored Faraday depths with a peak at 13.67 rad m^{-2} . The lower panel shows the amplitude, the real and imaginary parts of the residual signal. Light and dark grey dashed lines show 5σ and 3σ boundaries, respectively. 106
- 4.14 On the top: Mean and standard deviation RM maps of the Galactic foreground at the JVLA Abell 1314 field coordinates. On the bottom: On the top: Mean and standard deviation RM approximated maps of the Galactic foreground at the JVLA Abell 1314 field coordinates using bilinear interpolation 108
- 4.15 Regions used for extracting radial cluster properties are overlaid on the $0.3 - 2.0 \text{ keV}$ adaptively-smoothed, background-subtracted and exposure-corrected image from the combined MOS1, MOS2 & PN exposures. 110
- 4.16 Radial temperature profile for Abell 1314. Data points correspond to spectral fits of the emission in the core and annular regions shown in Figure 4.15 111

| | | |
|------|---|-----|
| 4.17 | $ \langle \text{RM} \rangle $, σ_{RM} and $\text{MAD}(\text{RM})$ of the polarised sources in the Abell 1314 cluster plotted against the projected distance of each source to the X-ray center (top row) and against the X-ray surface brightness at the position of peak polarisation for each source (bottom row). The uncertainties of the $ \langle \text{RM} \rangle $ and σ_{RM} are the $\pm 1\sigma$ considering n_{beam} samples for each source. Sources that cover an area with fewer than $5 n_{\text{beam}}$ are shown as open red circles and are not considered in the σ_{RM} and $\text{MAD}(\text{RM})$ plots. Uncertainties for $\text{MAD}(\text{RM})$ are derived from the median error on the RM measurement, $\text{med}(\sigma_\phi)$. The detected polarised sources are numbered according to Table 4.9. The components of IC708 are shown with yellow triangles and named as C, N and S for core, north lobe and south lobe, respectively, see Table 4.10. | 112 |
| 5.1 | Class diagram of the Self-calibration framework | 118 |
| 5.2 | Self-calibration improvement over the phase calibration loops on the eMERLIN dataset of Abell 1314. The annotation on each sub-image show the iteration number, where 0 corresponds to the image reconstructed after doing the parallel-hand calibration, and the rms noise. At the top of each colourbar the intensity peak of each sub-image is shown. | 119 |
| 5.3 | On the left: Total intensity image of Abell 1314 using JVL A (see Chapter 4). On the right: Higher resolution image of IC 708 using the eMERLIN radio telescope. The contours are drawn from a 4σ to 32σ level with increments of 2σ , where $\sigma = 0.17\text{mJy beam}^{-1}$. | 120 |
| 5.4 | On the left: Total intensity image of Abell 1314 using eMERLIN. On the center: Spectral index map masked at 4σ . On the right: Spectral index error map masked at 4σ . The contours are drawn from a 4σ to 32σ level with increments of 2σ , where $\sigma = 0.17\text{mJy beam}^{-1}$. | 120 |
| 5.5 | Amplitude and phase plots for 3C 286, baseline Defford-Pickmere and its first 3 spectral windows and correlation LL. | 122 |
| 5.6 | Amplitude and phase plots for 3C 286, baseline Defford-Pickmere and its first 3 spectral windows and correlation LR. | 123 |
| 5.7 | Amplitude and phase plots for 3C 286, baseline Defford-Pickmere and its first 3 spectral windows and correlation RL. | 124 |
| 5.8 | Amplitude and phase plots for 3C 286, baseline Defford-Pickmere and its first 3 spectral windows and correlation RR. | 125 |
| 5.9 | Amplitude and phase plots for 3C 286, baseline Mark2-Defford and its first 3 spectral windows and correlation LL. | 126 |
| 5.10 | Amplitude and phase plots for 3C 286, baseline Mark2-Defford and its first 3 spectral windows and correlation LR. | 127 |
| 5.11 | Amplitude and phase plots for 3C 286, baseline Mark2-Defford and its first 3 spectral windows and correlation RL. | 128 |
| 5.12 | Amplitude and phase plots for 3C 286, baseline Mark2-Defford and its first 3 spectral windows and correlation RR. | 129 |

| | | |
|------|---|-----|
| 5.13 | Single and multi band solutions for the cross-hand delay in the Abell 1314 eMERLIN dataset. | 130 |
| 5.14 | Amplitude vs frequency and amplitude vs antenna plots from the leakage calibration table before flagging outlier solutions. | 130 |
| 5.15 | Amplitude vs frequency and amplitude vs antenna plots from the leakage calibration table after flagging outlier solutions. | 131 |
| 5.16 | Polarisation angle solutions versus frequency, each spectral window is shown with a different color. | 132 |
| 5.17 | Polarisation fraction of radio galaxy IC 708 masked at 5σ in Stokes I. The white vectors on the figure on the left represent the polarisation angle not yet corrected by the Galactic Faraday rotation. | 133 |
| 5.18 | Polarisation and total intensity SNR maps of radio galaxy IC 708 masked at 5σ in Stokes I. | 134 |
| 6.1 | Time-averaged bandpass response from MeerKAT on J1939-6342. The portions of the spectrum marked in red are dominated by significant, consistent RFI across all observational data, leading to their exclusion from all datasets. | 137 |
| 6.2 | COSMOS MFS Stokes I continuum image at 1.28 GHz using Briggs weighting and robust -0.5 . The colorbar has a log scale and has been saturated to a minimum of 0.0 Jy beam^{-1} to show extended fainter emission. | 139 |
| 6.3 | PSNR, RMSE, AIC and BIC using all discrete wavelet families for reconstruction of MeerKAT simulated data using the discrete wavelet transform. First row shows scenario 1, second row for scenario 2 and third row for scenario 3. | 141 |
| 6.4 | PSNR, RMSE, AIC and BIC using all wavelet families for reconstruction of MeerKAT simulated data using the undecimated wavelet transform. First row shows scenario 1, second row for scenario 2 and third row for scenario 3. | 141 |
| 6.5 | On the top, from left to right: RMTF for the COSMOS wavelength squared sampling using spectral indices -1.0, 0.0 and 1.0. On the bottom left: Residual between RMTFs using $\alpha = -1.0$ and $\alpha = 0.0$. On the bottom right: Residual between RMTFs using $\alpha = 0.0$ and $\alpha = 1.0$ | 142 |
| 6.6 | On the left: RMTF for one of the fainter sources of the in-source catalog. This source has a fitted $\alpha \sim 100$. On the right: RMTF for the same source and sampling but forcing the spectral index to a value of -0.74. | 143 |
| 6.7 | Spectral index distribution for COSMOS in-source sources. The mean of the distribution is -0.598, the standard deviation is 8.797 and the mode is -0.74. | 143 |

- 6.8 polarised intensity of the maximum of the RM synthesis spectra for the dirty (left) and reconstructed (right) on-source (blue dots) positions plotted against the peak total intensity for each source. This plot is for the COSMOS field. The diagonal dashed lines represent lines of constant fractional polarisation of 1, 10 and 100%. The horizontal black and green line represent respectively the 99.9 percentile and the median plus 4 sigma of the off-source spectral peaks. 144
- 6.9 Histograms for dirty and reconstructed Faraday spectra for in-source sources with polarisation fractions above the 99.9 percentile. 144

List of Tables

| | | |
|-----|---|----|
| 1.1 | Frequency ranges, channel widths, and Faraday parameters for several radio telescopes, including LOFAR's Low Band Antenna (LBA) and High Band Antenna (HBA), and the L-band frequency range for JVLA, eMERLIN, and MeerKAT. For the MeerKAT telescope, two distinct L-band ranges are provided - the actual frequency range and the particular range used in this thesis for RM Synthesis | 40 |
| 3.1 | Abell 1314 JVLA simulation details | 77 |
| 3.2 | AIC, BIC, PSNR and RMSE for delta function basis. | 81 |
| 3.3 | AIC, BIC, PSNR and RMSE for discrete wavelets transforms (WT) and undecimated wavelet transforms (UWT) with the minimum AIC. | 81 |
| 3.4 | AIC, BIC, PSNR and RMSE for delta basis function combined with discrete wavelets transforms (D+WT) and undecimated wavelet transforms (D+UWT) with the minimum AIC. | 82 |
| 3.5 | AIC, BIC, PSNR and RMSE for discrete wavelets transforms (WT) and undecimated wavelet transforms (UWT) with the minimum AIC. | 82 |
| 3.6 | AIC, BIC, PSNR and RMSE for delta basis function combined with discrete wavelets transforms (D+WT) and undecimated wavelet transforms (D+UWT) with the minimum AIC. | 82 |
| 4.1 | Observational properties of Abell 1314 from the literature. | 91 |
| 4.2 | A1314 radio sources. Radio sources within the A1314 field detected in Stokes I at $\geq 5 \sigma_I$ are listed in order of increasing Right Ascension. Column [1] lists the source id as used in this work, [2] Right Ascension of the source in degrees, [3] Declination of the source in degrees, [4] peak flux density of the source at a frequency of 1.5 GHz, [5] Stokes I spectral index of the source at the position of the peak as determined from the VLA data used in this work, [6] distance of the source from the X-ray centre in kpc, and [7] indicates whether the source is also detected in polarisation at $\geq 6 \sigma_P$ | 91 |
| 4.3 | Abell 1314 JVLA radio observation details | 92 |
| 4.4 | Abell 1314 JVLA resolution and field-of-view details | 92 |
| 4.5 | 3C 286 coefficients details | 93 |
| 4.6 | 3C 147 coefficients details | 94 |

| | | |
|------|---|-----|
| 4.7 | Abell 1314 VLA RM-Synthesis details. | 100 |
| 4.8 | Different noise/variance quantities used in data reconstruction and analysis. | 101 |
| 4.9 | RM profile of Abell 1314 polarised sources. | 113 |
| 4.10 | RM profile of polarised source IC 708. | 113 |
| 6.1 | Observations for the MIGHTEE-POL Early Science Release. | 136 |
| 6.2 | MIGHTEE-POL image and cube properties for each pointing. | 138 |
| 6.3 | MeerKAT L-band simulation details | 140 |
| 6.4 | AIC, BIC, PSNR and RMSE for delta function basis. | 140 |
| 6.5 | AIC, BIC, PSNR and RMSE for discrete wavelets transforms (WT) and undecimated wavelet transforms (UWT) with the minimum AIC. | 140 |
| 6.6 | AIC, BIC, PSNR and RMSE for delta basis function combined with discrete wavelets transforms (D+WT) and undecimated wavelet transforms (D+UWT) with the minimum AIC. | 141 |
| 6.7 | AIC, BIC, PSNR and RMSE for delta basis function combined with discrete wavelets transforms (D+WT) and undecimated wavelet transforms (D+UWT) with the minimum AIC. | 141 |

List of Abbreviations

| | |
|---------|--|
| VLA | Very Large Array |
| JVLA | Karl Jansky Very Large Array |
| CS | Compressed Sensing |
| SKA | Square Kilometre Array |
| MIGHTEE | The MeerKAT International GHz Tiered Extragalactic Exploration |
| RM | Rotation Measure |

THE UNIVERSITY OF MANCHESTER

Abstract

Faculty of Science and Engineering
Department of Physics and Astronomy in the School of Natural Sciences

Doctor of Philosophy

Compressive Faraday Imaging for Next-Generation Radio Telescopes

by Miguel Angel Carcamo Vasquez

Over the past decade radio astronomy has grown considerably. Next-generation radio telescopes have pushed the boundaries of what is possible scientifically. Furthermore, the advent of broadband polarisation measurements with modern radio telescopes have enabled the investigation of the origin and evolution of magnetic fields using the RM Synthesis technique. This technique is based on the fact that there is Fourier relationship between polarized intensity (corrected by the spectral dependency) as a function of wavelength-squared and the Faraday dispersion function. However, the reconstruction of Faraday depth structures from incomplete spectral polarisation radio measurements is an under-constrained problem that requires additional regularisation. In this thesis, a compressed sensing framework for Faraday imaging named *cs-romer* along with a method to select the optimal basis/wavelet given the data are proposed. The framework is demonstrated on a variety of simulated scenarios and observational configurations. Additionally, *cs-romer* is demonstrated on real data from the JVLA and MeerKAT telescopes. The results of a JVLA analysis on the Abell 1314 cluster show that individual galaxies within Abell 1314 deviate from the behaviour expected for a Faraday-thin screen such as the intra-cluster medium and instead suggest that the Faraday rotation exhibited by these galaxies is dominated by their local environments. For MeerKAT we use the framework on the COSMOS field, showing that *cs-romer* is able to correct polarisation fraction outliers that are found when using the dirty Faraday spectra. In this work, I also developed two additional frameworks to calibrate cross-hand polarisation for eMERLIN observations towards Abell 1314, demonstrating the importance of such self-calibration by showing an improvement in signal-to-noise from 91.7 to 524.7.

Declaration of Authorship

I, Miguel Angel Carcamo Vasquez, declare that this thesis titled, “Compressive Faraday Imaging for Next-Generation Radio Telescopes” and the work presented in it are my own. I confirm that:

- This work was done wholly or mainly while in candidature for a research degree at this University.
- Where any part of this thesis has previously been submitted for a degree or any other qualification at this University or any other institution, this has been clearly stated.
- Where I have consulted the published work of others, this is always clearly attributed.
- Where I have quoted from the work of others, the source is always given. With the exception of such quotations, this thesis is entirely my own work.
- I have acknowledged all main sources of help.
- Where the thesis is based on work done by myself jointly with others, I have made clear exactly what was done by others and what I have contributed myself.



Signed:

Date: 13-07-2023

Copyright Statement

This page is a requirement, and must contain the exact words required by UoM. To double check that these words are up-to-date, go here: [University of Manchester Doctoral Presentation Regulations](#)

- (i) The author of this thesis (including any appendices and/or schedules to this thesis) owns certain copyright or related rights in it (the “Copyright”) and s/he has given The University of Manchester certain rights to use such Copyright, including for administrative purposes.
- (ii) Copies of this thesis, either in full or in extracts and whether in hard or electronic copy, may be made **only** in accordance with the Copyright, Designs and Patents Act 1988 (as amended) and regulations issued under it or, where appropriate, in accordance with licensing agreements which the University has from time to time. This page must form part of any such copies made.
- (iii) The ownership of certain Copyright, patents, designs, trademarks and other intellectual property (the “Intellectual Property”) and any reproductions of copyright works in the thesis, for example graphs and tables (“Reproductions”), which may be described in this thesis, may not be owned by the author and may be owned by third parties. Such Intellectual Property and Reproductions cannot and must not be made available for use without the prior written permission of the owner(s) of the relevant Intellectual Property and/or Reproductions.
- (iv) Further information on the conditions under which disclosure, publication and commercialisation of this thesis, the Copyright and any Intellectual Property and/or Reproductions described in it may take place is available in the University IP Policy (see [documents.manchester.ac.uk](#)), in any relevant Thesis restriction declarations deposited in the University Library, The University Library’s regulations (see [www.library.manchester.ac.uk/about/regulations/](#)) and in The University’s policy on Presentation of Theses

"We are the universe experiencing itself."

Carl Sagan

Acknowledgements

It has been a long four year journey. A journey in a different country where I have not only learned about astrophysics and magnetic fields and Faraday rotation, but also about attachment theory, human relationships, love and psychology.

I would like to start thanking my inner child and my wounds for teaching me that being vulnerable, emotional, self-conscious and loving is not a curse but a gift. Thank you also for showing me the real me, who was imprisoned by the machismo, insecure patterns and thoughts of not being vulnerable because someone is going to hurt me or judge me, or not being emotional because I have to be strong like a rock and keep going.

I would also like to thank my parents Mabel and Miguel, and my sister María Paz for their unconditional support and being with me this whole time. In this same paragraph, I would like to thank my family, aunts, uncles and cousins. I love you all with all my heart.

I want to thank my supervisor Anna, for your support and for being there when I needed you. You have always been there not only for academic questions or enquiries but also, and more importantly, for life stuff. I have always had found you very supportive, empathetic and a very good listener. Sometimes, that was the only thing I needed. Thank you also for trusting in me and for your help and advice. I really hope that we can keep working together in the future.

I cannot write this without thanking my psychotherapists, Valentina and Soledad. Thank you for your time, for providing me a secure space where I can show my vulnerabilities and emotions without fear of being judged, also for helping me on this journey of knowing myself better and being a better person. Thank you not only for teaching and showing me that people can change and heal through a secure attachment, but for experiencing it with me.

I would also like to thank Paddy, for his advice while being my co-supervisor and for being my supervisor while Anna was on maternity leave. He was always there to push me to write the Abell 1314 JVLA paper. He also was always there for questions and enquiries.

I want to use this space to thank all the JBCA people that I have met, travelled and talked with. Juanpi, Micah, Emma, Inigo and Fiona. You were always available when I felt like I had to talk with someone and you never judged anything I said. You were always there to give me your support. I wish the best to all of you and I hope that we can meet and talk again somewhere.

Finally, I want to acknowledge support from the National Agency for Research and Development (ANID) given by ANID PFCHA/DOCTORADO BECAS CHILE/2018-72190574 and ANID project Data Observatory Foundation DO210001.

To Lloyd...

Chapter 1

Introduction

1.1 Context

Over the past decade radio astronomy has grown substantially. Next generation radio telescopes such as ALMA in the millimetre waveband and LOFAR in the metre waveband have pushed the boundaries of what is possible scientifically. However, with every scientific opportunity produced by these new software-driven telescopes comes a new data challenge. Looking to the future, with even larger facilities such as the Square Kilometre Array (SKA) planned for construction, data challenges become even more substantial.

It is now well known that cosmic magnetic fields fill interstellar space, contribute significantly to the total pressure of interstellar gas, affect the evolution of galaxies and galaxy clusters and are essential for the formation of stars like our Sun. Nevertheless, answers to questions such as where do magnetic fields come from and how they evolve are still unknown (Widrow, 2002; Gaensler et al., 2004; Kandus et al., 2011; Subramanian, 2016; Martin-Alvarez et al., 2021).

One of the key science opportunities for next-generation telescopes is to investigate the origin and evolution of cosmic magnetic fields. This can be done by observing large, diffuse synchrotron radio sources such as radio halos and relics (e.g. Feretti, L. et al., 2001; Bonafede, A. et al., 2009; Cuciti, V. et al., 2021; Stuardi et al., 2021; Vacca et al., 2022; Stuardi, C. et al., 2022; Bonafede et al., 2022), cosmic filaments (e.g. Carretti et al., 2022a; Carretti et al., 2022b) and through the analysis of polarised emission from radio galaxies located at different projected distances with respect to the cluster centre (e.g. Govoni, F. et al., 2001; Bonafede, A. et al., 2010). The interaction of the intra-cluster medium (ICM), a magneto-ionic medium, with the linearly polarised synchrotron emission from these radio galaxies results in a rotation of the plane of polarisation known as Faraday rotation. This interaction will be produced by all magneto-ionic media along the line of sight and additional contributions will also come from the Galactic foreground and the intrinsic local contribution of the radio source itself (Brentjens, M. A. and de Bruyn, A. G., 2005).

Nevertheless, to truly understand magnetic fields, we require hundreds or maybe thousands of measurements of distant radio galaxies, pulsars, halos and relics. This is

where the unique angular and spectral resolution of next-generation comes into play. These instruments will allow us to make very large surveys of the sky, opening a new window into the magnetic universe (see examples of surveys with SKA precursor in Jarvis and Taylor et al., 2016 and Knowles, K. et al., 2022).

Even though the first paper on astronomical Faraday rotation was published by Burn in 1966, the literature is still light on this subject. In fact, it was not until the advent of broadband polarisation measurements when LOFAR became operational and when the Very Large Array (VLA) was upgraded and renamed to Karl G. Jansky Very Large Array in 2012, that a technique known as Rotation Measure (RM) Synthesis (Brentjens, M. A. and de Bruyn, A. G., 2005) began to be used by radio astronomers. This is based on the fact that Faraday rotation caused by a magneto-ionic plasma manifests as a rotation of the linearly polarised radio-wave's polarisation angle, appearing as a sinusoidal variation in the measured amplitude of Stokes Q & U as a function of wavelength squared. Consequently one can perform a Fourier inversion of the (Q,U) data with respect to wavelength squared in order to isolate the so-called "Faraday screen" in the corresponding Fourier space (Faraday depth). However, wavelength/frequency space cannot be measured completely by radio telescopes and, consequently, Faraday depth reconstruction suffers many of the same deconvolution issues as standard interferometric imaging. Even so, with the spectral resolution of the radio telescopes mentioned before, scientists were able to resolve Faraday depth structures and then infer physical parameters of the magnetized plasma (e.g. Stuardi et al., 2021; Vacca et al., 2022; Stuardi, C. et al., 2022).

In this thesis, I introduce a novel compressed sensing framework for Faraday imaging and provide a method to select the optimal basis or wavelet, considering the given data. In Chapter 1, I delve into the physical and mathematical foundations of synchrotron radiation, astronomical Faraday rotation, and RM Synthesis. In Chapter 2 I further explore the concepts of radio interferometry and aperture synthesis, both of which are central to this study. Chapter 3 is dedicated to the introduction of compressed sensing concepts and their respective applications. Within this chapter, I also detail how the proposed compressed sensing framework for Faraday imaging functions and how the selection process for the optimal basis operates using simulated data. A comparison between Faraday depth reconstructions, made using the compressed sensing framework, and the widely recognized RM-CLEAN method, brings the chapter to a close. In Chapter 4, I demonstrate the practical application of the compressed sensing framework using real JVLA data from Abell 1314. Chapter 5 focuses on processing the Abell 1314 data with the angular and spectral resolution provided by the eMERLIN radio telescope. Further, in Chapter 6, I discuss the application of the framework to the MIGHTEE-POL survey, which is currently being conducted with the MeerKAT telescope. Lastly, in Chapter 7, I put forward recommendations for future work and provide my concluding thoughts.

1.2 Plasma effects

Free charges often play an essential role in astrophysical applications. They determine the propagation properties of the medium. The concept of plasma refers to a gas that is so hot that its constituent atoms split up into electrons and ions (ionized gas). Since plasma is then made up of electrically charged particles, they are strongly influenced by electrostatic and magnetic field forces.

In this section I will review Maxwell equations to show how electric charges and electromagnetic fields are mathematically related.

1.2.1 Review of Maxwell's Equations for Electromagnetism

As radiation is an electromagnetic phenomena, it is useful therefore to give a brief view of the governing equations of electromagnetism. The following derivations are mainly based on Purcell and Morin, 2013 book. However, I highly recommend also checking Griffiths, 2017; Zangwill, 2012 and Jackson, 2003.

In the 18th century, experiments from Priestley, Cavendish, and Coulomb gave us important and founding information about the force between stationary charged objects. That is, the force produced on a charge q at point r by N point charges q_k at points r_k is given by Coulomb's law:

$$F = \frac{1}{4\pi\epsilon_0} \sum_{k=1}^N q q_k \frac{r - r_k}{|r - r_k|^3}. \quad (1.1)$$

If I define the charge density of the N point charges as

$$\rho(r) = \sum_{k=1}^N q_k \delta(r - r_k), \quad (1.2)$$

I can re-write Coulomb's law such that

$$F = qE(r), \quad (1.3)$$

where the vector electric field $E(r)$ is defined as

$$E(r) = \frac{1}{4\pi\epsilon_0} \int \rho(r') \frac{r - r'}{|r - r'|^3} d^3r'. \quad (1.4)$$

Thus, the electric field produced by an arbitrary charge distribution is the vector sum of the electric fields produced by each of its constituent pieces (Zangwill, 2012, Section 2.2.1). If I use the following mathematical identities

$$\nabla \frac{1}{|r - r'|} = -\frac{r - r'}{|r - r'|^3} \quad \text{and} \quad \nabla^2 \frac{1}{|r - r'|} = -4\pi\delta(r - r') \quad (1.5)$$

it is possible to show that

$$\nabla \cdot E = \frac{\rho}{\epsilon_0} \quad (1.6)$$

and

$$\nabla \times E = 0, \quad (1.7)$$

where Equation 1.6 is known as Gauss' law. The second (Equation 1.7) is only valid for electrostatics.

Later on, Ampere published the calculation of a force on a closed loop carrying a current I due to presence of N other loops carrying currents I_k . If r points to the dl element of loop I and r_k points to the dl_k element of the k -th loop, the Ampere equation for force in I is

$$F = -\frac{\mu_0}{4\pi} \oint I dl \sum_{k=1}^N \oint I_k \frac{r - r_k}{|r - r_k|^3} dl_k, \quad (1.8)$$

which we can re-write as

$$F = \oint I \times B(r) dl, \quad (1.9)$$

where $B(r)$ is written using the Biot and Savart (1820) form such that

$$B(r) = \frac{\mu_0}{4\pi} \sum_{k=1}^N \oint I_k \times dl_k \frac{r - r_k}{|r - r_k|^3}. \quad (1.10)$$

Additionally, if I define $j(r) = \rho(r)v(r)$ as the current density at any point r , where $v(r)$ characterizes the motion of the charge density at that point, the magnetic field produced by any time-independent current density is

$$B(r) = \frac{\mu_0}{4\pi} \int \frac{j(r') \times (r - r')}{|r - r'|^3} d^3r'. \quad (1.11)$$

As long as the current density satisfies the steady-current condition, in other words, $\nabla \cdot j = 0$. It is possible to show that current loops and permanent magnets satisfy the conditions

$$\nabla \cdot B = 0 \quad (1.12)$$

and

$$\nabla \times B = \mu_0 j, \quad (1.13)$$

where the first equation represents the Maxwell's second equation and the second, only valid for magnetostatics is known as the Ampere's law.

Maxwell's third law derives from Faraday's law of electromagnetic induction. Faraday made several experiments (see Faraday, 2012), however, as a simplification to the reader I would like to use an example depicted in Figure 1.1.

Faraday observed that current could be induced when a conductor cuts across the perpendicular magnetic field lines. He observed that whether the magnetic field changes or the conductor moves. Then, German mathematical physicists Neumann, Weber and Kirchhoff constructed the mathematical description of the phenomenon. Neumann began with the statement known as Lenz's law which describes that the current induced in a circuit is such as to oppose in the magnetic field flux through the circuit. In other words, changing the magnetic flux within a circuit produces an induced electromotive

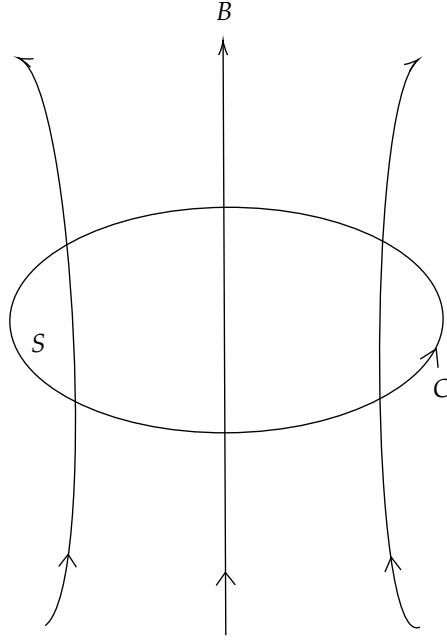


FIGURE 1.1: Presence of an induction B on closed circuit C formed by a conducting wire.

force (emf) or voltage within the circuit. Mathematically, this can be expressed as

$$\text{emf} = -\frac{d\Phi}{dt}, \quad (1.14)$$

where Φ is the magnetic flux within a circuit. We also can interpret the existence of the induced emf as indicating the presence of a induced electric field along the wire C . This can be written as

$$\oint_C E \, dl = -\frac{d\Phi}{dt}. \quad (1.15)$$

Finally, the total magnetic flux is simply the sum of the magnetic field over the area S enclosed by the wire C :

$$\Phi(t) = \int_S B(r, t) \, dS, \quad (1.16)$$

therefore, if I substitute Equation 1.16 into Equation 1.15 and apply the Stokes' theorem we have the third of Maxwell's equations given by

$$\int_S \nabla \times E \, dS = -\frac{d}{dt} \int_S B(r, t) \, dS = \int_S -\frac{dB(r, t)}{dt} \, dS.$$

Lastly, this can also be written as

$$\nabla \times E = -\frac{\partial B}{\partial t}. \quad (1.17)$$

At this point I have the following equations:

$$\begin{array}{ll}
\nabla \cdot E = \frac{\rho}{\epsilon_0} & \nabla \cdot B = 0 \\
\nabla \times E = -\frac{\partial B}{\partial t} & \nabla \times B = \mu_0 j
\end{array}
\tag{1.18}$$

We are assuming that all these equations, except Faraday's law are still correct when fields vary with time. One of the major contributions of James Maxwell was to find out that Equation 1.13 is incompatible with charge conservation and then showing that this inconsistency could be solved introducing an additional "current".

If I start by assuming that the divergence of a curl operator is always zero and apply this to our equations, we will see that for Equation 1.17 we have

$$\nabla \cdot (\nabla \times E) = \nabla \cdot \left(-\frac{\partial B}{\partial t}\right) = -\frac{\partial}{\partial t}(\nabla \cdot B), \tag{1.19}$$

where the left side is zero, and the right side is zero because of Equation 1.12. However, if we apply the same reasoning to Equation 1.13 we get

$$\nabla \cdot (\nabla \times B) = \mu_0(\nabla \cdot j). \tag{1.20}$$

And I know that for steady currents $\nabla \cdot j = 0$. However, for non-steady currents

$$\nabla \cdot j = -\frac{\partial \rho}{\partial t}. \tag{1.21}$$

To find the missing term I can make use of Gauss' law such that

$$\nabla \cdot j = -\frac{\partial \rho}{\partial t} = -\epsilon_0 \nabla \cdot \frac{\partial E}{\partial t}. \tag{1.22}$$

If I add this term to Ampere's law I have that

$$\nabla \times B = \mu_0 j + \mu_0 \epsilon_0 \frac{\partial E}{\partial t}, \tag{1.23}$$

which is known as the Ampere-Maxwell law and is the fourth of Maxwell's equations.

So far I have derivated the following Maxwell's equations according to the International System of Units (SI):

$$\begin{array}{ll}
\nabla \cdot E = \frac{\rho}{\epsilon_0} & \nabla \cdot B = 0 \\
\nabla \times E = -\frac{\partial B}{\partial t} & \nabla \times B = \mu_0 j + \mu_0 \epsilon_0 \frac{\partial E}{\partial t}
\end{array}
\tag{1.24}$$

To convert these equations to Gaussian units I will go back to Equation 1.1. This equation written in SI units contains the factor $1/4\pi\epsilon_0$, when using Gaussian units, this

factor is 1. Therefore, I can simply set $\epsilon_0 = 1/4\pi$. And since $\mu_0\epsilon_0 = 1/c^2$, I can also set $\mu_0 = 4\pi/c^2$ such that

$$\boxed{\begin{array}{ll} \nabla \cdot \mathbf{E} = 4\pi\rho & \nabla \cdot \mathbf{B} = 0 \\ \nabla \times \mathbf{E} = -\frac{\partial \mathbf{B}}{\partial t} & \nabla \times \mathbf{B} = \frac{4\pi}{c^2}\mathbf{j} + \frac{1}{c^2}\frac{\partial \mathbf{E}}{\partial t} \end{array}} \quad (1.25)$$

Since Lorentz force is defined as $\mathbf{F} = q\mathbf{v} \times \mathbf{B}$ in SI units, and as $\mathbf{F} = (q/c)\mathbf{v} \times \mathbf{B}$ in Gaussian units, the last step to convert Maxwell's equations to Gaussian units is to replace every \mathbf{B} to \mathbf{B}/c . Consequently, I get

$$\boxed{\begin{array}{ll} \nabla \cdot \mathbf{E} = 4\pi\rho & \nabla \cdot \mathbf{B} = 0 \\ \nabla \times \mathbf{E} = -\frac{1}{c}\frac{\partial \mathbf{B}}{\partial t} & \nabla \times \mathbf{B} = \frac{4\pi}{c}\mathbf{j} + \frac{1}{c}\frac{\partial \mathbf{E}}{\partial t} \end{array}} \quad (1.26)$$

1.3 Radio Emission Mechanisms

1.3.1 Synchrotron Emission

Through the whole reading of this thesis you will find out that the main source of radio waves being studied are those originating from synchrotron radiation, also known as magnetobremssstrahlung (Burke et al., 2019).

Russian astronomer Iosif Shklovsky proposed in 1953 that synchrotron radiation is produced when relativistic electrons spiral along magnetic field lines (Carroll and Ostlie, 2007). Mathematically, this all starts from the equation relating the magnetic field on a moving charge, q , (with velocity much less than the speed of light) also known as Lorentz force equation,

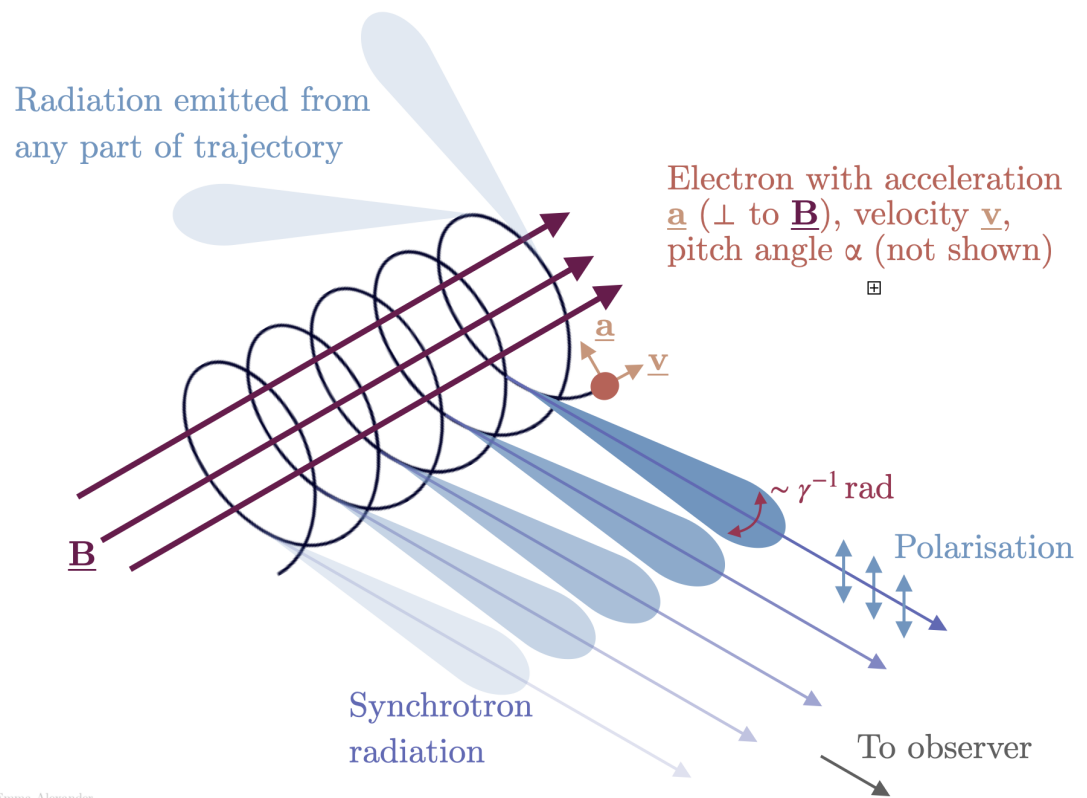
$$\mathbf{F} = q\left(\frac{\mathbf{v}}{c} \times \mathbf{B}\right), \quad (1.27)$$

where \mathbf{F} is the force acting on charge q with velocity \mathbf{v} due to a magnetic field, \mathbf{B} . Note that in this equation all boldface quantities are vectors. Additionally, the magnetic force is perpendicular to the particle velocity such that $\mathbf{F} \cdot \mathbf{v} = 0$. Therefore, no power is transferred to the charge and its kinetic energy remains constant. In a constant magnetic field the charge moves along a magnetic field on a uniform helical path with constant linear and angular speeds. This depicted in Figure 1.2.

If I replace \mathbf{F} by $m_q r_L \omega^2$, where $\omega = \mathbf{v}/r_L$ is the angular frequency and r_L is the Lorentz radius I can obtain the cyclotron frequency:

$$\omega_{\text{cyc}} = \frac{qB}{m_q c}, \quad (1.28)$$

which shows that the orbital frequency of non-relativistic charges is independent of the particle speed so long as $v \ll c$.



Emma Alexander

FIGURE 1.2: Diagram of synchrotron emission, arising from a charged particle moving along a helical path around an ordered magnetic field. The Lorentz force causing the acceleration a is perpendicular to the magnetic field vector \underline{B} , and both are also perpendicular to the circular component of the charge velocity \underline{v} . The radiation is concentrated in a beamwidth of $\sim 1/\gamma$ radians. (Obtained from Emma Alexander at <https://emmaalexander.github.io/resources.html>).

Before continuing with the case of what happens when we have relativistic charges, I need to recall the Lorentz factor, defined as

$$\gamma \equiv \frac{1}{\sqrt{1 - \beta^2}}, \quad (1.29)$$

where $\beta = v/c$.

Relativistic charges have a mass of $m = \gamma m_q \gg m_q$, therefore, their angular frequency is reduced such that

$$\omega_B = \frac{\omega_{\text{cyc}}}{\gamma} = \frac{qB}{\gamma m_q c}, \quad (1.30)$$

Any charged particle accelerated by a magnetic field will emit radiation. Thus, using the equation for total emitted radiation for relativistic particles P is (see Rybicki and Lightman, 1985, Equation 4.92)

$$P = \frac{2q^2}{3c^3} \gamma^4 (a_\perp^2 + \gamma a_\parallel^2). \quad (1.31)$$

If I write the Lorentz force equation for relativistic charges as

$$m_q \gamma \frac{d\mathbf{v}}{dt} = \frac{q}{c} \mathbf{v} \times \mathbf{B} \quad (1.32)$$

and separate the velocity components along the field \mathbf{v}_\parallel and in the plane normal to the field \mathbf{v}_\perp such that

$$a_\parallel = \frac{d\mathbf{v}_\parallel}{dt} = 0, \quad a_\perp = \frac{d\mathbf{v}_\perp}{dt} = \omega_B \mathbf{v}_\perp = \frac{qB}{\gamma m_q c} \mathbf{v}_\perp = \frac{qB}{\gamma m_q c} \sin \alpha, \quad (1.33)$$

where angle α between electron velocity \mathbf{v} and magnetic field \mathbf{B} is called the pitch angle.

I can therefore find that the total power, P , emitted by a relativistic charge is

$$P = \frac{2}{3} \frac{q^4 \gamma^2 B^2 v^2 \sin^2 \alpha}{m_q^2 c^5} = \frac{2}{3} \frac{q^4 \gamma^2 B^2 \beta^2 \sin^2 \alpha}{m_q^2 c^3}. \quad (1.34)$$

From Equation 6.16 in Rybicki and Lightman, 1985 I have that the averaged power per unit frequency is

$$P(\omega) = C_1 F\left(\frac{\omega}{\omega_c}\right), \quad (1.35)$$

where

$$\omega_c \equiv \frac{3\gamma^2 qB \sin \alpha}{2m_q c} \quad (1.36)$$

is defined as a critical frequency, C_1 is a constant of proportionality and F is a dimensionless function. By comparing the total power as evaluated over the integral over ω to Equation 1.34 I have that

$$P = \int_0^\infty P(\omega) d\omega = C_1 \int_0^\infty F\left(\frac{\omega}{\omega_c}\right) d\omega = \omega_c C_1 \int_0^\infty F(x) dx, \quad (1.37)$$

where $x \equiv \omega/\omega_c$. Note that it is not possible to know what $\int F(x) dx$ is until I specify $F(x)$. However, it is possible to regard its nondimensional value as arbitrary and set a convention for the normalization of $F(x)$. Thus, from Equations 1.34 and 1.36 I can conclude that for the highly relativistic case ($\gamma \gg 1$ or $\beta \approx 1$) the power per unit frequency emitted by each charged particle is

$$P(\omega) = \frac{\sqrt{3} q^3 B \sin \alpha}{2\pi m_q c^2} F\left(\frac{\omega}{\omega_c}\right). \quad (1.38)$$

It is important to highlight that the choice of $\sqrt{3}/2$ for the nondimensional constant has been made to anticipate the conventional choice for the normalization of F , discussed below.

Until now I have considered the radiation emitted by a single relativistic charge. However, in a realistic scenario such as astrophysical plasmas, I should consider a relativistic gas with a number-density distribution of electrons $N(E)$. The number of density of particles with energies between E and $E + dE$ (or γ and $\gamma + d\gamma$) is often approximated as power law such that

$$N(E)dE = CE^{-p}dE, \quad E_1 < E < E_2, \quad (1.39)$$

or, alternatively,

$$N(\gamma)d\gamma = C\gamma^{-p}d\gamma, \quad \gamma_1 < \gamma < \gamma_2, \quad (1.40)$$

where p is the particle distribution index and C is a quantity that varies with pitch angle.

By calculating the integral of $N(\gamma)d\gamma$ times the single particle radiation formula (see Equation 6.18 in Rybicki and Lightman, 1985) over all energies, or γ , I can calculate the total power radiated per unit volume per unit frequency, that is

$$P_{\text{tot}}(\omega) = C \int_{\gamma_1}^{\gamma_2} P(\omega) \gamma^{-p} d\gamma \propto \int_{\gamma_1}^{\gamma_2} F\left(\frac{\omega}{\omega_c}\right) \gamma^{-p} d\gamma. \quad (1.41)$$

Thus, if I change the variables of integration $x \equiv \frac{\omega}{\omega_c}$ again and noting $\omega_c \propto \gamma^2$, I find

$$P_{\text{tot}}(\omega) \propto \omega^{-(p-1)/2} \int_{x_1}^{x_2} F(x) x^{(p-3)/2} dx. \quad (1.42)$$

Here, the limits x_1 and x_2 correspond to the limits of γ_1 and γ_2 which depend on ω . We can approximate $x_1 \approx 0$ and $x_2 \approx \infty$ if the energy limits are sufficiently wide. Therefore, the integral is approximately constant and I end up with

$$P_{\text{tot}}(\omega) \propto \omega^{-(p-1)/2}, \quad (1.43)$$

where I can relate the spectral index s with the particle distribution index p by

$$s = \frac{p-1}{2}. \quad (1.44)$$

Finally, as an example, Figure 1.3 confirms that we do see a power-law frequency

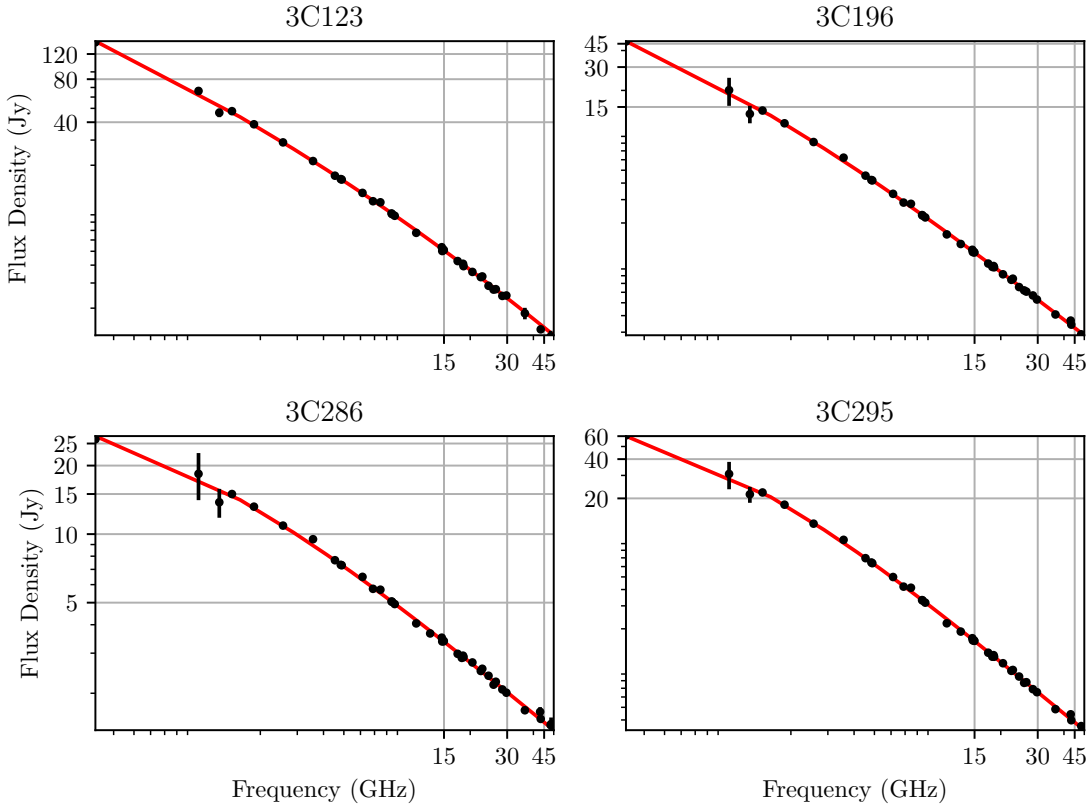


FIGURE 1.3: Flux densities of sources 3C 123, 3C 196, 3C 286 and 3C 295 for frequencies between 1 and 50 GHz. Derived flux densities from Perley and Butler, 2013 values are depicted as black dots. The red lines are the result of a power-law fitting on the flux density data.

spectrum for synchrotron emission. The figure shows flux densities as a function of frequency for sources 3C 123, 3C 196, 3C 286 and 3C 295. The black dots and their error bars are real data measured in Perley and Butler, 2013 and the red lines are a result of the power-law fitting on the data.

1.3.2 Polarisation of Synchrotron Emission

Before continuing, note that I can express Equation 1.38 as

$$P(\omega) = \frac{\sqrt{3}}{2\pi} \frac{q^3 B \sin \alpha}{m_q c^2} F(x), \quad (1.45)$$

where again $x \equiv \frac{\omega}{\omega_c}$ and $F(x)$ is a function that integrates a modified Bessel function of order 5/3:

$$F(x) \equiv x \int_x^\infty K_{5/3}(\xi) d\xi. \quad (1.46)$$

Due to the polarisation of synchrotron radiation, I need to split the radiation into its perpendicular and parallel (to the magnetic field) components. Hence, we have a function

$$G(x) \equiv x K_{2/3}(x) \quad (1.47)$$

expressed in terms a modified Bessel function of order 2/3 and we can define the power spectra of the polarised components as

$$P_{\perp,\parallel}(\omega) = \frac{\sqrt{3} q^3 B \sin \alpha}{4\pi m_q c^2} \begin{cases} F(x) + G(x) & (\perp B), \\ F(x) - G(x) & (\parallel B). \end{cases} \quad (1.48)$$

Notice that a single charge would be elliptically polarised in this scenario. However, when having a distribution of particles that varies smoothly with pitch angle, the elliptical components will cancel out (see Section 6.5 in Rybicki and Lightman, 1985). Thus, radiation is partially linearly polarised and it is possible to obtain the polarisation fraction for these particles as

$$\Pi(\omega) = \frac{P_{\perp}(\omega) - P_{\parallel}(\omega)}{P_{\perp}(\omega) + P_{\parallel}(\omega)} = \frac{G(x)}{F(x)}. \quad (1.49)$$

We can also extend Equation 1.49 for particles that follow a power law distribution incorporating the particle distribution index p such that

$$\Pi = \frac{p+1}{p+\frac{7}{3}}. \quad (1.50)$$

1.4 Astronomical Faraday Rotation

If I define electric and magnetic fields as space and time varying quantities such that

$$E(r, t) = E_0 e^{i(k \cdot r - \omega t)} \quad (1.51)$$

$$B(r, t) = B_0 e^{i(k \cdot r - \omega t)}, \quad (1.52)$$

where $k = (k_x, k_y, k_z)$ is the wave vector (in radians per meter) and ω is the angular frequency (in radians per second), then Maxwell's equations, see Section 1.2.1, become

| | |
|---|--|
| $ik \cdot E_0 = 4\pi\rho$ | $ik \cdot B_0 = 0$ |
| $ik \times E_0 = i\frac{\omega}{c} B_0$ | $ik \times B_0 = \frac{4\pi}{c} j - i\frac{\omega}{c} E_0$ |

(1.53)

Additionally, if I assume that the plasma has an electron density n and that there is no external magnetic field, therefore, each electron responds to an electric field following Equation 1.3 (Newton's law). Additionally, if from now on I denote an electron charge as $q = -e$, we have that

$$m \frac{dv(r, t)}{dt} = -eE(r, t), \quad (1.54)$$

and by integration $v(r, t)$ becomes

$$v(r, t) = \frac{eE(r, t)}{i\omega m}. \quad (1.55)$$

Replacing Equation 1.55 into the definition of current density given by

$$j = \rho(r, t)v(r, t) = -n(r, t)v(r, t)e, \quad (1.56)$$

I have

$$j(r, t) = \sigma E(r, t), \quad (1.57)$$

where the conductivity, σ , is

$$\sigma(r, t) = \frac{in(r, t)e^2}{\omega m}. \quad (1.58)$$

By calculating the derivative of charge density with respect to time and using Equation 1.21 I have

$$\begin{aligned} \frac{\partial \rho(r, t)}{\partial t} &= -e \frac{\partial n(r, t)}{\partial t} \\ \frac{\partial \rho(r, t)}{\partial t} &= -i\omega n(r, t)e \\ \frac{\partial \rho(r, t)}{\partial t} &= -i\omega \rho(r, t), \end{aligned} \quad (1.59)$$

and therefore,

$$\begin{aligned} \frac{\partial \rho(r, t)}{\partial t} + \nabla \cdot j(r, t) &= 0 \\ -i\omega \rho(r, t) + ik \cdot j(r, t) &= 0, \end{aligned} \quad (1.60)$$

such that

$$\rho(r, t) = \frac{k \cdot j(r, t)}{\omega} = \frac{\sigma(r, t)k \cdot E(r, t)}{\omega}. \quad (1.61)$$

Using these forms of $j(r, t)$ and $\rho(r, t)$ and introducing the dielectric constant defined as

$$\epsilon \equiv 1 - \frac{4\pi\sigma(r, t)}{i\omega}, \quad (1.62)$$

I can write Maxwell's equations as

| | |
|--|--|
| $ik \cdot \epsilon E_0 = 0$ | $ik \cdot B_0 = 0$ |
| $ik \times E_0 = i\frac{\omega}{c}B_0$ | $ik \times B_0 = -i\frac{\omega}{c}\epsilon E_0$ |

(1.63)

Here we find that k , E_0 and B_0 form an orthogonal right-hand vector triad where E_0 and B_0 are related such that

$$E_0 = \frac{\omega}{kc}B_0 \quad B_0 = \frac{\omega}{kc}\epsilon E_0,$$

then replacing B_0 I have

$$E_0 = \epsilon \left(\frac{\omega}{kc} \right)^2 E_0,$$

and consequently

$$c^2 k^2 = \epsilon \omega^2. \quad (1.64)$$

Substituting Equation 1.58 into 1.62 an alternative expression for the dielectric constant can be expressed as

$$\epsilon = 1 - \left(\frac{\omega_p}{\omega} \right)^2, \quad (1.65)$$

where ω_p is the plasma frequency defined as

$$\omega_p^2 = \frac{4\pi n(r, t) e^2}{m}. \quad (1.66)$$

Hence, I can substitute Equation 1.65 into 1.64 and calculate the dispersion relation connecting k and ω as

$$k = c^{-1} \sqrt{\omega^2 - \omega_p^2} \quad (1.67)$$

$$\omega^2 = \omega_p^2 + k^2 c^2. \quad (1.68)$$

I can notice that if $\omega < \omega_p$ the wave number is imaginary and therefore

$$k = \frac{i}{c} \sqrt{\omega_p^2 - \omega^2}. \quad (1.69)$$

It can be seen that the amplitude of the wave exponentially decreases with a factor of the order $2\pi c / \omega_p$. I can conclude that ω_p defines the *plasma cutoff frequency* below which there is not electromagnetic propagation.

Now I will consider the effect of an external fixed magnetic field \mathbf{B}_0 . Wave properties will then depend on the direction of the propagation relative to the direction of \mathbf{B}_0 . In order to this, I need to recall Equation 1.28 for cyclotron frequency ω_{cyc} and Lorentz force equation when both electric and magnetic field are present, that is

$$\mathbf{F} = -e(\mathbf{E} + \frac{\mathbf{v}}{c} \times \mathbf{B}_0) \quad (1.70)$$

$$m \frac{d\mathbf{v}}{dt} = -e\mathbf{E} - \frac{e}{c} \mathbf{v} \times \mathbf{B}_0. \quad (1.71)$$

Additionally, let's define the propagating wave as circularly polarised and sinusoidal

$$\mathbf{E}(t) = E_0 e^{-i\omega t} (\hat{\mathbf{x}} \mp i\hat{\mathbf{y}}), \quad (1.72)$$

where $-$ and $+$ correspond to right and left circular polarisation, respectively. For simplicity, I will assume that this wave propagates along a fixed magnetic field \mathbf{B}_0

$$\mathbf{B}_0 = B_0 \hat{\mathbf{z}}. \quad (1.73)$$

By substituting Equations 1.72 and 1.73 into Equation 1.71 it can be shown that the steady-state velocity $\mathbf{v}(t)$ is

$$\mathbf{v}(t) = \frac{-ie\mathbf{E}(t)}{m(\omega \pm \omega_{\text{cyc}})} \quad (1.74)$$

where ω_{cyc} is given in Equation 1.28. Additionally, if I substitute Equation 1.74 into 1.56 we can calculate a new expression for the dielectric constant such that

$$\epsilon_{\text{R,L}} = 1 - \frac{\omega_p^2}{\omega(\omega \pm \omega_{\text{cyc}})}, \quad (1.75)$$

where R corresponds to $+$ and L corresponds to $-$.

From this it is clear that the magnetic field of the plasma affects the velocity of one polarisation component of the wave, resulting in a delay and therefore a rotation in the polarisation angle. This effect is known as *Faraday rotation* and is illustrated in Figure 1.4.

The phase angle, ϕ , of a polarised wave travelling a distance d can be defined as

$$\phi_{\text{R,L}} = \int_0^d k_{\text{R,L}} ds, \quad (1.76)$$

where

$$k_{\text{R,L}} = \frac{\omega}{c} \sqrt{\epsilon_{\text{R,L}}}. \quad (1.77)$$

Therefore, the rotation of the polarisation angle $\Delta\phi$ is

$$\Delta\phi = \frac{\phi_{\text{R}} - \phi_{\text{L}}}{2}. \quad (1.78)$$

If we assume that $\omega \gg \omega_p$ and $\omega \gg \omega_{\text{cyc}}$ such that $\frac{\omega_p^2}{\omega(\omega \pm \omega_{\text{cyc}})}$ is a positive real number, I can approximate the square root in Equation 1.77 as

$$k_{\text{R,L}} \approx \frac{\omega}{c} \left[1 - \frac{\omega_p^2}{2\omega^2} \left(1 \mp \frac{\omega_{\text{cyc}}}{\omega} \right) \right]. \quad (1.79)$$

Replacing this latter result into Equation 1.76 and consequently in Equation 1.78 I have

$$\begin{aligned} \Delta\phi &= \frac{1}{2} \int_0^d (k_{\text{R}} - k_{\text{L}}) ds \\ &= \frac{1}{2} \int_0^d \frac{1}{c\omega^2} \omega_p^2 \omega_{\text{cyc}} ds. \end{aligned} \quad (1.80)$$

Finally, I can substitute ω_p^2 (see Equation 1.66) and ω_{cyc} (see Equation 1.28) to obtain the standard Faraday rotation measure (RM) formula:

$$\Delta\phi = \frac{2\pi e^3}{m^2 c^2 \omega^2} \int_0^d n_e B_{\parallel} ds \quad (1.81)$$

$$= \lambda^2 \text{RM} \quad (1.82)$$

Emma Alexander

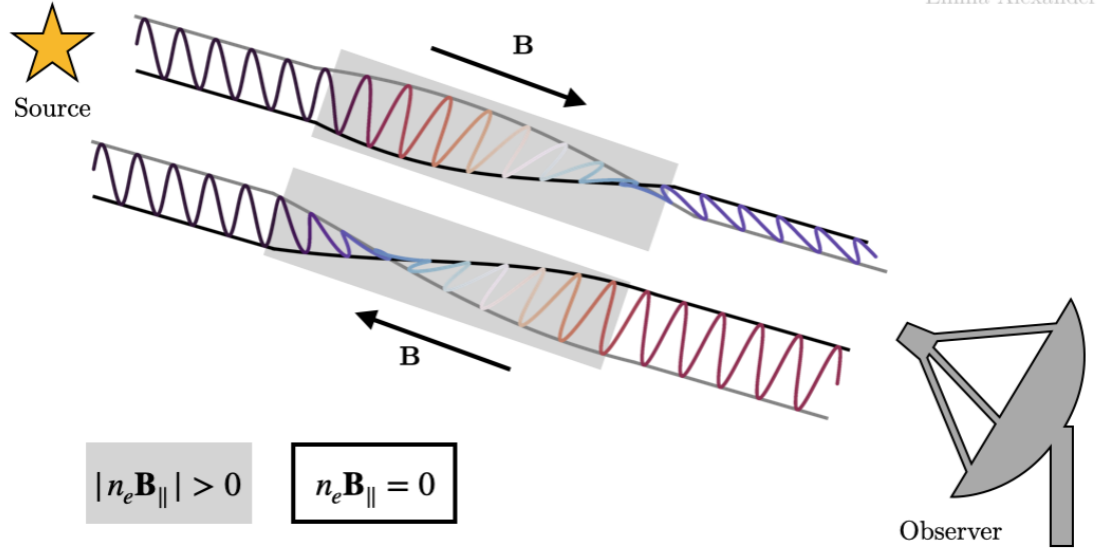


FIGURE 1.4: Representation of astronomical Faraday rotation. Two electromagnetic waves coming from an astronomical source and passing through magneto-ionic plasma (grey background) are shown. The waves pass through plasma with opposite orientations of magnetic field, therefore, the polarisation angles of the waves at the top and bottom are rotated clockwise and anti-clockwise, respectively. (Obtained from Emma Alexander at <https://emmaalexander.github.io/resources.html>).

where

$$\text{RM} = \frac{e^3}{2\pi m^2 c^4} \int_0^d n_e B_{\parallel} ds \quad (1.83)$$

and λ^2 is the wavelength squared of the wave.

Note that this formula holds in general if we use B_{\parallel} which is the component of \mathbf{B} along the line of sight. From equations 1.81 and 1.82 it can be seen that $\Delta\phi$ varies with frequency and consequently, with wavelength. Therefore, to study the information about the interstellar magnetic field it is necessary to make measurements at several frequencies in order to determine the value of the integral. Note that if the direction of the field changes often along the line of sight then these equations only result on a lower limit to cosmic magnetic field magnitudes.

1.5 The RM Synthesis Method

In the last section, I have highlighted that measurements at multiple frequencies are needed in order to calculate the integral in Equation 1.83. The construction of modern radio telescopes and their ability to measure polarised radio light at broadband frequencies have enabled the widespread use of the RM Synthesis technique (Burn, 1966; Brentjens, M. A. and de Bruyn, A. G., 2005). RM Synthesis considers the Fourier relationship between polarised intensity (corrected by the spectral dependency) as a function of wavelength-squared $P(\lambda^2)$ and the Faraday dispersion function (FDF) $F(\phi)$. Thus, I can recover the polarised intensity as a function of Faraday depth, ϕ , such that

$$F(\phi) = \int_{-\infty}^{\infty} \frac{P(\lambda^2)}{s(\lambda^2)} e^{-2i\phi\lambda^2} d\lambda^2, \quad (1.84)$$

where $s(\lambda^2)$ is the spectral dependence

$$s(\lambda^2) = \frac{I(\lambda^2)}{I(\lambda_0^2)} = \left(\frac{\lambda^2}{\lambda_0^2} \right)^{\alpha/2}, \quad (1.85)$$

and

$$P(\lambda^2) = |P(\lambda^2)| e^{2i\chi(\lambda^2)} = Q(\lambda^2) + iU(\lambda^2). \quad (1.86)$$

Note that $P(\lambda^2)$ can be recovered from the polarised intensity as a function of Faraday depth such that

$$\frac{P(\lambda^2)}{s(\lambda^2)} = \frac{1}{\pi} \int_{-\infty}^{\infty} F(\phi) e^{2i\phi\lambda^2} d\phi. \quad (1.87)$$

Faraday depth studies have allowed us to understand the physics of many astrophysical systems, including our own Galaxy (e.g. Iacobelli et al., 2013), external galaxies (e.g. Cantwell et al., 2020) and on larger scales the intra- and inter-cluster medium (e.g. Stuardi et al., 2021). Even though at this point RM Synthesis technique looks conceptually simple, in practice the implementation of this method and the interpretation of the resulting Faraday dispersion function are complicated by a number of different factors.

Firstly, Faraday depth is the Fourier conjugate variable of λ^2 , however, radio spectrometers sample Stokes parameters Q and U uniformly in frequency, not λ^2 . This irregular sampling introduces a similar computational complexity to the one encountered when imaging data from radio interferometers. A common solution is to use the Fast Fourier Transform (FFT) after re-sampling the original data onto a regular grid using a convolutional kernel. For RM Synthesis this approach has been implemented, for example, in the widely used PYRMSYNTH¹ package used for the LOFAR Two-metre Sky Survey (Van Eck et al., 2018) and in RMTTOOLS RM-CLEAN². Even in the case of using gridding, the inherent non-linear mapping of frequency to λ^2 results in a non-uniform distribution of measurements in this space. This introduces a multiplicative weighting function $W(\lambda^2)$ which in Faraday depth space produces a convolution of the true Faraday dispersion function with a transfer function such that

$$\tilde{F}(\phi) = F(\phi) * \text{RMTF}(\phi) = K \int_{-\infty}^{+\infty} \frac{W(\lambda^2)}{s(\lambda^2)} P(\lambda^2) e^{-2i\phi\lambda^2} d\lambda^2, \quad (1.88)$$

where

$$\text{RMTF}(\phi) = \frac{1}{K} \int_{-\infty}^{+\infty} \frac{W(\lambda^2)}{s(\lambda^2)} e^{-2i\phi\lambda^2} d\lambda^2 \quad (1.89)$$

¹<https://github.com/mrbell/pyrmsynth>

²<https://github.com/CIRADA-Tools/RM-Tools>

is commonly known as the Rotation Measure Transfer Function (RMTF) or, alternatively, the Rotation Measure Spread Function (RMSF) and K is defined as

$$K = \int_{-\infty}^{+\infty} \frac{W(\lambda^2)}{s(\lambda^2)} d\lambda^2. \quad (1.90)$$

The second complication is that $P(\lambda^2)$ does not exist at $\lambda < 0$. In the imaging case the sky brightness distribution is always real, however, $F(\phi)$ is hardly ever a purely real quantity and therefore a lack of measurements at $\lambda^2 < 0$ is a fundamental limitation when attempting to reconstruct a Faraday signal. The consequence of this is that the problem of deconvolving the RMTF from the Faraday depth spectra (e.g. Heald, 2009) is inherently under-constrained due to the irregular sampling and the non-existence of data values at $\lambda < 0$, causing ambiguity between different solutions.

Thirdly, another important limitation is the finite bandwidth of radio telescopes and therefore the finite range of wavelength-squared $\Delta\lambda^2$ available in the data. Moreover, specific channels from an observation may need flagging or excision due to corrupting effects, increasing the irregularity of the sampling and worsen the form of the RMTF. Such effects may include radio frequency interference (RFI) (see Section 2.2 for details) and instrumental problems.

The deconvolution of Faraday depth signals in such under-constrained context may introduce spurious structures, whilst also being unlikely to reconstruct all true physical structures (Macquart et al., 2012; Pratley et al., 2020). In order to address this problem, attempts of using a suitable prior or regularisation during optimisation to compensate for the missing information have been made (e.g. Akiyama et al., 2017b; Cooray et al., 2020; Ndiritu et al., 2021; Pratley et al., 2021).

Finally, three important parameters need to be taken into account when reconstructing a signal in Faraday depth space. These are the channel width $\delta\lambda^2$, the width of the λ^2 distribution $\Delta\lambda^2$ and the shortest wavelength squared λ_{\min}^2 . Using these latter we can determine the full-width-at-half-maximum (FWHM) of the RMTF $\delta\phi$, the largest scale sensitivity in Faraday depth space max – scale and the maximum and the maximum observable Faraday depth $|\phi_{\max}|$ as

$$\delta\phi \approx \frac{2\sqrt{3}}{\Delta\lambda^2}, \quad (1.91)$$

$$\text{max – scale} \approx \frac{\pi}{\lambda_{\min}^2}, \quad (1.92)$$

and

$$|\phi_{\max}| \approx \frac{\sqrt{3}}{\delta\lambda^2}. \quad (1.93)$$

Different radio telescopes are able to observe the same frequency band. However, observations differ in bandwidth and spectral resolution. For example, Table 1.1 shows the value of Faraday parameters for different telescopes at their lower observing frequencies. These values are relevant since they will be used in different chapters of this thesis.

| Radio telescope | Frequency range GHz | Channel width Hz | $\delta\phi$ rad m ⁻² | max-scale rad m ⁻² | $ \phi_{\max} $ rad m ⁻² |
|----------------------|------------------------|---------------------|-------------------------------------|----------------------------------|--|
| LOFAR LBA | 0.030 - 0.080 | 767.9 | 0.040 | 0.224 | 1314.138 |
| LOFAR HBA | 0.120 - 0.180 | 767.9 | 0.999 | 1.133 | 39030.162 |
| JVLA | 1.008 - 2.031 | 1024024.0 | 51.96 | 144.190 | 25954.890 |
| eMERLIN | 1.230 - 1.740 | 125000.0 | 122.384 | 109.057 | 250580.770 |
| MeerKAT | 0.880 - 1.680 | 26123.0 | 42.422 | 98.774 | 695012.767 |
| MeerKAT ^a | 0.887 - 1.380 | 493493.5 | 51.672 | 66.568 | 25810.220 |

^a Frequency range and channel width used for MeerKAT MIGHTEE-POL RM Synthesis.

TABLE 1.1: Frequency ranges, channel widths, and Faraday parameters for several radio telescopes, including LOFAR's Low Band Antenna (LBA) and High Band Antenna (HBA), and the L-band frequency range for JVLA, eMERLIN, and MeerKAT. For the MeerKAT telescope, two distinct L-band ranges are provided - the actual frequency range and the particular range used in this thesis for RM Synthesis

Chapter 2

Interferometry

In this chapter, I review important concepts on the context of interferometry that will be used in during the reading of this thesis. Additionally, I provide a simplified analysis of interferometry.

2.1 Radio Interferometers

Interferometry has been crucial to obtain a higher angular resolution than that obtained by single dish antennas. Interferometer arrays can collect data from many small antennas to produce results equivalent to a single very large antenna. The best way to understand how interferometers work is by looking at the basic two-element interferometer geometry illustrated in Figure 2.1. In practice radio sources are observed by a collection of two-element interferometers, each with a cosine-wave and sine-wave gain pattern rippling across the source, with a spatial frequency and orientation determined by the particular antenna pair (baseline) (Burke et al., 2019). The number of interferometer pairs for a collection of N_{ant} antennas is $N_{\text{ant}}(N_{\text{ant}} - 1)/2$, because a single telescope cannot form a pair with itself. Each pair is at a distance D apart, and forms a baseline vector which connects the phase centres of the two antennas. Furthermore, the two antennas are pointed at an angle θ ; however, the signals are out of sync because there is a path difference where it takes a bit longer for the radio signal to reach one antenna than the other. In other words, there is a length difference between signals. This difference is defined as

$$\Delta l_g = D \sin \theta . \quad (2.1)$$

Additionally, I can divide the physical length difference by the speed of light to get the time delay:

$$\tau_g = \Delta l_g / c = D \sin \theta / c . \quad (2.2)$$

Finally, with these values it is possible to correlate the signals and therefore determine the location of the signal in the sky very precisely. These values are time dependent as

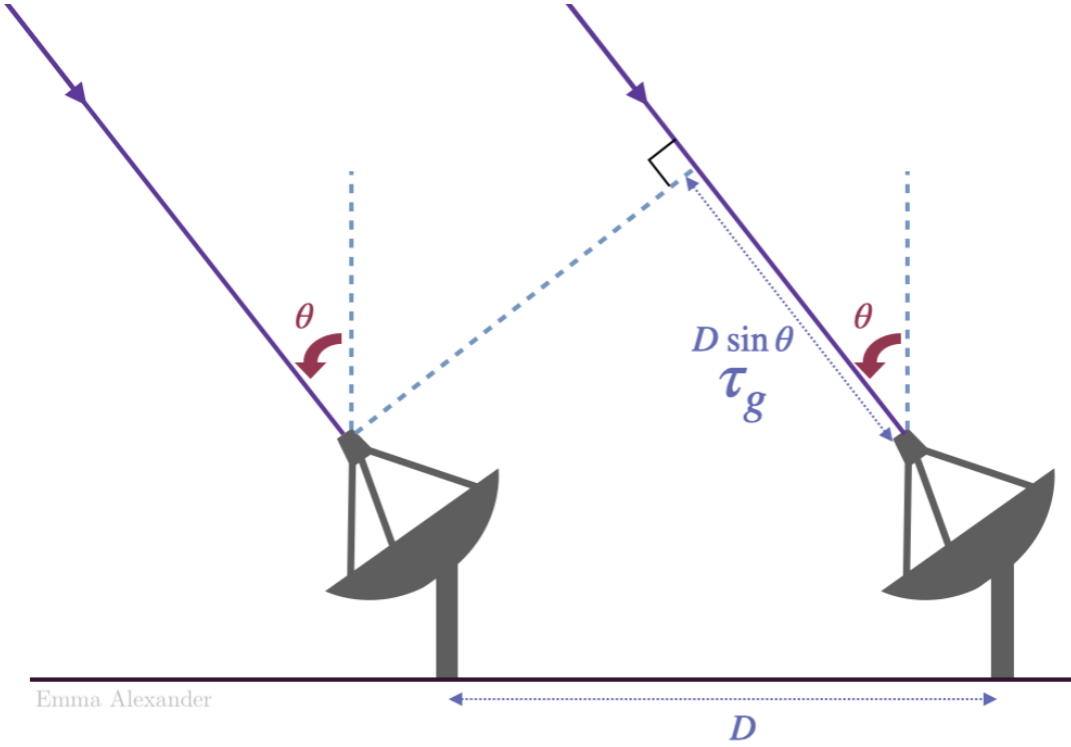


FIGURE 2.1: Diagram to show the two-element interferometer and to illustrate the principles of aperture synthesis. Two receiver dishes are pointed at an angle θ from the zenith towards a single far-field point source. The antennas are at a distance D apart (the baseline between them). There is a timing offset of τ_g , due to the light travel distance offset of $D \sin \theta$, which is used to combine the signals of the two dishes. (Obtained from Emma Alexander at <https://emmaalexander.github.io/resources.html>).

as the source moves across the sky as time passes and θ changes. Strictly speaking, the source stays stationary and the earth rotates.

From this point forward, mathematical derivations are based on the discussion article by Scaife (2020). Firstly, it is important to note that radio interferometers differ from optical interferometers in their direct imaging of the sky. Instead, each baseline measures the mutual coherence of the incident electric field at the two antennas, which is known as *visibility*. A visibility is defined as

$$V_{ij} = \langle E(r_i, t) E^*(r_j, t) \rangle_t, \quad (2.3)$$

where i and j represent the indices of the antennas, $\langle \rangle_t$ denotes the time average, and E^* denotes the complex conjugate of the electric field E .

According to the van Cittert-Zernike theorem, a visibility V_{ij} is equivalent to a Fourier component of the radio sky brightness, $I(l, m)$. I can mathematically express this relationship as

$$V(u, v, w) = \int \frac{A(l, m) I(l, m)}{\sqrt{1 - l^2 - m^2}} e^{-2\pi i (ul + vm + w\sqrt{1 - l^2 - m^2} - 1)} dl dm \quad (2.4)$$

where i represents the imaginary unit $\sqrt{-1}$, l and m are the direction cosines, and (u, v, w) represents the baseline separation in a Cartesian frame projected towards the observing

direction in units of wavelength. The kernel $A(l, m)$ corresponds to the primary beam (PB) and represents the solid angle reception pattern of the individual antennas. It is commonly modelled as a Gaussian function (Taylor et al., 1999).

During extended observations, it is important to note that the projected length of an individual pair of antennas towards a specific direction in the sky undergoes deterministic changes as a result of Earth's rotation. This characteristic presents a unique advantage, as it enables the expansion of the range of Fourier measurements obtained from a finite array. By capitalizing on this phenomenon, the sampling of Fourier measurements can be extended, leading to enhanced data acquisition capabilities. The concept of filling the Fourier plane by using Earth's rotation directly is known as *Earth rotation aperture synthesis* and was developed in 1960 by Ryle and Hewish. Further information and fundamentals of this technique can be found in Chapter 4 of A. Richard Thompson, 2004a and in Section 10.6 of Burke et al., 2019.

It is important to highlight that the separation in the forward direction, denoted as w , is typically small enough to be disregarded for most interferometers. Therefore, in such cases, the relationship can be approximated as a two-dimensional Fourier transform. Furthermore, it should be noted that the coverage of the Fourier plane can be enhanced by adding antennas, extending integration times, or incorporating additional array configurations into the dataset. Visibilities can also be sampled across a range of frequencies to fill gaps in the measured Fourier plane. Thus, the observation of small-scale emission from sources requires longer baselines and higher frequency measurements, whereas the observation of large-scale extended emission necessitates observations made with smaller baselines and lower frequencies.

In order to recover the measured sky brightness distribution, a direct approach is to invert the relationship in Equation 2.4. It is important to note that measurements consist of irregular samples of the Fourier spectrum, obtained from a finite number of antenna separations in the array, denoted as $S(u, v)$. Thus, I have

$$I_{\text{meas}}(l, m) = \int S(u, v) V(u, v) e^{2\pi i(ul + vm)} du dv, \quad (2.5)$$

where $S(u, v)$ can be expressed as a sum

$$S(u, v) = \sum_{j=1}^M \delta(u - u_j, v - v_j), \quad (2.6)$$

where M represents the total number of samples (visibilities) across all baselines. For N_τ time samples and N_f spectral channels, $M = (N_{\text{ant}} \times (N_{\text{ant}} - 1)/2) \times N_\tau \times N_f$.

Commonly, the fast Fourier transform (FFT) is used to obtain I_{meas} . This choice is motivated by the more efficient computational scaling of the FFT algorithm compared to the traditional discrete Fourier transform (DFT). The issue that arises here is that the FFT requires measurements to be regularly sampled in the spatial domain, whereas visibilities are regularly sampled only in time and frequency. At this point, visibilities undergo

a process known as *gridding*, which involves gridding the visibility data using a convolutional kernel $C(u, v)$ (to minimize the effects of aliasing), thereby creating a regularly spaced grid in the Fourier domain. The gridded visibility data, denoted as $V_{\text{grid}}(u_k, v_k)$, can then be mathematically expressed as:

$$V_{\text{grid}}(u_k, v_k) = [[V(u, v) \cdot S(u, v)] * C(u, v)] \cdot \text{III}(u_k, v_k), \quad (2.7)$$

where $\text{III}(u_k, v_k)$ represents the sampling function.

Each natively sampled visibility (also known as *continuous* visibility) is associated with an estimated root mean square (rms) noise, represented by $\sigma(u, v)$. As a result, the weight of a visibility is expressed as

$$\omega(u, v) = \frac{1}{\sigma^2(u, v)}. \quad (2.8)$$

These weights can be incorporated into the gridding process to amplify or attenuate different areas of the Fourier domain, thereby emphasizing distinct spatial features. Further details on anti-aliasing convolution kernels and weighting schemes will be discussed later in this section. Thus, the weighting function can be directly applied to the continuous data, resulting in

$$V_{\text{grid}}(u_k, v_k) = [[V(u, v) \cdot S(u, v) \cdot \omega(u, v)] * C(u, v)] \cdot \text{III}(u_k, v_k), \quad (2.9)$$

Now, it is possible to apply the inverse FFT to calculate an image. This image must be corrected for the introduced anti-aliasing kernel, and the weights need to be normalized, as given by

$$I_{\text{meas}} = \frac{\text{FFT}^{-1}[V_{\text{grid}}]}{(\sum \omega(u, v)) \text{FFT}^{-1}[C]}. \quad (2.10)$$

This process yields what is commonly referred to as a *dirty image*, since it has not yet been corrected for $S(u, v)\omega(u, v)$. Note that this operation results in a convolution on the image domain, as demonstrated by the following relationship

$$V(u, v) \cdot [S(u, v)\omega(u, v)] \iff I(l, m) * B(l, m), \quad (2.11)$$

where $B(l, m)$ is the point spread function (PSF), also known in radio interferometry as *synthesized beam*. This function is defined as the Fourier transform of the irregular weighted sampling, denoted as

$$B(l, m) = \text{FT}^{-1}[S(u, v) \cdot \omega(u, v)]. \quad (2.12)$$

2.1.1 Visibility Weighting

When gridding visibilities, different weighting schemes, $\omega(u, v)$, can be used in order to alter the instrument's natural response function (PSF) and to minimize sidelobes. The most well-known weighting functions in the literature are:

- Natural: Sums weights (proportionally inverse of the noise variance) when data is gridded into the same $u - v$ cell. Thus, higher $u - v$ gridded density might result in higher weights.
- Uniform: Gives weights inversely proportional to the sampling density function. In this case, original weights are gridded in the uv cell, and then the new weight is calculated as $\omega_i = \frac{\omega_i}{W_k}$, where W_k is the gridded weight in the k -th cell.
- Briggs or robust: Provides a compromise between natural and uniform weighting. It creates an elliptical Gaussian that smoothly varies between natural and uniform weighting based on the signal-to-noise ratio (SNR) of the measurements and a tunable parameter defined as a noise threshold. The weight scheme used is $\omega_i = \frac{\omega_i}{1 + W_k \cdot f^2}$, where W_k are the gridded weights as in uniform and

$$f^2 = \frac{(5 \cdot 10^{-R})^2}{\frac{\sum_k W_k^2}{\sum_i \omega_i}},$$

where R is the robust parameter and is such that $R = 0$ gives a good trade-off between resolution and sensitivity. If $R = -2.0$ then the scheme will be close to uniform weighting and if $R = 2.0$ the scheme will be close to natural weighting.

- Super-uniform: Uniform weighting computes the sampling density function in a grid with the same size as the $u - v$ grid. Depending on the cell and grid size, uniform weighting is reduced to natural weighting. For example, if the field of view is bigger than the primary beam size or if the field of view is smaller than the synthesized beam, both cause super-uniform to reduce to natural weighting. Super-uniform weighting separates the weighting from the field size. Instead, the sidelobes of the synthesized image are minimized over some arbitrary grid size.
- uv -taper: Applies a multiplicative Gaussian taper to the spatial frequency grid to increase the detectability of extended an Gaussian shape sources. Can be used with any of the weighting schemes.

In Figure 2.2, each column presents the *dirty image* (top) and *dirty beam* (bottom) of various common weighting schemes employed in the imaging process. These schemes, displayed from left to right, include natural weighting, Briggs weighting, and uniform weighting. Natural weighting, being the default choice, emphasizes maximum sensitivity and signal-to-noise ratio, while Briggs weighting introduces a compromise between sensitivity and image resolution by incorporating a user-defined parameter R . On the other hand, uniform weighting achieves high-resolution imaging by assigning equal weight to all visibilities, thereby maximizing the spatial details captured in the image. By visually examining these figures, the differences and trade-offs among the weighting schemes become apparent. From left to right, it is evident how the image resolution increases and how spatial details, such as the gaps in the protoplanetary disk, become more pronounced. By observing the colorbars, it is also noticeable how sensitivity decreases.

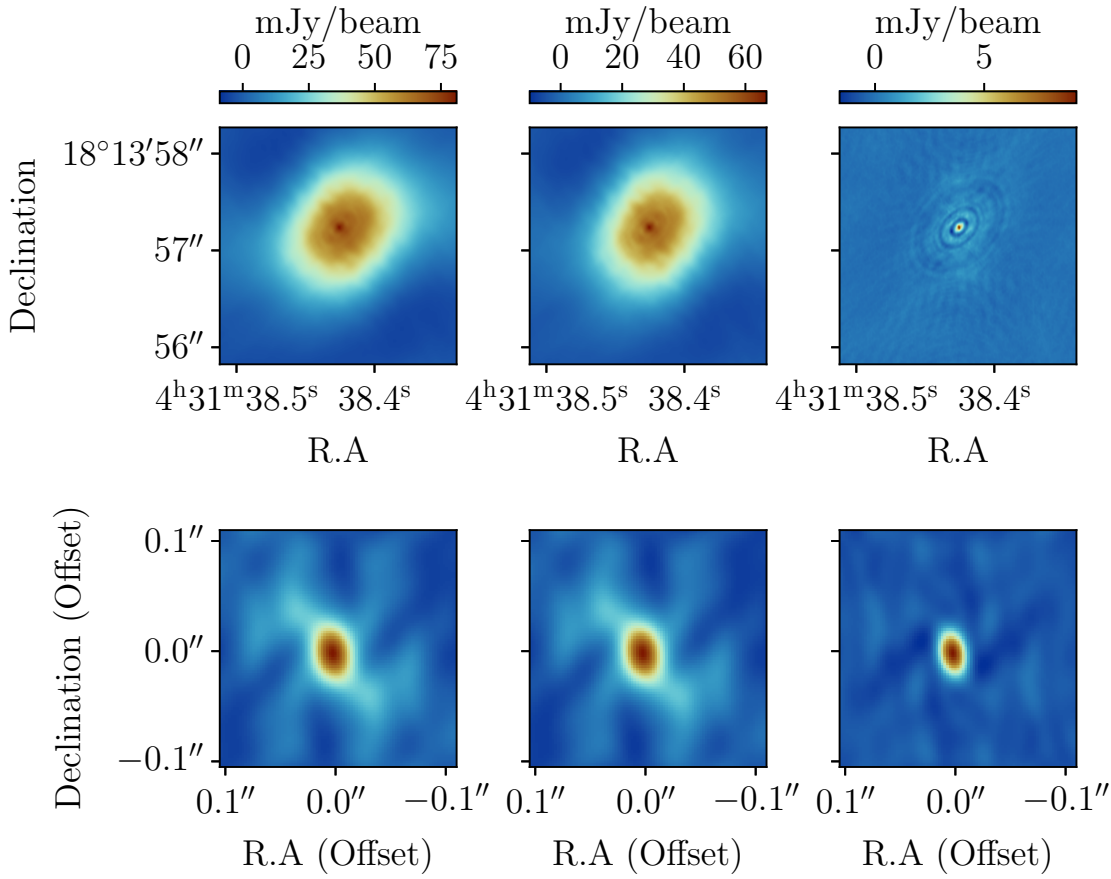


FIGURE 2.2: Dirty images (top) and dirty beams (bottom) of HL Tauri Band 6 ALMA data. Weighting schemes from left to right: Natural weighting, Briggs with robust parameter equal 0.0 (a balance between natural and uniform) and uniform weighting.

This provides valuable insights into the impact of weight selection on the resulting image quality and scientific interpretation.

2.1.2 Anti-aliasing Considerations

It is important to recall that gridding has a great impact in the resultant image. For instance, if $C(u, v) = 1$ is assumed and no convolution kernel is used, aliasing artifacts could appear in the image if some sources are near the edges or outside the field of view.

Suppose that I construct a model with a hyperbolic secant in the center of an image as in Figure 2.3a. Then, the Fourier transform of this source can be calculated analytically as

$$\mathcal{F}(\text{sech}(ax)) = \frac{\pi}{a} \text{sech}\left(\frac{\pi^2}{a}u\right).$$

Note that if $a = \pi$, the Fourier transform is easier to model and to test since

$$\mathcal{F}(\text{sech}(\pi x)) = \text{sech}(\pi u).$$

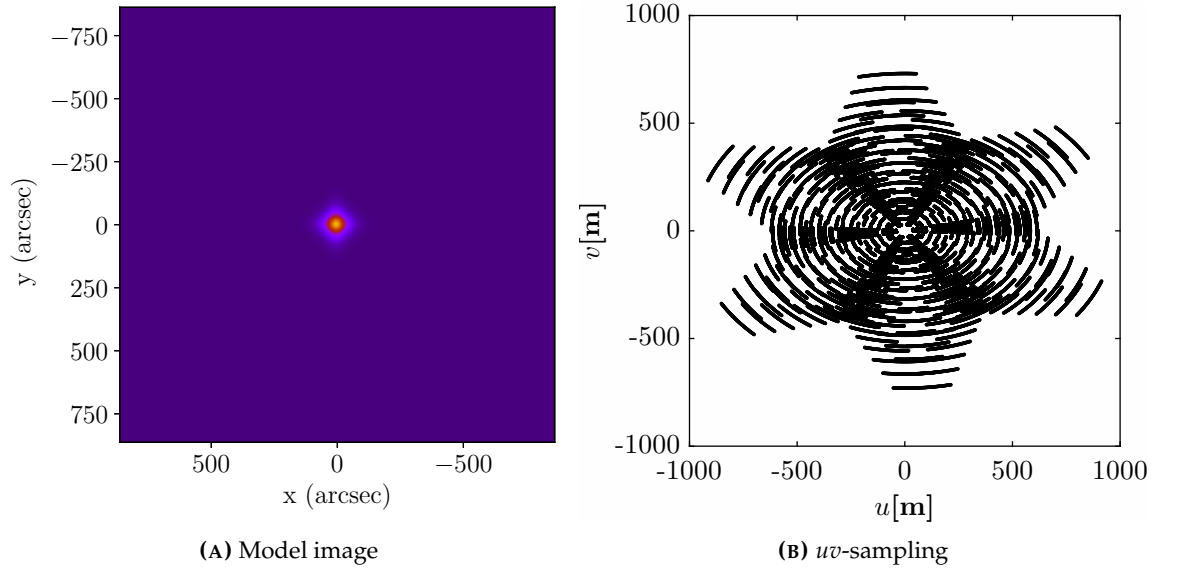


FIGURE 2.3: (a) True model image with a hyperbolic secant at the center. (b) Visibility sampling

Since the Fourier transform can be calculated analytically, I have created a custom script to sample visibilities simulating a one hour observation with the VLA radio telescope in D-array (most compact configuration) at 5GHz, resulting in a field of view is approximately 8.4 arcminutes. Additionally, I have assumed that the astronomical pointing direction moves across the local celestial meridian. In this case, a data sample is taken every 6 minutes (0.1 hours) at a declination of $\delta = 45^\circ$. Figure 2.3b shows the resultant uv plane with 106,002 simulated visibilities. The resultant dirty image of this sampling can be seen in Figure 2.4a. Aliasing artifacts are not expected because there are no sources near the edges or outside the field of view.

However, if I add a source outside the field of view in the down-right direction, for example at position $(-676.5, 676.5)$ arcseconds, then aliasing artifacts will appear. An experiment making a dirty image allocating each data sample into the nearest grid cell shows that the source outside the field of view is barely seen and that sampling pattern forms artifacts that are all over the image (see Figure 2.4b).

There are three common approaches to avoid aliasing problems. The first, is to make the image large enough that there are no sources of interest near the edges of the image. The second, is to avoid undersampling. And finally, to use a gridding convolution function/kernel $C(u, v)$ whose Fourier transform c drops off very rapidly beyond the edge of the image (Taylor et al., 1999). $C(u, v)$ is always real and even and is usually separable $C(u, v) = C_1(u)C_2(v)$. It is important to note that next following choices are truncated to an interval of width of m grid cells. That is, $C(u) = 0$ for $|u| > m\Delta u/2$, where Δu represents the cell size in the one dimensional grid. The typical choices for C in one dimension are:

- Pillbox: $C(u)$ takes the value of 1 if $|u| \leq m\Delta u/2$ and 0 otherwise. Therefore, a convolution using $m = 1$ is equivalent to simply summing data in each cell.

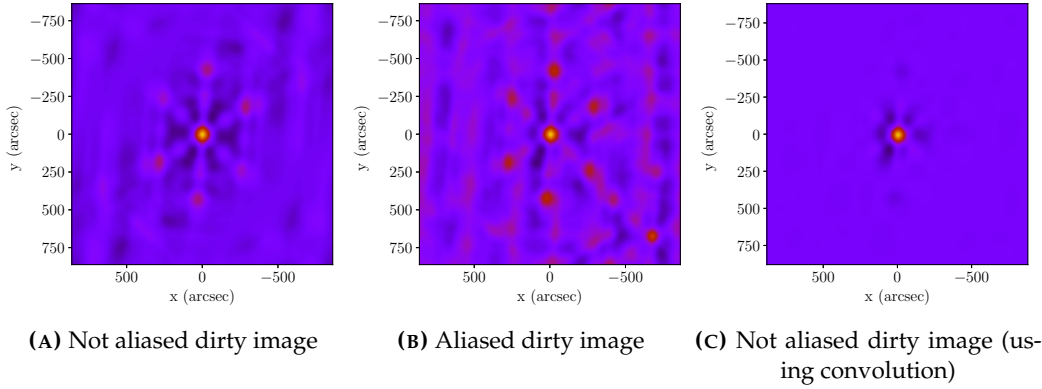


FIGURE 2.4: (a) Dirty image of one hyperbolic secant. (b) Dirty image of two hyperbolic secants but one has been moved outside the field of view. (c) Dirty image of (b) using a Gaussian kernel.

- Exponential: $C(u) = \exp\left[-\left(\frac{|u|}{w\Delta u}\right)^\alpha\right]$. Typically $m = 6$, $w = 1$, and $\alpha = 2$. In other words, a truncated Gaussian with a size of 6 pixels.
- Sinc: $C(u) = \text{sinc}\left(\frac{u}{w\Delta u}\right)$. Typically $m = 6$, $w = 1$.
- Exponential times sinc: $C(u) = \exp\left[-\left(\frac{|u|}{w_1\Delta u}\right)^\alpha\right] \text{sinc}\left(\frac{u}{w_2\Delta u}\right)$. Typically $m = 6$, $w_1 = 2.52$, $w_2 = 1.55$ and $\alpha = 2$. That is, a Gaussian-tapered sinc function.
- Spheroidal functions: $C(u) = |1 - \eta^2(u)|^\alpha \cdot \psi_{\alpha_0}\left(\frac{2u}{m\Delta u}, \eta(u)\right)$, with ψ_{α_0} a 0-order spheroidal function, $\eta(u) = \frac{2u}{m\Delta u}$ and $\alpha > -1$. For $\alpha = 0$ this is a 0-order prolate spheroidal wave function. Choosing $\alpha > 0$ gives higher alias rejection near the center of the image, at the expense of alias rejection near the edges.

As an example, Figure 2.4c shows that artifacts mentioned before have disappeared after convolving the gridded visibilities with a Gaussian kernel with $m = 6$ and $w = 1$.

2.2 RFI Excision

Technology is growing rapidly, being more and more affordable and available as time passes. It has been forecasted that in 2023 approximately 7.33 billion people in the world will have a smartphone¹, and with the increasing of internet accessibility and the growing social networks, radio transmitters have become a daily basis media to communicate.

As a consequence of the latter, the radio spectrum gets crowded and since the signals of radio transmitters are several order of magnitude stronger than sky observations, interferences and perturbations are produced on the observed astronomical signal. This is known as radio frequency interference (RFI). In this section I will summarize the methods used in this thesis to detect and excise RFI.

¹<https://www.statista.com/statistics/218984/number-of-global-mobile-users-since-2010/>

The Common Astronomy Software Applications (CASA) package² is the main software to process data from radio telescopes such as the Atacama Large Millimeter/sub-millimeter Array (ALMA) and the Karl G. Jansky Very Large Array (VLA). This software is a suite for analysis and reduction of radio data with a Python (IPython) interface. In this section, I will only focus on its RFI excision functions but further information can be found in McMullin et al., 2007 and The CASA Team et al., 2022.

- **manual:** This mode receives the exact selection of the data from the user about the data that needs to be flagged. For example, a user could specify antennas, baselines, spectral windows, channels, correlations and other parameters.
- **clip:** Uses data ranges in order to flag visibilities. For instance, a user could flag all the data where amplitude values are greater than 1.
- **quack:** Generally in observations it may happen that the array settles down at the start of the scan. Therefore quack mode can be used to remove data at scan boundaries.
- **tfcrop:** This method is typically used on uncalibrated non-bandpass corrected (see subsection 2.3.2) data and is optimized to flag strong narrow-band RFI. It creates a 2D time-averaged-frequency of the visibility amplitudes for each field, spectral window, time range and baseline. It uses a polynomial fit to the bandshape of the spectrum, then flags the data that deviate from the fit.
- **rflag:** Uses a sliding window statistical (root-mean squared) filter. This autoflagging algorithm iterates the data through chunks of time. Then for each chunk it calculates statistics and flags the data based on the thresholds the user supplies.

Another known software to excise RFI from data is *aoflagger*³ (Offringa, A. R. et al., 2012) which detects RFI in the time-frequency domain with existing techniques and then applies two-dimensional interference mask. It finds adjacent intervals that can be likely affected by RFI in the time or frequency domain. This is done by using the scale-invariant rank (SIR) operator which is a one-dimensional mathematical morphology technique.

Finally, it is important to remark that modern and next-generation radio telescopes will produce data at very high rates, making supervised solutions as the ones above unusable. In this context, deep learning approaches are now being studied in order to learn to discriminate RFI from all known astronomical signals, see e.g. Mesarcik et al., 2022.

2.3 Parallel-hand calibration

The *calibration* of interferometric data is crucial to detect, remove and correct for atmospheric factors and instrumental effects that may interfere with the scientific objective

²<http://casa.nrao.edu>

³<https://gitlab.com/aroffringa/aoflagger>

of the measurement. Before reconstructing an image from visibilities it is important to perform this calibration since there might be factors associated with an antenna, pair of antennas or their electronics. Put in other words, the process of calibration turns the numerical output from the cosine and sine correlators into complex visibilities on a known scale and corrects their time and frequency dependence (Burke et al., 2019).

In this thesis I will separate the calibration process into a series of steps:

- Set the flux density scale.
- Delay calibration.
- Bandpass calibration.
- Complex gain calibration.

The observed visibility amplitudes have units of flux density and must be rescaled such that the result is in units of Janskys. This can be done by observing a strong compact source which its flux density is known and varies only slightly over time. Examples of well-known compact flux calibrators are 3C 48, 3C 138, 3C 147 and 3C 286.

Commonly, radio-astronomy data sets contain visibility data of the source which is the subject of research interest, also known as the *target source*, and the calibrator sources. An uncalibrated visibility can be expressed as a function of the true source intensity, $I(l, m)$, the time-dependent complex gain factor,

$$G_{ij}(t) = g_i(t)g_j^*(t), \quad (2.13)$$

which is a function of the antenna pair, (i, j) , and the normalised primary beam pattern, $A_N(l, m)$, such that:

$$V(u, v, w) = G_{ij}(t) \int \int \frac{A_N(l, m)I(l, m)}{\sqrt{1-l^2-m^2}} e^{-2\pi i(ux+vy+w\sqrt{1-l^2-m^2}-1)} dl dm. \quad (2.14)$$

As has been noted, to calibrate G_{ij} the interferometer observes an unresolved calibrator source, to which the measured response is

$$V_c(u, v, w) = G_{ij}(t)S_c, \quad (2.15)$$

where c indicates a calibrator and S_c its flux density at the phase centre. Amplitudes and phases are considered separately to calibrate the gain. This is due to differences in the mechanisms of how errors propagate between these two quantities. An instance of this is that atmospheric changes can affect phase fluctuations but have roughly no effect on amplitude. Mathematically the calibration of the target source visibility can be described as:

$$V(u, v, w) = \frac{V(u, v, w)_{\text{uncal}}}{G_{ij}} = V(u, v, w)_{\text{uncal}} \frac{S_c}{V_c(u, v, w)}. \quad (2.16)$$

The calibration source is usually placed at the phase center of its field. Therefore, since the calibrator is assumed to be unresolved, the phase is an indirect measure of the instrumental phase. Hence, when phase-calibrating the target the calibrator phase is subtracted from the observed phase and the amplitude is calibrated using the moduli of visibility terms. Note that when two frequency channels have been observed in opposite polarisations at each antenna, calibration is performed separately for each one. Additionally, when observing polarised emission, further calibration is needed. This approach will be described in the next section.

2.3.1 Delay calibration

Inaccurate antenna positions and timing data might introduce small deviations into radio observations. These variations are noticeable as a time-constant linear phase slope as a function of frequency in the correlated data for a single baseline. This slope is known as the delay and can be found across the whole baseband in each spectral window. In order to solve for the delays on parallel-hands, a short time interval on a strong source is needed. This allows one to achieve high signal to noise in the solutions without including the time dependent variations.

2.3.2 Bandpass calibration

Frequency dependency of the instrumental response across the reception band is not constant, therefore this must be corrected. In practice, the visibility data is measured at different frequency channels. Thus, the gain factor, $G_{ij}(t)$ in Equations 2.14 and 2.16, can be generalized to include a frequency-dependent term $B_{ij}(\nu)$, such that

$$G_{ij}(\nu, t) = G_{ij}(t)B_{ij}(\nu). \quad (2.17)$$

In order to calibrate $B_{ij}(\nu)$, a short time interval strong source is also needed to achieve high signal to noise for the solution. Therefore, the same calibrator is often used for delay and bandpass calibration.

2.3.3 Complex gain calibration

To better understand the calibration details for the time-dependent complex gain factor $G_{ij}(t)$, it is necessary to separate it into amplitude $a_{ij}(t)$ and phase $\phi_{ij}(t)$. The variations in the amplitude gains can arise from changes in the atmospheric absorption, electronic path gains and antenna pointing. These effects are commonly small and vary slowly in time at centimetre and longer wavelengths. By repeatedly switching between the target and a nearby compact source when making an observation it is possible to account for these variations. However, the angular separation and timescale between the target and the source is set by the phase calibration, which will be explained below.

According to Burke et al., 2019, there are a number of factors that can cause temporal variations in phase:

- Changes in the troposphere and ionosphere.
- Changes in the electronic path of the correlator.
- Imperfect corrections in the the real-time frequency transfer system.
- Unmonitored drifts in the independent atomic frequency standards used in VLBI.

In general, the angular separation and timescales between the target and the calibration source would depend on the coherence time and the size of the isoplanatic patch (see Chapter 10.7.3 of Burke et al., 2019). However, for radio telescopes that observe the sky at frequency ranges between 1.5 - 15 GHz with baseline separations ranging from JVLA-A to eMERLIN, the separation and the switching time between the target and the calibration source would be up to 5 degrees and 10 minutes, respectively.

2.4 Polarisation calibration

It is known that the state of the radiation field is described by the superposition of two orthogonal polarisations (Taylor et al., 1999). Moreover, four correlations describe the spatial coherence of this vector field. Some radio-telescopes can use circular polarisation feeds to sample left circular (L) and right circular (R) polarisation (LCP and RCP, respectively), others use linear polarisation feeds to sample horizontal (X) and vertical (Y) polarisation. Depending on the case, this results in four visibility functions LL , RR , RL and LR for a circular feed and XX , YY , XY and YX for a linear feed. If polarisation channels were exactly orthogonal (if voltage signal from the channels were exactly proportional to the orthogonal electric fields) then cross-hand visibilities would be also calibrated. However, in practice this proportionality is not obtained and further calibration for the cross-hand correlations is needed.

Polarisation observations and studies are crucial in radio astronomy to understand specific processes in the Universe. Four parameters were introduced by George Stokes in 1852 to measure polarisation. These parameters are related to the amplitudes of the electric field E_x and E_y , resolved in two directions normal to the direction of the propagation (see A. Richard Thompson, 2004a). Of the four parameters, I represents the total intensity, Q and U represent the linear polarised component and V represents the circular polarised component. Note that Q , U and V can have positive and negative values depending on the position angle or sense of rotation of the polarisation. These parameters can be represented by images and therefore each has an associated visibility function in Fourier space, V_I , V_Q , V_U and V_V . Even though these cannot be measured independently, they are a linear combination of the four correlations produced by a radio-telescope. Therefore, for a circular feed I have

$$\begin{aligned}
V[RR] &= V_I + V_V, \\
V[LL] &= V_I - V_V, \\
V[RL] &= (V_U - iV_Q)e^{-2i\chi}, \\
V[LR] &= (-V_U - iV_Q)e^{2i\chi},
\end{aligned} \tag{2.18}$$

and for a linear feed

$$\begin{aligned}
V[XX] &= V_I + V_Q, \\
V[YY] &= V_I - V_Q, \\
V[XY] &= (V_U + iV_V), \\
V[YX] &= (V_U - iV_V),
\end{aligned} \tag{2.19}$$

where χ is the parallactic angle, which determines the orientation of the feed with respect to the sky.

2.4.1 Cross-hand delay calibration

It is important to note that a good complex gain and bandpass calibration will only correct for parallel-hand delay. However, this procedure typically leaves a single cross-hand delay (and phase) from the reference antenna. A consideration to check if this delay is present is to look at the cross-hand phases as a function of frequency. This will show the cross-hand delay as a slope in frequency. A detailed look into the cross-hand delay and the current implemented method to solve this in radio astronomy software can be found in Cotton, 2012.

2.4.2 Leakage calibration

In practice feeds are not exactly orthogonal. This causes a small amount of RCP to show up in the LCP feed channel, and vice-versa. This effect is commonly known as *leakage*. For linearly polarised antennas it is possible to write the received voltage signals v'_x and v'_y as

$$\begin{aligned}
v'_x &= v_x + D_x v_y \\
v'_y &= v_y + D_y v_x
\end{aligned} \tag{2.20}$$

where x and y subscripts indicate two orthogonal planes of polarisation, v terms are signals received using an ideal polarised antenna and D terms are the leakage.

For a pair of antennas (i, j) the measured correlator outputs R'_{xx} , R'_{xy} , R'_{yx} and R'_{yy} can be expressed as

$$\begin{aligned}
\frac{R'_{xx}}{g_{xi}g_{xj}^*} &= R_{xx} + D_{xi}R_{yx} + D_{xj}^*R_{xy} + D_{xi}D_{xj}^*R_{yy}, \\
\frac{R'_{xy}}{g_{xi}g_{yj}^*} &= R_{xy} + D_{xi}R_{yy} + D_{yj}^*R_{xx} + D_{xi}D_{yj}^*R_{yx}, \\
\frac{R'_{yx}}{g_{yi}g_{xj}^*} &= R_{yx} + D_{yi}R_{xx} + D_{xj}^*R_{yy} + D_{yi}D_{xj}^*R_{xy}, \\
\frac{R'_{yy}}{g_{yi}g_{yj}^*} &= R_{yy} + D_{yi}R_{xy} + D_{yj}^*R_{yx} + D_{yi}D_{yj}^*R_{xx},
\end{aligned} \tag{2.21}$$

where g represents the complex voltage gains of the corresponding signal channels. This equation can also be written in terms of Stokes visibilities as

$$\begin{aligned}
\frac{R'_{xx}}{g_{xi}g_{xj}^*} &= V_I + V_Q \cos(2\chi) + V_U \sin(2\chi), \\
\frac{R'_{xy}}{g_{xi}g_{yj}^*} &= V_I(D_{xi} + D_{yj}^*) - V_Q \sin(2\chi) + V_U \cos(2\chi) + jV_V, \\
\frac{R'_{yy}}{g_{yi}g_{yj}^*} &= V_I(D_{yi} + D_{xj}^*) - V_Q(2\chi) + V_U \cos(2\chi) - jV_V, \\
\frac{R'_{yx}}{g_{yi}g_{xj}^*} &= V_I - V_Q \cos 2\chi - V_U \sin 2\chi.
\end{aligned} \tag{2.22}$$

Similarly, for a circular polarised feed

$$\begin{aligned}
\frac{R'_{rr}}{g_{ri}g_{rj}^*} &= R_{rr} + D_{ri}R_{lr} + D_{rj}^*R_{rl} + D_{ri}D_{rj}^*R_{ll}, \\
\frac{R'_{rl}}{g_{ri}g_{lj}^*} &= R_{rl} + D_{ri}R_{ll} + D_{lj}^*R_{rr} + D_{ri}D_{lj}^*R_{lr}, \\
\frac{R'_{lr}}{g_{li}g_{rj}^*} &= R_{lr} + D_{li}R_{rr} + D_{rj}^*R_{ll} + D_{li}D_{rj}^*R_{rl}, \\
\frac{R'_{ll}}{g_{li}g_{lj}^*} &= R_{ll} + D_{li}R_{rl} + D_{lj}^*R_{lr} + D_{li}D_{lj}^*R_{rr},
\end{aligned} \tag{2.23}$$

which in terms of Stokes visibilities results in

$$\begin{aligned}
\frac{R'_{rr}}{g_{ri}g_{rj}^*} &= V_I + V_V, \\
\frac{R'_{rl}}{g_{ri}g_{lj}^*} &= V_I(D_{ri} + D_{lj}^*) - (-V_U + iV_Q)e^{-j2\chi}, \\
\frac{R'_{lr}}{g_{li}g_{rj}^*} &= V_I(D_{li} + D_{rj}^*) - (V_U + iV_Q)e^{j2\chi}, \\
\frac{R'_{ll}}{g_{li}g_{lj}^*} &= V_I - V_V.
\end{aligned} \tag{2.24}$$

In practice, leakage terms D are calculated using observations of a known unpolarised source in the sky or a source which has sufficiently good parallactic angle coverage. Hence, using all the baselines it is possible to find two leakage terms per antenna and the measured correlations.

2.4.3 Polarisation angle calibration

Another effect that needs to be calibrated is the phase difference between polarisation channels. The normal parallel hand phase calibration calibrates the phase of one polarisation channel of each antenna with respect to the phase of that same channel of the reference antenna (Taylor et al., 1999). Commonly, after parallel hand calibration there will be a remaining phase difference between the two polarisation channels. For each antenna this difference is the same to that of the reference antenna. It is known that cross-hand phase has information about a visibility's Stokes' parameters Q and U , and therefore, the instrumental phase difference must be removed. Phase difference with the reference antenna is normally removed by observing a source with a known polarisation position angle. Note that the phase difference for only one antenna is needed. Hence, only one baseline is needed and commonly one of the shortest baselines is used to observe this calibrator source.

When doing polarisation calibration it is important to consider that there exist only two linearly polarised sources (3C 286 and 3C 138) with position angles that do not tend to vary. These sources are commonly used to calibrate the phase difference for oppositely polarised channels. Additionally, it is important to highlight that polarisation observations are made for sources that are small compared with the size of the main beam due to the increasing variation of polarisation toward the beam edges.

2.5 Interferometric Imaging

At this point, it can be stated that the principles of radio interferometry, as outlined in Section 2.1, are now well-established. However, in this section, I will discuss several issues that need to be examined. Firstly, the shape of the dirty/synthesized beam $B(l, m)$ depends on how we distribute our measurements $S(u, v)$. As I mentioned earlier, we can enhance this aspect by incorporating additional antennas into the array or by extending the observation time to take advantage of Earth's rotation and maximize coverage in the Fourier plane. Nevertheless, it is important to note that a radio interferometer array inherently possesses a minimum and maximum separation between antennas. The former impedes sampling of the zero-spacing and nearby measurements, while the latter inevitably imposes finite resolution on the final image. These limitations, coupled with the irregularity of our sampling, result in a sampling function that necessarily yields zero values in specific regions of the visibility grid V_{grid} . Therefore, employing a division in Fourier space to compensate for these areas becomes unfeasible.

Many algorithms have been proposed for solving the deconvolution/image synthesis problem. A colloquially known procedure in radio astronomy is the CLEAN heuristic (Hogbom, 1974; Schwarz, 1978). This algorithm uses a variation on matching or basis pursuit (Lannes et al., 1997), which is a pure greedy-type algorithm (Temlyakov, 2008). Image reconstruction in CLEAN is performed in image plane using a convolution relationship, and it is quite efficiently implemented using Fast Fourier Transforms. However, this traditional approach incorporates a number of approximations and compromises. For example, the algorithm is supervised. This means that the user could indicate iteratively in which region of the image the algorithm should focus. Also, statistical interpretation of resulting images and remaining artifacts are far to be described by a well founded theory. More information of this algorithm and its implementation can be found in The CASA Team et al., 2022.

Another well known algorithm is the Maximum Entropy Method (MEM). This method is based on a maximum likelihood argumentation since interferometer are assumed to be corrupted by Gaussian noise. The main goal of this method is to solve a non-linear optimization problem with an entropy regularization term as follows

$$\hat{I}_{MEM} = \arg \min_{I \geq G} \Phi(I, V^o; \lambda, G), \quad (2.25)$$

where

$$\Phi(I, V^o; \lambda, G) = \frac{1}{2} \sum_k \left| \frac{V_k^o - V_k^m}{\sigma_k} \right|^2 + \lambda \sum_i \frac{I_i}{G} \log \frac{I_i}{G}. \quad (2.26)$$

In Equation 2.26, V_k^o and V_k^m are observed and model visibilities, respectively. σ_k is the standard deviation of each sample, G is a positive lower bound constraint for the sky image I and λ is the penalization factor.

Additionally, works like Cárcamo et al. (2018) have included other terms as a Laplacian and a non-positive entropy regularization used in (Casassus et al., 2018; Cieza et al.,

2017), respectively. Resulting images of MEM have been considered to have higher resolution and less artifacts than CLEAN images (Cornwell and Evans, 1985; Narayan and Nityananda, 1986; Donoho et al., 1992). Even though this method is not used by all the community in a regular basis due to its high computational demands (Taylor et al., 1999; Cornwell and Evans, 1985; Donoho et al., 1992), a GPU version of this method (Cárcamo et al., 2018) has been proposed reducing the computational time and obtaining a speedup of 1000x compared with the serialized version.

Figure 2.5 shows CLEAN, MEM model and restored images. Note that as expected, deconvolution methods return a better estimation of the image in comparison of the dirty image using a gridding and a Inverse Fourier Transform as in Figure 2.2. Additionally, it can be seen that MEM model image has a better resolution than CLEAN. In (Cárcamo et al., 2018), it was empirically studied using simulated point sources that MEM resolution is about 1/3 of CLEAN.

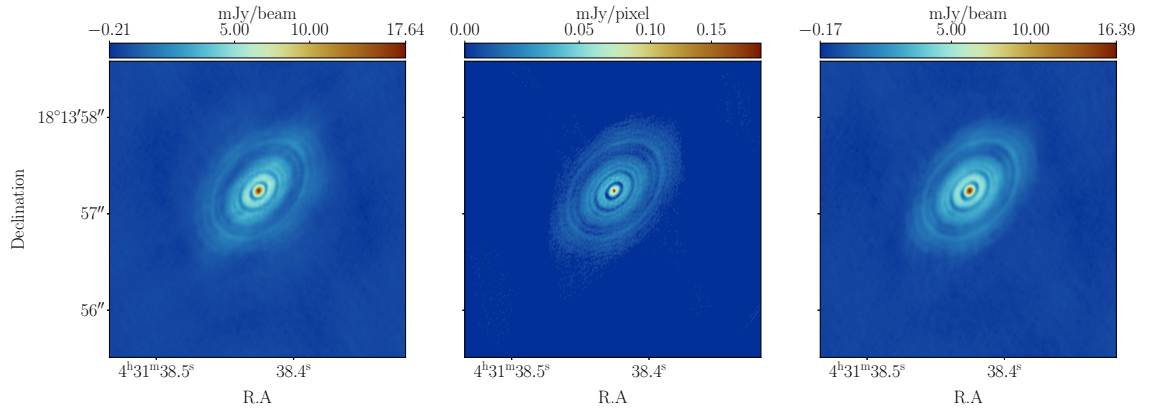


FIGURE 2.5: From left to right: CLEAN, MEM model and restored MEM images from Cárcamo et al., 2018 using HL Tauri Band 6 ALMA data.

2.5.1 Model Image Representations and Multi-Frequency Synthesis

In the field of radio astronomy, different image synthesis methods employ diverse approaches to represent model images. Among these techniques, multi-frequency synthesis stands out as a powerful tool for reconstructing high-resolution images by combining radio observations at multiple frequencies. A crucial element in the domain of multi-frequency synthesis relates to the characterization of image representations. Various strategies have been developed, including representing the image as a collection of point sources, a combination of point sources and Gaussians through a multi-scale approach, as well as employing a power-law representation.

Literature shows that CLEAN (Hogbom, 1974) version implemented in AIPS models the sky image as a collection of point sources or delta functions. However, last features of the algorithm as multi-scale CLEAN (Cornwell, 2008) implemented in CASA (McMullin et al., 2007; The CASA Team et al., 2022) represent the sky brightness as a summation of components of emission (Gaussians and point sources) having different size scales (widths) instead of just delta functions.

Additionally, as I mentioned earlier, it is a common practice in radio astronomy to carry out observations at multiple radio frequencies within a specific range to improve the sampling of visibilities in Fourier space. This frequency range typically extends approximately $\pm 15\%$ from the central frequency value. However, as explained in Chapter 1, the mechanisms governing the emission of continuum radio waves in astrophysical sources exhibit frequency-dependent characteristics. To account for this and overcome the limitations imposed by significant frequency variations, the sky brightness image at a chosen reference frequency ν_0 is modeled using a power-law relationship such that

$$I_\nu(l, m) = I_{\nu_0}(l, m) \left(\frac{\nu}{\nu_0} \right)^{\alpha(l, m)}, \quad (2.27)$$

where I_{ν_0} is the sky brightness at the reference frequency ν_0 and α is the spectral index that varies with (l, m) and can be interpreted as the dependency of radiative flux on frequency.

A basic approach to obtain a spectral index is to reconstruct each frequency channel of a continuum dataset separately and then use a log interpolation to get an average of α . However, this method is restricted to the sensitivity of the instrument and the spatial-frequency coverage and its solutions are not consistent (Rau and Cornwell, 2011). In fact, the source can only be studied at the angular resolution of the lowest frequency (Rau and Cornwell, 2011). For example, this method has been used in (Casassus et al., 2015) to get an spectral index for the HD 142527 protoplanetary disk ALMA datasets. However, a better proposed solution in the state of the art is to combine frequency measurements during image reconstruction using a MFS algorithm. The first approaches of multi-frequency synthesis appeared in (Conway et al., 1990), where the term *multi-frequency synthesis* is denoted and explained, and a method using double deconvolution is proposed and detailed. This work claims that the total bandwidth of a continuum dataset must amount a maximum of $\sim 10\%$ the central frequency. Also, this approach was the precursor of multi-frequency CLEAN (MF-CLEAN) proposed in (Sault and Wieringa, 1994). MF-CLEAN approximates the spectral model function using a Taylor-polynomial expansion around the reference frequency. Thus, Taylor coefficients are computed via least-squares.

To solve the multi-scale problem in a multi-frequency regime, a combination of the general ideas of MF-CLEAN and Multi-Scale CLEAN (MS-CLEAN) (Cornwell, 2008) have been proposed in (Rau and Cornwell, 2011). This algorithm models the sky brightness as a summation of centered and scaled extended components and uses the Taylor-polynomial expansion to reconstruct the sky image and the spectral dependency from the sky brightness distribution. Currently this methods are part of the Common Astronomy Software Applications (CASA) package (McMullin et al., 2007), and they are the most widely used by the community today.

CLEAN has not been the only method used to reconstruct a spectral index image from visibilities. In fact, Bayesian approaches as the maximum entropy method were used to deconvolve a spectral dependency image from VLBI datasets using a Taylor expansion of

Equation 2.27 and optimizing the objective function with the method of Lagrange multipliers (Bajkova, 2008; Bajkova and Pushkarev, 2011).

Even though there is a variety of imaging algorithms available and other algorithms based on compressed sensing that will be discussed in the next chapter, our choice for the data analysis in this thesis is CASA's `tclean` algorithm. This decision is primarily driven by the requirement of reconstructing spectro-polarimetric cubes for the rotation measure (RM) analysis. Unfortunately, not all software packages offering imaging options include this specific functionality. Therefore, we have opted for CASA's `tclean` as it provides the necessary tools for reconstructing spectro-polarimetric cubes, which are essential for our research. However, it is worth noting that the lack of software options with this specific functionality opens avenues for the development of novel methods using regularized maximum likelihood (RML) approaches and compressed sensing techniques.

2.5.2 Self-Calibration

As a variation in time of the troposphere and ionosphere, phase errors expressed as a fraction of radian may be much larger than in visibility amplitudes. If the calibration is uncertain and the resulting images does not have the expected signal-to-noise the usual approach is to iterate between an imager and derive new calibration information from the resulting model images. Self-calibration is an iterative procedure used in radio-astronomy and consists on modelling the complex antenna gains as free parameters and deriving them together with the intensity flux. A first approach to self-calibration (Taylor et al., 1999) could be use the least-mean-squared method to minimise the difference between observed V_{ij}^o and the derived model visibilities V_{ij}^m as in Equation 2.14.

$$\sum_{\text{time}} \sum_{i < j} \omega_{ij} |V_{ij}^o - g_i g_j^* V_{ij}^m(I)|^2. \quad (2.28)$$

This equation can also be re-written as

$$\sum_{\text{time}} \sum_{i < j} \omega_{ij} |V_{ij}^m(I)|^2 |x_{ij} - g_i g_j^*|^2, \quad (2.29)$$

where

$$x_{ij} = \frac{V_{ij}^o}{V_{ij}^m(I)}, \quad (2.30)$$

and ω_{ij} is the inverse of the variance of V_{ij}^o . Note that when the model approaches to an accurate solution, x_{ij} becomes proportional to the antenna gains modelling the response to a calibrator. The procedure starts with an initial model image I and calculates x_{ij} and consecutively determines antenna gains factors for each integration period within the observation. The gains are applied to calibrate the observed visibilities and the imager is run again. The steps are repeated until convergence. In practice, most of the times

self-calibration is performed first only solving for the phases complex gain and then correcting the amplitudes at a later stage.

Although theoretically simple, in practice self-calibration might turn into a trial and error algorithm for scientists. Commonly the procedure starts looping solution intervals and solving the phases for each one of them. The intervals can be long as the scan sampling and then it might decrease in time. If solutions are found over that range of time, then the solution can be applied. Every time that a new solution is found it is important to check if the signal-to-noise ratio has improved. Additionally, phase vs. time plots for each antenna in the array need to be checked such that solutions smoothly vary, if they not it is better to manually flag the outliers or to keep the last and better signal-to-noise solution. Then, if solutions were found and applied the idea is to continue re-imaging the corrected datasets and using the model to found new-solutions in the next time intervals. Since amplitudes vary slowly in time than phase, solution intervals tend to be longer. Again, the idea is to loop the time intervals and apply solutions if the above conditions are accomplished. It is important to check the results carefully in this step since amplitude corrections are more subject to deficiencies in the model image.

Chapter 3

Compressed Sensing Faraday Reconstruction

The work in this chapter is published as part of the paper “CS-ROMER: A novel compressed sensing framework for Faraday depth reconstruction”, Miguel Cárcamo, Anna M. M. Scaife, Emma L. Alexander, and J. Patrick Leahy, 2022, Monthly Notices of the Royal Astronomical Society, arxiv:2205.01413.

In this chapter, I will review pivotal concepts of compressed sensing that are essential for the comprehension of this thesis, alongside conducting a literature review. Subsequently, I will introduce our unique compressed sensing framework, which has undergone testing with simulated data under varied scenarios. This framework is then compared to the well-established method, RM-CLEAN.

3.1 Compressed Sensing

Compressed Sensing (CS), also known as compressive sensing or sparse sampling, is a cutting-edge paradigm that challenges the Nyquist-Shannon theorem for data acquisition under certain conditions. CS posits that sparse high-dimensional signals, subject to specific constraints, can be recovered from far fewer samples or measurements than those required by traditional methods, which necessitate sampling at a rate at least twice the signal bandwidth. When applied to signal processing, the method is designed to extract an accurate signal from an incompletely sampled dataset (A. Richard Thompson, 2004b). The success of this method hinges on the volume of information provided to constrain the signal solution while ensuring consistency with the measurements (A. Richard Thompson, 2004b). These constraints include sparsity, non-negativity, compactness, and the smoothness of the signal.

For example, let x be a measured signal of length N , or a representation of it in some basis. This can be written as $x = \sum_i^N c_i \phi_i$, where $\{\phi_i\}_{i=1}^N$ is a set of linearly independent vectors and $\{c_i\}_{i=1}^N$ are unique coefficients that represent signal x . If we let Φ be the $N \times N$ matrix with columns given by ϕ_i we can represent this relationship in a compact manner such that $x = \Phi c$.

Technically, x is not measured directly. Instead, $M < N$ linear measurements are acquired using a $M \times N$ *sensing matrix* or a linear transform. This can be mathematically represented as $y = Ax$. Here, matrix A is considered a *dimensionality reduction* since it maps \mathbb{R}^N , where N is generally large, into \mathbb{R}^M , where M is much smaller than N . In this scenario (when $M \ll N$ measurements are taken) an ill-posed problem arises. This means that for any particular true signal an infinite number of signals x , will yield the same measurements y . At this point, the theoretical question that arises is how can we recover the original signal x from measurements y ?

To fully recover the signal, a compressible representation of x as a k -sparse vector must be imposed. In other words, if x has k nonzero elements, then the signal can be measured using a linear operation and a number of measurements $M \approx k \log N$. Note that if x is not sparse (has many non-zero elements) it can also be modelled as a superposition of coefficients from a given basis, Φ . Some examples of commonly used bases/dictionaries are wavelets, curvelets, Fourier components, etc. The most well known wavelet families are the Haar wavelet family (Haar, 1910) and the Daubechies wavelet family (Daubechies et al., 1992).

There are a wide variety of methods available to reconstruct a signal from measured data. Given measurements y and knowing that signal x is sparse I can intent to solve the following optimization problem

$$\hat{x} = \arg \min_x \|x\|_0 \text{ subject to } x \in \mathcal{B}(y), \quad (3.1)$$

where $\mathcal{B}(y)$ ensures that \hat{x} is consistent with the data y . In an ideal case $\mathcal{B}(y) = \{x : Ax = y\}$ if the measurements are not corrupted by noise. Otherwise, $\mathcal{B}(y) = \{x : \|y - Ax\|_2^2 \leq \epsilon\}$. The main problem with this approach is that the zero-norm function, which counts the non-zero elements of a vector, is non-convex and finding a solution that approximates the true minimum is generally non-deterministic polynomial-time hard (NP-hard) and computationally very intensive (Natarajan, 1995).

Donoho (2006) and Candes and Tao (2006) discovered that under general conditions it is possible to solve (relax) the problem stated above by using a basis pursuit or enforcing convexity in the $\|\cdot\|_0$. That is, considering a Laplacian prior or a L1 regularization as

$$\hat{x} = \arg \min_x \|x\|_1 \text{ subject to } x \in \mathcal{B}(y), \quad (3.2)$$

and that $\mathcal{B}(y)$ is convex, then the problem has been translated into a computationally feasible one that can be solved with efficient methods from convex optimization.

Here, the L_1 norm of a vector is defined as the sum of the absolute values of each component of the vector:

$$\|x\|_1 = \sum_{t=1}^N |x_t|. \quad (3.3)$$

Note that from a Bayesian perspective the L_1 norm can be seen as the negative logarithm of a Laplacian prior distribution on each t component of x (see Section 5 Tibshirani,

1996).

In the presence of noise, Equation 3.2 can also be written as a unconstrained problem:

$$\hat{x} = \arg \min_x \frac{1}{2} \|Ax - y\|_2^2 + \eta \|x\|_1, \quad (3.4)$$

where the first term is equivalent to the squared sum of the data residuals and η is a regularization parameter that determines the importance between minimizing the L1-norm and the measurement residuals.

3.1.1 Sparsity, incoherence and RIP

To ensure sparse recovery of a signal in presence of noise, CS relies on two conditions. Sparsity and incoherence applied through the Restricted Isometry property (RIP).

At the beginning of Section 3.1 I have defined our signal as $x = \Phi c$, where c is considered a k -sparse vector since it contains a small number of k non-zero elements.

I can define coherence as the largest correlation between any row of a sensing matrix A and any column of a representation basis Φ . The less the coherence between these two matrices, the fewer measurements are needed to recover the signal (Candes and Wakin, 2008). A common example of maximal incoherence occurs when using a Fourier sensing matrix and a canonical (delta functions) representation basis. Mathematically, coherence is defined as

$$\mu(A, \Phi) = \sqrt{n} \max_{1 \leq k, j \leq n} |\langle A_k, \Phi_j \rangle|. \quad (3.5)$$

If both sparsity and incoherence conditions are satisfied, then it can be said that matrix $A\Phi$ meets the k -RIP, and therefore, all subsets of k columns taken from $A\Phi$ are nearly orthogonal. Thus, the optimization problem on Equation 3.4 can be solved with high probability.

Defining RIP, let $k = 1, 2, \dots$, and let an isometry constant $\delta_k < 1$ of a matrix $A\Phi$ such that

$$(1 - \delta_k) \|x\|_2^2 \leq \|A\Phi x\|_2^2 \leq (1 + \delta_k) \|x\|_2^2, \quad (3.6)$$

holds for all k -sparse vectors x . Thus, the property holds when $A\Phi$ approximately preserves the Euclidean distance of k -sparse signals. This equivalent to say that all subsets of k columns taken from $A\Phi$ are nearly orthogonal.

3.1.2 Regularization

Until here I have defined the problem using a regularization for sparsity such as L1-norm. However in CS and signal reconstruction, Total Variation (TV) (see Poon, 2015; Krahmer et al., 2017), often computed as

$$\text{TV}(x) = \sum_i |x_{i+1} - x_i|, \quad (3.7)$$

in its 1-dimensional version and

$$\text{TV}(x) = \sum_{i,j} |x_{i+1,j} - x_{i,j}| + |x_{i,j+1} - x_{i,j}|, \quad (3.8)$$

in its 2-dimensional version, and Total Squared Variation (TSV) computed as

$$\text{TSV}(x) = \sum_i |x_{i+1} - x_i|^2, \quad (3.9)$$

in its 1D version and

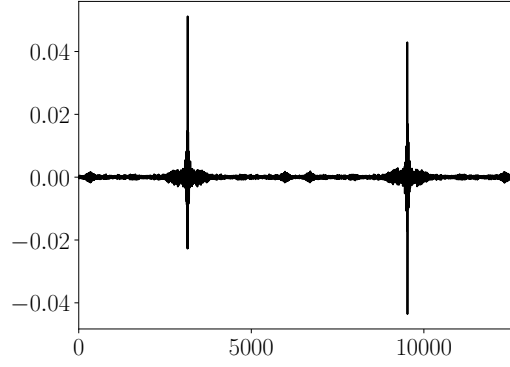
$$\text{TSV}(x) = \sum_i \sum_{j,j'} |x_{i+1,j} - x_{i,j}|^2 + |x_{i,j+1} - x_{i,j}|^2, \quad (3.10)$$

in its 2D version. These regularisation techniques, have a rich history of use in the field of astrophysics, underpinning various key studies. Notably, they were instrumental in analysis of Faraday rotation and the polarised structure of astrophysical jets, as referenced in Akiyama et al., 2018 and Akiyama et al., 2017b. Moreover, these methods played a critical role in the Event Horizon Telescope's (EHT) landmark achievement of capturing the first-ever image of a black hole, detailed in The Event Horizon Telescope Collaboration et al., 2019. These examples illustrate how such regularisation methods contribute to significant advancements in the reconstruction of radio signals. Note that while TV can also be seen as the L1-norm for adjacent pixel differences and minimizes the gradients and favor smoother signals (A. Richard Thompson, 2004a) with flat regions separated by edges (The Event Horizon Telescope Collaboration et al., 2019), TSV only favor those signals with smooth edges.

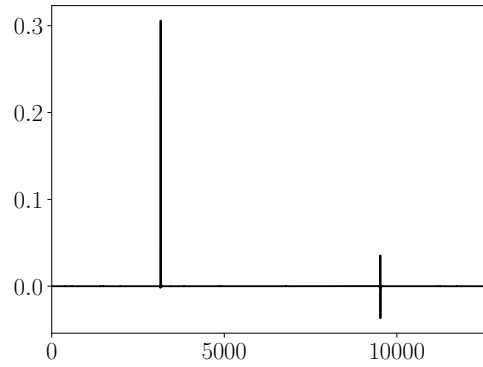
Another well-known regularization is the L2-norm, that can be seen as the negative logarithm of a Gaussian prior distribution. However, this prior will fail when producing a sparse solution. As an example, Figure 3.1 shows the difference between optimisation on a set of delta basis function coefficients using method of L2-minimization and basis pursuit (L1-norm). If a L1-norm is used, sparse coefficients are exactly recovered. In turn, a traditional linear method based in L2-minimization fails reconstructing sparse coefficients. This is because the Laplacian distribution is highly peaked and bears heavy tails in comparison to Gaussian distribution (Wiaux et al., 2009). In other words, Laplacian prior has a greater distribution mass around zero, while Gaussian distribution is more diffuse around its center.

3.1.3 CS Optimization methods

As I previously mentioned, L1 minimization can be addressed using general-purpose convex optimization methods such as steepest descent, conjugate gradient (CG), and Quasi-Newton Methods (Nocedal and Wright, 2006; Press et al., 2007; Elad et al., 2007). Additionally, proximal splitting methods as *Alternating-direction method of multipliers* (ADMM) (Yang and Zhang, 2011; Boyd et al., 2011) and *Simultaneous-direction method of multipliers*



(A) L2 norm minimization



(B) L1 norm minimization

FIGURE 3.1: Example of optimisation of delta basis function coefficients using a L2 (on top) and L1 (on bottom) minimization.

(SDMM) have been used to optimize a certain objective function. In general, proximal methods solve optimization problems of the form

$$\min_{x \in \mathbb{R}^N} f_1(x) + \dots + f_s(x)$$

where $f_1(x), \dots, f_s(x)$ are convex lower semicontinuous functions from \mathbb{R}^N to \mathbb{R} , not necessarily differentiable (Carrillo et al., 2014).

The first splits the objective function in two parts and it optimizes them separately. Then, the algorithm performs a dual variable update. The second method is a generalization of ADMM to a sum of more than two functions (Carrillo et al., 2014).

Iterative algorithms have also been developed to solve these problems in the context of CS. These methods estimate coefficients or the sparse signal iteratively until reach a convergence criterion. The most common algorithms are the *Orthogonal Matching Pursuit* (OMP) and *Iterative Hard Thresholding* (IHT). OMP (Cai and Wang, 2011) on each iteration correlates the columns of A with the signal residual (obtained by subtracting the estimation of the signal with the observed measurement) until reaching a limit on the number of iterations or accomplishing the requirement $y \approx A\hat{x}$. On the other hand, IHT

(Blumensath and Davies, 2009) starts from an initial signal estimate $\hat{x}_0 = 0$ and iterates a gradient descent step using the hard thresholding operator on x , which sets all entries to zero except for the entries of x with largest magnitude. These steps are repeated until meeting a convergence criterion.

Another important algorithm that will be mentioned throughout this thesis is the Fast Iterative Shrinkage-Thresholding Algorithm (FISTA, see Beck and Teboulle, 2009a). This method is used when we need to minimise a cost function:

$$x = \arg \min_x F(x) = f(x) + g(x), \quad (3.11)$$

The function $f(x)$ is a smooth convex function, continuously differentiable with a Lipschitz continuous gradient $L(f)$ such that:

$$\|\nabla f(x) - \nabla f(y)\| \leq L(f)\|x - y\| \quad \text{for every } x, y \in \mathbb{R}. \quad (3.12)$$

and the function $g(x)$ is a continuous convex function, which might not be smooth. FISTA is an upgrade to the Iterative Shrinkage-Thresholding Algorithm (ISTA, see Kowalski, 2014), as it introduces a momentum term to help speed up the convergence rate, which was slower in ISTA.

One of the main aspects of FISTA is the Lipschitz constant L . When the gradient of a function is Lipschitz continuous, the Lipschitz constant can be found, this ensures that the distance of the gradient between two points does not exceed the product of this constant and the distance between the points themselves. If the Lipschitz constant is known for the smooth part of the function, FISTA can use it to decide the step size. In this case, FISTA uses Algorithm 1, where $p_{gL}(y)$ is a proximal function defined as

Algorithm 1 FISTA with constant step size

Input: $L = L(f)$ - A Lipschitz constant of ∇f

Step 0. $y_1 = x_0, t_1 = 1$

Step k. ($k \geq 1$) Compute

$$x_k = p_{gL}(y_k) \quad (3.13)$$

$$t_{k+1} = \frac{1 + \sqrt{1 + 4t_k^2}}{2} \quad (3.14)$$

$$y_{k+1} = x_k + \left(\frac{t_k - 1}{t_{k+1}} \right) (x_k - x_{k-1}) \quad (3.15)$$

$$p_{gL}(y) = \arg \min_x \left\{ g(x) + \frac{L}{2} \left\| x - \left(y - \frac{1}{L} \nabla f(y) \right) \right\|^2 \right\}. \quad (3.16)$$

However, not always the Lipschitz constant is known. In these cases, a method called backtracking line search can be used. This technique starts with an initial estimate for

the step size and then gradually reduces it until a certain condition is satisfied. This ensures the step size is not too large, making FISTA a versatile tool that can be used in a wide range of scenarios where the Lipschitz constant might not be known. In this case, Algorithm 2 is used.

Algorithm 2 FISTA with backtracking

Input: Take $L_0 > 0$ and $\eta > 1$

Step 0. $y_1 = x_0, t_1 = 1$

Step k. ($k \geq 1$) Find the smallest non-negative integer i_k such that

$$F(p_{g\bar{L}}(y_k)) \leq Q_{g\bar{L}}(p_{g\bar{L}}(y_k), y_k) \quad (3.17)$$

with $\bar{L} = \eta^{i_k} L_{k-1}$

Set $L_k = \eta^{i_k} L_{k-1}$ and compute

$$x_k = p_{gL}(y_k) \quad (3.18)$$

$$t_{k+1} = \frac{1 + \sqrt{1 + 4t_k^2}}{2} \quad (3.19)$$

$$y_{k+1} = x_k + \left(\frac{t_k - 1}{t_{k+1}} \right) (x_k - x_{k-1}) \quad (3.20)$$

A drawback of FISTA is that it does not guarantee steady, monotonic convergence. This means that the value of the objective function may not decrease with each iteration. To address this issue, a modified version of FISTA, known as Monotone FISTA or MFISTA (Beck and Teboulle, 2009b), was developed. This version ensures that the value of the objective function decreases after each iteration, thereby guaranteeing the monotonic convergence of the algorithm.

3.2 Applications of Compressive Sensing to radio astronomy

CS proves to be a technique well-suited to handling large computing/data problems, given its ability to significantly compress data sizes through the use of basis coefficients. This compression can be viewed as an additional constraint to the ill-posed problem, potentially leading to better regularization. The first applications of this theory to image synthesis in radio astronomy were done by Wiaux et al. where simulated images of different radio sources (random Gaussians and string signals) were used to demonstrate that the CS method can have better results than classic imaging techniques. Then (Puy et al., 2009) discusses the importance of the effect of non-negligible component directions using simulated data and compressive sensing for reconstruction. Specifically, they simulate sparse signals in Gaussian waveforms and use a basis pursuit algorithm and gridded visibilities for reconstruction. In (Wenger et al., 2010) the work of Wiaux et al. is extended proposing a compressive sensing framework called *SparseRI*. This framework

solves a functional of the form

$$\|y - F(x)\|_2^2 + \lambda f(x),$$

where y is the vector of measurements, F is the Fourier transform and x is the sky image to be reconstructed. The parameter λ can be chosen by the user so that the first term lies within the expected noise level, and $f(x)$ can either be the L1 norm of the coefficients of x in a sparsity basis, like Daubechies wavelets (Daubechies, 1992), or the total variation of the gradient of the sky brightness x . This framework is tested using real and simulated data and is compared with CLEAN, obtaining comparable results.

In Li, F. et al., 2011a, another compressive sensing approach to reconstruct radio interferometry images is proposed. This work test a partial Fourier reconstruction method, that is to apply the L1 norm directly to the gridded Fourier transform. Also, the work tests the isotropic undecimated wavelet transform (IUWT) since it is very well suited for astronomical sky sources. In fact, the author states that the undecimated and redundant wavelet transforms preserve translation-invariance, and that many sources in the universe are isotropic. Finally, both CS methods are optimized using the FISTA algorithm to reconstruct and test the algorithm using ASKAP simulated data.

Consequently, in Carrillo et al., 2012, Carrillo et al. presents an algorithm for radio interferometry imaging named *Sparsity Averaging Reweighted Analysis* (SARA) that assumes that sky signals are sparse in many bases, such as, the Dirac basis, wavelet bases or in their gradient which pretends to represent a powerful prior. This algorithm imposes positivity in the image and uses a reweighted L1 minimization to approach the solution to a L0 norm. Additionally the author tests his algorithm with simulated data generated by random variable density profiles at low frequencies. In the work of Garsden et al., 2015 a FISTA algorithm is proposed for reconstructing real and synthetic LOFAR images. In this work, the dictionary chosen is the *starlet* transform (Starck et al., 2011) or *isotropic undecimated wavelet* since it has been shown that it is useful in astronomical image reconstruction. This transform decomposes an image c_0 of $N \times N$ pixels in a set of coefficients $W = \{w_1, \dots, w_j, c_j\}$ as a superposition:

$$c_0[k, l] = c_j[k, l] + \sum_{j=1}^J w_j[k, l].$$

This paper also proposes a strategy where threshold applied to wavelets is fixed only from the noise distribution at each basis scale.

The main difference between Carrillo et al. an other authors (Wenger et al.) is that Carrillo et al. solves a problem with the form of Equation 3.2 with the Douglas-Rachford splitting algorithm. In turn, other authors solve Equation 3.4 using FISTA. The Douglas-Rachford algorithm minimizes the L1 norm iteratively a then projects the result on the constrained problem (Equation 3.2) until some criteria is reached. This projection requires an iterative process as the backward-forward algorithm to solve the optimization problem. Additionally, it requires the calculation of the norm of the basis to guarantee

convergence. If visibilities are gridded then the norm can be computed and have a fast convergence rate. However, if visibilities are in a continuous space the norm is unknown and it will not be precise enough to converge. Given that this algorithm does not have a parallel structure to solve large-scale problems, Carrillo et al., drawing on the SARA algorithm, extended his previous work (Carrillo et al., 2012) and published PURIFY. This algorithm utilises compressed sensing techniques to reconstruct actual continuous interferometric measurements. Specifically, the authors employ the simultaneous-direction method of multipliers (SDMM) and compare its results with CLEAN.

Concerning parallelization and distributed computing, in Repetti et al., 2016 two compressive sensing algorithms for radio interferometry are proposed. These algorithms solve the sparsity averaging problem proposed in Carrillo et al., 2012 using the alternating direction method of multipliers (ADMM) and using the primal-dual (PD) method. This methods decompose the original problem into simpler and easier problems, each one associated with a term of the objective function. The main difference between these two algorithm is that ADMM offers a partial splitting of the objective function whereas PD allow the full splitting for operators and functions. In fact, in this work PD can work selecting a random fraction of visibilities at each iteration, being flexible in terms of memory requirements a computational loads. Since terms can be splitted, both algorithms are highly parallelizable and can be distributed in different computing processors. This algorithms are compared with the SDMM algorithm and with CLEAN and using simulated data.

In Pratley et al., 2017, the PURIFY software is enhanced with the addition of the following features: a new optimization method named proximal alternating direction method of multipliers (P-ADMM), the code has been redesigned a re-implemented in C++ and different convolutional kernels were added for gridding and degriding. In this paper, the discussion is mainly centered on how different convolutional kernels affect the quality of the sparse image reconstruction. In this discussion, simulated data using real model images of M31 and 30Dor of 256×256 pixels and 131,072 visibilities are used. Also, the author discusses differences between images recovered by PURIFY and CLEAN using real data from the VLA and ATCA telescopes.

Finally, the work conducted by Akiyama et al., 2017b utilizes compressed sensing techniques to reconstruct Stokes parameter images (I , Q , U , V) from simulated polarized data models of M87. This approach incorporates regularization techniques, such as the L_1 norm for sparsity enforcement and TV for enhancing smoothness. The optimization process employs the MFISTA algorithm with backtracking to calculate the Lipschitz constant. Additionally, in another study by Akiyama et al., 2017a, the same regularization functions are employed to optimize the visibility amplitudes and closure phase. In this case, the quasi-Newton method, specifically the limited-memory Broyden-Fletcher-Goldfarb-Shanno (L-BFGS-B) algorithm, is utilized as an approximation of the BFGS algorithm while efficiently managing computer memory resources. In Kuramochi et al., 2018, the same optimization algorithm is used to minimize the L_1 norm and the Total Squared Variation (TSV) as an application to image the black hole shadow. Simulated

observations of radio models of black holes were used to test the reconstructions.

3.3 Applications of Compressive Sensing to 1D data

Before I discuss the existing literature on the use of compressed sensing (CS) for solving the Faraday Rotation Measurement problem in one-dimensional data, it is important to highlight the work by Bell, M. R. and Enßlin, T. A., 2012. This article outlines the conventional two-step technique, known as 2+1D Faraday imaging, which involves the following steps:

1. Calibration and self-calibration (if necessary) of the visibility data.
2. Separate deconvolution of the Stokes Q and U parameters at each frequency, using a reconstruction algorithm, to generate a spectro-polarimetric cube.
3. Restoration of each slice of the cube with the same common restoring beam.
4. Reconstruction of Faraday depth for all lines of sight.

Even though this approach is the most used in the literature, it has certain drawbacks. Firstly, reducing the resolution of all slices of the spectro-polarimetric cube can cause significant issues. Changes in resolution and intensity of polarised intensity in λ^2 -space can shift the Faraday depth of the emission, leading to systematic errors. Secondly, the reconstruction of Faraday depth for all lines of sight is based on deconvolved maps, which are reconstructed using a non-linear algorithm. Consequently, any artefacts introduced by these algorithms can be amplified during RM Synthesis, further impacting the final results.

The article also proposes a new approach that avoids the aforementioned disadvantages. This approach calculates the deconvolved Faraday dispersion function (see 1.88) by combining aperture and rotation measure synthesis imaging and deconvolution into a single algorithm/step. This is accomplished by gridding visibility measurements in (u, v, λ^2) using a convolutional kernel, applying the FFT algorithm to obtain the 3D dirty Faraday dispersion function, and then employing a 3D CLEAN-like algorithm. The authors refer to this method as 3D Faraday imaging.

From this point onward, the papers that I will reference in this section will be those specifically using the 2+1D Faraday imaging approach, focusing on reconstruction methods in one-dimensional data.

One of the first works in this area has been done by Frick et al., 2010. This study demonstrates the applicability of the known Mexican Hat wavelet to decompose the Faraday Depth Spectrum.

Then in Li, F. et al., 2011b the synthetic data simulated in Brentjens, M. A. and de Bruyn, A. G., 2005 is reconstructed. In particular, three algorithms for the reconstruction of thin and thick Faraday depth structures were implemented. All the implementations

use FISTA to minimize the L1 norm whether in Faraday Spectrum space (using and identity matrix) or in Daubechies-8 space. The difference between algorithms lies on which space these structures are sparse. The first algorithm is named *CS-RM Thin* and was implemented to reconstruct thin structures of the Faraday Spectrum. This structures are itself sparse if Faraday depth space, and therefore, a delta basis must be applied to the data. However, thick structures are not sparse in Faraday Depth space, and they are assumed to be in Daubechies-8 space. Therefore, the second algorithm is called *CS-RM Thick* and reconstructs mainly thick structures minimizing the L1 norm in the wavelet space. Finally, a mix of these two algorithms named *CS-RM Mix* was implemented to reconstruct both thin and thick structures at the same time. This is basically done applying both algorithms to the data, and then summing up the results.

Another study that employs Compressed Sensing (CS) to reconstruct Faraday Depth Spectrum signals is Andreut et al., 2011. This work uses the Matching-Persuit (MP) algorithm, a L1-norm regularization and a boxcar dictionary in order to reconstruct both thin and thick Faraday signals. Each atom ϕ_j of the dictionary Φ is defined on Equation 3.21 where $j = j(a, b)$, $a > 0$ its a scale and $b \in \mathbb{R}$ its a translation.

$$\phi_{j(a,b)}(\phi) = \begin{cases} 1/\sqrt{a} & \text{if } b \leq \phi < b + a, \\ 0 & \text{otherwise} \end{cases} \quad (3.21)$$

According to the authors, this dictionary is able to capture sources with arbitrary thickness. Given that the Faraday Depth grid in this case has a length of M , coordinates ϕ_m and a sampling resolution of ϕ_R , it is possible to discretize the boxcar dictionary as in Equation 3.22:

$$\phi_j(\phi_m) \equiv \phi_{j(s,l)}(\phi_m) = \begin{cases} 1/\sqrt{s\phi_R} & \text{if } l \leq m < l + s, \\ 0 & \text{otherwise,} \end{cases} \quad (3.22)$$

where the maximum width of the boxcar atom is $a_{max} = S\phi_R$ and $S \leq M/2$, then each scale $a = s\phi_R$ where $s = 1, 2, \dots, S$ and each translation $b = l\phi_R$ where $l = 0, 1, \dots, M - s$.

To illustrate the method two experiment layouts were made. The first simulates both noiseless and noisy cases of Westerbork Synthesis Radio Telescope (WSRT) observations in a frequency range of 315-375 MHz spread over 126 channels. The second simulates Arecibo telescope data in the frequency range of 1225-1525 MHz spread over 200 channels. The simulated Faraday Depth sources were a thin source and two different thick sources one thicker than the other.

Even though this works promote sparsity on a certain basis. The work of Akiyama et al., 2018 uses a tradeoff between sparsity and smoothness in Faraday Depth space using regularizations such as L1-Norm and TV or TSV. This is done using the FISTA algorithm and uses a Faraday Depth model from Ideguchi et al., 2014 with both Faraday thin and thick structures at a frequency band from 300 to 3000 MHz to test the procedure. The results are compared with an RMCLEAN version from Miyashita et al., 2016.

The work made by Cooray et al., 2020 improves the latter work using an iterative restoration algorithm based on the projected gradient descent. The algorithm is named Constraining and Restoring iterative Algorithm for Faraday Tomography (CRAFT). At each iteration, different assumptions of the Faraday Depth Spectrum can be made such as sparsity and considering that some parts of the spectrum are result of the RMSF. In this work the smoothing of the polarisation angle can also be added as a constraint.

There are two things to note in these works. Both create data in Faraday Depth space and then go to λ^2 -space using a DFT. However, doing this implies that the λ^2 -space is implicitly regularly-spaced. It is worth to note that an irregular λ^2 -space adds not only adds an additional layer of noise to the problem but also a problem similar to what happens in image synthesis. Also note that in this works the simulations do not account for the fact of frequency channel excision due to RFI, instrumental problems or calibration.

Finally, the study conducted by Pratley et al., 2021 introduces a convex non-parametric QU fitting algorithm for Faraday depth spectra. This novel approach projects onto λ^2 -space and constraints the polarised flux at negative wavelengths squared to zero. This method significantly contributes to tackling the under-constrained issue prevalent in the reconstruction of Faraday depth spectra. It provides a solution for dealing with negative wavelengths squared, which are not natively sampled.

However, one potential caveat of this approach lies in its assumption that negative wavelength squared samples are zero. Theoretically, these samples do not exist, thus rendering this portion of the data an empty set. By assuming these values to be zero, the method may inadvertently introduce systematic uncertainties or biases.

3.4 Faraday Spectra Reconstruction

The Faraday spectra reconstruction problem can be solved using a Regularized Maximum Likelihood (RML) method in order to select one signal among many feasible. In section 1.5 we not only have shown that measurements are noisy and incomplete but also that they belong to an irregular space and that the problem is inherently under-constrained due to $P(\lambda^2 < 0) = \emptyset$. The idea behind the RML is to reduce the solution space choosing data that fit the measurements to within the noise level. Among these, choose signals constrained to have certain features, such as sparsity or edge-smoothed signal.

In this work I propose a CS-framework that solves the problem stated on Equation 3.4 extending the objective function adding TV and TSV regularizations in order to impose edge-smoothed constraints when needed. Consequently, I aim to solve the following optimization problem

$$\hat{x} = \arg \min_x \left\{ f(x) + g(x) \right\} \quad (3.23)$$

where

$$f(x) = \frac{1}{2} \sum_{k=0}^M \left| \frac{P_k^o - P_k^m(x)}{\sigma_k} \right|^2, \quad (3.24)$$

is commonly seen in the literature as a χ^2 term and is considered a convex smooth function, and $g(x)$ is a convex function that is non-differentiable in some region and can be either

$$g(x) = \eta_1 L1(x) + \eta_2 TV(x) , \quad (3.25)$$

or

$$g(x) = \eta_1 L1(x) + \eta_2 TSV(x) , \quad (3.26)$$

where x can be the signal itself or a wavelet representation of it and $L1$, TV and TSV are defined in Equations 3.3, 3.7 and 3.9, respectively. P^o is a M -size vector containing the observed polarised intensity measurements as a function of λ^2 and P^m denotes the model measurements which are functions of the signal estimate calculated using Equation 1.87. Finally, σ_k^2 is the variance for channel k . Before continuing, it is important to highlight that our framework will first calculate main parameters involved in Faraday Depth reconstruction as in Li, F. et al., 2011b and Brentjens, M. A. and de Bruyn, A. G., 2005. First, the framework calculates λ_{\min}^2 and λ_{\max}^2 . Then, $\Delta\lambda^2$ and $\delta\lambda^2$ are computed as

$$\Delta\lambda^2 = \lambda_{\max}^2 - \lambda_{\min}^2 \quad (3.27)$$

and

$$\delta\lambda^2 = \frac{\sum_{i=0}^N \lambda_{i+1}^2 - \lambda_i^2}{N} , \quad (3.28)$$

respectively. These can in turn be used to define the resolution in Faraday depth space, the largest scale in Faraday depth to which the data is inherently sensitive and the maximum observable Faraday depth. In Brentjens, M. A. and de Bruyn, A. G., 2005 and our framework these are approximated as in Section 1.5.

Thus, the framework selects the cell-size in Faraday Depth space as $\phi_R = \delta\phi/\rho$, where ρ is the oversampling factor which can be selected as 4 or 5. From Li, F. et al., 2011b we can use $||\phi_{\max}||$ to calculate the length of the grid in Faraday Depth space as

$$n = \left\lceil \frac{2||\phi_{\max}||}{\phi_R} \right\rceil$$

Given that the observed measurements reside in an irregular space and the Faraday Depth space exists on a regular grid, the framework provides two options for estimating the model data. The first and more intuitive option is to grid the observed measurements, which can be achieved by estimating P^m from Faraday spectra using just a DFT or FFT. The alternative option involves the use of the Non-Uniform Fast Fourier Transform (NUFFT) (Lin, 2018), which executes an FFT on non-uniformly sampled data. This is accomplished by conducting an FFT on the signal and then performing a min-max interpolation (Fessler and Sutton, 2003). Once a method to approximate the model data points has been identified, the subsequent step is to employ an optimization method to minimize either Equation 3.25 or 3.26.

In this work, I have chosen to use the monotonic version of the Fast Iterative Shrinkage-Thresholding Algorithm (MFISTA) for the reconstruction process (Beck and Teboulle, 2009b). The FISTA method and its monotonic variant have been employed in previous studies on reconstruction of Faraday spectra, as demonstrated by Li, F. et al., 2011b and Akiyama et al., 2018. Furthermore, the efficacy of this method with regularizations such as Total Variation (TV) and Total Squared Variation (TSV) has been established, as highlighted in the work by Akiyama et al., 2017b and Kuramochi et al., 2018.

The gradient calculation of $\nabla f(y_k)$ is done by estimating the model visibilities as explained above. It is important to highlight that if we are using a basis representation we need to reconstruct the Faraday Depth space from coefficients before estimating the model measurements. Then, we apply the IDFT to the residuals as shown on the right part of Equation 1.88. The calculation of the proximal function p_{gL} when only having the L_1 -norm function as a regulariser can be done analytically. That is

$$\text{prox}_{\lambda g}(y) = \arg \min_x \left\{ \|x\|_1 + \frac{1}{2\lambda} \|x - y\|_2^2 \right\}.$$

The optimality condition for this problem is

$$\begin{aligned} 0 &\in \partial(\|x\|_1) + \nabla \left(\frac{1}{2\lambda} \|x - y\|_2^2 \right) \\ 0 &\in \text{sign}(x) + \frac{(x - y)}{\lambda} \iff y = x + \lambda \text{sign}(x) \\ x &= y - \lambda \text{sign}(x) \end{aligned}$$

From here, we can detect three conditions:

$$s(y) = \begin{cases} y - \lambda, & y \geq \lambda \\ 0, & |y| \leq \lambda \\ y + \lambda, & y \leq -\lambda. \end{cases}$$

which can be written as

$$s(y) = \max(|y| - \lambda, 0) \text{sign}(y).$$

This is commonly known as the soft-thresholding operator and it sets small values to zero while it shrinks large values toward zero. In order to incorporate TV and TSV regularisations, we have implemented a fast gradient projection algorithm just as Beck and Teboulle, 2009b and Akiyama et al., 2017b. In practice, the Fast Projected Gradient (FGP) method is replaced by the soft-thresholding operator.

Numerous attempts have been made to automatically calculate regularization parameters beforehand (see Hansen, 2000; Belge et al., 2002; Karl, 2005; Bauer and Lukas, 2011; Shi et al., 2018). As a preliminary approach in this framework, I have considered only L1 regularization. Since I can estimate the theoretical noise, denoted as σ , of our signal from the dirty Faraday spectrum where $\phi \geq |\phi_{\max}|$ or from the data weights, I calculate the

parameter η_1 by minimizing the scalar objective function

$$\hat{\eta}_1 = \arg \min_{\eta_1} \{ |\sigma_{\eta_1}(\hat{r}) - 5\sigma| \}, \quad (3.29)$$

where \hat{r} represents the residuals in Faraday depth space. By minimizing this objective function, I can determine the regularization parameter such that the resulting residuals have a root mean square (rms) value of 5 times the theoretical noise. This latter number can also be parameterized within the framework, thereby allowing an η_1 parameter to produce a lower or higher rms.

In the case the signal can be represented by a wavelet dictionary, the framework offers the set of discrete wavelet transforms (DWT) from package pywt (Lee et al., 2019). However, sometimes the DWT can cause problems due to its shift variance and poor directional properties (Golilarz and Demirel, 2017). As an alternative, and as a way to reconstruct both thin and thick Faraday structures, I have added the Undecimated Wavelet Transform (UWT) 1D functions from Lee et al., 2019 to our framework. Another motivation is that it has been shown that the use of the thresholding function and UWT can improve results in image denoising and reconstruction applications (Starck et al., 2007; Offringa and Smirnov, 2017), and even though there have been studies of wavelets in the Faraday Measurement Synthesis context, the UWT has not been tested yet.

3.5 Application to Simulated Data

To illustrate and test the compressed sensing algorithm I am going to use the following equations to analytically simulate Faraday depth spectra on three scenarios. First, we consider polarised emission from the lobe of a radio galaxy as:

$$\begin{aligned} P_{\text{rg}}(\lambda^2) &= S_{v_0} \left(\frac{\lambda^2}{\lambda_{\text{ref}}^2} \right)^{\alpha/2} \exp(2i\phi_1\lambda^2) \\ &= S_{v_0} \left(\frac{\lambda^2}{\lambda_{\text{ref}}^2} \right)^{\alpha/2} [\cos(2\phi_1\lambda^2) + i \sin(2\phi_1\lambda^2)]. \end{aligned} \quad (3.30)$$

where S_{v_0} is the intensity at the reference frequency, α is the spectral index and ϕ_1 is the single Faraday Depth value. This can be also seen as a thin Faraday source on Faraday-space. In this case, the simulated source will have an intensity of 0.035 Jy/beam and the Faraday Depth ϕ_1 will be at -200 rad m^{-2} .

The second scenario has been adopted from the top-hat function in (Brentjens, M. A. and de Bruyn, A. G., 2005) which represents a Faraday Thick component. I have generalised the equations (see Equation 3.32) such that a component of width ϕ_{fg} could be centered at any ϕ_0 value. In this case the simulated source will have an intensity of 0.035 Jy/beam and a width of 140 rad m^{-2} including a range of Faraday Depths from 130 to 270 rad m^{-2} . I have chosen this value because it is very close to the maximum recoverable width structure.

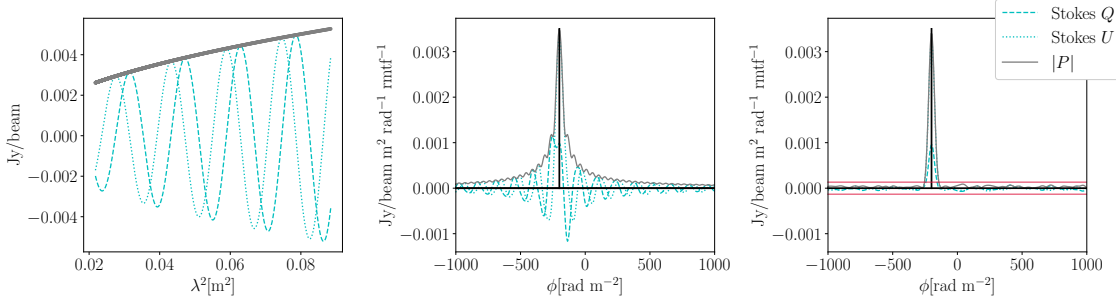


FIGURE 3.2: Scenario 1. On the left we show the simulated polarisation data as a function of λ^2 . In the center, the dirty Faraday depth spectrum of the same data. On the right, the reconstructed Faraday depth spectrum from a noisy and incomplete realisation of these data with $\sigma_{QU} = 0.7 \text{ mJy/beam}$ with a 30% removal fraction, using the delta basis function. The theoretical $\pm 5\sigma_\phi$ noise boundary for complex Faraday depth is shown as red lines.

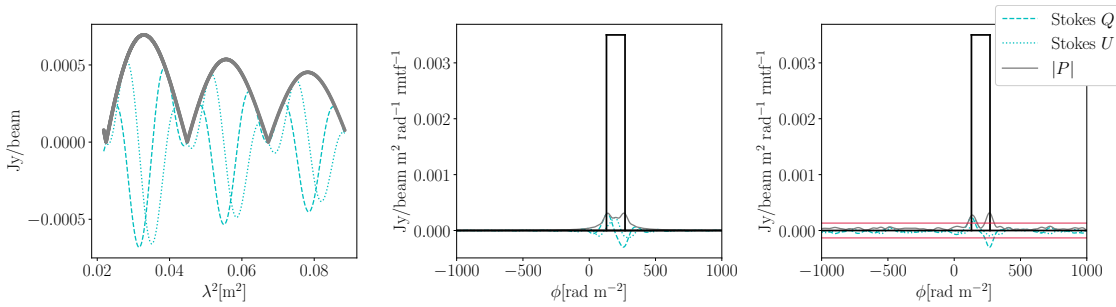


FIGURE 3.3: Scenario 2. On the left we show the simulated polarisation data as a function of λ^2 . In the center, the dirty Faraday depth spectrum of the same data. On the right, the reconstructed Faraday depth spectrum from a noisy and incomplete realisation of these data with $\sigma_{QU} = 0.7 \text{ mJy/beam}$ with a 30% removal fraction, using the delta basis function. The theoretical $\pm 5\sigma_\phi$ noise boundary for complex Faraday depth is shown as red lines.

$$F_{\text{gal}}(\phi) = \begin{cases} S_{v_0}(\phi_{\text{fg}})^{-1} & \phi_0 - \frac{\phi_{\text{fg}}}{2} < \phi < \phi_0 + \frac{\phi_{\text{fg}}}{2} \\ 0 & \text{elsewhere} \end{cases} \quad (3.31)$$

$$\begin{aligned} P_{\text{gal}}(\lambda^2) &= \frac{S_{v_0}}{\lambda^2 \phi_{\text{fg}}} \sin(\lambda^2 \phi_{\text{fg}}) e^{(2i\lambda^2 \phi_0)} \\ &= S_{v_0} e^{(2i\lambda^2 \phi_0)} \text{sinc}(\lambda^2 \phi_{\text{fg}}) \end{aligned} \quad (3.32)$$

Finally, the third scenario is a mixture of a Faraday thin source and a Faraday thick source. This is done by simply summing the resulting complex polarisation intensities from previous scenarios

$$P_{\text{tot}}(\lambda^2) = P_{\text{gal}}(\lambda^2) + P_{\text{rg}}(\lambda^2). \quad (3.33)$$

The frequency range and parameters employed across all scenarios align with those for JVLA, as depicted in Table 1.1.

To be consistent with channel excision due to RFI and calibration we have randomly taken data out. Particularly, for all three scenarios I have taken out different fractions of

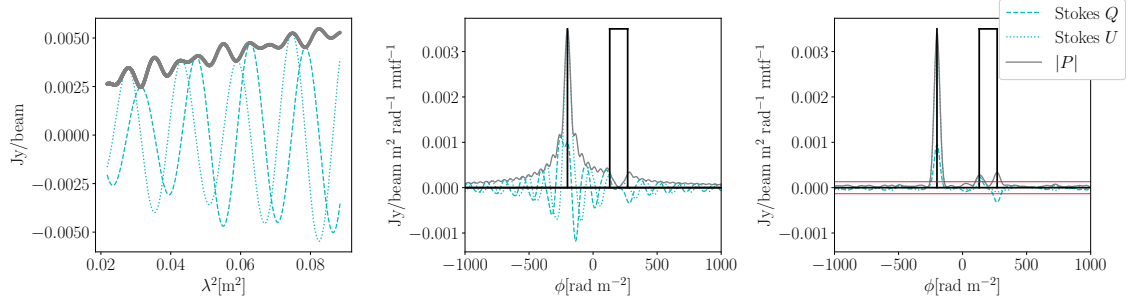


FIGURE 3.4: Scenario 3. On the left we show the simulated polarisation data as a function of λ^2 . In the center, the dirty Faraday depth spectrum of the same data. On the right, the reconstructed Faraday depth spectrum from a noisy and incomplete realisation of these data with $\sigma_{QU} = 0.7$ mJy/beam with a 30% removal fraction, using the delta basis function. The theoretical $\pm 5\sigma_\phi$ noise boundary for complex Faraday depth is shown as red lines.

| Scenario | ϕ_1 [rad m ⁻²] | ϕ_{fg} [rad m ⁻²] | ϕ_0 [rad m ⁻²] | S_{ν_0} [Jy/beam] |
|----------|------------------------------------|---------------------------------------|------------------------------------|--------------------------|
| 1 | -200 | - | - | 0.035 |
| 2 | - | 140 | 200 | 0.035 |

TABLE 3.1: Abell 1314 JVLA simulation details

the total data points. Therefore, different datasets were made with removal fraction in a range from 0.0 to 0.9 in regular steps of 0.1.

Finally, to make the scenarios even more realistic I have also added different levels of Gaussian random noise with levels of fraction of the peak that go from 0.0 to 0.9 in regular steps of 0.1.

To illustrate how the data looks like Figure 3.5 depicts plots of λ^2 -space on scenario 1 using removal fractions of 0.2, 0.5 and 0.8 as well as using 0.2, 0.5 and 0.8 fractions of the peak as noise.

3.5.1 Evaluation Metrics

This section aims to explain the different evaluation metrics used in this work in order to evaluate the Faraday Rotation Measurement Synthesis framework and its different solutions obtained from the simulated scenarios.

Peak-signal-to-noise ratio (PSNR)

Before continuing, it is important to define what is meant by the restored Faraday signal. Similarly to imaging in radio interferometry, most of the time the resulting *model* signal will not represent the system's resolution. Therefore, to create the *restored* signal the resulting model signal is convolved with a zero mean Gaussian that has a standard deviation equivalent to that of the RMTF.

The peak-signal-to-noise (PSNR) metric computes the maximum value of a signal divided by the corrupting noise that affects its fidelity. Since Faraday-space signals are

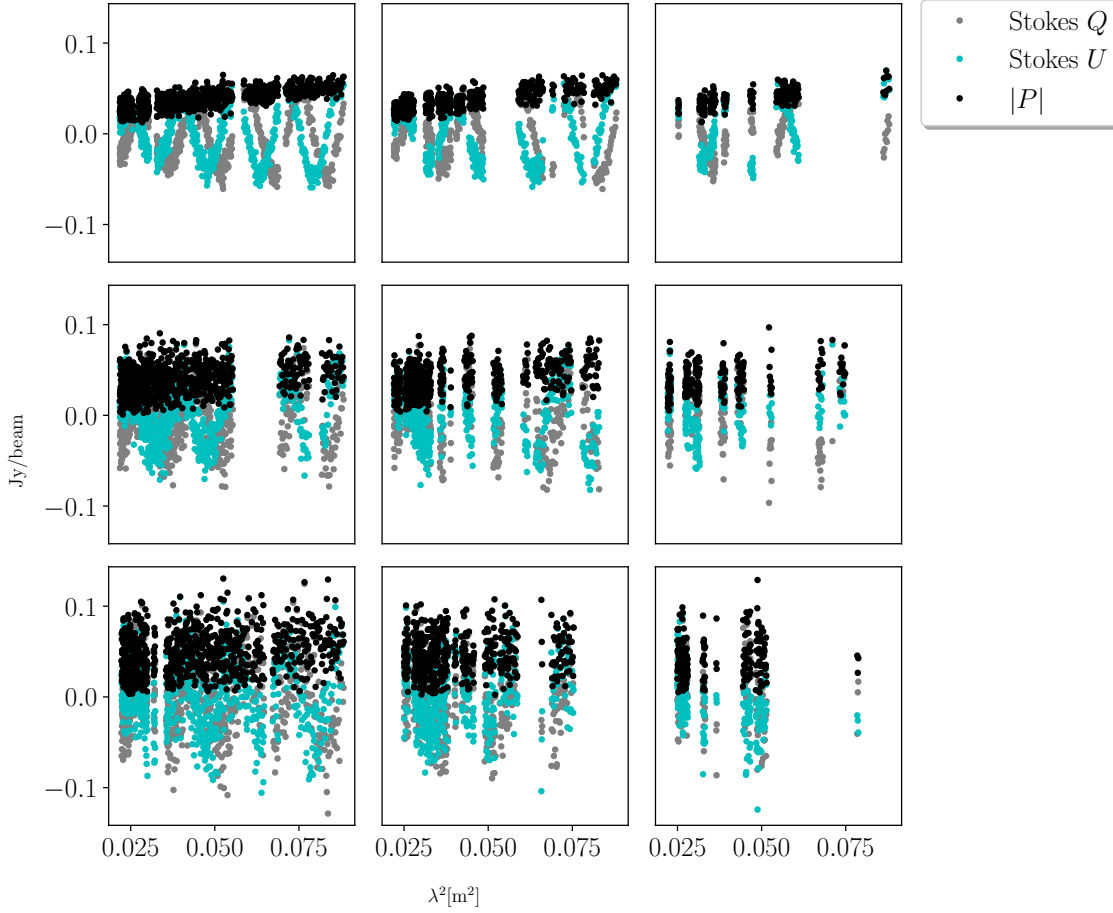


FIGURE 3.5: Scenario 1 with different amounts of noise and removal fractions. First row has a noise fraction of 0.2 of the peak, second row 0.5 and third row 0.8. First column has a removal fraction of 0.2, second column 0.5 and last column 0.8.

complex, we can take the maximum of the absolute value of the restored signal as the peak. The noise is calculated as the standard deviation of the residuals in Faraday depth space. This can be written as

$$\text{PSNR} = \frac{\max\{|F|\}}{\sigma}$$

where F represents the restored Faraday depth signal and σ is the standard deviation of the residuals in the same space, calculated as the arithmetic mean of the rms noise on the real and imaginary components of the Faraday depth spectrum:

$$\sigma = \frac{\sigma_{\text{REAL}} + \sigma_{\text{IMAG}}}{2}. \quad (3.34)$$

Root Mean Squared Error (RMSE)

One way to assess the reconstruction and how well the model fits the observed measurements is calculating the Root Mean Squared Error (RMSE). When the reconstruction reaches its end, the framework returns the residuals and we can use these to calculate the

RMSE as

$$\text{RMSE} = \sqrt{\frac{\sum_i |r_i|^2}{2n}}. \quad (3.35)$$

Therefore, the RMSE can be interpreted as the average distance between the model and the observed data. The lower this distance is, the better the fit is.

Sparsity

As has been noted previously, sparsity can be defined as the number of non-zero elements, k , in a data vector of length n . The fewer the number of non-zero elements, the sparser the data. Here I calculate the percentage of non-zero elements, s , in the resulting parameters after optimization. This can be the sparse Faraday-space representation of the data, or the basis coefficient representation. When working with coefficients that have a real representation, this can be written as the proportion between non-zero coefficients and the length of the coefficient vector

$$s = 100 \cdot k/n. \quad (3.36)$$

However, since Faraday-space is complex, I need to calculate sparsity for the real and for the imaginary parts as

$$s = 100 \cdot (k_{\text{REAL}} + k_{\text{IMAG}}) / (2 \cdot n). \quad (3.37)$$

Model selection criterion: AIC and BIC

Given the fact that the deconvolution of Faraday depth spectra is an ill-posed problem, many models will be able to fit the data. Additionally, since we are using multiple scenarios to test different basis representations, we would like to know which model best approximates the data. To do this we use the Akaike Information Criterion (AIC) and the Bayesian Information Criterion (BIC) defined as

$$\text{AIC} = n \log \left(\frac{\|y - \hat{y}(x)\|_2^2}{n} \right) + 2 \cdot \text{df}, \quad (3.38)$$

and

$$\text{BIC} = n \log \left(\frac{\|y - \hat{y}(x)\|_2^2}{n} \right) + \text{df} \log n, \quad (3.39)$$

respectively. Here, y represents the complex observed data vector of length n and \hat{y} represents the estimated data, and x can be either the Faraday depth spectrum or the coefficient vector. Following Shi et al., 2018, df is an estimate of the degrees of freedom of x , which is defined as the number of non-zero entries, that is $\text{df} = k$.

Although in Shi et al., 2018 AIC and BIC have been used as a part of the optimisation process, here I calculate them using the estimated data only after convergence. In summary, the only difference between the AIC and BIC is that the BIC takes into account the logarithm of the total size of the estimator. Here we are looking for the sparser signal

that best minimizes the residual sum of squares (RSS). In that sense, in the BIC the function will also be penalized if the size of the signal is large. However, since I am testing for different percentages of removal fraction, which will remove data randomly in λ^2 -space, this can change the size of the Faraday depth space and consequently the size of the wavelet representation. Therefore, I suggest that n should be equal to the number of measurements in λ^2 -space, such that the AIC and BIC metrics show the sparsest signal with the best RSS. Further information about the use of the AIC and BIC can be found in “Appendix E: Model Selection Criterion: AIC and BIC” 2014; Ding et al., 2018.

In order to study which wavelet family best represents certain scenarios I have made 50 realizations for each of the scenarios described in Section 3.5, fixing the noise and removal fractions to 0.7 mJy/beam and 0.3, respectively. This allows me to calculate the mean and standard deviation of each metric. I have used only orthogonal wavelet families and the delta function basis. It is important to highlight that when using wavelet transforms we always use the maximum number of decomposition levels defined for the DWT. For a signal of length n and a filter of length p this is defined as

$$\text{max_level} = \left\lfloor \log_2 \left(\frac{n}{p-1} \right) \right\rfloor. \quad (3.40)$$

The results of this process for the DWT are shown in Figure 3.6. For the corresponding UWT the number of decomposition levels is given by $\log_2(n)$ and the results of these experiments are shown in Figure 3.7 for undecimated wavelets.

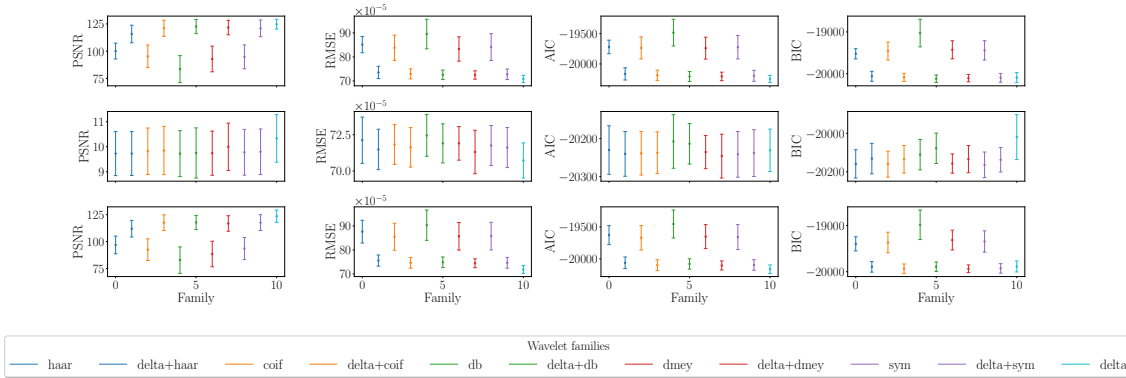


FIGURE 3.6: PSNR, RMSE, AIC and BIC using all discrete wavelet families for reconstruction using the discrete wavelet transform. First row shows scenario 1, second row for scenario 2 and third row for scenario 3.

From Figure 3.6 and Figure 3.7 it can be seen that although the average values of the RMSE, AIC and BIC tend to be lowest for the delta function basis, the best values for wavelets can be obtained using the discrete Meyer, Haar, symlets and coiflets filters. However, when combining the wavelets with the delta function basis the best metrics are obtained using the discrete Meyer, Haar and Daubechies families.

Note that although AIC and BIC tend to be higher for UWT, one must take into account that the number of coefficients are larger than in the discrete wavelet transform case since the UWT does not use any downsampling or upsampling.

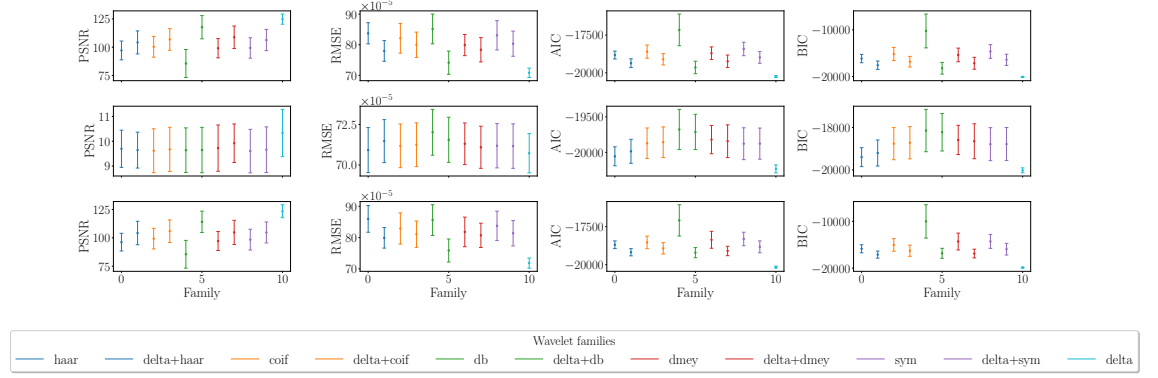


FIGURE 3.7: PSNR, RMSE, AIC and BIC using all discrete wavelet families for reconstruction using the undecimated wavelet transform. First row shows scenario 1, second row for scenario 2 and third row for scenario 3.

| | Scenario 1 | Scenario 2 | Scenario 3 |
|-------------|-----------------------------------|-----------------------------------|-----------------------------------|
| AIC | -20248.78 ± 60.24 | -20231.11 ± 55.93 | -20163.09 ± 66.42 |
| BIC | -20093.34 ± 120.40 | -20019.56 ± 116.71 | -19887.35 ± 119.22 |
| PSNR | 124.79 ± 4.49 | 10.33 ± 0.95 | 123.53 ± 5.72 |
| RMSE | $(70.83 \pm 1.52) \times 10^{-5}$ | $(70.73 \pm 1.21) \times 10^{-5}$ | $(71.85 \pm 1.62) \times 10^{-5}$ |

TABLE 3.2: AIC, BIC, PSNR and RMSE for delta function basis.

From these results I have selected the best wavelet families to be those that have the lowest AIC and BIC average values. These are summarised in Tables 3.3 and 3.4 where all the metrics for the three scenarios and wavelet and undecimated transforms are presented. Then I have repeated the same process by selecting the best wavelets within those families for each of the cases. These results are presented in Tables 3.5 and 3.6. As a comparison we also present these results for the delta function basis in Table 3.2. Note that even though the WT works better than UWT according to the AIC and BIC, the difference is small. The tests show that PSNR and RMSE are improved when using UWT. This can be attributed to the fact that the UWT is considered a multiscale decomposition (Starck et al., 2007).

Figures 3.8 – 3.10 show the results of 50 realisations for the three scenarios using removal fractions and noise fractions from 0.1 to 0.9. Figure 3.8 show the results using the delta function basis and Figure 3.10 show the results using the undecimated wavelet transform (UWT).

Very different results can be observed in Figure 3.10 when comparing the outcomes of the discrete wavelet transform with the undecimated wavelet transform. While the PSNR

| | Scenario 1 | | Scenario 2 | | Scenario 3 | |
|---------------------|-----------------------------------|-----------------------------------|-----------------------------------|-----------------------------------|-----------------------------------|-----------------------------------|
| | WT | UWT | WT | UWT | WT | UWT |
| Best wavelet family | dmey | haar | sym | haar | coif | haar |
| AIC | -19739.53 ± 180.53 | -18823.76 ± 260.78 | -20241.77 ± 60.25 | -20054.28 ± 133.15 | -19671.22 ± 191.22 | -18690.92 ± 252.91 |
| BIC | -19427.18 ± 216.16 | -16156.66 ± 893.47 | -20163.74 ± 66.63 | -19398.75 ± 446.16 | -19369.09 ± 222.83 | -15865.54 ± 861.84 |
| PSNR | 92.86 ± 11.78 | 97.11 ± 8.30 | 9.78 ± 0.92 | 9.70 ± 0.75 | 92.44 ± 10.03 | 96.22 ± 7.80 |
| RMSE | $(83.30 \pm 5.06) \times 10^{-5}$ | $(83.74 \pm 3.46) \times 10^{-5}$ | $(71.76 \pm 1.38) \times 10^{-5}$ | $(70.92 \pm 1.38) \times 10^{-5}$ | $(85.49 \pm 5.64) \times 10^{-5}$ | $(85.97 \pm 4.26) \times 10^{-5}$ |

TABLE 3.3: AIC, BIC, PSNR and RMSE for discrete wavelets transforms (WT) and undecimated wavelet transforms (UWT) with the minimum AIC.

| | Scenario 1 | | Scenario 2 | | Scenario 3 | |
|---------------------|-----------------------------------|-----------------------------------|-----------------------------------|-----------------------------------|-----------------------------------|-----------------------------------|
| | D+WT | D+UWT | D+WT | D+UWT | D+WT | D+UWT |
| Best wavelet family | db | db | dmey | haar | dmey | db |
| AIC | -20207.76 ± 81.40 | -19644.59 ± 414.10 | -20246.30 ± 57.76 | -19984.59 ± 168.32 | -20104.92 ± 70.98 | -19211.01 ± 332.61 |
| BIC | -20120.36 ± 90.66 | -18232.65 ± 1254.23 | -20134.18 ± 70.59 | -19203.41 ± 612.72 | -19937.21 ± 82.66 | -16832.39 ± 1064.69 |
| PSNR | 122.61 ± 6.49 | 117.66 ± 10.28 | 10.00 ± 0.95 | 9.64 ± 0.72 | 116.75 ± 7.20 | 114.13 ± 9.43 |
| RMSE | $(72.55 \pm 1.96) \times 10^{-5}$ | $(74.14 \pm 3.78) \times 10^{-5}$ | $(71.31 \pm 1.49) \times 10^{-5}$ | $(71.47 \pm 1.32) \times 10^{-5}$ | $(74.45 \pm 1.85) \times 10^{-5}$ | $(75.87 \pm 3.68) \times 10^{-5}$ |

TABLE 3.4: AIC, BIC, PSNR and RMSE for delta basis function combined with discrete wavelets transforms (D+WT) and undecimated wavelet transforms (D+UWT) with the minimum AIC.

| | Scenario 1 | | Scenario 2 | | Scenario 3 | |
|---------------------|-----------------------------------|-----------------------------------|-----------------------------------|-----------------------------------|-----------------------------------|-----------------------------------|
| | WT | UWT | WT | UWT | WT | UWT |
| Best wavelet family | dmey | haar | sym7 | haar | coif17 | haar |
| AIC | -19739.53 ± 180.53 | -18823.76 ± 260.78 | -20257.25 ± 49.57 | -20054.28 ± 133.15 | -19744.98 ± 156.91 | -18690.92 ± 252.91 |
| BIC | -19427.18 ± 216.16 | -16156.66 ± 893.47 | -20188.55 ± 55.79 | -19398.75 ± 446.16 | -19450.36 ± 185.29 | -15865.54 ± 861.84 |
| PSNR | 92.86 ± 11.78 | 97.11 ± 8.30 | 9.86 ± 1.01 | 9.70 ± 0.75 | 93.95 ± 8.68 | 96.22 ± 7.80 |
| RMSE | $(83.30 \pm 5.06) \times 10^{-5}$ | $(83.74 \pm 3.46) \times 10^{-5}$ | $(71.45 \pm 1.28) \times 10^{-5}$ | $(70.92 \pm 1.38) \times 10^{-5}$ | $(83.30 \pm 4.48) \times 10^{-5}$ | $(85.97 \pm 4.26) \times 10^{-5}$ |

TABLE 3.5: AIC, BIC, PSNR and RMSE for discrete wavelets transforms (WT) and undecimated wavelet transforms (UWT) with the minimum AIC.

and RMSE plots exhibit similar trends, the AIC and BIC plots display notable discrepancies. It is important to note that AIC and BIC do not agree, as observed in the previous plots. One reason for this divergence can be attributed to the nature of the undecimated wavelet, which does not perform coefficient decimation at every transformation level. Consequently, this leads to a higher number of coefficients, potentially including an increased number of non-zero coefficients that represent the Faraday depth signal. As a result, the value of df is higher, which penalizes the BIC. It is important to acknowledge that, in certain cases, the number of available data points may be significantly fewer than the number of parameters, which can cause the AIC to encounter challenges and requiring correction (see e.g. Hurvich and Tsai, 1989; Hurvich et al., 2002).

3.5.2 Comparison with RM-CLEAN

At this point in the thesis, I have tested three different scenarios for Faraday depth spectra reconstruction, using the AIC and BIC metrics to select the wavelets that best fits the data. Another well known method for reconstructing Faraday spectra is the RM-CLEAN algorithm, which is based on the CLEAN imaging heuristic proposed by Hogbom in 1974. Given the complex nature of Faraday depth signals, the algorithm works by iteratively finding the maximum in the absolute values of the residual signal. It then subtracts a scaled and shifted RMTF from the residual and adds the subtracted flux into the model signal. This process continues until the maximum in the absolute values of the residual signal falls below a set threshold. Finally, the RM-CLEANed signal is obtained by

| | Scenario 1 | | Scenario 2 | | Scenario 3 | |
|---------------------|-----------------------------------|-----------------------------------|-----------------------------------|-----------------------------------|-----------------------------------|-----------------------------------|
| | D+WT | D+UWT | D+WT | D+UWT | D+WT | D+UWT |
| Best wavelet family | db7 | db34 | dmey | haar | dmey | db38 |
| AIC | -20231.67 ± 61.31 | -19931.31 ± 204.32 | -20246.30 ± 57.76 | -19984.59 ± 168.32 | -20104.92 ± 70.98 | -19365.93 ± 274.70 |
| BIC | -20149.23 ± 68.95 | -19110.59 ± 660.77 | -20134.18 ± 70.59 | -17275.06 ± 914.83 | -19937.21 ± 82.66 | -16832.39 ± 1064.69 |
| PSNR | 123.42 ± 6.28 | 123.11 ± 6.22 | 10.00 ± 0.95 | 9.64 ± 0.72 | 116.75 ± 7.20 | 117.38 ± 6.58 |
| RMSE | $(71.98 \pm 1.55) \times 10^{-5}$ | $(72.47 \pm 1.96) \times 10^{-5}$ | $(71.31 \pm 1.49) \times 10^{-5}$ | $(71.47 \pm 1.32) \times 10^{-5}$ | $(74.45 \pm 1.85) \times 10^{-5}$ | $(74.60 \pm 2.13) \times 10^{-5}$ |

TABLE 3.6: AIC, BIC, PSNR and RMSE for delta basis function combined with discrete wavelets transforms (D+WT) and undecimated wavelet transforms (D+UWT) with the minimum AIC.

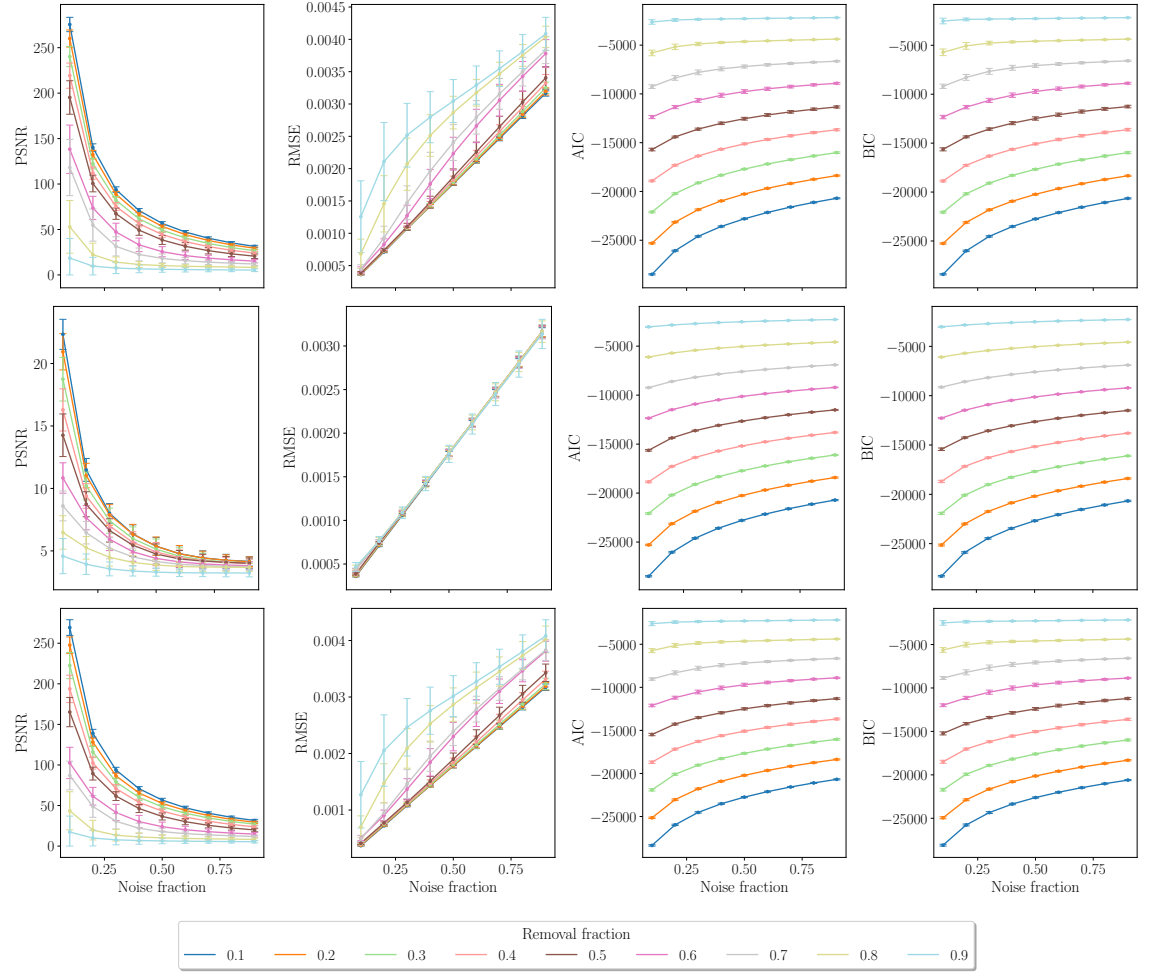


FIGURE 3.8: PSNR, RMSE, AIC and BIC for delta function basis reconstruction. First row shows scenario 1, second row for scenario 2 and third row for scenario 3.

convolving the model signal with the clean beam, which is typically a Gaussian fitted to the absolute values of the RMTE, and then adding the residual signal. This process is outlined in Algorithm 3.

Algorithm 3 Hogbom RM-CLEAN

- 1: **Input:** Dirty Faraday depth signal $\tilde{F}(\phi)$, RMTE $\text{RMTE}(\phi)$, clean RMTE $\text{RMTE}_c(\phi)$, gain g , threshold τ
 - 2: **Initialize:** residual signal $R = \tilde{F}(\phi)$, model signal $M = 0 + 0j$
 - 3: **while** $\max(|R|) > \tau$ **do**
 - 4: Find location ϕ of maximum in $|R|$
 - 5: $f = g \times R(\phi)$
 - 6: $M(\phi) = M(\phi) + f$
 - 7: Subtract scaled and shifted dirty beam from residual: $R = R - f \times \text{RMTE}(\phi - \phi')$
 - 8: **end while**
 - 9: **Output:** RM-CLEANed signal $F_c = M \otimes \text{RMTE}_c + R$
-

In order to draw comparisons between the method I propose in this thesis and RM-CLEAN, the same three scenarios previously examined will be deployed. This will yield

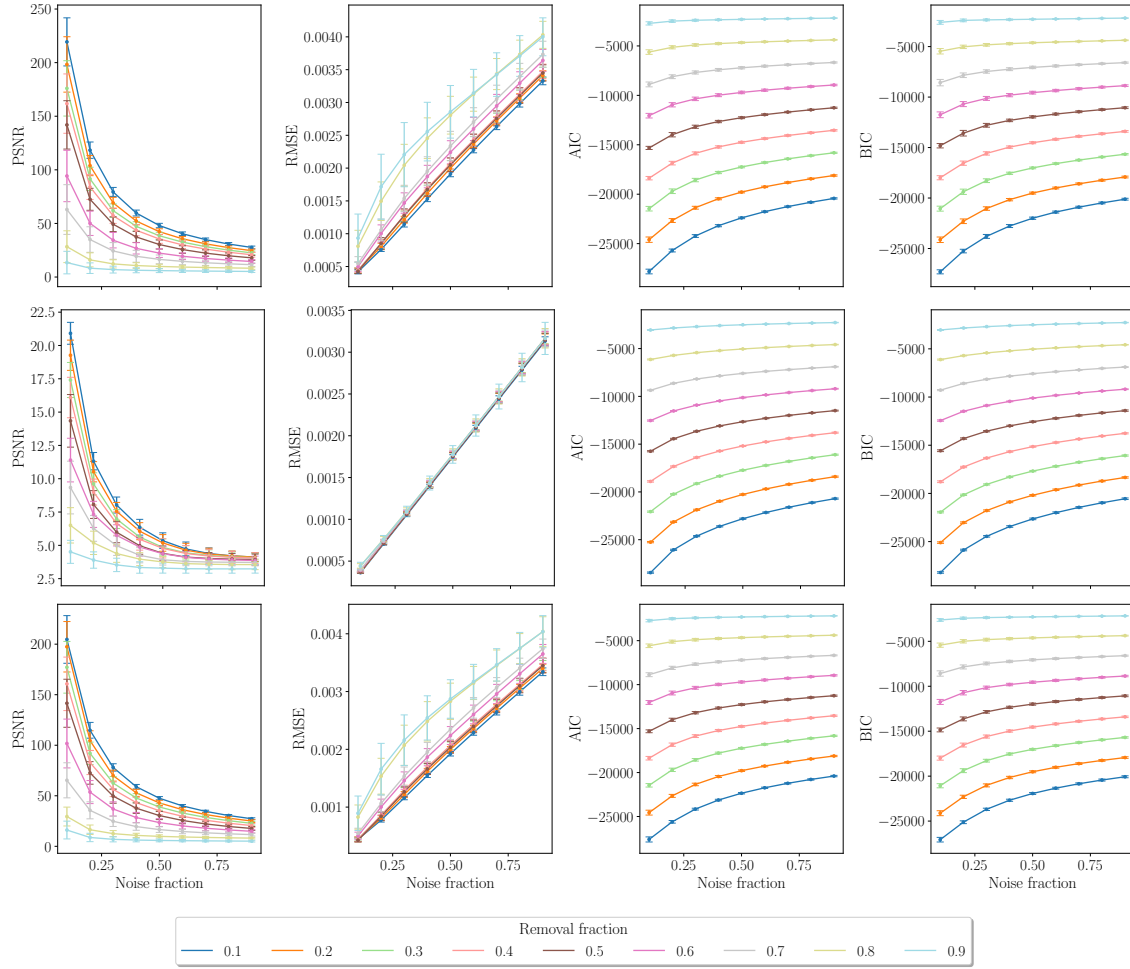


FIGURE 3.9: PSNR, RMSE, AIC and BIC using a discrete wavelet basis reconstruction. The first row shows Scenario 1, the second row shows Scenario 2 and the third row shows Scenario 3. We have used wavelets `dmey`, `haar` and `sym9`, respectively.

insights into the behaviour of RM-CLEAN during the reconstruction of both thin and thick Faraday depth spectra and afford a comparison with the proposed compressed sensing framework. The intensity of the thick source has been increased to $105 \text{ mJy beam}^{-1}$ to ensure its visibility in the plots. It is of importance to note that due to the absence of measurements at low frequencies in λ^2 -space, part of the signal intensity and the shape of these sources may become distorted.

In each scenario, I will conduct a comparative analysis of Faraday depth spectra reconstructions, utilising both the proposed framework and RM-CLEAN¹. The comparison will include reconstructions employing the delta basis function in isolation (that is, L_1 norm regularisation on Faraday depth spectrum), as well as those that incorporate the optimally selected discrete and undecimated wavelets as determined in the preceding subsection. Figures 3.11, 3.12, and 3.13 exhibit Faraday depth reconstructions of simulated scenarios using a variety of methods. Each top panel illustrates the restored, model, and dirty Faraday depth amplitudes, while the corresponding bottom panel presents the

¹<https://github.com/CIRADA-Tools/RM-Tools>

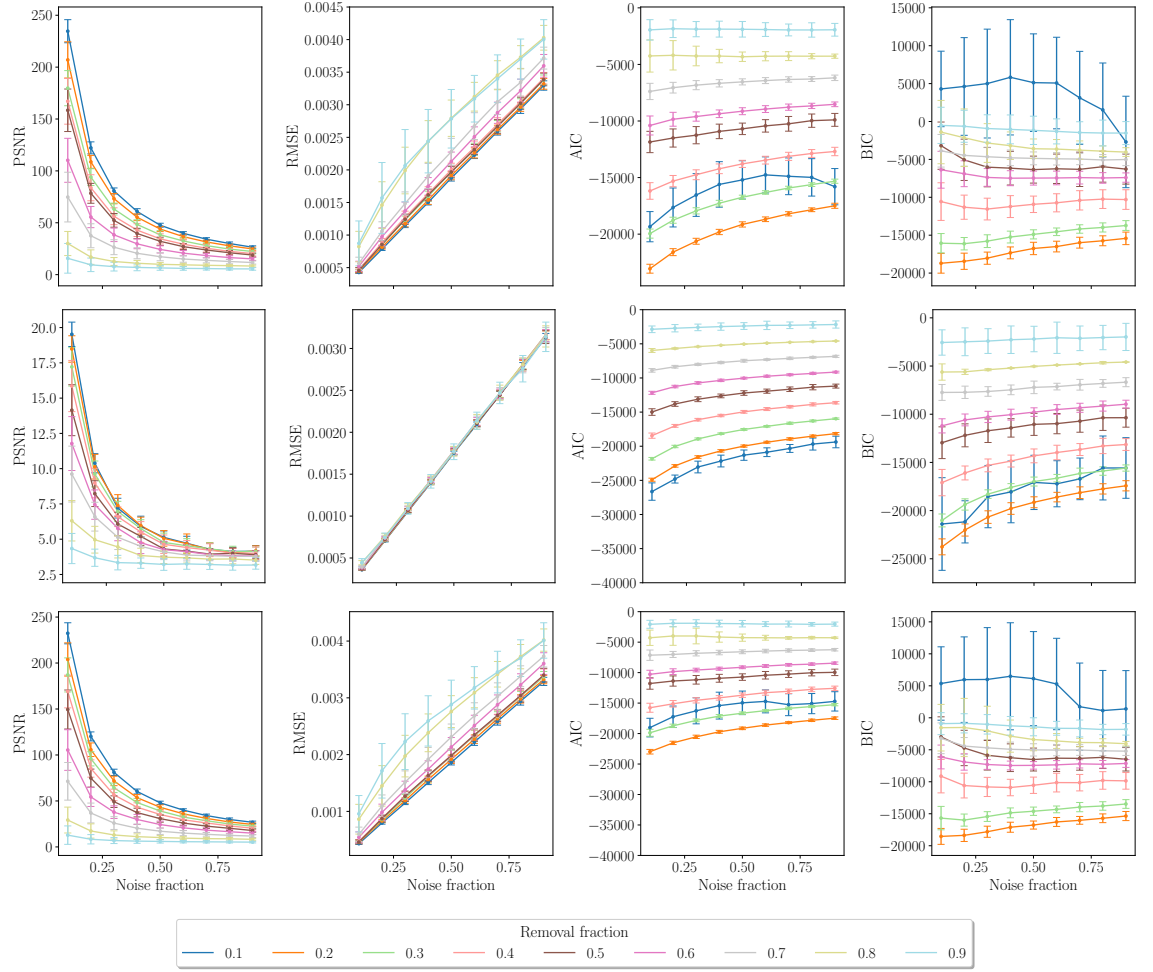


FIGURE 3.10: PSNR, RMSE, AIC and BIC using an undecimated wavelet basis reconstruction. First row shows scenario 1, second row for scenario 2 and third row for scenario 3. We have used wavelets *coif3*, *haar* and *haar*, respectively.

residuals.

Firstly, Figure 3.11 portrays an assortment of reconstructions for a thin source (Scenario 1). While all strategies effectively reconstruct the thin source and reduce the RMFTF sidelobes to a level below 5σ , only the reconstructions employing the delta basis function and RM-CLEAN achieve a peak value close to the simulated one (35 mJy beam^{-1}). Specifically, the reconstruction using the delta basis function and RM-CLEAN generate peak values of 34.21 ± 0.25 and $35.19 \pm 0.25 \text{ mJy beam}^{-1}$, respectively. In contrast, the hybrid methods that combine the delta basis function with the discrete wavelet db7 and the undecimated wavelet db34 yield peak values of 33.14 ± 0.22 and $33.55 \pm 0.22 \text{ mJy beam}^{-1}$, respectively. Importantly, for all methods, the Faraday depth at peak, ϕ_{peak} , aligns closely with the simulated value, within the error margins, which stands at -200 rad m^{-2} .

Secondly, reconstructions of the modified Scenario 2 are depicted in Figure 3.12. As I mentioned before, due to the lack of measurements at low frequencies in λ^2 -space, the polarised intensity and shape of thick sources are distorted. Therefore, it is not possible to compare the resulting polarised intensity peaks with the simulated value. Instead, it can be reported that none of the methods are able to reach the polarised intensity values of

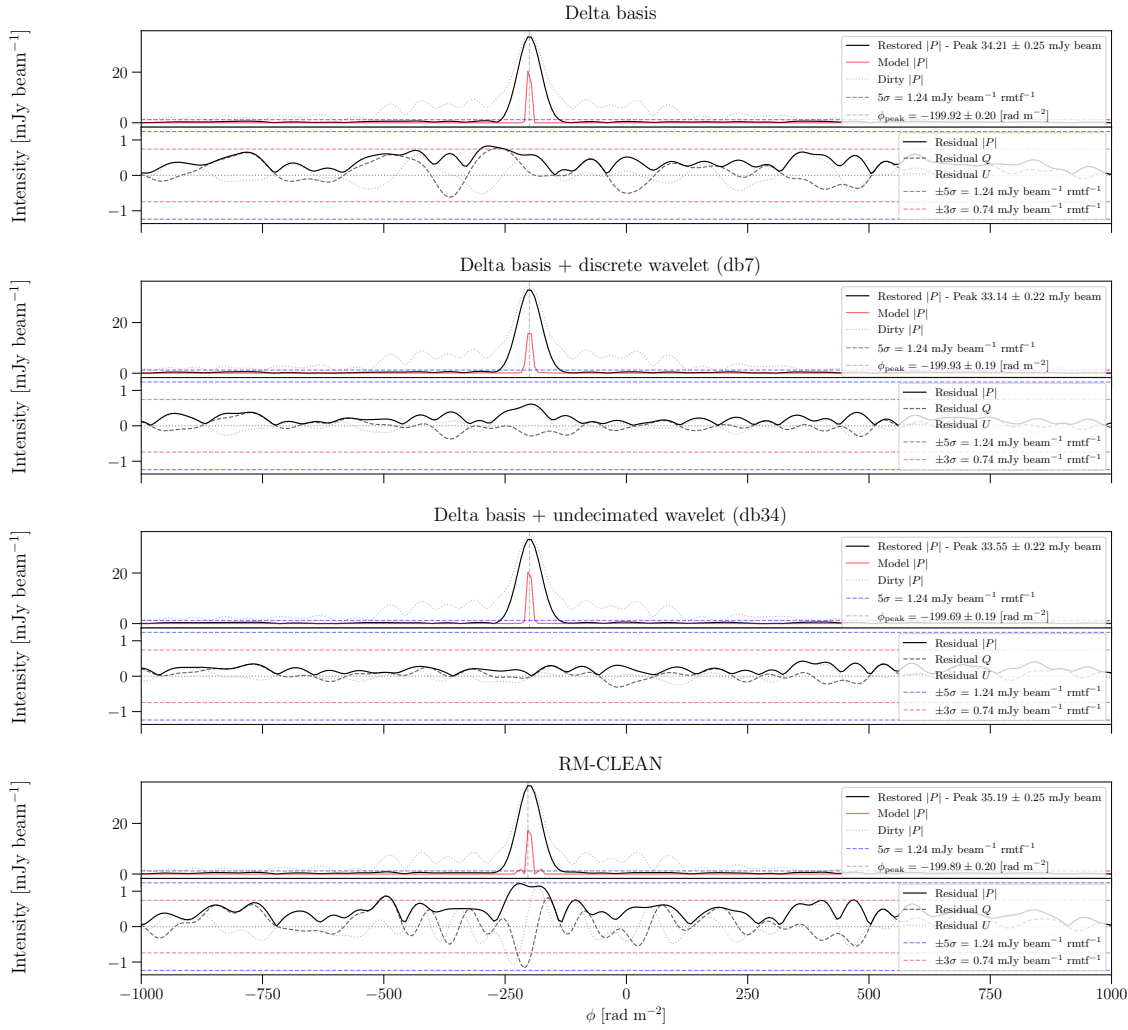


FIGURE 3.11: Faraday depth reconstructions of a simulated thin source (Scenario 1). From top to bottom: reconstructions using the delta basis function, the delta basis function combined with the discrete wavelet db7, the delta basis function combined with the undecimated wavelet db34, and RM-CLEAN. In each plot, the top panel displays the amplitude values of the restored (black), model (red), and dirty Faraday depth spectrum (dotted grey). The vertical dashed grey line indicates the position at the peak in Faraday depth. The horizontal dashed blue line represents the theoretical 5σ boundary on the amplitude of polarized intensity. The bottom panel illustrates the amplitude, real, and imaginary parts of the residuals. Red and blue dashed lines represent the theoretical $\pm 5\sigma$ and $\pm 3\sigma$ noise boundaries, respectively.

the dirty Faraday depth spectrum. However, the delta basis function combined with the dmey discrete wavelet and RM-CLEAN are able to reach the highest polarised intensity values with peaks of 8.51 ± 0.23 and 8.50 ± 0.25 mJy beam $^{-1}$, respectively. Additionally, it is observable that when using the haar undecimated wavelet, part of signal from the top of the thick source is reconstructed. On the contrary, all other methods show structures as if two very close point sources were reconstructed.

Thirdly, Figure 3.13 depicts the reconstruction of modified Scenario 3, which combines a thin source and a thick source. Similar to Scenario 1, it can be observed that RM-CLEAN and the delta basis function are capable of reconstructing the highest polarised

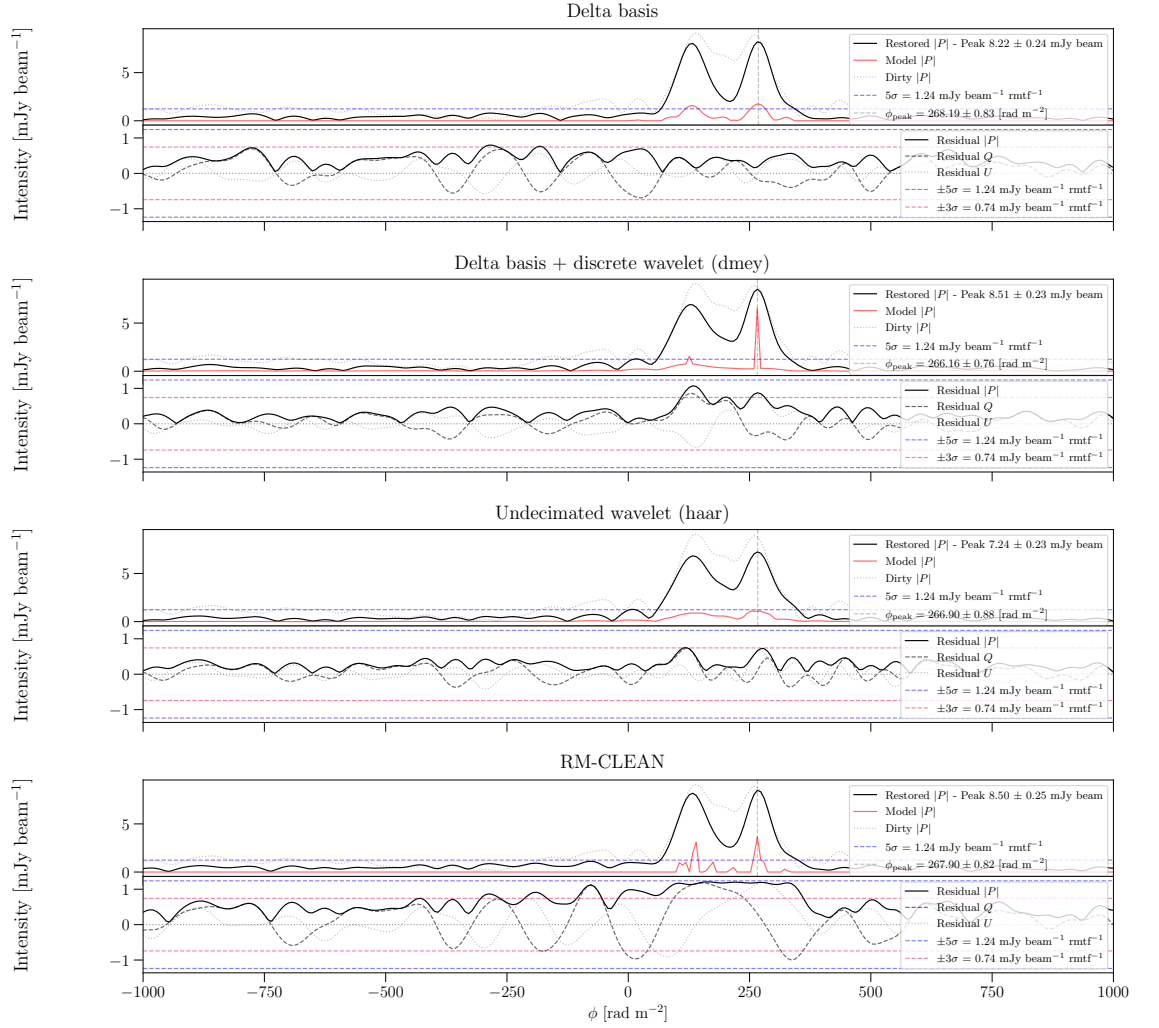


FIGURE 3.12: Faraday depth reconstructions of a simulated thick source (modified Scenario 2). The source polarised intensity has been increased to $0.11 \text{ mJy beam}^{-1}$ to ensure its visibility in the plots. From top to bottom: reconstructions using the delta basis function, the delta basis function combined with the discrete wavelet *dmey*, the undecimated wavelet *haar*, and RM-CLEAN. In each plot, the top panel displays the amplitude values of the restored (black), model (red), and dirty Faraday depth spectrum (dotted grey). The vertical dashed grey line indicates the position at the peak in Faraday depth. The horizontal dashed blue line represents the theoretical 5σ boundary on the amplitude of polarized intensity. The bottom panel illustrates the amplitude, real, and imaginary parts of the residuals. Red and blue dashed lines represent the theoretical $\pm 5\sigma$ and $\pm 3\sigma$ noise boundaries, respectively.

intensity values, yielding peaks of 35.58 ± 0.25 and $34.38 \pm 0.25 \text{ mJy beam}^{-1}$, respectively. Furthermore, for all the methods, the Faraday depth at the peak, ϕ_{peak} , aligns closely with the simulated value, mirroring the reconstructions in Scenario 1. Conversely, the thick sources exhibit the same pattern as if two very close point sources were reconstructed, consistent across all the reconstruction methods.

In this chapter, I have delved into the fundamentals of compressed sensing and its specific applications within the field of radio astronomy. Our exploration also extended to the unique opportunities offered by one-dimensional applications of compressed sensing within this domain. A crucial component of this chapter has been the introduction of

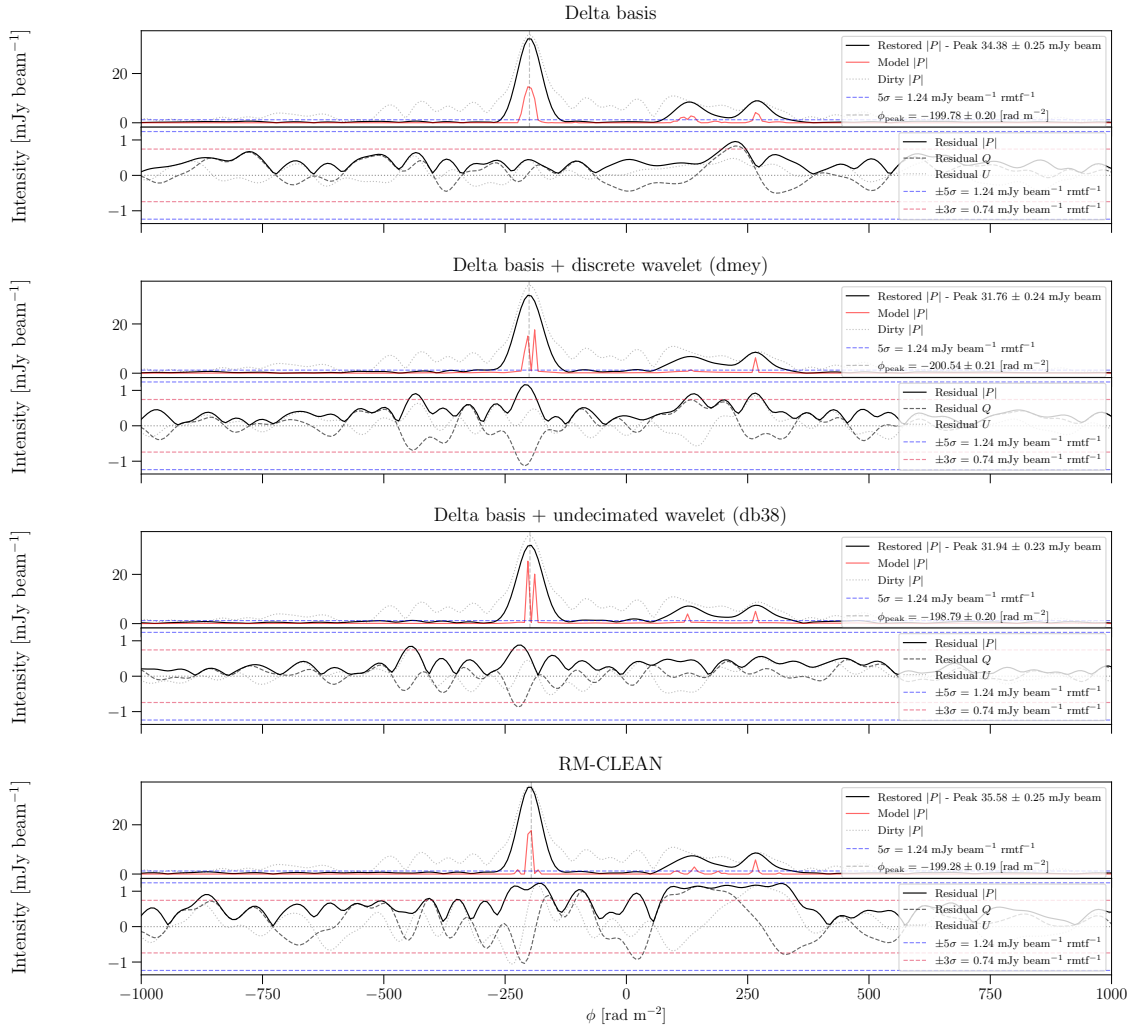


FIGURE 3.13: Faraday depth reconstructions of a simulated thin and thick source (modified Scenario 3). The source polarised intensity has been increased to $0.11 \text{ mJy beam}^{-1}$ to ensure its visibility in the plots. From top to bottom: reconstructions using the delta basis function, the delta basis function combined with the discrete wavelet *dmey*, the delta basis function combined with the undecimated wavelet *db38*, and RM-CLEAN. In each plot, the top panel displays the amplitude values of the restored (black), model (red), and dirty Faraday depth spectrum (dotted grey). The vertical dashed grey line indicates the position at the peak in Faraday depth. The horizontal dashed blue line represents the theoretical 5σ boundary on the amplitude of polarized intensity. The bottom panel illustrates the amplitude, real, and imaginary parts of the residuals. Red and blue dashed lines represent the theoretical $\pm 5\sigma$ and $\pm 3\sigma$ noise boundaries, respectively.

our novel compressed sensing framework, *cs-romer*.

A significant part of the discussion in this chapter is centered around evaluation metrics, highlighting the importance of meticulously selecting an optimal wavelet basis. As I have established, this step is crucial in attaining the most effective representation of Faraday depth data, given a specific observational set-up.

I have also conducted an in-depth comparison between our *cs-romer* framework and RM-CLEAN. Through this comparative analysis, I have not only validated the effectiveness of our approach but have also showcased *cs-romer*'s potential as a viable alternative

to the established methods in the field.

It is essential to emphasize that *cs-romer* is capable of performing 1+2D Faraday imaging by reconstructing Faraday depth spectra on multiple lines of sight within a spectro-polarimetric cube. However, the *cs-romer* framework is not designed for direct extension to 3D reconstruction.

Rather than attempting to force the framework into this role, a more practical and efficient approach would be to incorporate 3D imaging directly into an imager. This would entail integrating a Faraday depth cube as a parameter in the objective function and fitting visibilities using a 3D Fourier transform.

Thus, through the exploration of the intricacies of compressed sensing and the unveiling of *cs-romer*, we have expanded the array of data processing tools available for use in radio astronomy. We aspire that the potential of our proposed framework will contribute to enhancing the quality and efficiency of radio astronomical data processing.

Chapter 4

JVLA Abell 1314

The work in this chapter is published as part of the paper “CS-ROMER: A novel compressed sensing framework for Faraday depth reconstruction”, Miguel Cárcamo, Anna M. M. Scaife, Emma L. Alexander, and J. Patrick Leahy, 2022, Monthly Notices of the Royal Astronomical Society, arxiv:2205.01413.

4.1 Abell 1314 Case Study

Abell 1314 (A1314; $z = 0.034$) is a nearby low-mass merging galaxy cluster with a highly disturbed density profile. The observational properties of this cluster are summarised in Table 4.1. From shallow *XMM-Newton* observations, Wilber, A. et al., 2019 calculated the 0.5 – 2.4 keV X-ray luminosity of A1314 to be $0.17 \times 10^{44} \text{ ergs s}^{-1}$, which is higher than that previously found by Ledlow et al., 2003 using ROSAT data, and hence derived a mass of $M_{500} = 0.68 \times 10^{14} M_{\odot}$ using the scaling relation of Reichert, A. et al., n.d.

Although no deep observations of A1314 have been made in the X-ray, a significant number of radio studies have been undertaken due to the complex nature of the radio emission associated with the cluster galaxies. The brightest of these, IC 708 and IC 711, are bent-tail galaxies, with IC 711 in particular having a very long radio tail extending for almost a mega-parsec in a SE-NW direction across the cluster (Vallee and Wilson, 1976). Observations from 2016 with the GMRT (Srivastava and Singal, 2020) showed a spectral break part of the way along the tail of IC 711, and suggested that this may have arisen due to local environmental factors within the cluster. This was supported by later observations, which showed low-levels of diffuse emission perpendicular to the main direction of the IC 711 tail, again indicating a disturbance within A1314 (Sebastian et al., 2017).

Despite the disturbed nature of the cluster, recent radio observations with the LOFAR and GMRT telescopes did not detect a radio halo (Wilber, A. et al., 2019), but the authors suggest that this may be due to the very low mass of this system. However, they did detect irregularly-shaped diffuse radio emission likely to be associated with historic AGN activity from IC 712. They also noted that the spectral index map of the extended

| Property | Value | Reference |
|------------------|---|--------------------------|
| R.A. (J2000) | 11 34 48.7 | Mahdavi and Geller, 2001 |
| δ (J2000) | +49 02 25 | Mahdavi and Geller, 2001 |
| z | 0.034 | Popesso, P. et al., 2004 |
| L_X | $0.17 \times 10^{44} \text{ ergs s}^{-1}$ | Wilber, A. et al., 2019 |
| M_{500} | $0.68 \times 10^{14} M_\odot$ | Wilber, A. et al., 2019 |

TABLE 4.1: Observational properties of Abell 1314 from the literature.

| ID | R.A. (deg) | Dec (deg) | S_{peak} (mJy/bm) | α | Distance (kpc) | Pol? [Y/N] |
|-----------------|---------------|--------------|-------------------------------|----------|-------------------|---------------|
| 1 | 173.454 | 48.987 | 9.11 | -0.73 | 520.2 | Y |
| 2 | 173.496 | 49.046 | 32.04 | -0.72 | 390.7 | N |
| 3 ^a | 173.497 | 49.062 | 156.69 | -0.43 | 378.9 | Y |
| 4 | 173.498 | 48.941 | 2.57 | 0.12 | 538.7 | N |
| 5 | 173.521 | 49.106 | 4.24 | -0.82 | 331.5 | Y |
| 6 | 173.571 | 49.152 | 14.11 | -0.53 | 291.1 | N |
| 7 | 173.621 | 48.951 | 1.29 | -1.83 | 397.6 | N |
| 8 | 173.632 | 49.048 | 1.59 | 0.57 | 179.4 | N |
| 9 ^b | 173.694 | 48.956 | 41.27 | -0.22 | 353.0 | Y |
| 10 ^c | 173.705 | 49.078 | 27.97 | -0.72 | 36.9 | Y |
| 11 | 173.713 | 49.203 | 1.87 | -1.20 | 291.0 | N |
| 12 | 173.761 | 49.193 | 4.29 | -0.63 | 277.6 | Y |
| 13 | 173.803 | 48.967 | 11.17 | -0.98 | 357.6 | Y |
| 14 | 173.933 | 49.038 | 3.62 | -0.68 | 400.0 | N |
| 15 | 173.942 | 48.921 | 3.55 | 0.41 | 590.1 | Y |

^a IC708. ^b IC711. ^c IC712.TABLE 4.2: A1314 radio sources. Radio sources within the A1314 field detected in Stokes I at $\geq 5\sigma_I$ are listed in order of increasing Right Ascension. Column [1] lists the source id as used in this work, [2] Right Ascension of the source in degrees, [3] Declination of the source in degrees, [4] peak flux density of the source at a frequency of 1.5 GHz, [5] Stokes I spectral index of the source at the position of the peak as determined from the VLA data used in this work, [6] distance of the source from the X-ray centre in kpc, and [7] indicates whether the source is also detected in polarisation at $\geq 6\sigma_P$.

head-tail radio galaxy IC 711 indicates signs of disturbance, consistent with the findings of Srivastava and Singal, 2020.

Here I use a combination of archival X-ray and radio observations to derive the magnetic field properties of A1314 as a function of location within the cluster.

4.2 JVLA Data Reduction

In this section, I use the JVLA data with the aim of demonstrating and testing the CS approach to Faraday Rotation Measurements using a real radio-astronomical dataset. The data that I use here can be accessed in the VLA archive under project ID 18A-172¹. The

¹<https://archive.nrao.edu/archive/advquery.jsp>

observation, spanning three hours, was conducted in January 2019 in the L-Band (1.008-2.031,GHz, see Table 1.1) and employed the C configuration. This information is summarised in Tables 4.3 and 4.4.

| Obs. Date | Obs. Time [hr] | Band | JVLA Array | Beam [arcmin] | σ_{rms} [mJy/beam] |
|--------------|-------------------|------|---------------|----------------------|-------------------------------------|
| January 2019 | 3 | L | C | $0.27' \times 0.25'$ | 0.29 |

TABLE 4.3: Abell 1314 JVLA radio observation details

| Parameter | Value | Description |
|------------------------|-------------|--------------------|
| λ_{min} | 0.148 m | Minimum wavelength |
| λ_{max} | 0.297 m | Maximum wavelength |
| B_{max} | 3373.853 m | Maximum baseline |
| D_{min} | 25 m | Dish size |
| Δx | 9.02 arcsec | Resolution |
| FOV | 40.8 arcmin | Field-of-view |

TABLE 4.4: Abell 1314 JVLA resolution and field-of-view details

As has been described in Chapter 2 the main steps of the data reduction are parallel-hand calibration, polarisation calibration and self-calibration. In the case of this observation I have manually inspected the data before parallel-hand calibration in order to find anomalies and/or RFI. Subsequently the I used the VLA pipeline to calibrate the parallel-hand data. To use the pipeline I followed the polarisation calibration CASA guide². I ran the pipeline and then restored the Measurement Set to the state before polarisation calibration since this latter part will be done using our custom polarisation calibration framework.

4.2.1 RFI Excision

Before doing polarisation calibration I inspected the amplitude vs. frequency plots of the cross-hand data for each spectral window in order to identify RFI and instrumental anomalies in the data. These were flagged using the automated statistical algorithms `rflag` and `tfcrop` in CASA. I use the first to remove the residual RFI and although the use of `tfcrop` is optional, we use it to decrease the amount of residual RFI in the parallel-hand data. I note that the RFI removal works better over short frequency intervals (no more than 3 spectral windows). Therefore, I first use the command `flagdata` with the following parameters to flag the residual RFI on parallel hands:

```
mode    = 'tfcrop'
correlation = ''
freqfit = 'line'
```

²https://casaguides.nrao.edu/index.php?title=CASA_Guides:polarisation_Calibration_based_on_CASA_pipeline_standard_reduction:_The_radio_galaxy_3C75-CASA5.6.2

Then I used the same command for cross-hand data, but with the following parameters:

```
mode      = 'rflag'
correlation = 'LR,RL'
spw       = '0'
extendflags = True
```

Note here that spectral window 0 is the frequency interval most affected by RFI. Then we repeat the same command using spectral windows intervals such that:

```
mode      = 'rflag'
correlation = 'LR,RL'
spw       = '1~2'
extendflags = True
```

and we repeat until we get to the last spectral window.

4.2.2 Calibration models

By considering the available calibrators in the observation data, I chose 3C 286 as the polarisation angle calibrator and the unpolarised source 3C 147 as the leakage calibrator. I then used the four-step polarisation calibration framework, described in more detail in Chapter 2: fitting the calibrator data to known flux density, polarisation angle and polarisation fraction models, calibrating for cross-hand delays, calibrating for leakage, and lastly calibrating for polarisation angle.

The polarisation calibration framework begins by using the Taylor coefficients of 3C 286 and 3C 147 and their errors as stored in CASA from (Perley and Butler, 2017), see Table 4.5 and Table 4.6, to calculate their flux densities as a function of frequency using the following expression:

$$\log(S_\nu) = \sum_{n=0} a_n \log_{10}(\nu)^n. \quad (4.1)$$

However, the CASA task `setjy` requires coefficients using the following representation:

$$S_\nu = S_0 \left(\frac{\nu}{\nu_0} \right)^{\alpha + \beta \log_{10} \left(\frac{\nu}{\nu_0} \right)} \quad (4.2)$$

and therefore I need to fit the spectral index, α , and the spectral curvature, β , to the flux densities calculated from Equation 4.1. The red line in Figure 4.1 shows the fitted flux density from these coefficients.

TABLE 4.5: 3C 286 coefficients details

| Coefficient | Value | σ |
|-------------|---------|----------|
| a_0 | 1.2481 | 0.0005 |
| a_1 | -0.4507 | 0.0009 |
| a_2 | -0.1798 | 0.0011 |
| a_3 | 0.0357 | 0.0009 |

TABLE 4.6: 3C 147 coefficients details

| Coefficient | Value | σ |
|-------------|---------|----------|
| a_0 | 1.4516 | 0.0010 |
| a_1 | -0.6961 | 0.0017 |
| a_2 | -0.2007 | 0.0050 |
| a_3 | 0.0640 | 0.0044 |
| a_4 | -0.0464 | 0.0035 |
| a_5 | 0.0289 | 0.0025 |

To model linearly polarised intensity data, `setjy` takes arrays of coefficients $p = [p_0, p_1, \dots, p_n]$ and $x = [x_0, x_1, \dots, x_n]$ as inputs. These coefficients model the polarised fraction,

$$\frac{P_\nu}{I_\nu} = \sum_{n=0} p_n \left(\frac{\nu - \nu_0}{\nu_0} \right)^n, \quad (4.3)$$

and the polarisation angle:

$$\chi_\nu = \frac{1}{2} \arctan \frac{U_\nu}{Q_\nu} = \sum_{n=0} x_n \left(\frac{\nu - \nu_0}{\nu_0} \right)^n. \quad (4.4)$$

Once I have all the coefficients it is possible to call `setjy` which creates Stokes I, Q, and U point source models (Stokes V is set to zero) for 3C 286 and 3C 147. Note that 3C 147 is unpolarised at these frequencies and therefore Stokes Q, U and V will be equal to zero for this calibrator.

4.2.3 Cross-hand delay calibration

The framework continues with the cross-hand delay calibration, which solves cross-hand delays due to the residual difference between correlations R and L on the reference antenna. I have chosen 3C 286 as the cross-hand delay calibrator since we know that it has polarised signal in the RL and LR correlations. There are two ways to solve for cross-hand delays. The first option is to solve for a multiband delay, which fits the cross-hand delay across the entire baseband. The second option is to solve the cross-hand delays independently for each spectral window. In this case, I have chosen the first option. This is performed using the CASA task `gaincal` with the parameter `gaintype='KCRSS'`. This will create the cross-hand delay calibration solution table.

4.2.4 Leakage calibration

Using the unpolarised calibrator 3C 147 it is possible to derive the D-terms for the JVLA dataset, see Chapter 2. This is done using the CASA task `polcal` with parameters:

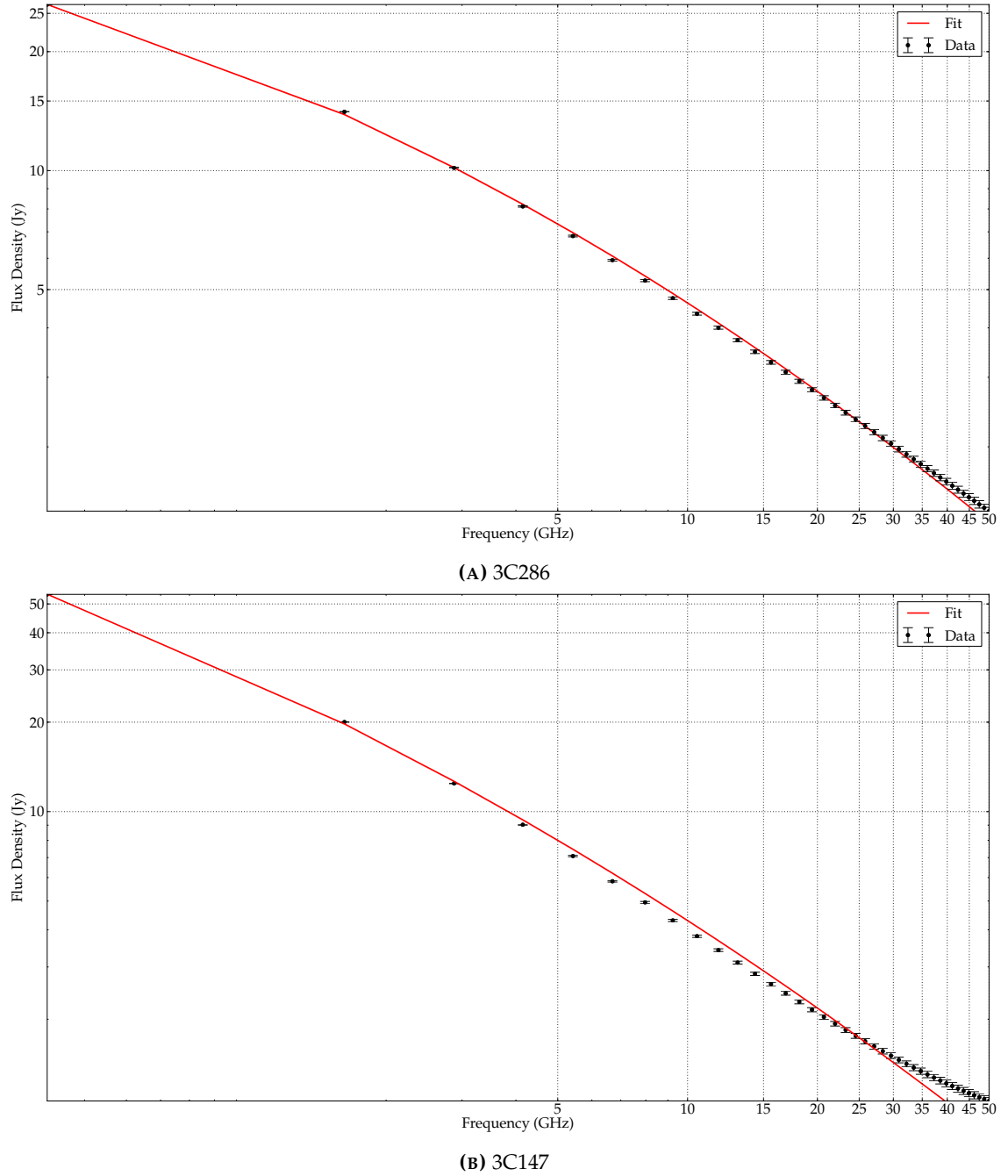


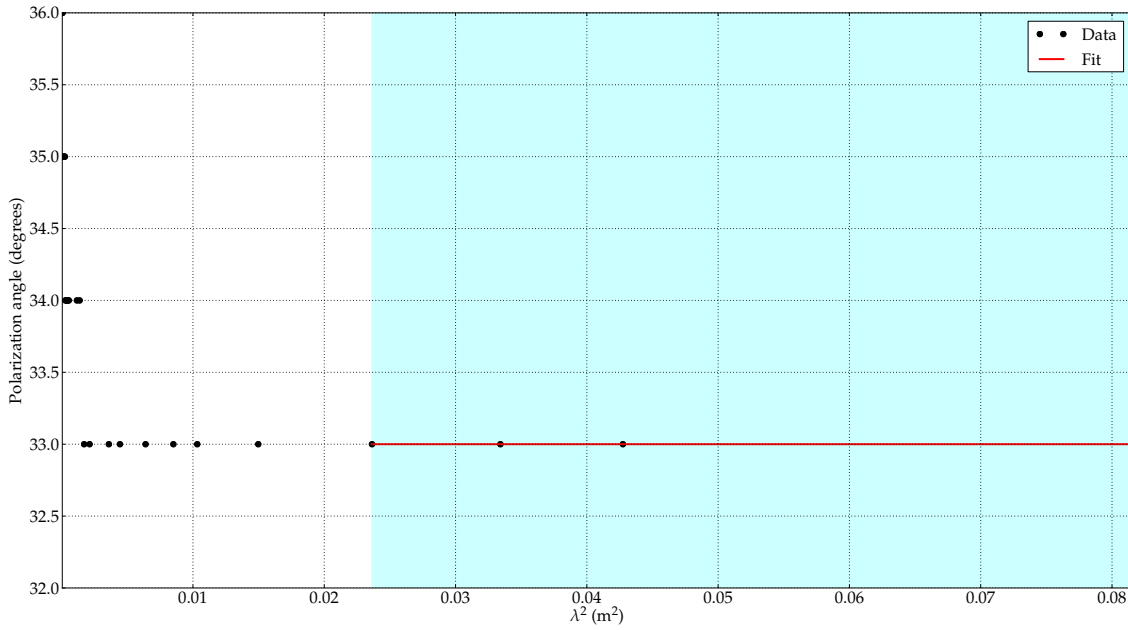
FIGURE 4.1: 3C 286 and 3C 147 flux densities from Perley and Butler, 2017 (black lines) and their respective fitted flux densities using Equation (4.2) (red lines).

```

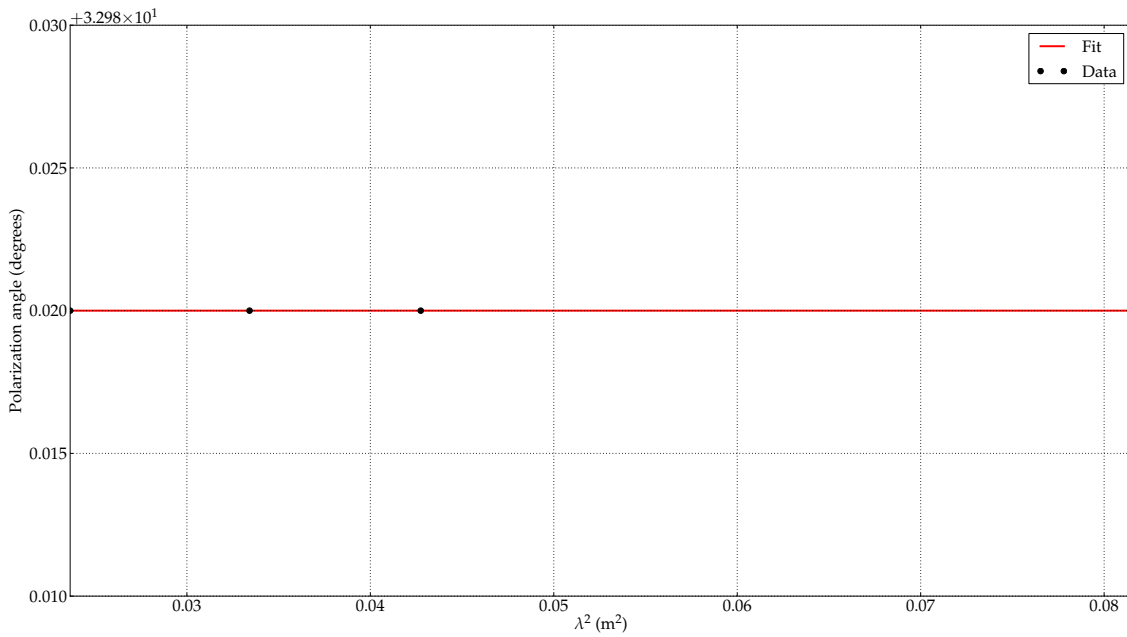
refant = []
poltype = 'Df'
gaintable = ['JVLAdataset.Kcross']
combine = 'scan'

```

The 'Df' parameter means that we are solving for leakage terms, D , on a per channel basis, f , and assuming zero intrinsic polarisation. I also need to add the cross-delay calibration table as parameter and map its unique spectral window (0) solution to all the other spectral windows.



(A) Polarisation angle fit for 3C 286 along the wavelength squared axis

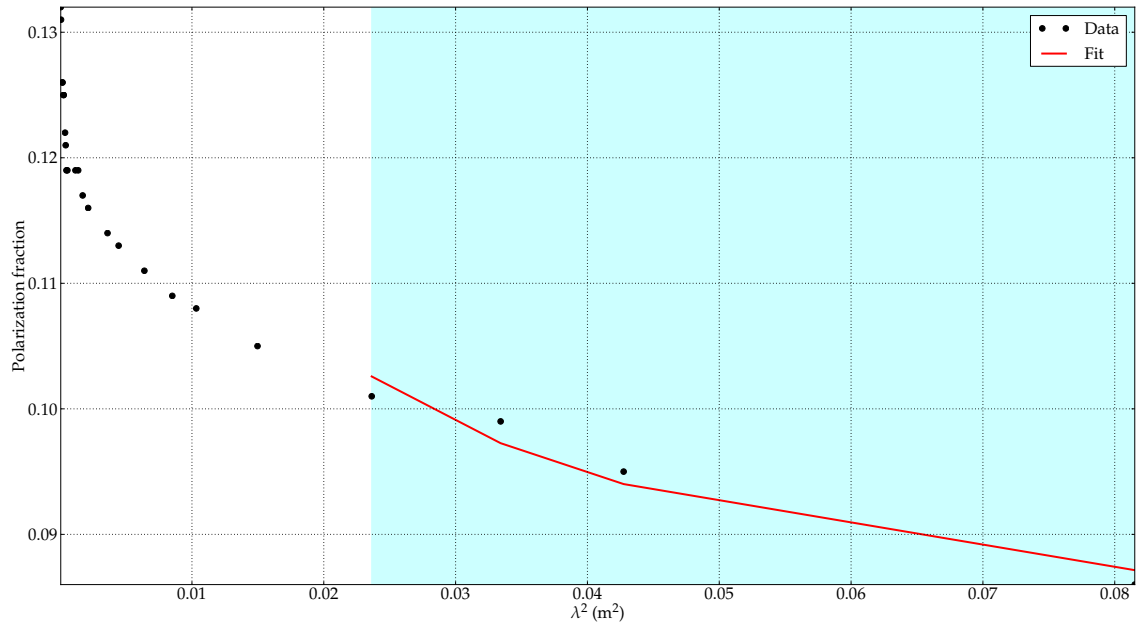


(B) Zoom-in

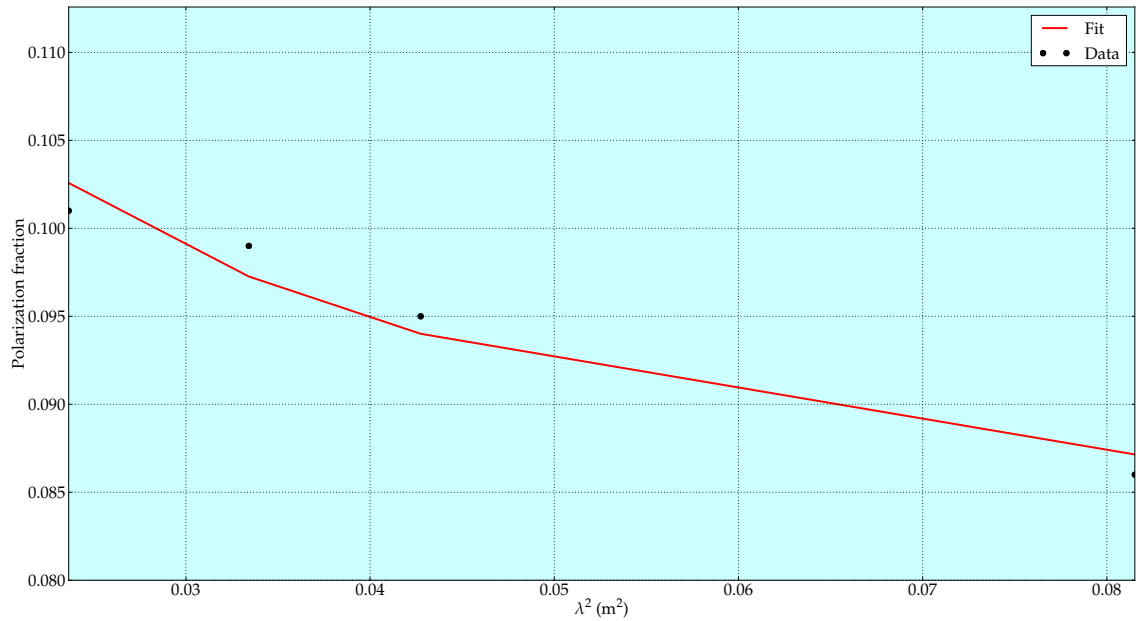
FIGURE 4.2: Polarisation angle fit for 3C 286. Each black marker represent a datum taken from the VLA polarimetry webpage. The red line represents the fit along the wavelength squared axis. The shade on cyan color represent the frequency bandwidth used for this JVLA dataset.

4.2.5 Polarisation angle calibration

I have already modelled the flux, polarisation fraction and polarisation angle of 3C 286 as a function of frequency. As noted previously, this is equivalent to modelling a point source with Stokes I, Q and U as a function of frequency. To obtain an accurate polarisation angle, we calibrate using the CASA task `polcal` using parameter `poltype='Xf'`, which means that we are calibrating polarisation angle, X , as a function of frequency, f .



(A) Polarisation fraction fit for 3C 286 along the wavelength squared axis



(B) Zoom-in

FIGURE 4.3: Polarisation fraction fit for 3C 286. Each black marker represent a datum taken from the VLA polarimetry webpage. The red line represents the fit along the wavelength squared axis. The shade on cyan color represent the frequency bandwidth used for this JVLA dataset.

in this step I used parameters

```
gaintable = ['JVLAdataset.Kcross', 'JVLAdataset.D0']
poltype   = 'Xf'
spwmap    = [[0,0,0,0,0,0,0,0], []]
combine   = 'scan'
```

Note that the gaintable parameter accumulates past calibration tables. From the polcal

task, the final calibration table is created and now we can apply all of these to our data to get a corrected data set. This is done using `applycal` and the following parameters

```
gaintable = ['JVLAdataset.Kcross', 'JVLAdataset.D0', 'JVLAdataset.X0']
spwmap    = [[0,0,0,0,0,0,0,0], [], []]
applymode = 'calflagstrict'
```

4.2.6 Calibration checks

To verify the successful application of polarisation calibration, it is recommended to inspect certain plots of the corrected data, specifically, amplitude versus frequency and phase versus frequency plots of the calibrators. Additionally, multi-frequency images of the calibrators, specifically Stokes Q and U, can be produced. If the calibration has been performed correctly, a polarisation angle of 33 degrees in the polarisation angle calibrator and a very low polarisation fraction in the leakage calibrator would be expected. Furthermore, an accurate evaluation of leakage and polarisation angle can be achieved by imaging the calibrators per spectral window. This would enable us to examine polarisation angle, polarisation fraction and leakage along the frequency axis.

4.2.7 Imaging

Following calibration for parallel-hands and cross-hands, I imaged the target using multi-scale multi-frequency synthesis (MFS) using the CASA task `tclean` with 128 w-projection planes. I made Stokes I, Q and U images of the entire field, 22×22 arcminutes, with a cell size of 1.3 arcseconds. Finally, I used `widebandpbcor` to correct for the primary beam. The calibrated total intensity image has a noise level of 0.09 mJy/beam and a peak flux density of 156.69 mJy/beam. Self-calibration was not applied in this instance.

To produce Stokes I, Q and U cubes in preparation for RM Synthesis, I use the CASA multi-scale `tclean` task with option `specmode='cubedata'` to create multi-frequency spectral cubes. Afterwards, I restored all frequency channels using a PSF equal in size to that of the MFS image, see Table 4.3.

4.3 Faraday Imaging

Before RM-Synthesis I need to prepare the data and look for outliers that might affect the quality of the reconstruction. Firstly, all the channels from the resulting cubes are checked by `cs-romer`, following which 33.79% of the frequency slices from the cubes were discarded since they resulted in empty images. This is mainly due to frequency channels flagged during parallel and cross hand calibration. I calculate the rms noise in each slice of the Q and U cubes, resulting in σ_Q and σ_U values for each channel, see Table 4.8. Assuming $\sigma_Q \approx \sigma_U$, we define $\sigma_{QU} = \frac{\sigma_Q + \sigma_U}{2}$. From this, I calculate the mean and the standard error of σ_{QU} as $\langle \sigma_{QU} \rangle$ and $\hat{\sigma}_{QU}$, respectively. Subsequently, I flag an additional 12.01% of the data slices that have $\sigma_{QU} > \langle \sigma_{QU} \rangle + 5\hat{\sigma}_{QU}$. Finally, I select those lines of

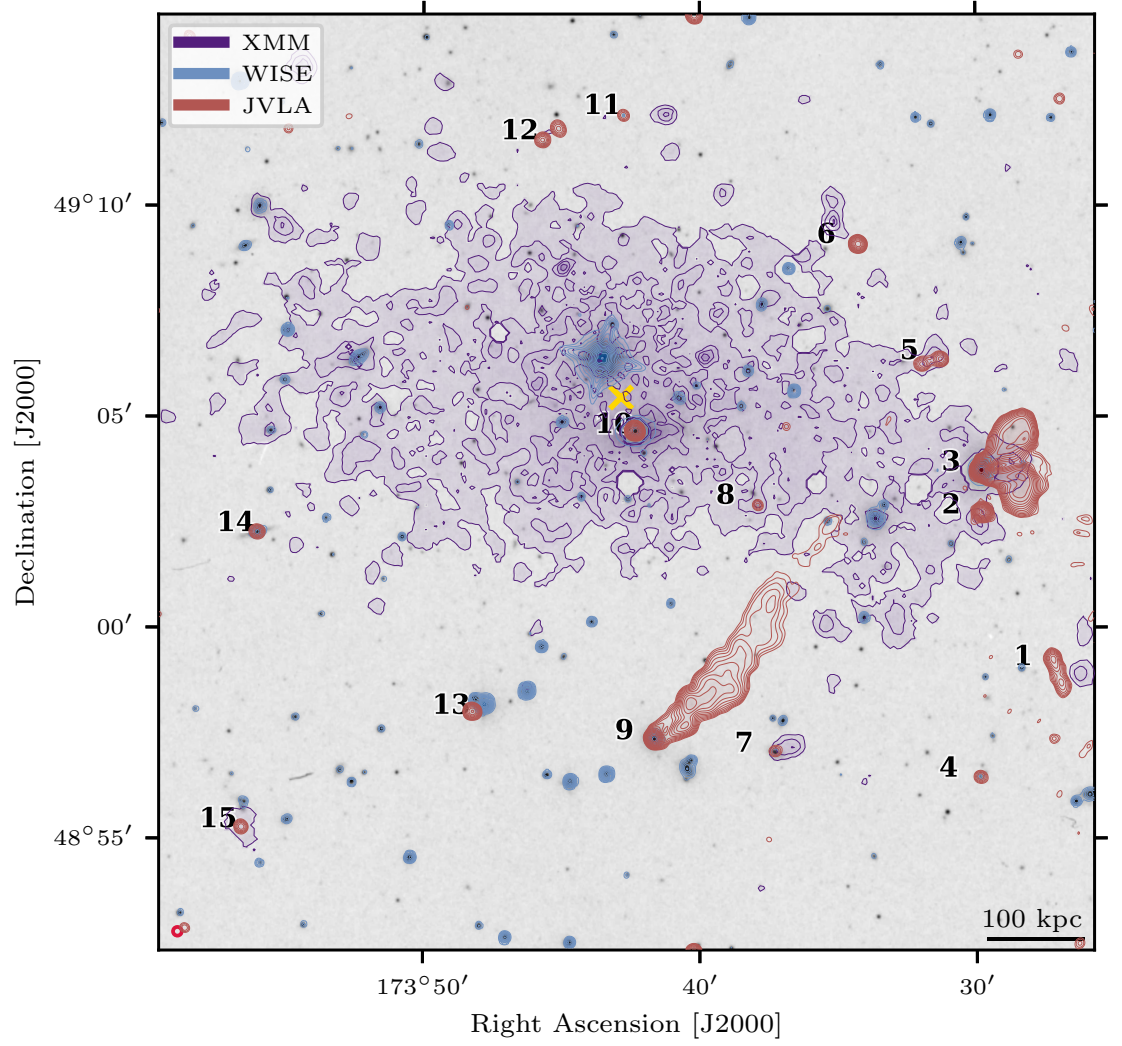


FIGURE 4.4: Overlay image of cluster Abell 1314. Image of the SDSS optical spectral with three overlaid contours. Purple contours represent the X-ray XMM-Newton point-source subtracted surface brightness. Blue contours represent the WISE $3.4\,\mu\text{m}$ infrared emission. Finally, red contours represent the VLA C-configuration total intensity radio emission at 1.5 GHz. The contours start at 3.75σ , 50σ and 5.0σ , respectively and all of them are spaced by a factor of 2. σ value for radio contours is listed in Table 4.3. The eleven detected radio galaxies are marked with numbers and the cluster center is marked with a yellow cross. See Table 4.2 for further information about each source.

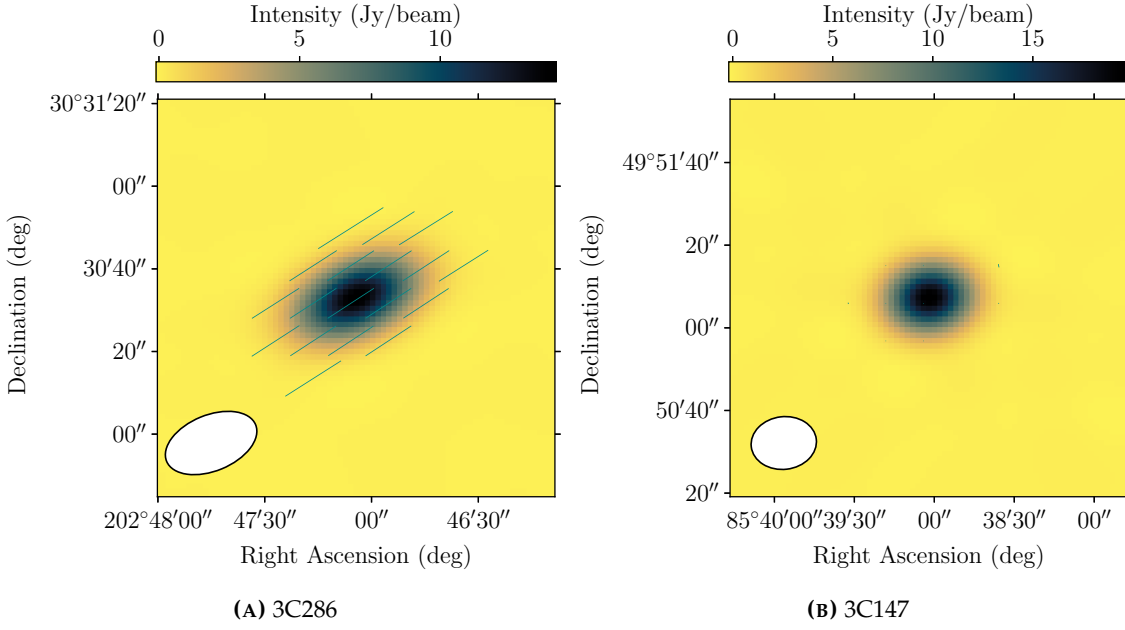


FIGURE 4.5: Total intensity images of 3C 286 (left) and 3C 147 (right). The vector lines show the polarisation angle and their magnitudes show their polarisation fraction.

| Parameter | $\delta\phi$ | max-scale | $ \phi_{\max} $ | ϕ_R |
|------------------------------|--------------|-----------|-----------------|----------|
| Value [rad m ⁻²] | 54.4 | 129.7 | 13540.6 | 6.8 |

TABLE 4.7: Abell 1314 VLA RM-Synthesis details.

sight where both total intensity and polarised intensity in the MFS images are greater than $3\sigma_I$ and $3\sigma_P$, respectively. The quantity σ_P is the noise in integrated Stokes P, which has a Ricean distribution with a standard deviation equivalent to the rms in integrated Stokes Q and U. We denote this quantity σ_P to differentiate it from the channel noise, σ_{QU} , see Table 4.8. This results in a total of 678 channels and 16,280 unflagged lines of sight to be reconstructed.

I run *cs-romer* over the $P(\lambda^2)$ cube using weights calculated directly from each slice as $W(\lambda^2) = 1/\sigma_{QU}^2(\lambda^2)$, that is, natural weights. These weights were chosen for the Faraday depth spectra reconstruction to maximize signal sensitivity by leveraging intrinsic data characteristics. Given the preprocessing step where data slices with $\sigma_{QU} > \langle\sigma_{QU}\rangle + 5\hat{\sigma}_{QU}$ were flagged and treated as outliers, natural weights provide a statistically robust reconstruction with enhanced signal-to-noise ratio. The framework then calculates a Faraday depth reconstruction with parameters as shown in Table 4.7.

As highlighted in Section 3.4, the regularisation parameter η can be calculated by minimising Equation 3.29. This function receives three inputs: the reconstruction algorithm, the wavelength squared measurements and the theoretical noise. In the case of real data, where σ_ϕ is unknown a priori, there are multiple possible approaches to calculate this latter quantity. The first is to use the measured noise from the Stokes Q and U frequency

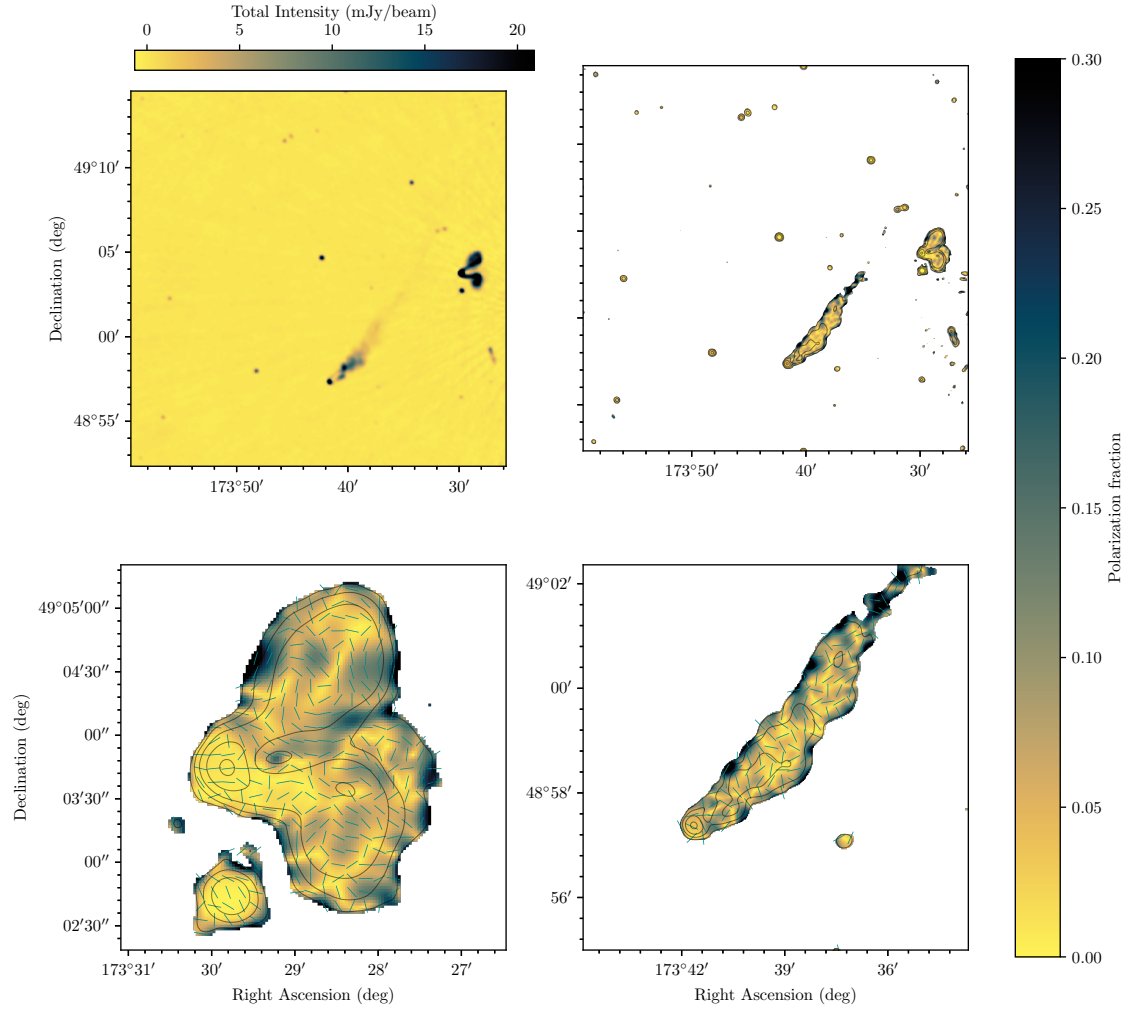


FIGURE 4.6: On top: Full field total intensity and polarisation fraction maps. On bottom: Zoom in on polarisation fraction maps of IC708 (left) and IC711 (right). Polarisation angles is represented as cyan vectors on bottom figures.

| Noise quantity | Definition | Method of measurement/calculation |
|----------------------------|---|---|
| σ_I | Noise in integrated Stokes I | Measured from MFS Stokes I image using the rms in an off-source region. |
| σ_P | Noise in integrated Stokes P | Measured from MFS Stokes Q & U images using the rms in an off-source region. |
| σ_Q | Channel noise in Stokes Q | Measured from each Stokes Q channel image using the rms in an off-source region. |
| σ_U | Channel noise in Stokes U | Measured from each Stokes U channel image using the rms in an off-source region. |
| σ_{QU} | Arithmetic mean of QU channel noise | Calculated from σ_Q and σ_U . |
| σ_ϕ | Theoretical noise in Faraday depth space (real/imaginary parts) | Reciprocal of the square root of the sum of the frequency channel weights. |
| σ'_ϕ | Measured noise in Faraday depth space (real/imaginary parts) | Measured as the rms of the reconstructed Faraday depth spectrum in the regions $ \phi > 0.8 \phi_{\max}$. |
| σ_{RM} | Faraday dispersion | See Equation 4.8. |
| $\Delta\phi_{\text{peak}}$ | Faraday uncertainty at peak | See Equation 4.6. |

TABLE 4.8: Different noise/variance quantities used in data reconstruction and analysis.

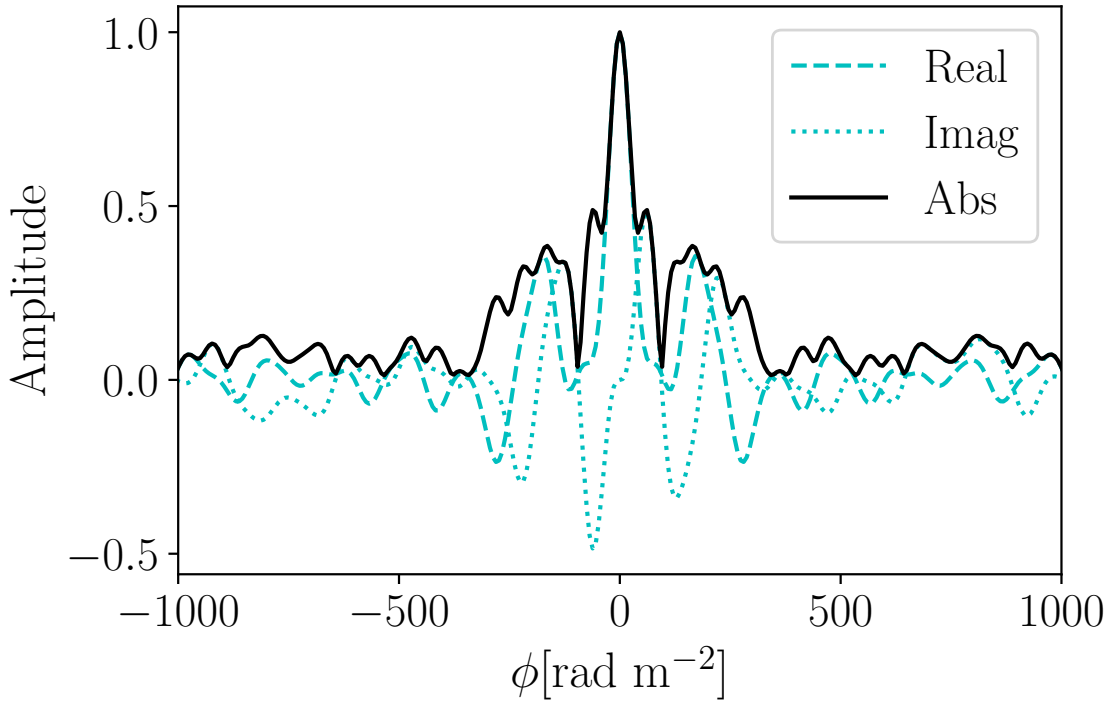


FIGURE 4.7: RMFTF for the VLA Abell 1314 data.

channels and to calculate

$$\sigma_\phi = \left[\sqrt{\sum_{i=1}^N W_i(\lambda^2)} \right]^{-1}, \quad (4.5)$$

where N is the number of unflagged frequency channels; alternatively one might estimate σ_ϕ directly from the dirty Faraday depth spectrum towards each polarisation detection. This second approach is best done using the edges of the spectrum, which are expected to contain least contamination due to sidelobe structure; however, tests using simulated data as described in Section 3.5 suggest that σ_ϕ calculated directly from the Faraday depth spectrum will always be over-estimated when significant structure is present, regardless of whether it is measured using a direct rms calculation or using the median absolute deviation (MAD), which is in principle more robust to outliers such as those from residual sidelobe structure. Therefore for the reconstruction in this work I calculate σ_ϕ using the first of these methods and I note that this approach gives σ_ϕ values consistent with the empirically measured rms recovered from empty, i.e. structure-free, lines of sight in Faraday depth.

Unlike Stuardi et al., 2021, who use an average spectral index of $\alpha = 1$ for all lines of sight, I use the `tclean` MFS spectral index image to reconstruct Faraday depth spectra. Following the results described in Section 3.5 and shown in Table 3.2, we use the delta basis function for reconstruction. Faraday depth spectra are recovered for 16,280 lines of sight over the range $[-\phi_{\max}, \phi_{\max}]$. The RMFTF for these data is shown in Figure 4.7.

I compare the rms of the residuals for each reconstructed line of sight to the theoretical value of σ_ϕ calculated from the weights on the spectral data. Unlike the reconstructions

of the simulated scenarios in Section 3.5, for some lines of sight the measured rms differs from the theoretical value, and we suggest that this is likely due to residual RFI contamination in the real VLA data. We find that the rms of the residuals for the VLA data is consistent with that calculated using the edges of the clean Faraday depth spectrum, which I estimate using the regions where $|\phi| > 0.8 \phi_{\max}$ and refer to as σ'_ϕ , see Table 4.8.

The *cs-romer* framework outputs the following data products: a dirty Faraday depth cube, a Faraday depth model cube, a Faraday depth residual cube and a restored Faraday depth cube. RM images for each polarised source are shown in Figures 4.8-4.12. These show the peak Faraday depth, ϕ_{peak} , the uncertainty at the peak, $\Delta\phi_{\text{peak}}$, calculated as

$$\Delta\phi_{\text{peak}} = \frac{\delta\phi}{2P/\sigma'_\phi}, \quad (4.6)$$

and the fractional polarisation, using polarised intensity corrected for Ricean bias such that

$$P = \sqrt{|F(\phi_{\text{peak}})|^2 - 2.3\sigma'^2_\phi} \quad (4.7)$$

(George et al., 2012), where σ'_ϕ is calculated as described above. The polarisation fraction is calculated by dividing P by the Stokes I MFS image in regions where the emission exceeds both a $6\sigma_P$ and $5\sigma_I$ threshold.

4.4 Polarised radio galaxies

Eight radio sources in the A1314 field have detectable polarised emission above a level of $6\sigma_P$, see Table 4.2. For each of these sources we calculate the pixel-wise average rotation measure across the source, $\langle\text{RM}\rangle$, the observed standard deviation of the RM across the source, $\sigma_{\text{RM,obs}}$, and the median error of the RM estimate, $\text{med}(\sigma'_\phi)$. The true dispersion of the RM across the source is then calculated as

$$\sigma_{\text{RM}} = \sqrt{\sigma_{\text{RM,obs}}^2 - \text{med}(\sigma'_\phi)^2}. \quad (4.8)$$

The value of σ_{RM} is shown for each source in Table 4.9, along with the median RM for each source, $\text{med}(\text{RM})$, and the median absolute deviation (MAD) value, which is considered to provide an improved estimate of the true dispersion when outliers are present in the data. Sources which cover a sky area smaller than 5 synthesized beams do not have dispersion, standard deviation or MAD values calculated due to an insufficiency of independent samples.

4.4.1 IC 708

The wide angle tail galaxy IC 708 (Source 3; Table 4.2; Figures 4.8 and 4.9) shows significant structure in polarisation across its lobes and this is reflected in the high RM dispersion value of $\sigma_{\text{RM}} = 46.688 \text{ rad m}^{-2}$ for this source, see Figure 4.8 and Table 4.9. The host galaxy of IC 708 has a much higher RM than the lobes: $\phi_{\text{peak}} = 109.3 \pm 0.12 \text{ rad m}^{-2}$,

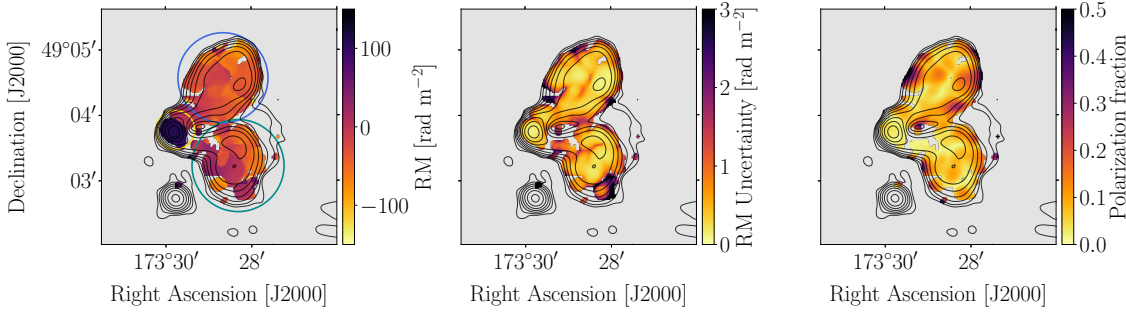


FIGURE 4.8: IC 708. Contours show radio total intensity in increments of 1σ from 5σ . Greyscale shows: (left) the observed peak rotation measure; (centre) the uncertainty on the observed rotation measure, σ_ϕ ; and (right) the polarisation fraction, P/I ; all for the region where $P > 6\sigma_{QU}$. The regions of the image are used to define the core, the north and south lobes of this galaxy. as described in Section 4.4.1, this is indicated by yellow, blue and cyan circles, respectively.

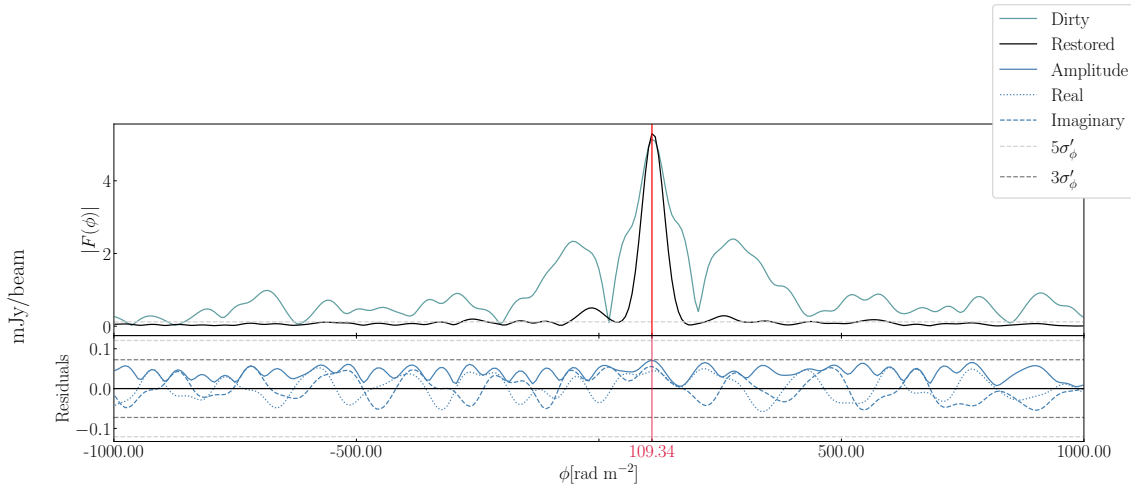


FIGURE 4.9: Line of sight at the core of IC 708. The upper panel shows the dirty and the restored Faraday depths with a peak at $109.34 \text{ rad m}^{-2}$. The lower panel shows the amplitude, the real and imaginary parts of the residual signal. Light and dark grey dashed lines show 5σ and 3σ boundaries, respectively.

suggesting that it is affected by more local magneto-ionic structure from the interstellar medium of the host galaxy. Table 4.10 shows RM statistics separately for the core region, and the North and South lobes of IC 708. The areas used to define these regions are indicated in Figure 4.8. I note that the high RM dispersion indicated for the core region is heavily affected by the sharp transition in RM at the base of the jet for the Northern lobe.

4.4.2 IC 711

The head-tail radio galaxy IC 711 (Source 9; Table 4.2; Figures 4.10 and 4.11) has a similarly high RM dispersion to IC 708 with a value of $\sigma_{RM} = 35.49 \text{ rad m}^{-2}$. The full extension of the long tail of emission associated with this source seen at 144, 240 and 610 MHz (Sebastian et al., 2017; Wilber, A. et al., 2019) is not visible in these higher frequency VLA data at this resolution. We note however that the discrete compact source listed as

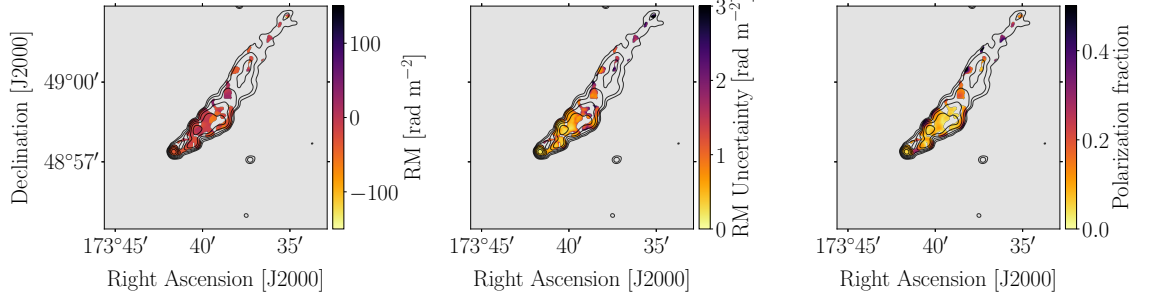


FIGURE 4.10: IC 711. Contours show radio total intensity in increments of 1σ from 5σ . Greyscale shows: (left) the observed peak rotation measure; (centre) the uncertainty on the observed rotation measure, σ_ϕ ; and (right) the polarisation fraction, P/I ; all for the region where $P > 6\sigma_{QU}$.

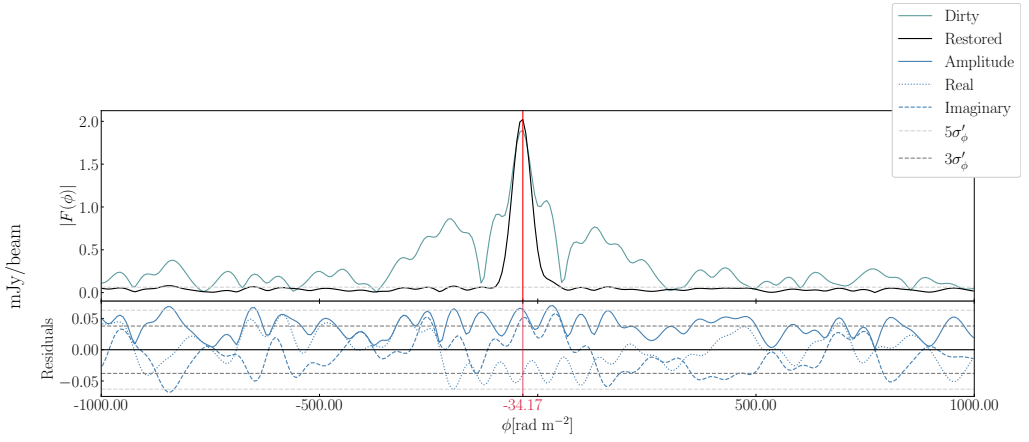


FIGURE 4.11: Line of sight at the core of IC 711. The upper panel shows the dirty and the restored Faraday depths with a peak at $-34.17 \text{ rad m}^{-2}$. The lower panel shows the amplitude, the real and imaginary parts of the residual signal. Light and dark grey dashed lines show 5σ and 3σ boundaries, respectively.

Source 6 in Table 4.2 and shown in Figure 4.4, is coincident with the location of the northern east-west extension of emission perpendicular to the main tail of IC 711. This abrupt turn in the direction of the diffuse emission from IC 711 was first noted by Srivastava and Singal, 2020 and also detected by Sebastian et al., 2017 and Wilber, A. et al., 2019. Those works proposed that the turn in emission was potentially due to a disturbance caused by ram pressure or shocks propagating outwards in the intra-cluster medium. We suggest that alternatively this emission may not be part of the tail from IC 711 but instead could be associated with Source 6.

4.4.3 IC 712

IC 712 (Source 10; Table 4.2; Figures 4.12 and 4.13) is the brightest cluster galaxy in A1314 (Lin and Mohr, 2004) and closest to the X-ray centre with a projected distance of $\sim 40 \text{ kpc}$, see Table 4.2. The source appears compact in both Stokes I and polarisation, with a small offset of the polarised emission from the peak total intensity, see Figure 4.12.

The Faraday depth spectrum of IC 712 shows a single Faraday thin structure, see Figure 4.13, with a peak value of $\phi_{\text{peak}} = 13.67 \pm 0.89 \text{ rad m}^{-2}$. It has been suggested that

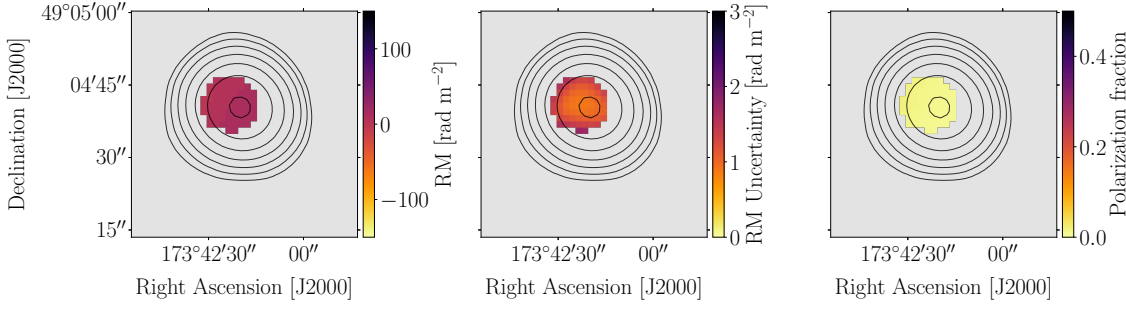


FIGURE 4.12: IC 712. Contours show radio total intensity in increments of 1σ from 5σ . Greyscale shows: (left) the observed peak rotation measure; (centre) the uncertainty on the observed rotation measure, σ_ϕ ; and (right) the polarisation fraction, P/I ; all for the region where $P > 6\sigma_{\text{QU}}$.

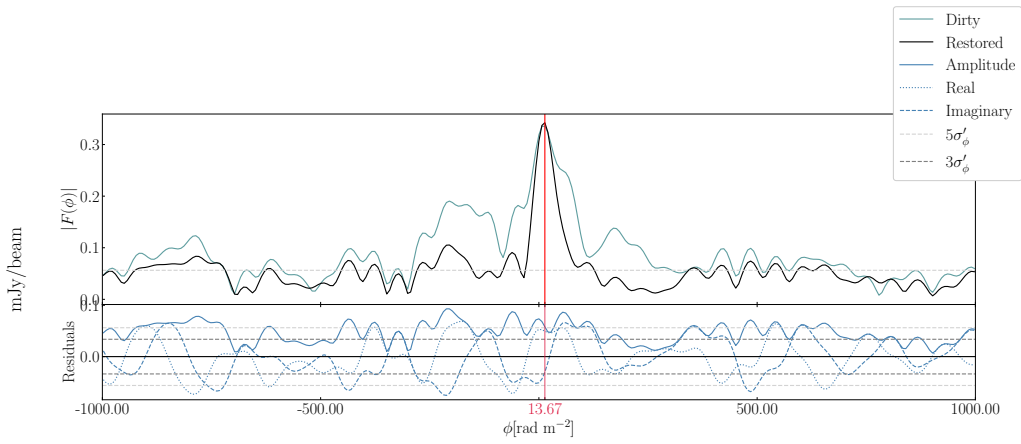


FIGURE 4.13: Line of sight at the core of IC 712. The upper panel shows the dirty and the restored Faraday depths with a peak at 13.67 rad m^{-2} . The lower panel shows the amplitude, the real and imaginary parts of the residual signal. Light and dark grey dashed lines show 5σ and 3σ boundaries, respectively.

RMs smaller than the FWHM of the RMTF are expected to differ from their true value by about 5% due to the presence of leakage at $\phi = 0 \text{ rad m}^{-2}$ (Jagannathan et al., 2017), which would increase the uncertainty on this measurement to $\Delta\phi_{\text{peak}} \simeq 3 \text{ rad m}^{-2}$.

4.5 Galactic contribution

To correct for foreground Galactic rotation, in *cs-romer* I have implemented an option to read the HEALPix image model from Hutschenreuter et al., 2022 and use a bilinear interpolation of those data to calculate the mean and standard deviation of the Galactic RM for each line of sight. I denote the interpolated mean image as ϕ_{GAL} and the de-rotation of this value can be applied directly as a shift in λ^2 space. Thus, *cs-romer* optionally applies this operation directly to the $P(\lambda^2)$ cube as follows

$$\hat{P}(\lambda^2) = P(\lambda^2)e^{-2i\phi_{\text{GAL}}\lambda^2}, \quad (4.9)$$

where $\hat{P}(\lambda^2)$ denotes the de-rotated complex polarisation.

The mean RM of the Galactic contribution for the Abell 1314 field is $\langle\phi_{\text{GAL}}\rangle = -12 \pm 4$ rad/m² (Hutschenreuter et al., 2022). Since this is systematically different from zero, I choose to subtract it from the VLA measurements. This is performed by querying the Galactic foreground RM mean and standard deviation maps provided by Hutschenreuter et al., 2022. These foreground maps are significantly lower resolution than the JVLA data, and cover the A1314 field using ~ 13 pixels. The `cs-romer` framework uses a bilinear interpolation across the field-of-view to approximate the Galactic foreground at the position of each pixel in the VLA data. The mean Galactic RM values for each line-of-sight are then derotated as a shift to each line of sight for the polarised intensity in λ^2 space using Equation 4.9.

4.6 X-ray data analysis

A1314 was observed by XMM-Newton in November 2003 during rev. 725 (ObsID: 0149900201) with a total exposure time of 18.4 ks. The observation was performed in full frame mode for the MOS cameras and the PN detector, all using the medium filter. Observation data files (ODFs) were downloaded from the XMM-Newton archive and processed with the XMM-SASv19.1.0 software for data reduction (Gabriel et al. 2004). Processing was performed following the steps of the XMM-Newton Extended Source Analysis Software (XMM-ESAS) pipeline (Snowden et al. 2008; Kuntz & Snowden 2008). I used the tasks `emchain` and `epchain` to generate calibrated event files from raw data. We excluded all the events with `PATTERN > 4` for PN data and with `PATTERN > 12` for MOS data. Bright pixels and hot columns were removed by applying the expression `FLAG == 0`. The data were observed to be free of significant periods of high background induced by solar flares and the statistical thresholding provided by the `mos-filter` and `pn-filter` tasks was used to remove any residual contamination. The remaining exposure times after cleaning were 16.7 ks for MOS1, 16.9 ks for MOS2, and 12.9 ks for PN.

Point-like sources were detected using the XMM-ESAS task `cheese`, which combines data from all three EPIC detectors to provide source lists and masks for removing such sources from images and spectra. The compact X-ray source associated with the host galaxy of IC708 was masked manually as it lies close to CCD boundaries for the MOS1 and MOS2 detectors. The `mos-spectra` and `pn-spectra` tasks were used to create redistribution matrix files (RMFs), auxiliary response files (ARFs) and exposure maps for the full field of view of each detector, and these were then used to create models of the quiescent particle background (QPB) in each case. The rate-hardness plots for each of the CCDs with unexposed corners were inspected to check for CCDs in anomalous states; no CCDs were excluded on this basis. A combined 0.3 – 2.0 keV data set was created assuming a power-law spectrum with $\alpha = 0.7$ and a 2×10^{20} cm⁻² H I absorption. The resulting 0.3 – 2.0 keV combined background-subtracted exposure-corrected image with point sources masked is shown in Figure 4.15.

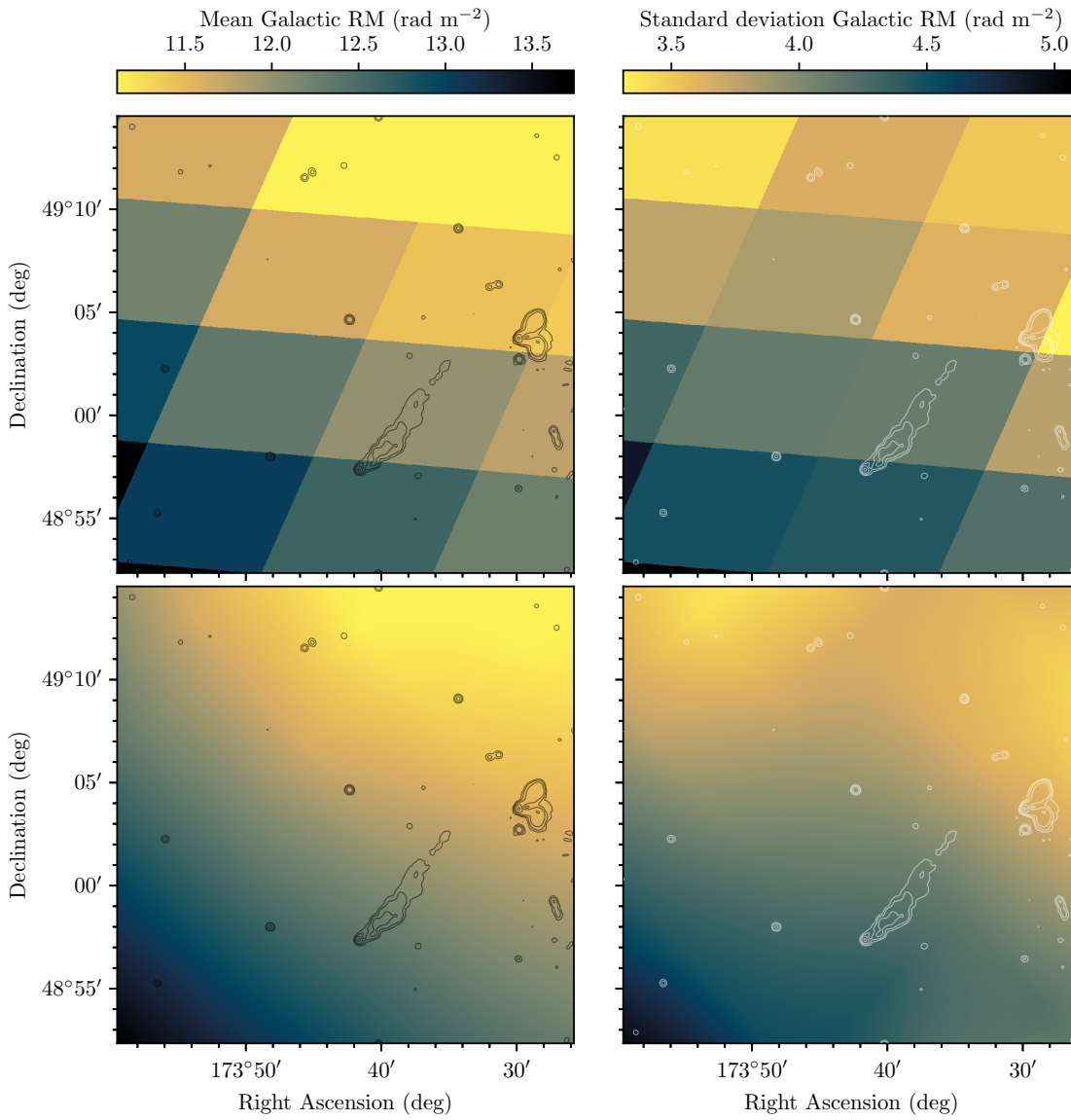


FIGURE 4.14: On the top: Mean and standard deviation RM maps of the Galactic foreground at the JVL A Abell 1314 field coordinates. On the bottom: On the top: Mean and standard deviation RM approximated maps of the Galactic foreground at the JVL A Abell 1314 field coordinates using bilinear interpolation

X-ray spectra were fitted jointly to data from the three EPIC detectors using the Xspec software (Arnaud, 1996). The fitted model included instrumental spectral lines at energies of 1.496 keV (Al Kalpha) and 1.75 keV (Si Kalpha) in the MOS data and at energies of 1.496 keV (Al Kalpha) and near 8 keV (Cu; 71, 7.5, 7.9, 8.2, 8.5 keV) in the PN data, spectral lines due to solar wind charge exchange at 0.56 and 0.65 keV, and a cosmic background component linked for all spectra and constrained additionally through the inclusion of a background spectrum extracted from an annulus between $1 - 2^\circ$ radius from the X-ray peak of A1314 using the ROSAT All-Sky Survey diffuse background maps³ (Sabol and Snowden, 2019) and associated response files. The cosmic background component is modelled as a combination of a cool ($E \sim 0.1$ keV) unabsorbed thermal component representing emission from the Local Hot Bubble or heliosphere, a cool ($E \sim 0.1$ keV) absorbed thermal component representing emission from the cooler halo, a higher temperature ($E \sim 0.25 - 0.7$ keV) absorbed thermal component representing emission from the hotter halo and/or intergalactic medium, and an absorbed power law with $\alpha \sim 1.46$ representing the unresolved background of cosmological sources. The cluster emission itself is modelled using an absorbed thermal component, represented by an apec model.

In addition to the above components, broken power-laws are included in the fits for all three of the EPIC detectors to account for any residual soft-proton background emission that was not been completely removed by the time-dependent filtering applied during the data reduction process.

The non-detector components of the fit were scaled by solid angle separately for each detector using values from the XMMSAS `proton_scale` task. Absorption was fixed using the Galactic value⁴ of $N_H = 1.53 \times 10^{20} \text{ cm}^{-2}$ (HI4PI Collaboration: et al., 2016) and a redshift value of $z = 0.034$ was used for all fits.

I have extracted a radial temperature profile from the data by fitting spectra from five annular regions with a width of two arcminutes each, as well as a central core region with a radius of two arcminutes. These regions are shown in Figure 4.15. Spectra were fitted independently for each region. The results from these fits are shown in Figure 4.16, where it can be seen that the central region is marginally cooler than the outer regions of the cluster.

4.7 Radio RM profiles

Radial profiles of the absolute average RM, RM dispersion and median absolute deviation for all sources detected in polarisation are shown in Figure 4.17. The radial distance of each source is calculated as the projected distance from the X-ray peak (11h34m51.36s +49d05m27.6s) to the position of peak polarisation within the given source. Sources that extend over areas smaller than $n_{\text{beam}} = 5$ are excluded from the σ_{RM} and MAD(RM) profiles, as they have insufficient independent samples to be considered. The separate components of radio galaxy IC 708 are also indicated in Figure 4.17.

³<https://heasarc.gsfc.nasa.gov/cgi-bin/Tools/xraybg/xraybg.pl>

⁴<https://heasarc.gsfc.nasa.gov/cgi-bin/Tools/w3nh/w3nh.pl>

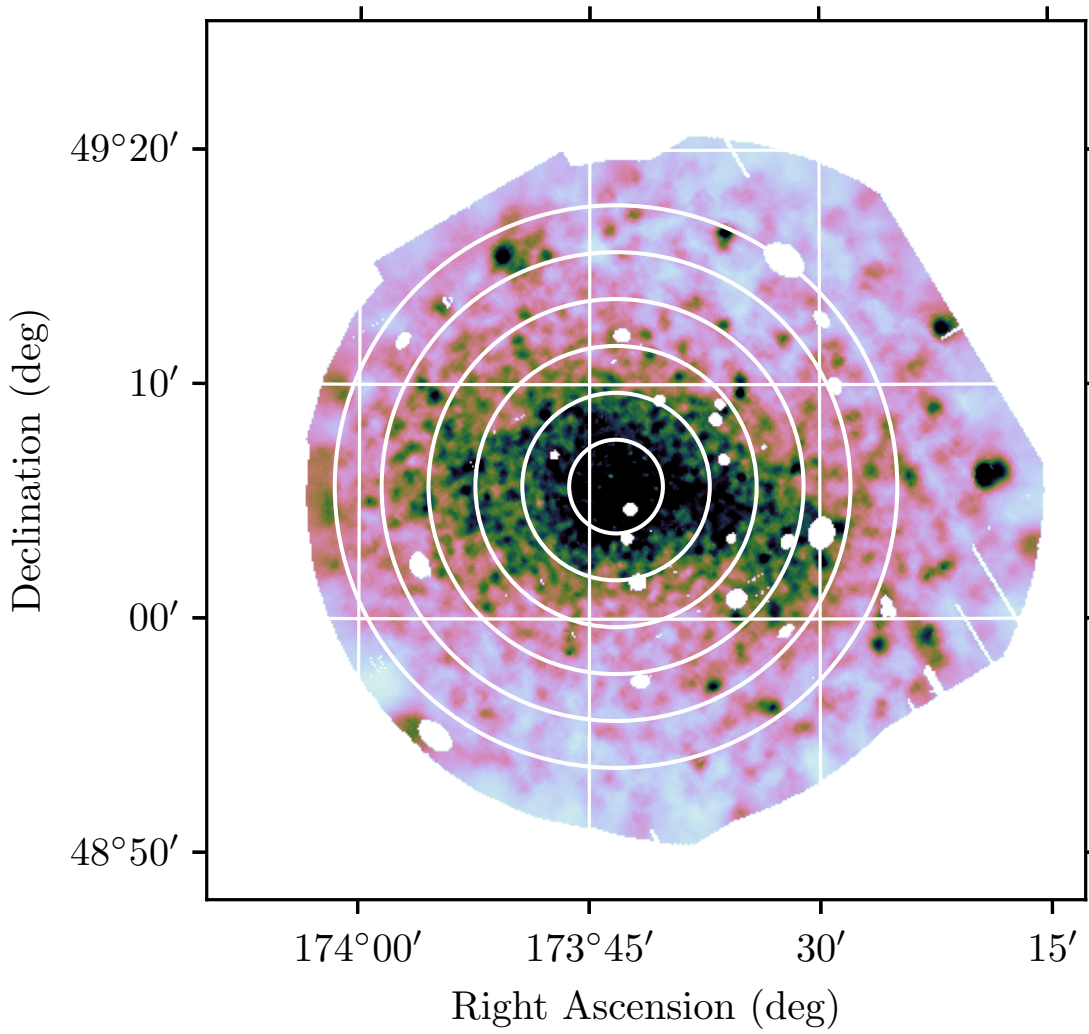


FIGURE 4.15: Regions used for extracting radial cluster properties are overlaid on the 0.3 – 2.0 keV adaptively-smoothed, background-subtracted and exposure-corrected image from the combined MOS1, MOS2 & PN exposures.

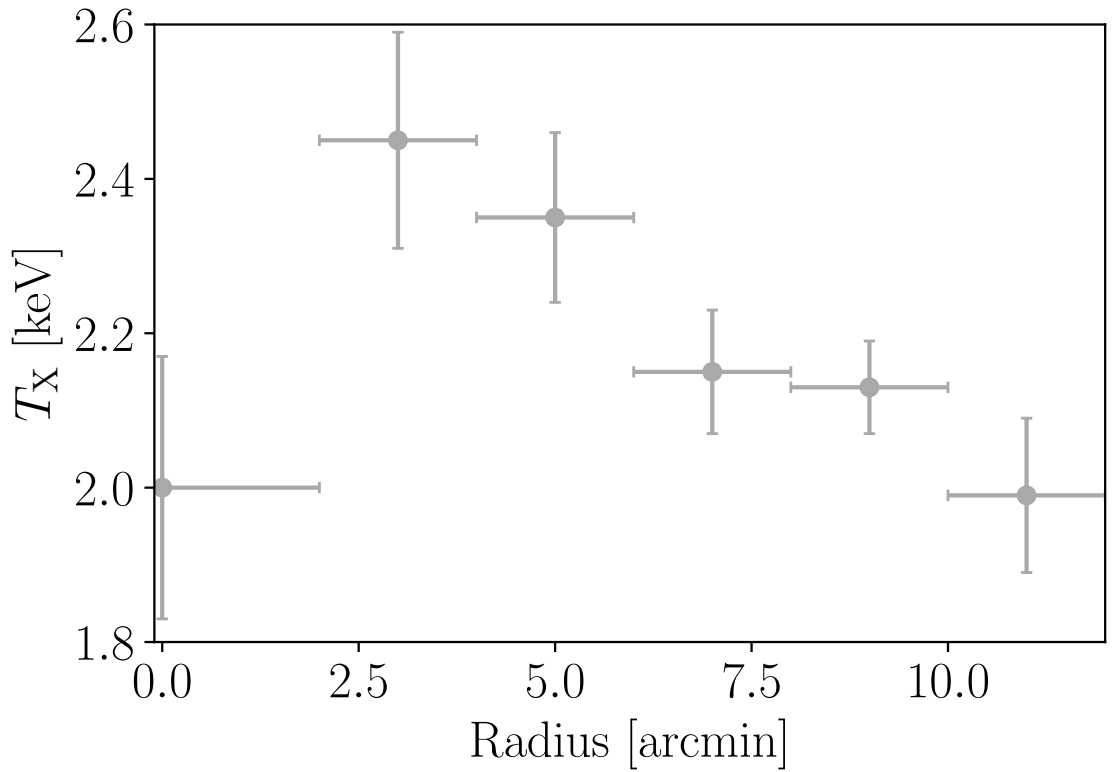


FIGURE 4.16: Radial temperature profile for Abell 1314. Data points correspond to spectral fits of the emission in the core and annular regions shown in Figure 4.15

Unlike the work of Stuardi et al., 2021, which performed a similar analysis for the galaxy cluster Abell 2345, a radial trend is seen only in the absolute average RM, with RM dispersion and MAD(RM) values not indicating any clear systematic behaviour. These results suggest that for A1314, the local RM contribution to each source dominates over the contribution of the ICM. This is particularly notable for the galaxy IC 708 for two reasons: firstly the average RM of the host deviates substantially from the radial behaviour seen in the absolute average RM for other sources, indicating that the host galaxy of IC 708 has a significant local contribution to its RM; secondly, the difference in the MAD values between the North and South lobes of IC 708 indicates a variance that also cannot be accounted for by the changes in the local ICM, which is quite similar for these closely located regions. This second point is supported by the lower panels of Figure 4.17, which show the RM profiles as a function of X-ray surface brightness (see Section 4.6 for further information about the data reduction), a proxy for electron density in the ICM. Once again, although the surface brightness local to both lobes of IC 708 is similar, the MAD(RM) values are highly discrepant. As noted by Stuardi et al., 2021, the MAD(RM) is expected to be the most robust estimator of RM dispersion and hence the best measure with which to distinguish local from large-scale environments.

Furthermore, the Faraday depth spectrum towards the core of IC 708, see Figure 4.9, shows a potential deviation from the Faraday-simple structure that would be expected from an external Faraday-thin screen such as the ICM. The Faraday depth spectrum for

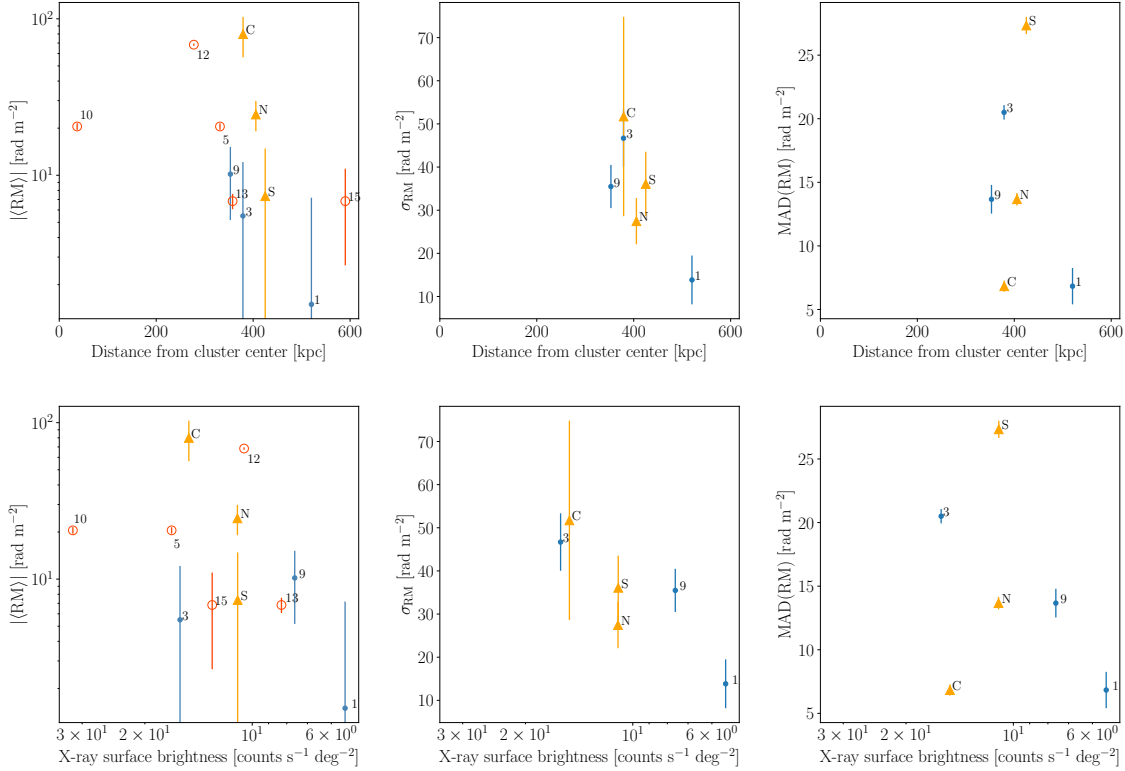


FIGURE 4.17: $|\langle \text{RM} \rangle|$, σ_{RM} and MAD(RM) of the polarised sources in the Abell 1314 cluster plotted against the projected distance of each source to the X-ray center (top row) and against the X-ray surface brightness at the position of peak polarisation for each source (bottom row). The uncertainties of the $|\langle \text{RM} \rangle|$ and σ_{RM} are the $\pm 1\sigma$ considering n_{beam} samples for each source. Sources that cover an area with fewer than $5 n_{\text{beam}}$ are shown as open red circles and are not considered in the σ_{RM} and MAD(RM) plots. Uncertainties for MAD(RM) are derived from the median error on the RM measurement, $\text{med}(\sigma_{\phi})$. The detected polarised sources are numbered according to Table 4.9. The components of IC708 are shown with yellow triangles and named as C, N and S for core, north lobe and south lobe, respectively, see Table 4.10.

| ID | z | $\langle \text{RM} \rangle$ (rad m ⁻²) | $\langle \text{RM} \rangle^a$ (rad m ⁻²) | σ_{RM} (rad m ⁻²) | med(RM) (rad m ⁻²) | MAD(RM) (rad m ⁻²) | med(σ_ϕ) (rad m ⁻²) | n_{beam} |
|----|-------|---|---|--|-----------------------------------|-----------------------------------|--|-------------------|
| 1 | — | -1.5 | -14.1 | 13.8 | — | 6.8 | 1.4 | 6.0 |
| 3 | 0.032 | -5.5 | -17.2 | 46.7 | -13.7 | 20.5 | 0.6 | 49.3 |
| 5 | — | 17.9 | 7.8 | 3.6 | 20.5 | — | 1.3 | 0.8 |
| 9 | 0.032 | -10.2 | -22.4 | 35.5 | -13.7 | 13.7 | 0.9 | 50.3 |
| 10 | 0.033 | 22.8 | 9.3 | 6.3 | 20.5 | 6.8 | 1.3 | 0.7 |
| 12 | — | -55.1 | -72.8 | 21.1 | -68.3 | — | 1.5 | 0.5 |
| 13 | — | 7.1 | -6.0 | 0.8 | 6.8 | — | 1.1 | 1.3 |
| 15 | — | 6.8 | 0.0 | — | 6.8 | — | 4.1 | 0.1 |

^a Galactic-contribution-subtracted $\langle \text{RM} \rangle$.

TABLE 4.9: RM profile of Abell 1314 polarised sources.

| Component | z | $\langle \text{RM} \rangle$ (rad m ⁻²) | $\langle \text{RM} \rangle^a$ (rad m ⁻²) | σ_{RM} (rad m ⁻²) | med(RM) (rad m ⁻²) | MAD(RM) (rad m ⁻²) | med(σ_ϕ) (rad m ⁻²) | n_{beam} |
|------------|-------|---|---|--|-----------------------------------|-----------------------------------|--|-------------------|
| Core | 0.032 | 79.8 | 68.5 | 51.7 | 116.2 | 6.8 | 0.4 | 5.1 |
| North lobe | — | -24.5 | -36.8 | 27.5 | -20.5 | 13.7 | 0.5 | 23.7 |
| South lobe | — | -7.4 | -18.5 | 36.1 | -6.8 | 27.3 | 0.7 | 18.7 |

^a Galactic-contribution-subtracted $\langle \text{RM} \rangle$.

TABLE 4.10: RM profile of polarised source IC 708.

the host of IC 708 shows an extension of polarised emission from the main peak that is detected at a significance of $\sim 20 \sigma'_\phi$. This structure could be caused by the Faraday thin peak being embedded in a more local Faraday thick region. Such structure would be geometrically consistent with the presence of a compact source embedded within an envelope of emitting and rotating material. Or alternatively, rather than mixing of Faraday rotation and emission, such complexity could be caused by structure in an unresolved screen associated with the host galaxy. Slight deviations from purely Faraday thin structure are also seen in the Faraday depth spectra for IC 711 and IC 712, see Figures 4.11 & 4.13; however, we note that these sources are not detected at such high significance in polarisation as IC 708 and therefore the presence of additional structure is less well-defined.

Unlike IC 708, the head-tail radio galaxy IC 711 has an average RM that is low compared to the general radial decrease observed for other sources. The reason for this discrepancy can be seen in Figure 4.4, where it is clear that the majority of the radio emission recovered for IC 711 lies outside the main X-ray emitting region and consequently this source will experience lower rotation than sources embedded within the higher density regions of the ICM. This is also clear from the lower panel of Figure 4.17, where IC 711 (Source 9) is associated with the second lowest surface brightness measurement.

Chapter 5

eMERLIN Cluster Sample

5.1 Abell 1314

In the preceding Chapter 4, I introduced the Abell 1314 cluster. To the best of my knowledge, there are no Very Long Baseline Interferometry (VLBI) observations of Abell 1314 in the existing literature. Thus, this chapter unveils one of the first studies of the radio galaxy IC 708 (see Subsection 4.4.1) employing high-angular resolution and high sensitivity radio telescope observations on its core using eMERLIN.

In the course of reviewing the literature, I came across studies that investigated polarisation in Active Galactic Nuclei (AGN) and quasars using VLBI observations (see e.g. Flatters, 1987; Lüdke et al., 1998; Casadio et al., 2017). More recent works have delved into the study of the polarisation of Messier 87 (M87) using the Event Horizon Telescope (see e.g. Collaboration et al., 2021). Yet, a critical aspect not addressed in these studies is the Faraday rotation caused by regions with non-zero magnetic fields. Furthermore, while some studies have explored the Faraday rotation induced by AGN (see e.g. Reynolds et al., 2001; Gabuzda and Chernetskii, 2003; Hovatta et al., 2012; Motter and Gabuzda, 2017), their methodology employs a slope-fitting approach (e.g., χ^2 fitting). This approach is known for its insensitivity to $n\pi$ ambiguities and its simplification to a single RM-component. This gap in the existing literature presents a significant opportunity. Specifically, there is scope for contributing original findings by using the Rotation Measure (RM) Synthesis technique and the *cs-romer* framework to enhance our understanding of magnetic fields.

Before delving deeper into Abell 1314, it is crucial to note that eMERLIN is a radio-interferometer and a Square Kilometre Array (SKA) pathfinder instrument. It consists of an array of seven radio telescopes that span 217 km across Great Britain. These features position eMERLIN as an outstanding scientific resource, as it attains a resolution of ~ 0.15 arcseconds at 1.5 GHz (L-band, see Table 1.1). This resolution is akin to what SKA1-MID would observe in this frequency range, which further reinforces the significance of the findings in this chapter.

Abell 1314 has been studied as part of project CY4234, which initially proposed eMERLIN observations for 14 polarised sources situated within 10 "normal" clusters. These are

clusters devoid of widespread cooling flows or potent synchrotron haloes. The proposal's primary aim was to offer updated RM measurements for these targets, employing QU-fitting and RM Synthesis techniques. Moreover, this project intends to investigate the impact of resolution on the estimates of magnetic field strength. Understanding this bias is pivotal for refining the cosmic magnetism science case for SKA, especially since SKA1-MID will have baseline lengths akin to eMERLIN. As illuminated by Feretti, L. et al., 1995, resolution holds a key role in studies of cosmic magnetic fields. This work's results highlight the considerable effect that the resolution at which RM structures across embedded radio galaxies in galaxy clusters are observed has on the inferred magnetic field strengths. This effect is attributed to the range of reversal scale lengths examined. An increase in resolution by approximately a factor of 2 was found to systematically enhance the recovered polarisation percentage on sub-arcsecond scales by up to 10%. Therefore, improved resolution is vital for accurately extracting the power spectrum of RM fluctuations within resolved structures in embedded cluster galaxies. Ultimately, attaining a resolution enhancement could potentially offer more precise constraints on the magnetic fields present within these clusters.

5.2 eMERLIN Data Reduction

In this section I will explain the pre-processing and data reduction steps for the eMERLIN observation. Abell 1314 was observed on 16-01-2017 for 14 hours and 27 minutes at L-band (see Table 1.1). All antennas except Darnhall were included in the observation. The dataset includes observation of 0319+415 (3C 84) for pointing and leakage calibration, 1331+305 (3C 286) for flux and polarisation angle calibration, 1153+4931 for phase calibrator and 1407+286 for bandpass calibration.

5.2.1 RFI Excision

For L-band datasets the eMERLIN CASA pipeline contains specific aoflagger LUA¹ recipes for each calibrator and the target. However, default RFI excision for the target and the point source calibrator are very mild. For the case of the Abell 1314 dataset I had to modify the scripts for sources OQ208, 1153+4931 and the target in order to make the RFI excision more aggressive.

Additionally, due to the presence of residual RFI on the target and for 1153+4931 in spectral windows 3, 4 and 5 I have used `flagdata` with `mode='tfcrop'` to flag those measurements.

5.2.2 Parallel-hand Calibration

In order to calibrate the parallel-hands (refer to Section 2.3), I used a modified version of the eMERLIN CASA pipeline². This adapted pipeline chiefly employs modular CASA

¹<https://www.lua.org/about.html>

²https://github.com/e-merlin/eMERLIN_CASA_pipeline

functions to read the IDI-FITS files supplied by the eMERLIN observatory and produce a parallel-hand calibrated measurement set. Besides, this pipeline leverages aoflagger with custom strategies/recipes and CASA tasks to eliminate RFI from the calibrators and the target. The pipeline primarily comprises two significant steps: *pre-processing* and *calibration*.

The *pre-processing* phase involves converting the FITS-IDI file into a measurement set (MS) using the CASA task `importfitsidi`, applying Hanning smoothing and excising RFI (see 5.2.1 for details).

The *calibration* phase is responsible for executing the standard parallel-hand calibration on continuum data, discovering solutions using only the inner approximately 90% channels of each spectral window. First, I would like to explain the calibrators used by eMERLIN to understand the pipeline steps for calibration. Initially, to perform the calibration our data needs:

1. The target source itself.
2. The phase calibrator. Normally, this is a source very close to the target and bright enough to calibrate the telescope gains (amplitude and phase). These vary with time since some phase data can rotate on timescales of minutes. Specifically for eMERLIN the phase calibrator is observed for 3 minutes, followed by 7 minutes of observation on the target, this is repeated for the length of the whole observation.
3. The flux calibrator. For eMERLIN this source is 3C 286 (1331+305) which flux density is not variable and is well known. However, it is resolved by eMERLIN and therefore only the shortest baselines contain the full flux. Consequently, L-band and C-band models were made to calibrate all telescopes.
4. The band pass calibrator. Most common sources for eMERLIN are 0555+398, OQ208 (1407+286) and 2134+004. Even though these slowly vary in time, all of them are unresolved by eMERLIN and therefore all baselines have the same flux. Additionally, spectral behaviour is very well understood. This source is used to calibrate the bandpass response.

The calibration macro-step then comprises initializing the source models using the observatory model for 3C 286, followed by the generation of the bandpass table using the CASA task `bandpass`. Subsequently, the pipeline constructs a new calibration table by solving the parallel-hand delays with the task `gaincal`. Using the same task, it then corrects phase and amplitude gains.

The next step involves adjusting the flux to account for the higher resolving power of eMERLIN. This is achieved by presuming that 3C 286 can be represented by a 2D Gaussian of an angular size θ_s and by representing the resolving power of a given baseline as a function of frequency, ν , and antenna separation, B , by $\theta(\nu, B)$. Consequently, the

reduction in central flux density, $S(\nu_0)$, due to finite θ_s is given by:

$$\frac{S'(\nu_0)}{S(\nu_0)} = \frac{\theta(\nu, B)^2}{\theta(\nu, B)^2 + \theta_s^2} = \frac{1}{1 + \rho(\nu, B)}, \quad (5.1)$$

where the resolved fraction, $\rho(\nu, B)$, is given by

$$\rho(\nu, B) = \frac{\theta_s^2}{\theta(\nu, B)^2}. \quad (5.2)$$

By using $\theta(\nu, B) = k/(\nu B)$ we can write

$$\rho(\nu, B) = \left(\frac{\nu B}{\nu_{\text{Lov-Pi}} B_{\text{Lov-Pi}}} \right) \cdot \rho_{\text{Lov-Pi}}, \quad (5.3)$$

where $\nu_{\text{Lov-Pi}}$, $B_{\text{Lov-Pi}}$ are the reference frequency and the antenna separation of the Lovell-Pickmere baseline, and $\rho_{\text{Lov-Pi}}$ is value fixed at 0.04.

If I bootstrap the flux density scale of 3C 286 using `fluxscale` and then correct by its flux, it is possible to re-calculate the bandpass and the amplitude calibration tables including the spectral index information.

The final step is then to apply all the calibration tables to the measurement set. Additionally, as an optional final step it is possible to flag residual RFI on the target using `flagdata` with `mode='rflag'`.

5.2.3 Self-Calibration

As I mentioned in Chapter 2, when handling heterogeneous arrays, the visibility weightings do not provide the best outcome for sensitivity. For instance, in e-MERLIN the Cambridge (Cm) antenna is more sensitive than the rest of the antennas of the array. Consequently, to reconstruct an optimal image, the Cm antenna must have larger weights than others before self-calibration. In order to do this, it is possible to use CASA's `statwt` task which re-calculates the weights according to their variance.

Self-calibration procedures are often hard to code at first and need a lot of trial and error to get a robust code that actually works. Additionally, a self-calibration procedure can change drastically depending on the source and radio-interferometer. Therefore, in order to mitigate possible errors and to decrease the programming time, an object oriented self-calibration framework named `snow`³ has been developed in this project. As it can be seen in Figure 5.1, this framework mainly consists in two classes: `Self-cal` and `Imager`. The first contains variables and functions that are useful or can be shared between the only-phase and phase-amplitude procedures. Three child classes inherit information from `Self-cal`: `Phase-cal`, `Amp-cal` and `Amp-phase-cal`. Each of these classes instantiate variables such as solution interval, interpolation method, imager and calibration mode differently. According to A. Richard Thompson, 2004a; Chael et al., 2018 the self-calibration procedure can be performed with any imager (see Section 2.5) as long as

³<https://github.com/miguelcarcamov/snow>

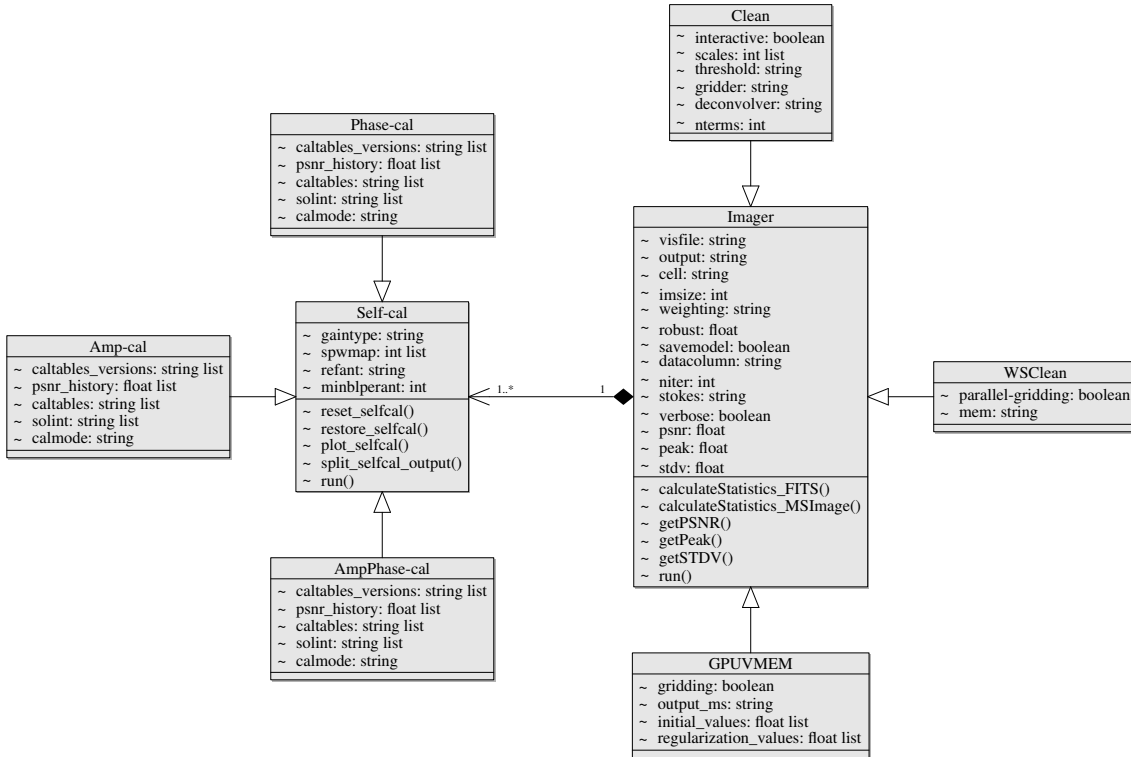


FIGURE 5.1: Class diagram of the Self-calibration framework

they store the model visibilities. Thus, the idea behind the class `Imager` is to plug any imaging algorithm into the self-cal workflow, allowing scientists to test different imaging schemes and to build a model according to their needs. The relationship between `Imager` and `Self-cal` classes is quite simple. While self-calibration can work only by having an imager, the imager can be part of multiple self-calibration classes.

Taking into account that the scan length for the Abell 1314 eMERLIN dataset is around 7 minutes, for the self-calibration of this dataset I have done five rounds of only phase calibration using `tclean`, natural weights and setting `solint` = ['inf', '3.5min', '2min', '1min', '30s']. This will be useful to get as much extended emission as possible. After finishing the rounds using the framework, the peak-signal-to-noise of the images improve from 91.7 to 524.7. Figure 5.2 shows the improvement of the peak intensity and the rms noise on the images over the phase calibration loops. After self-calibration, we image all Stokes maps using MFS `tclean` and saving the model column. This will allow us to find residual RFI that might be present in the data. We flag these latter using `tfcrop` and `rflag`. Finally, we use the task `statwt` in order to re-calculate the weights.

5.2.4 Total Intensity Images

Having completed the parallel-hand pre-processing, I have imaged the eMERLIN dataset using MFS `tclean` using Briggs weighting, robust 0.5 and cell size of 0.02 arcseconds. The resulting image can be seen in Figure 5.3, which illustrates a comparison of the JVLA (on the left) and eMERLIN (on the right) images. The image clearly shows the core of IC S708 at a resolution 65 times higher than the JVLA. In fact, the beam of this eMERLIN

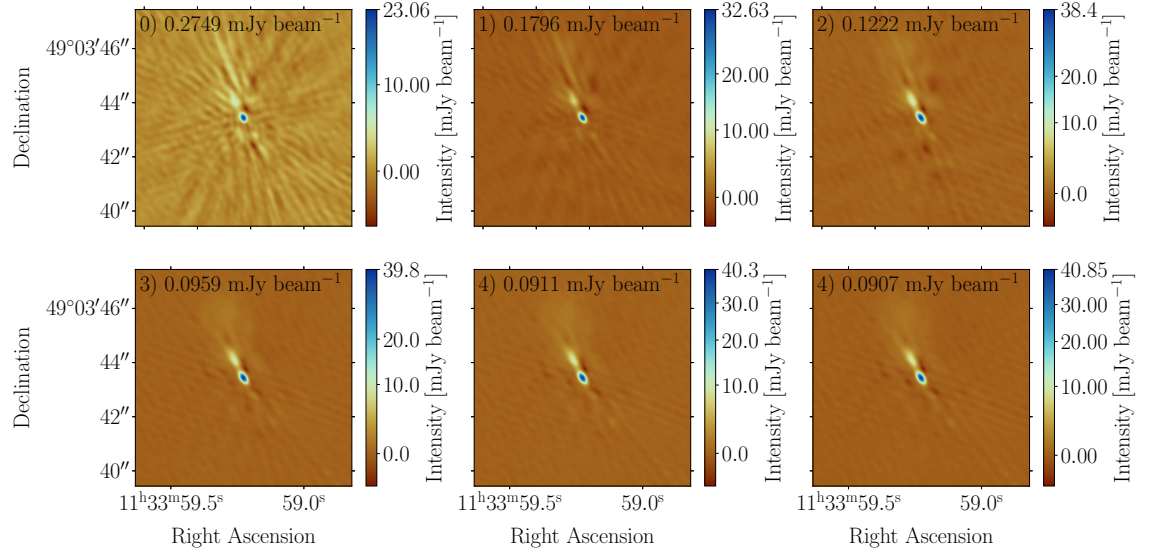


FIGURE 5.2: Self-calibration improvement over the phase calibration loops on the eMERLIN dataset of Abell 1314. The annotation on each sub-image show the iteration number, where 0 corresponds to the image reconstructed after doing the parallel-hand calibration, and the rms noise. At the top of each colourbar the intensity peak of each sub-image is shown.

image has a size of $0.4'' \times 0.2''$ whilst the JVLA image has a beam size of $12.4'' \times 11.7''$. Additionally, it can be seen some lower extended emission filament at the north-east of the core at 4σ and 8σ level, where $\sigma = 0.17 \text{ mJy beam}^{-1}$. The peak at the core has an intensity of $39.8 \text{ mJy beam}^{-1}$.

Additionally, Figure 5.4 reports the spectral index map for the IC 708 eMERLIN image. It can be seen that at the core, the spectral index is $0.07 \pm 4.5 \times 10^{-4}$. At the extended emission the mean spectral index is -0.5 ± 0.2 .

5.3 eMERLIN Polarisation Calibration

In this section I will give details of the polarisation calibration for the Abell 1314 eMERLIN dataset.

5.3.1 Cross-hand problems in CASA

Before continuing with the cross-hand calibration details, I need to report a problem that I have encountered in versions of CASA up to 5.8. Raw eMERLIN datasets use the FITS-IDI format, therefore, in order to process them using CASA and convert them to a measurement set we need to use the task `importfitsidi`. Here, I have found that parallel-hand data is correctly labelled according to their respective correlation (LL, RR). However, some cross-hand data are not (i.e. correlation RL is really LR). I have found out that this issue is dependent on the baseline direction definition. For instance, whilst North-South baselines like Mark2-Defford suffer this problem, the South-North baselines such as Defford-Pickmere do not. Thus, for a typical eMERLIN dataset with 15 baselines, 9 will suffer this reverse labelling and 6 will have their cross-hand correlations

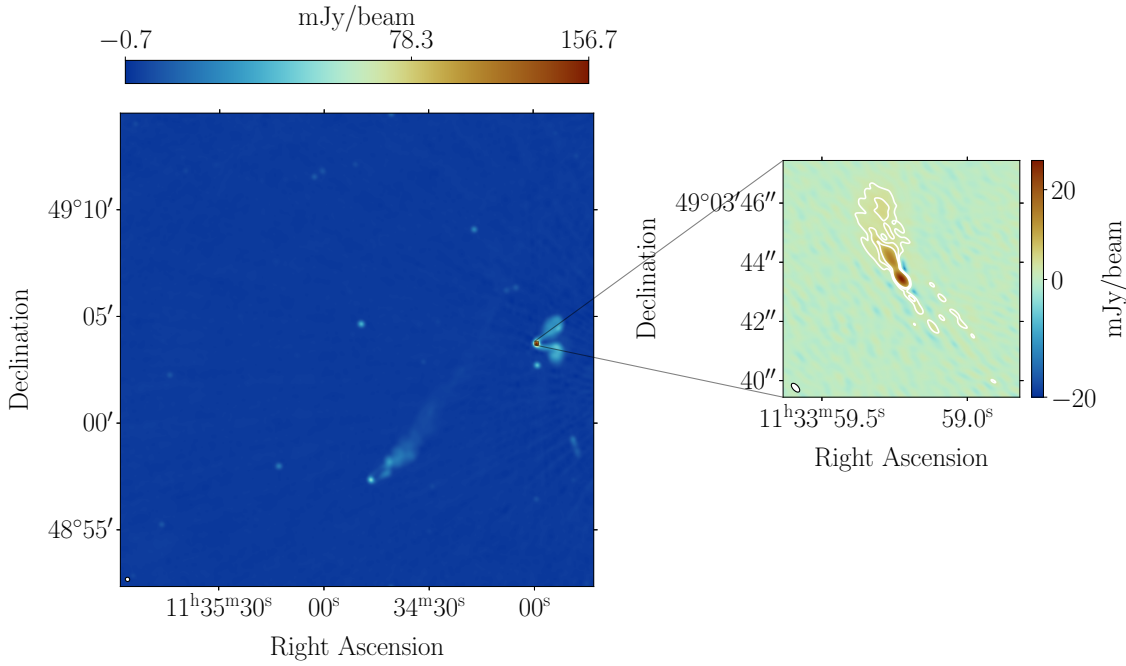


FIGURE 5.3: On the left: Total intensity image of Abell 1314 using JVLA (see Chapter 4). On the right: Higher resolution image of IC 708 using the eMERLIN radio telescope. The contours are drawn from a 4σ to 32σ level with increments of 2σ , where $\sigma = 0.17 \text{ mJy beam}^{-1}$.

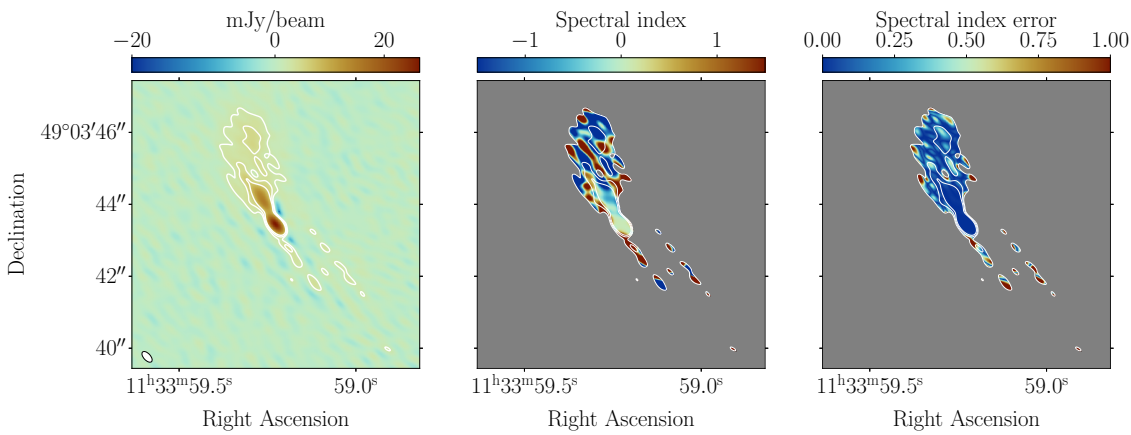


FIGURE 5.4: On the left: Total intensity image of Abell 1314 using eMERLIN. On the center: Spectral index map masked at 4σ . On the right: Spectral index error map masked at 4σ . The contours are drawn from a 4σ to 32σ level with increments of 2σ , where $\sigma = 0.17 \text{ mJy beam}^{-1}$.

labeled correctly. To confirm this I have compared amplitude and phase plots for the first 3 spectral windows of 3C 286. I have done this by inspecting the data read directly as FITS-IDI using AIPS, and the measurement set made after conversion. Hence, from Figures 5.5, 5.6, 5.7 and 5.8 it is possible to confirm that baseline Defford-Pickmere does not suffer a mismatch on the labelling of the cross-hand data. However, if we look at Figures 5.9, 5.10, 5.11 and 5.12 we can see that something is wrong with the cross-hand correlations because the CASA plot for correlation LR and RL are similar to AIPS plots of correlations RL and LR, respectively.

Finally, it is important to emphasize that due to this problem the polarisation calibration using CASA versions below 5.8 will fail as some of the cross-hand correlations are mislabelled. Hence, I found two ways to fix this issue and proceed with the cross-hand calibration. One workaround is to use the `casacore` software⁴ after converting the dataset from FITS-IDI to measurement set and swap the cross-hand correlations on those affected baselines. This was the technique used to process these data during early versions of our reduction. The other solution, and the one I now use for the results in this thesis, is to update CASA software to a version above 5.7⁵.

5.3.2 Cross-hand Calibration

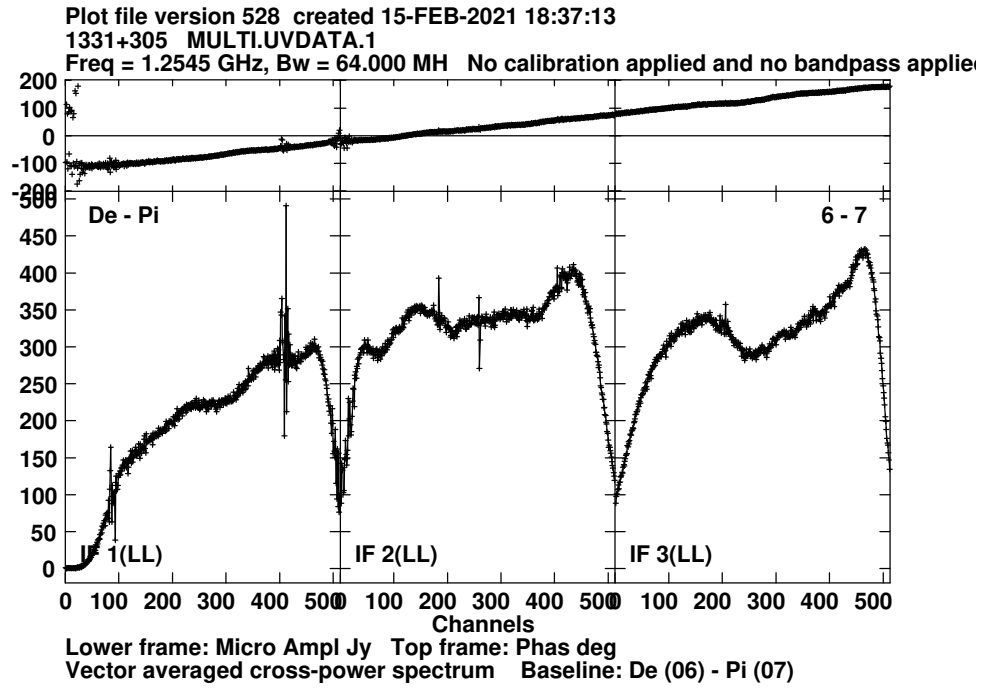
As we now have the measurement set with the correct labels for the cross-hand correlations, we can proceed with the cross-hand calibration, which for this dataset is done in five steps. Firstly, I derive the flux density and polarisation properties of the polarisation angle calibrator (3C 286) as shown in Subsection 4.2.2. Secondly, I derive the flux density of the leakage calibrator (3C 84) using the CASA task `fluxscale` on the eMERLIN pipeline amplitude and phase calibration table. Thirdly, I determine the instrumental delay between the two cross-hand correlations. Fourthly, I solve for the frequency-dependent leakage terms using an unpolarised source, such as 3C 84. Finally, I solve for the polarisation angle by using a source with known polarisation angle, such as 3C 286. Just as in the parallel-hand calibration, we use $\sim 90\%$ of the inner channels to find solutions for these tables.

Cross-hand delay calibration

At this step I derive the residual L-R delay on the reference antenna (Mk2) by using the CASA task `gaincal` and `gaintype='KCRSS'` and 3C 286 which I know has polarised signal in the cross-hand correlations. Since the delay solutions are very stable across all spectral window (see Figure 5.13a) I created a single calibration table by fitting the cross-hand delay for the entire baseband, also known as a multiband delay. Consequently a single solution with a value of 108.421 nanoseconds (see Figure 5.13b) is used.

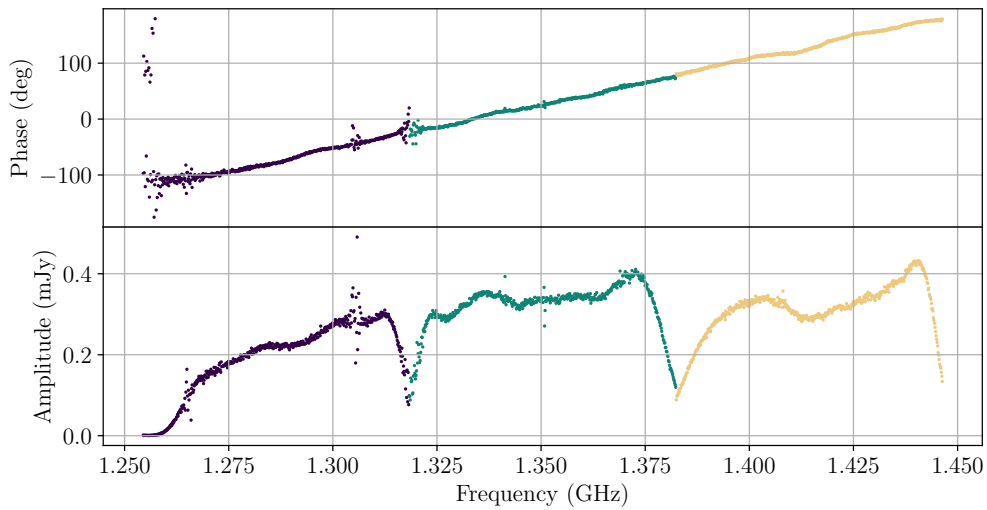
⁴<https://github.com/casacore/casacore>

⁵This update became available on 26-05-2021



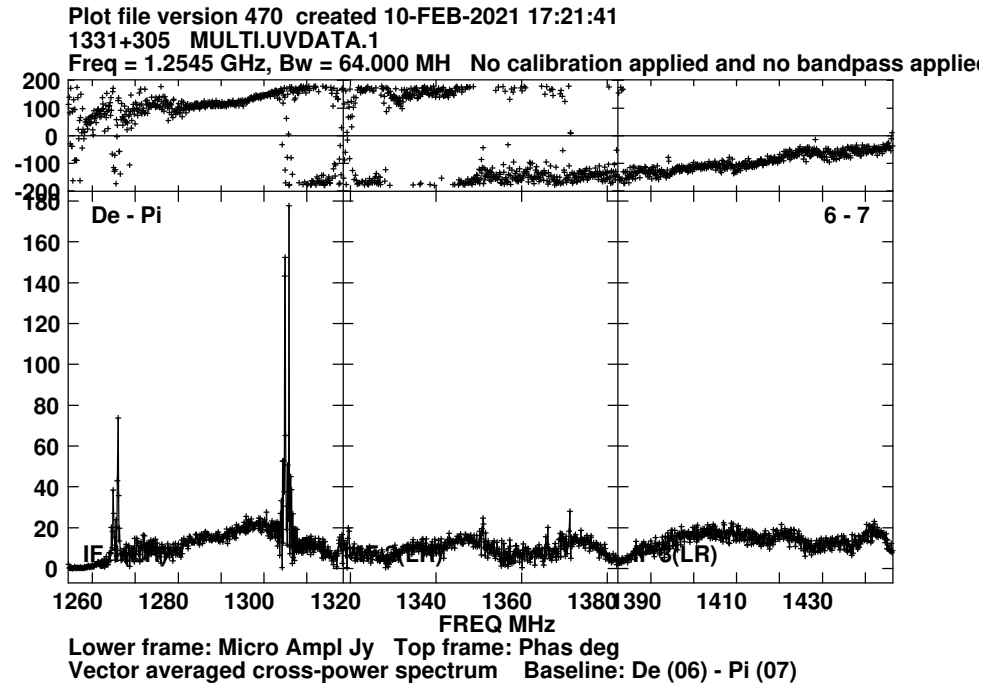
(A) AIPS

Baseline De&Pi - Correlation LL



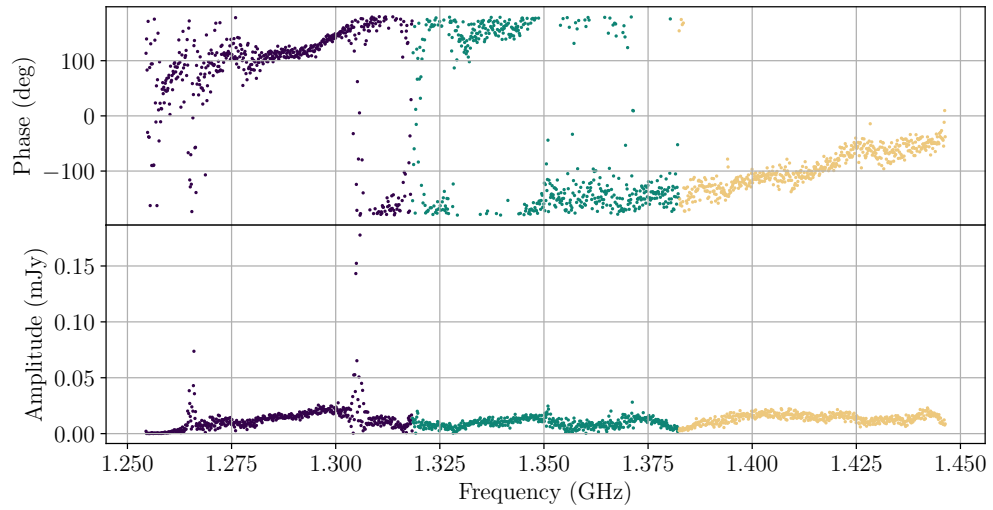
(B) CASA

FIGURE 5.5: Amplitude and phase plots for 3C 286, baseline Defford-Pickmere and its first 3 spectral windows and correlation LL.



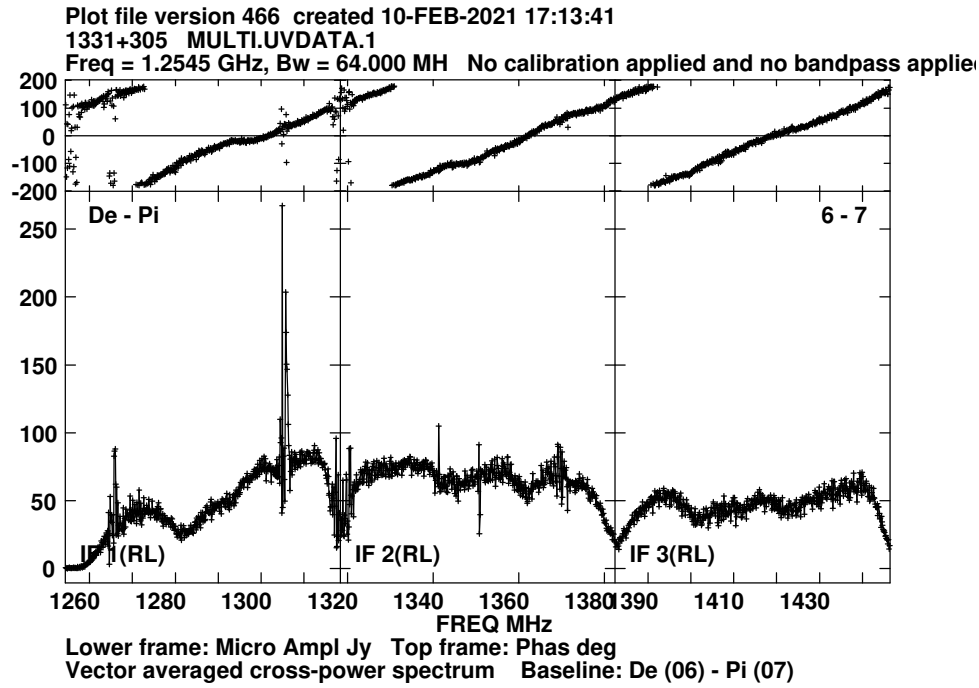
(A) AIPS

Baseline De&Pi - Correlation LR



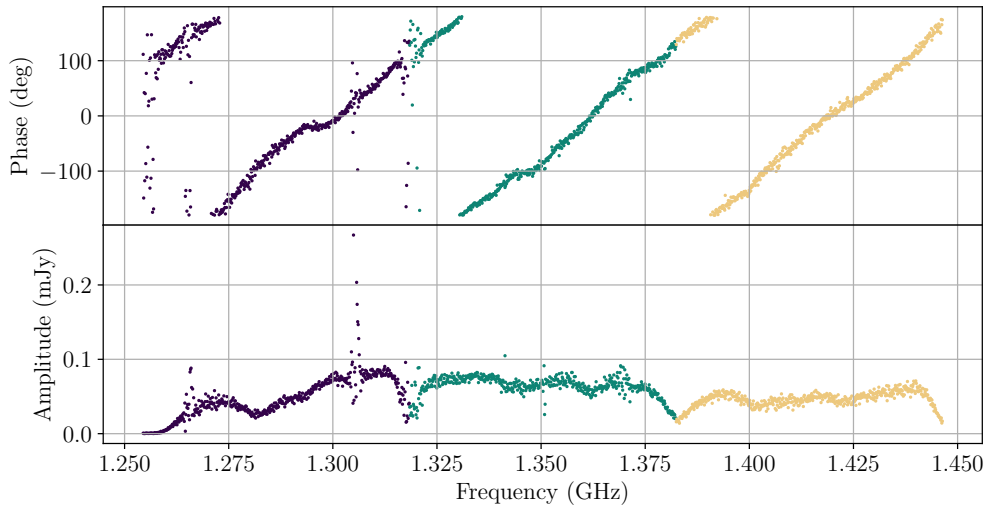
(B) CASA

FIGURE 5.6: Amplitude and phase plots for 3C 286, baseline Defford-Pickmere and its first 3 spectral windows and correlation LR.



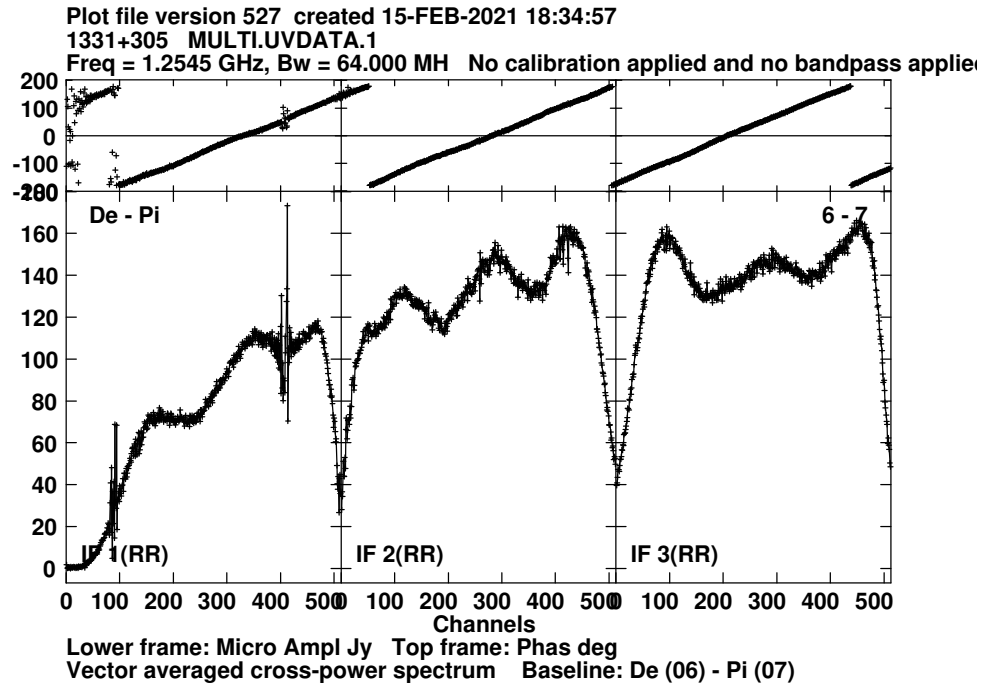
(A) AIPS

Baseline De&Pi - Correlation RL



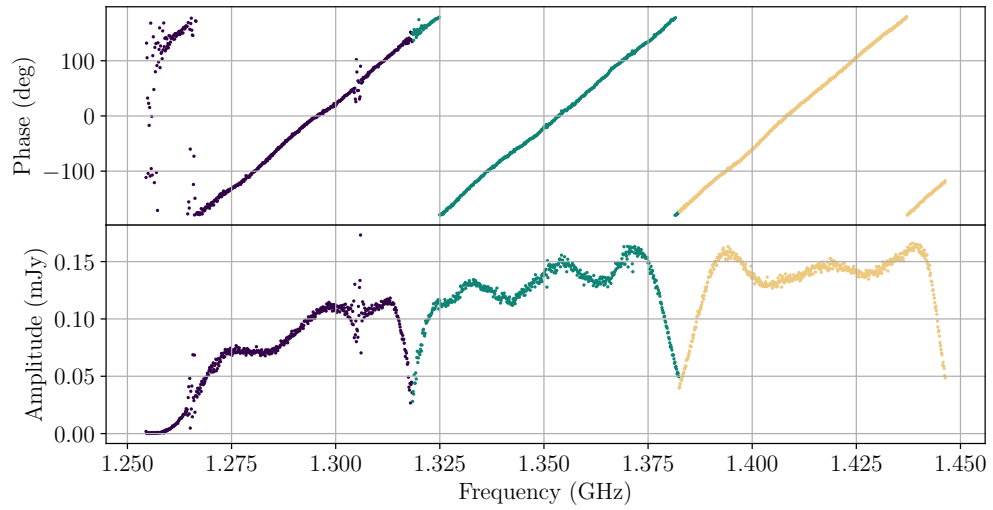
(B) CASA

FIGURE 5.7: Amplitude and phase plots for 3C 286, baseline Defford-Pickmere and its first 3 spectral windows and correlation RL.



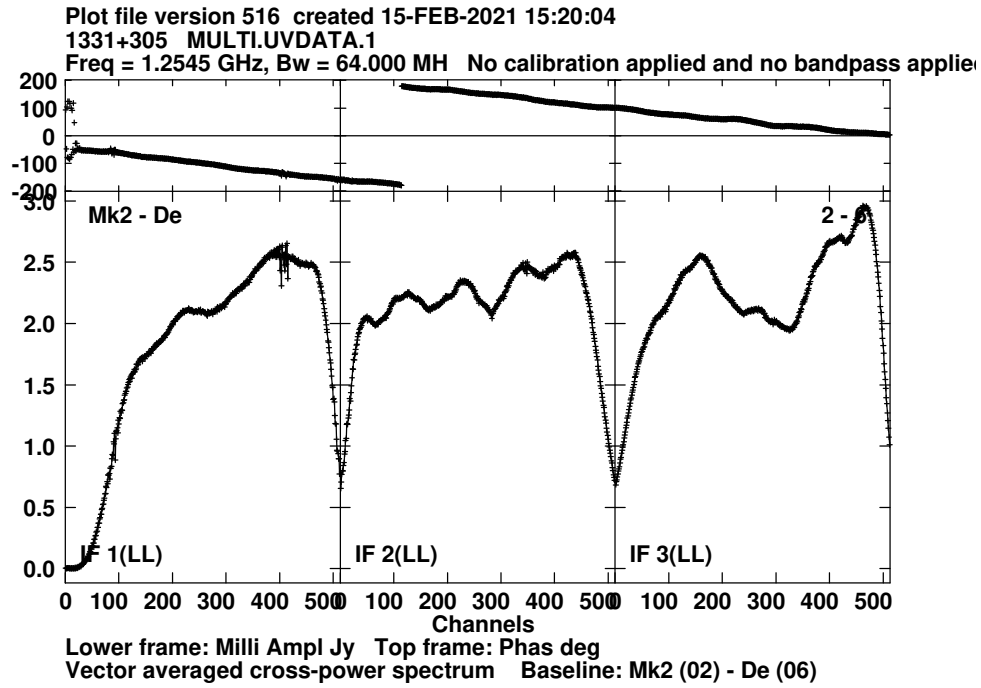
(A) AIPS

Baseline De&Pi - Correlation RR



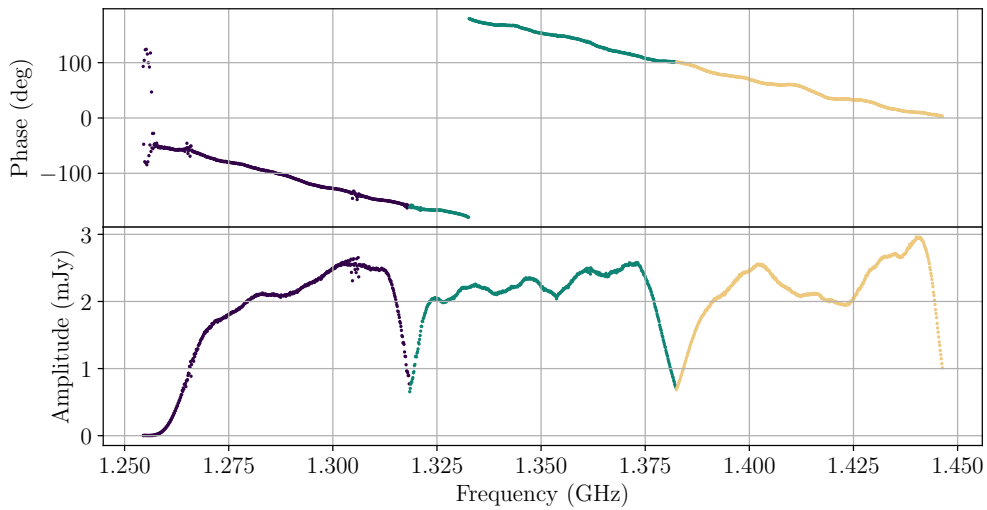
(B) CASA

FIGURE 5.8: Amplitude and phase plots for 3C 286, baseline Defford-Pickmere and its first 3 spectral windows and correlation RR.



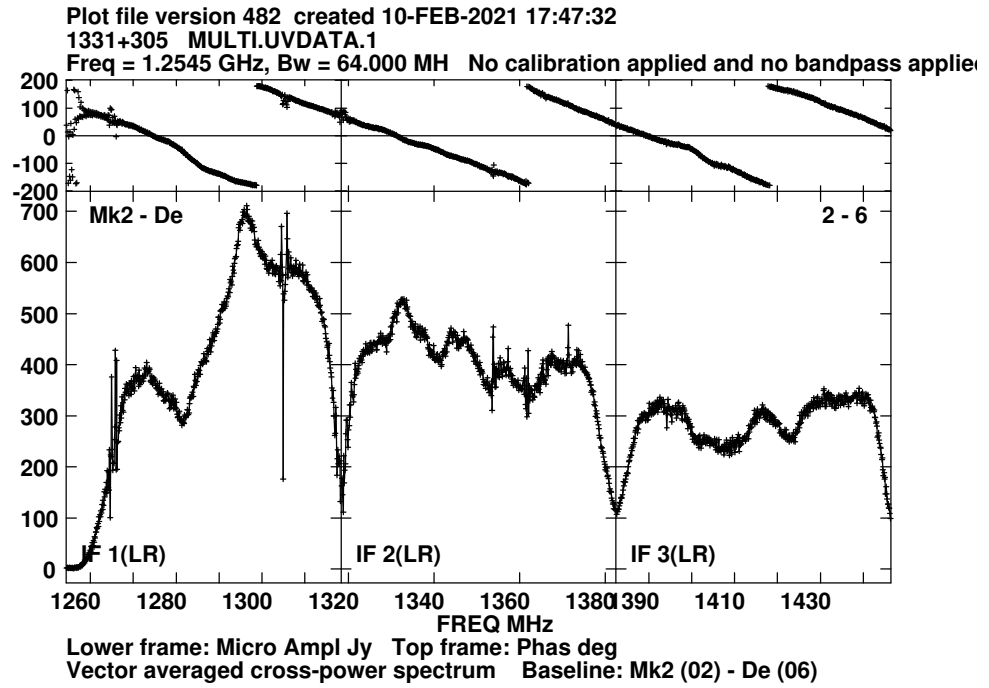
(A) AIPS

Baseline Mk2&De - Correlation LL



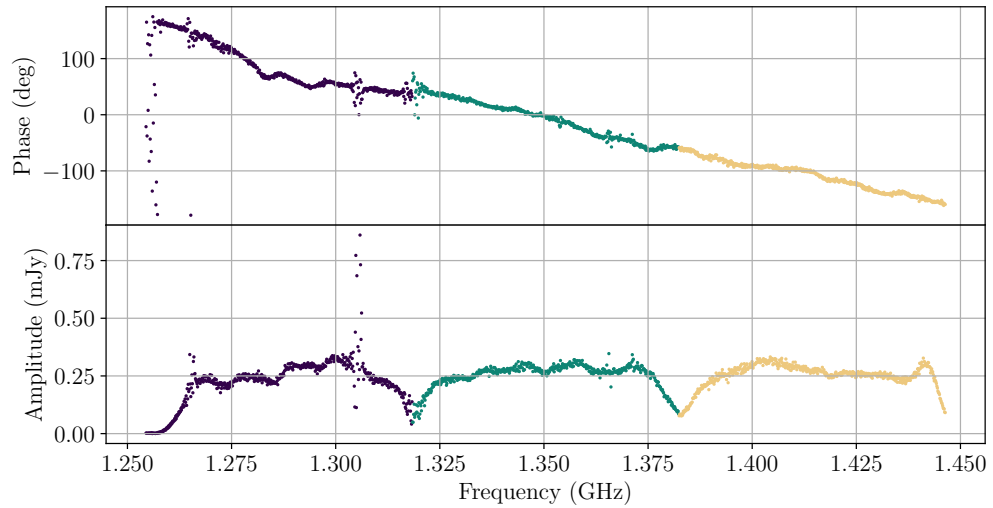
(B) CASA

FIGURE 5.9: Amplitude and phase plots for 3C 286, baseline Mark2-Defford and its first 3 spectral windows and correlation LL.



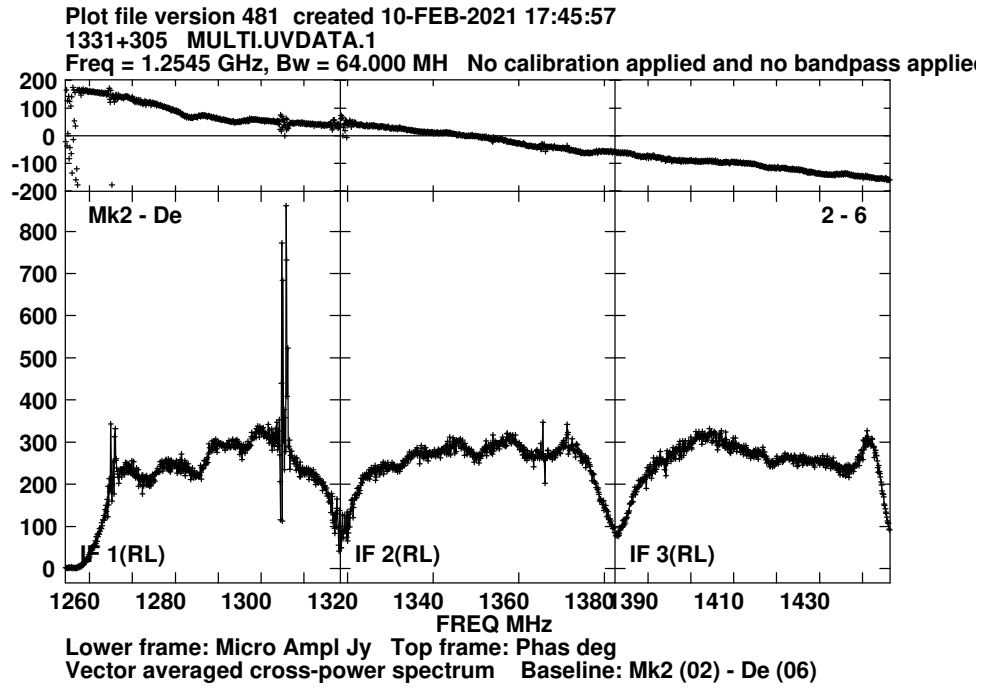
(A) AIPS

Baseline Mk2&De - Correlation LR



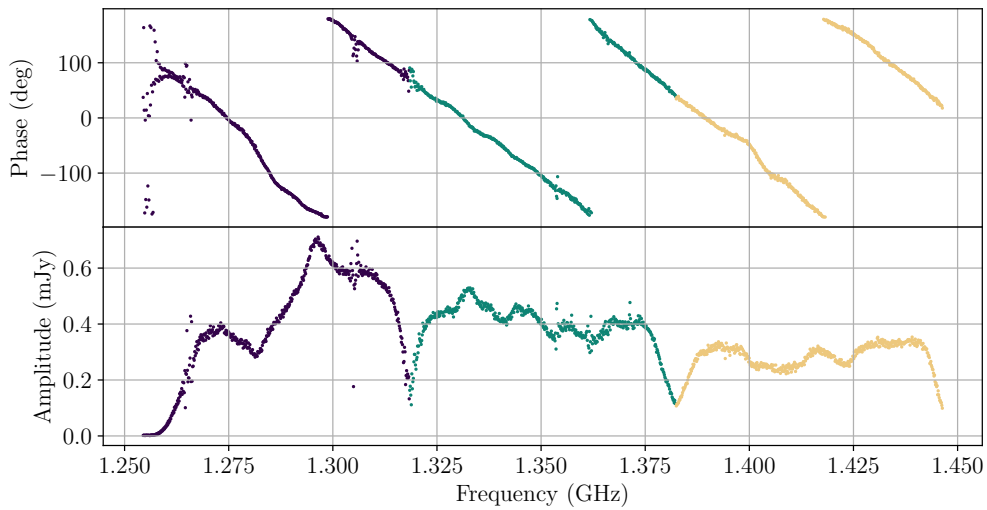
(B) CASA

FIGURE 5.10: Amplitude and phase plots for 3C 286, baseline Mark2-Defford and its first 3 spectral windows and correlation LR.



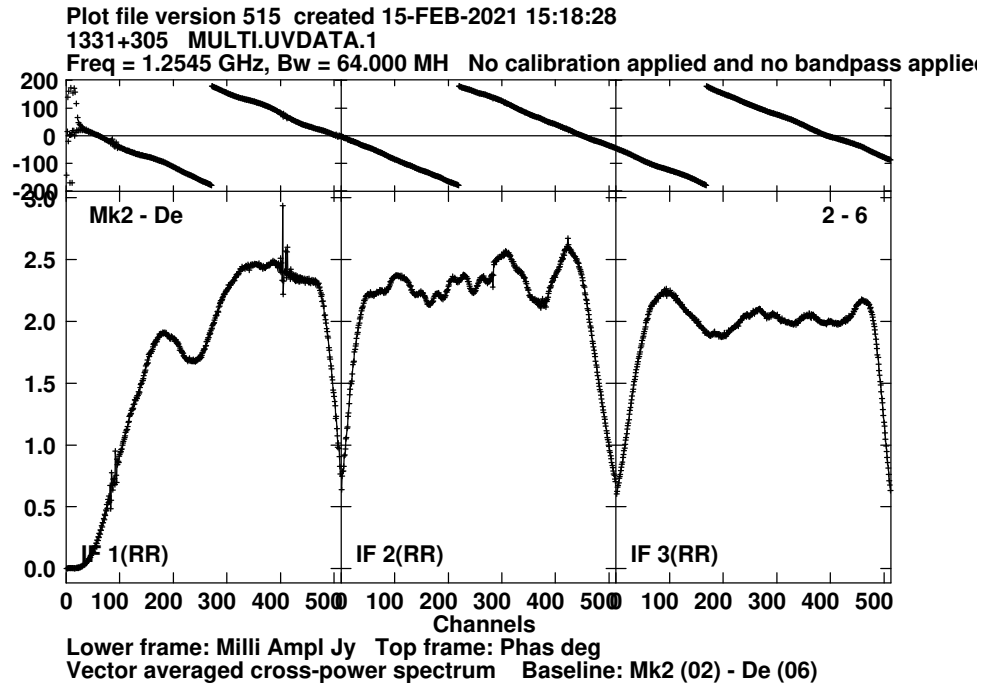
(A) AIPS

Baseline Mk2&De - Correlation RL



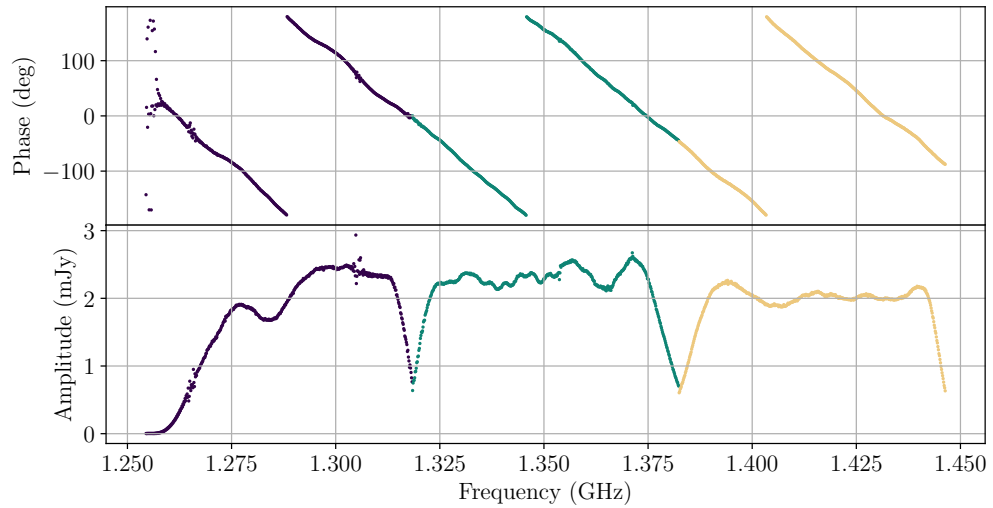
(B) CASA

FIGURE 5.11: Amplitude and phase plots for 3C 286, baseline Mark2-Defford and its first 3 spectral windows and correlation RL.



(A) AIPS

Baseline Mk2&De - Correlation RR



(B) CASA

FIGURE 5.12: Amplitude and phase plots for 3C 286, baseline Mark2-Defford and its first 3 spectral windows and correlation RR.

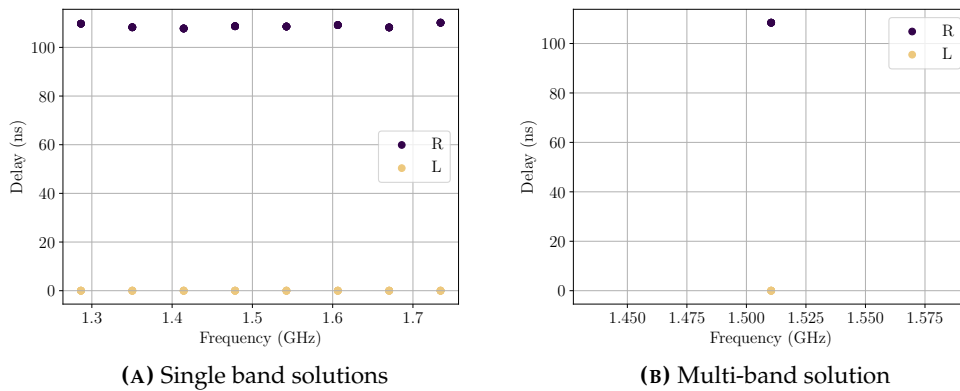


FIGURE 5.13: Single and multi band solutions for the cross-hand delay in the Abell 1314 eMERLIN dataset.

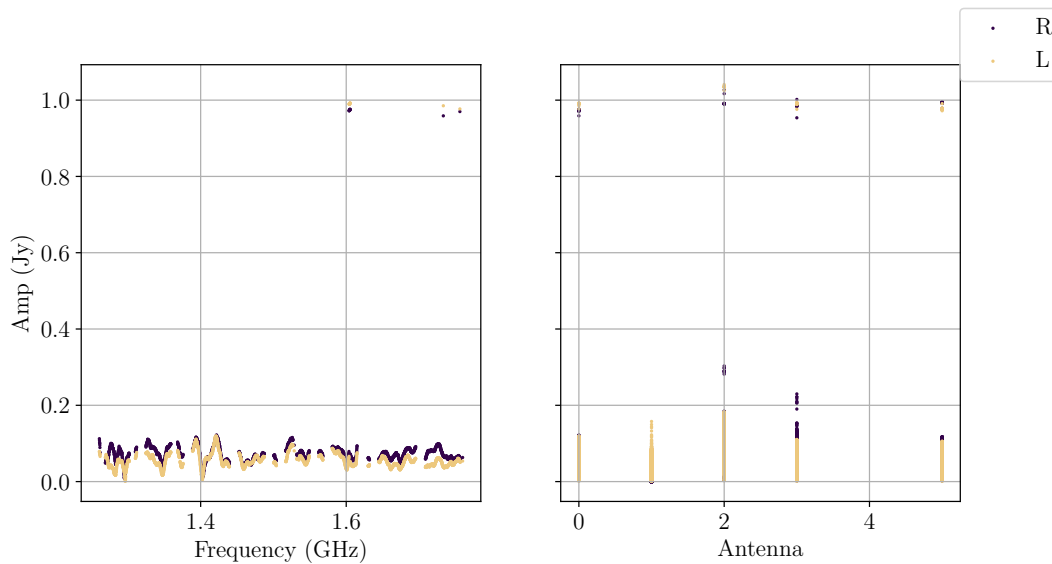


FIGURE 5.14: Amplitude vs frequency and amplitude vs antenna plots from the leakage calibration table before flagging outlier solutions.

Leakage calibration

To derive the leakage solutions I used the CASA task `polcal` and the flux density model of the unpolarised source 3C 84. It is important to note we need to find one solution over the entire run per spectral channel of 0.125 MHz. I have done this by setting the parameters `poltype='Df'`, `solint='inf,0.125MHz'` and `combine='scan'`. By looking at the leakage calibration table, specifically plotting amplitude versus frequency and versus antenna, we can spot some outlier solutions with amplitudes above 0.2 Jy (see Figure 5.14). These outliers are most likely due to residual RFI, therefore we flag these solutions from the leakage calibration table using the CASA task `flagdata` and obtain the plots shown in Figure 5.15.

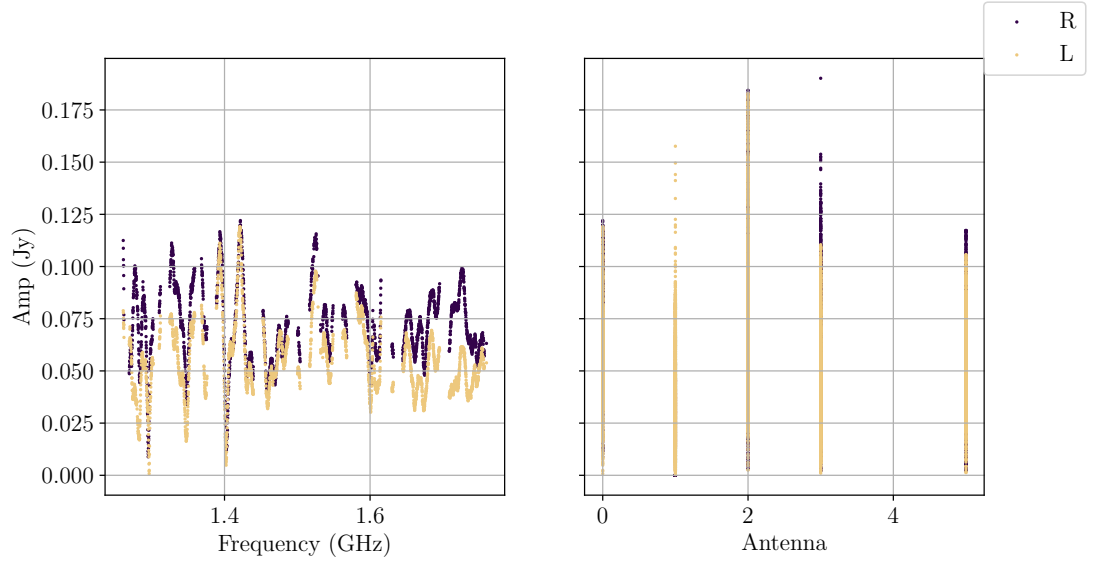


FIGURE 5.15: Amplitude vs frequency and amplitude vs antenna plots from the leakage calibration table after flagging outlier solutions.

Polarisation angle calibration

At this point I have already solved the cross-hand delays and the leakage. In order to obtain an accurate polarisation angle, I need to calibrate the R-L phases using the 3C 286 model and the CASA `polcal` again but this time with `poltype='Xf'`. After creating the calibration table, I can inspect the gain phase solutions versus frequency as shown in Figure 5.16. As R-L delays are solved the polarisation angle solutions do not show a significant slope in phase. Additionally, it can be seen that the phases connect from one spectral window to each other, this is because I have used the single multiband solution.

At this point, I have all the necessary polarisation calibration tables and we can apply them using the CASA task `applycal`.

5.3.3 Polarisation Images

Taking into account the CASA bug that prevented the reconstruction of the polarimetric spectral cubes, the analysis was limited to the available data. Therefore, I focused on investigating the polarization properties of radio galaxy IC 708 using the multi-frequency images.

Having applied the polarization calibration, we were able to generate maps of Stokes I, Q, and U using the `tclean` algorithm with Briggs weighting and robust 0.5. From these maps, I calculated the polarization fraction and angle.

Figure 5.17 presents the polarization fraction of IC 708, with a 5σ mask applied in Stokes I. The figure also displays vectors representing the polarization angle, which are yet to be corrected for the Faraday rotation induced by both the Abell 1314 cluster and the Milky Way galaxy. In this analysis, we observed that while the core exhibited negligible polarization (with a percentage ranging from 2% to 3%), the north-west extended

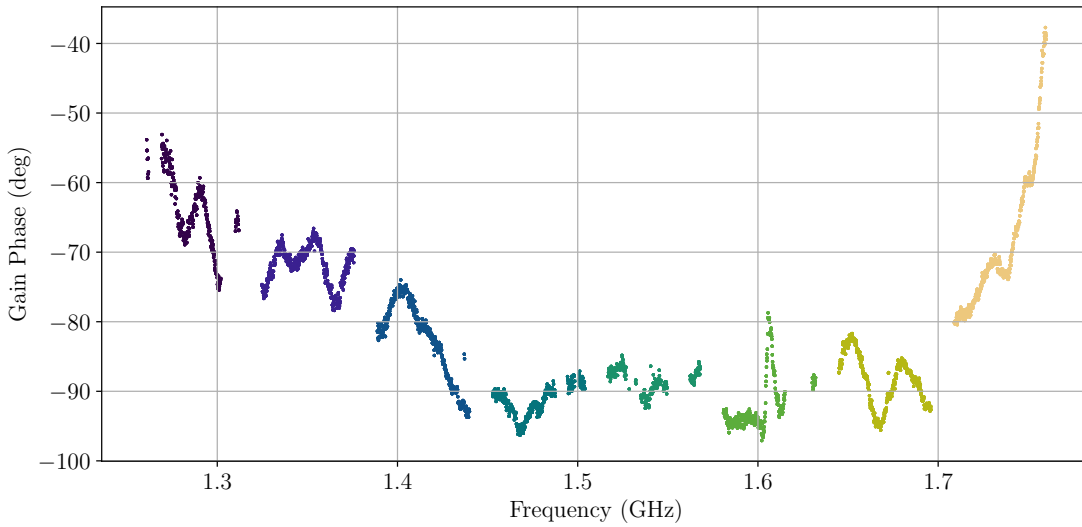


FIGURE 5.16: Polarisation angle solutions versus frequency, each spectral window is shown with a different color.

emission filament displayed a polarization fraction approximately ranging from 0.1 to 0.5.

To further evaluate the significance of the polarization signal, we examined the polarization and total intensity signal-to-noise ratio (SNR) maps, as shown in Figure 5.18. Notably, the peak value in the total intensity SNR map reached 279.346, whereas the peak value in the polarization SNR map was approximately $4\sigma_{\text{QU}}$, where σ_{QU} equals $0.14 \text{ mJy beam}^{-1}$. Thus, it became evident from the MFS maps that the polarization signal was not significant. Using an upper threshold of $8\sigma_{\text{QU}}$, equivalent to $1.14 \text{ mJy beam}^{-1}$, and considering the inability to reconstruct eMERLIN polarimetric cubes, I established that no RM Synthesis can be performed.

Despite the limitations imposed by the CASA bug, the analysis of the available data for radio galaxy IC 708 offers valuable insights into its polarization properties within the Abell clusters. The results emphasize the need for further investigations and improvements in the reconstruction process, as well as the importance of resolving the CASA bug to enable a more comprehensive analysis of the Faraday depth cubes.

Throughout this study, the eMERLIN telescope has proven to be a valuable tool as an SKA pathfinder in facilitating our observations and generating essential data. Despite the challenges faced, the analysis conducted in this chapter highlights the capabilities and limitations of eMERLIN, setting the stage for future advancements in the study of cosmic magnetism within Abell clusters.

In conclusion, while the CASA bug hindered the complete reconstruction of the polarimetric spectral cubes and the subsequent Faraday depth analysis, the analysis of the available data for radio galaxy IC 708 provided meaningful insights into its polarization characteristics. Further research is warranted to address the limitations encountered and to explore the magnetic phenomena in Abell clusters more comprehensively. The eMERLIN telescope, as an SKA pathfinder, demonstrates its potential in studying the magnetic

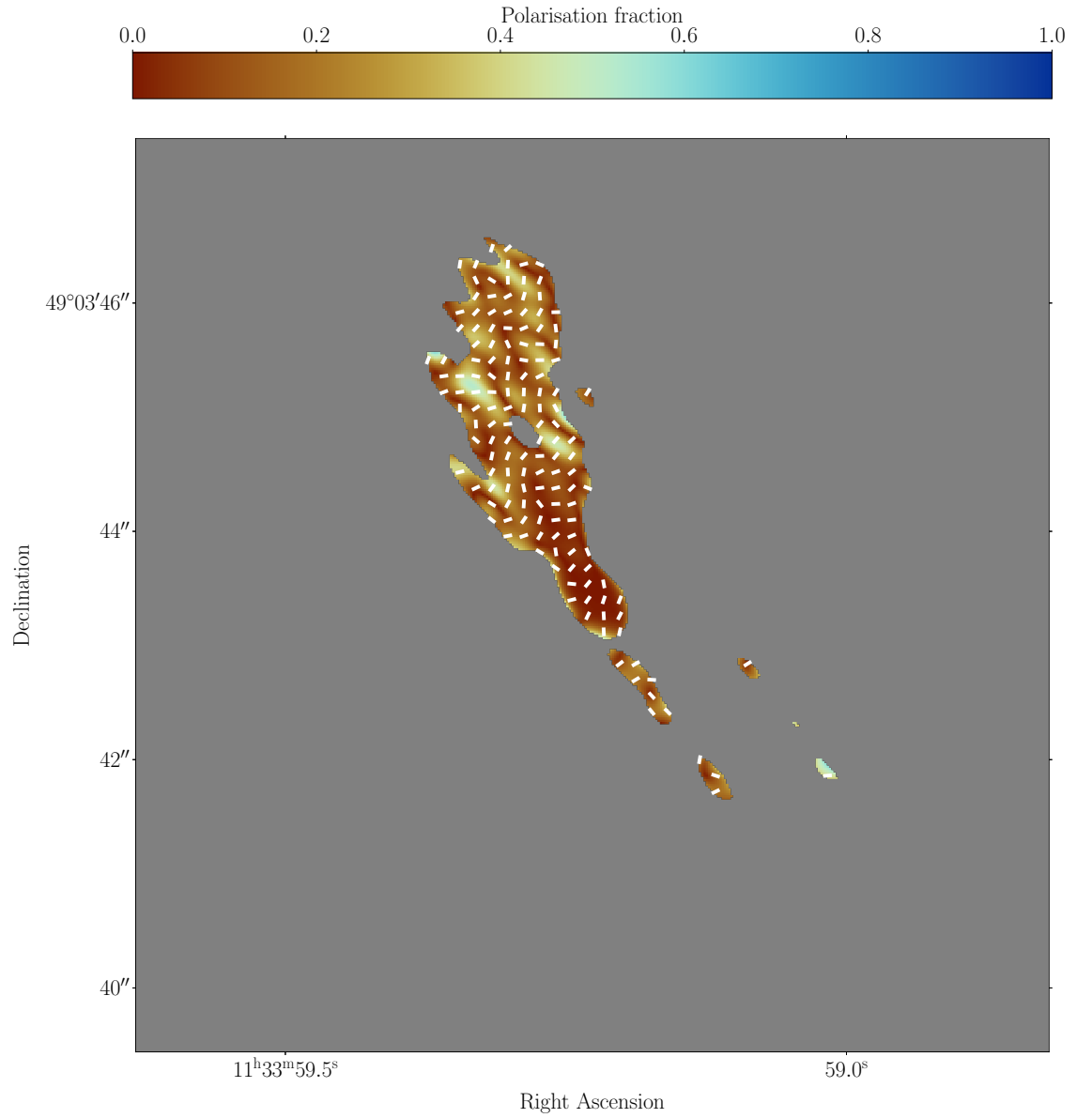


FIGURE 5.17: Polarisation fraction of radio galaxy IC 708 masked at 5σ in Stokes I. The white vectors on the figure on the left represent the polarisation angle not yet corrected by the Galactic Faraday rotation.

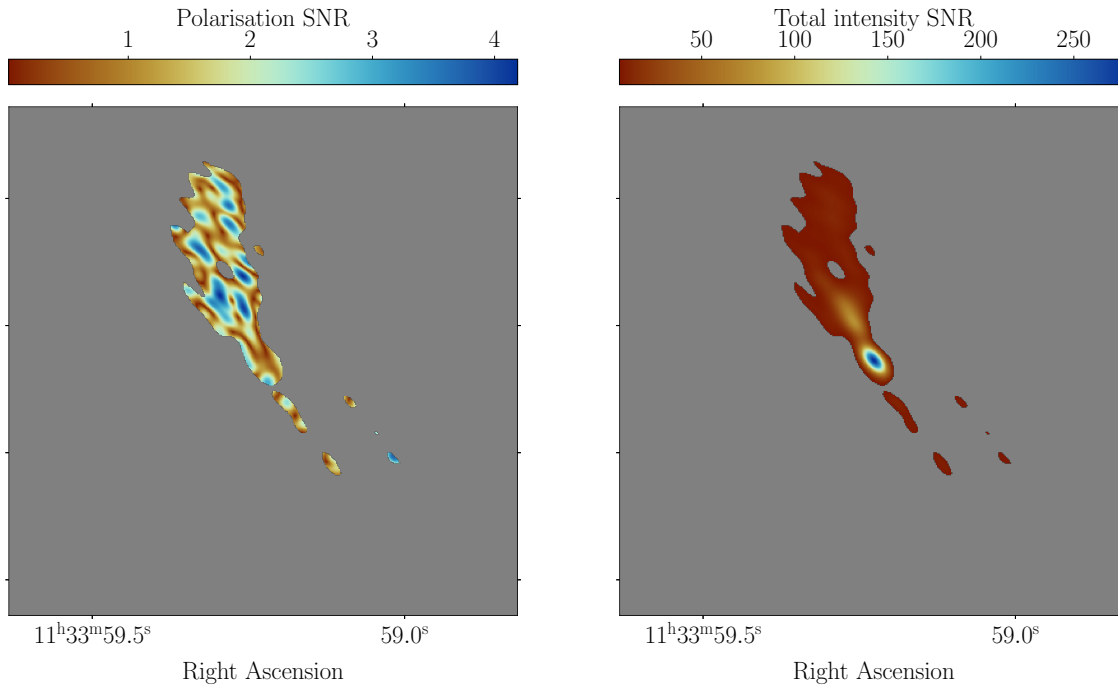


FIGURE 5.18: Polarisation and total intensity SNR maps of radio galaxy IC 708 masked at 5σ in Stokes I.

properties of these clusters and holds promise for future advancements in this field of research.

Chapter 6

MeerKAT Deep Field

Part of the work in this chapter is published in the paper “A Compressed Sensing Faraday Depth Reconstruction Framework for the MeerKAT MIGHTEE-POL Survey”, Miguel Cárcamo, Anna M. M. Scaife, Russ Taylor, Matt Jarvis, Micah Bowles, Srikrishna Sekhar, Lennart Heino, Jeroen Stil., 2022 3rd URSI Atlantic and Asia Pacific Radio Science Meeting (AT-AP-RASC), 2022, pp. 1-4, doi: 10.23919/AT-AP-RASC54737.2022.9814329.

Though studying the linearly polarised emission passing through magneto-ionic gas in galaxy clusters provides important information about galaxy formation, evolution, and cosmic magnetism, there remains considerable value in investigating the voids, namely, the empty spaces between radio galaxies.

In conducting these observations, I employ MeerKAT, a South African radio telescope located on the Karoo Plateau. Comprising 64 antennas, each with a diameter of 13.5 meters, and arranged with a maximum separation distance of 8 kilometers, MeerKAT’s correlator offers up to 32,798 frequency channels, which enables the observation of the L-band frequency range (refer to Table 1.1). These capabilities allow for the effective coverage of a sky area of 1.5 square degrees with an impressive resolution of 4.5 arcseconds, positioning MeerKAT as an ideal instrument for a comprehensive survey of the southern sky.

In this context, the MeerKAT MIGHTEE survey, a large-scale project that I am part of, is designed to study galaxy evolution. The project aspires to generate valuable data products covering various scientific domains, including total intensity, broad-band continuum science, HI spectral-line science, and spectro-polarimetric science. The survey targets imaging of four extragalactic fields: COSMOS, XMM-LSS, CDFS, and ELAIS S1 (Jarvis and Taylor et al., 2016). Observations are conducted within the L-band frequency range, with multiple pointings intended to be mosaicked into a final image. The anticipated broad-band sensitivity of the survey is approximately 2 microjanskys per beam (Heywood and al., 2021). Initial data sets for shared-risk early science projects are already being assembled for each category, utilizing early observations of COSMOS and XMM-LSS.

The early science observations for MIGHTEE encompass four distinct pointings. The first pointing is centered on the COSMOS field, while the subsequent three pointings in XMM-LSS, which are labeled as XMMLSS-12, XMMLSS-13, and XMMLSS-14, are neighboring and overlapping. Each of these pointings was observed twice for approximately 8 hours, while the COSMOS pointing was observed three times for an identical duration of 8 hours each. The number of antennas used in each observation fluctuated between 59 to 64. I present further details and a summary of these observations in Table 6.1.

| Pointing | Date (yyyy-mm-dd) | time (h) | N antennas |
|-----------|----------------------|-------------|------------|
| XMMLSS_12 | 2018-10-06 | 8.02 | 59 |
| XMMLSS_12 | 2018-10-11 | 8.05 | 63 |
| XMMLSS_13 | 2018-10-07 | 8.07 | 59 |
| XMMLSS_13 | 2018-10-12 | 8.03 | 62 |
| XMMLSS_14 | 2018-10-08 | 8.03 | 60 |
| XMMLSS_14 | 2018-10-13 | 8.00 | 62 |
| COSMOS | 2018-04-19 | 8.65 | 64 |
| COSMOS | 2018-05-06 | 8.39 | 62 |
| COSMOS | 2020-04-26 | 7.98 | 59 |

TABLE 6.1: Observations for the MIGHTEE-POL Early Science Release.

6.1 MeerKAT MIGHTEE-POL Data Reduction

The visibility data were calibrated using different sources as calibrators for the COSMOS and XMM-LSS fields. For the COSMOS field, J0408–6565 was used as the primary calibrator, J1008+0740 as the secondary calibrator, and J1331+3030 (3C 286) as the polarisation calibrator. For the XMM-LSS pointings, J1939–6342 served as the primary calibrator to establish the flux density scale, as well as a bandpass calibrator and for deriving the leakage solutions. The secondary calibrator, J0201–1132, was observed every 20 to 30 minutes during the 8-hour track to monitor time-dependent complex gains. Moreover, the source J0521+1638 (3C 138) was used as the polarisation angle calibrator, which was observed once or twice during a track.

The calibration of visibility data and imaging in full polarisation mode was performed on the ilifu cloud facility using the CASA-based IDIA pipeline ¹. The pipeline initially partitions the L-band RF MHz into 15 spectral windows ranging from 880 MHz to 1680 MHz, resulting in the creation of multi-MS files processed concurrently using the ilifu SLURM manager. During this stage, strong persistent RFI has been detected as shown in Figure 6.1. The contaminated data has been removed through automated flagging within the frequency ranges of 933-960 MHz, 1163-1299 MHz, and 1525-1630 MHz. The subsequent step in the pipeline involves using observations of the primary calibrator to measure the frequency-dependent gains using an absolute flux bandpass solution.

¹<https://idia-pipelines.github.io/docs/processMeerKAT>

Solutions are then applied, and leakage terms are derived. As mentioned earlier, complex gains are calculated using the secondary calibrator. This is achieved by utilizing the CASA task `gaincal` and setting `gaintype='T'`, ensuring that any polarised signal in the secondary calibrator does not affect the relative X and Y gains derived from the primary calibrator. Finally, the polarisation calibrator is used to solve for the polarisation angle. At this stage, the median XY phase spectrum is fitted with a 3rd degree polynomial, and the calibration solution tables are applied.

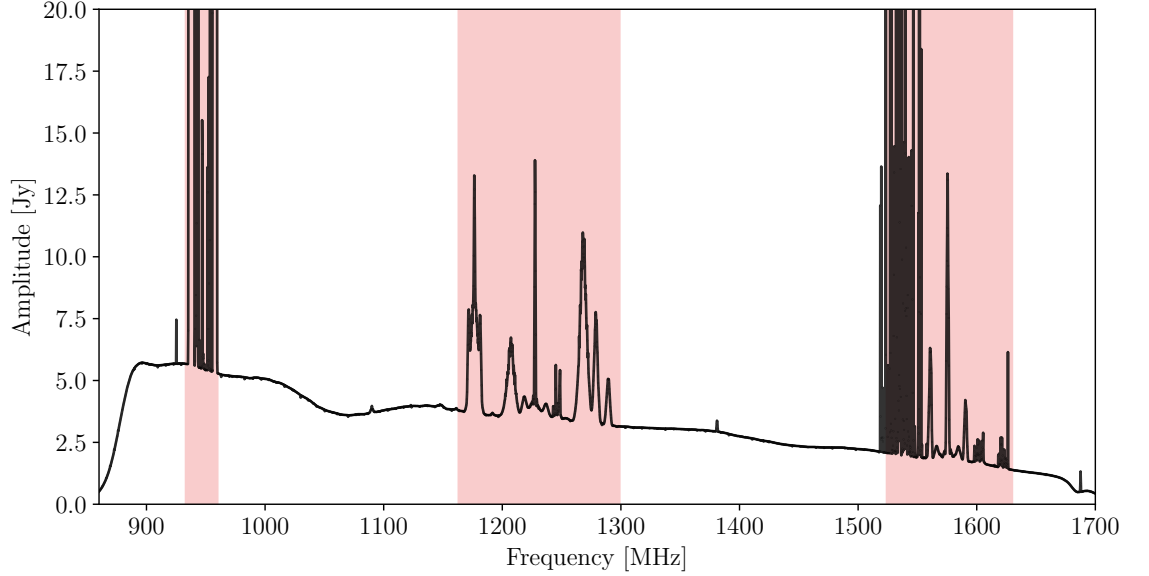


FIGURE 6.1: Time-averaged bandpass response from MeerKAT on J1939-6342. The portions of the spectrum marked in red are dominated by significant, consistent RFI across all observational data, leading to their exclusion from all datasets.

Following calibration, the separated multi-MS files were merged into a single measurement set containing the calibrated visibility data. This dataset undergoes self-calibration using CASA, with `gaintype='T'` set to preserve the relative X and Y gains. Two cycles of self-calibration were performed using the imager `tclean`, utilizing the full dimensions of the primary beam image (6144×6144), a cell size of 1.5 arcseconds, and a robust parameter of -0.5 . In the first cycle, calibration is done solely for phase, while in the second cycle, both phase and amplitude are solved for.

Several data products were generated after reducing the visibility data using `tclean` and combining the visibilities from multiple observations. Firstly, MFS broadband images for Stokes I, Q, U, and V were produced using Briggs weighting and robust parameters of -0.5 and $+0.4$. The central coordinates of the four image sets and the restoring beams of the MFS images (with a robust parameter of -0.5) are listed in Table 1. Additionally, Figure 2 shows the MFS continuum Stokes I image of the COSMOS field. Secondly, spectro-polarimetric hypercubes (I, Q, U, V) are created for the calibrators and target fields, using a robust parameter of 0.0 . Two types of hypercubes were generated: the first maintains the native resolution for each frequency slice, while the second smooths all frequency slices to a common resolution of 18 arcseconds. The frequency range of the

hypercubes is 794 MHz (887-1680 MHz), with a channel width of 2.51 MHz. Frequency channels affected by persistent RFI are replaced with not-a-number (NaN) slices. Consequently, the frequency ranges of contiguous correct data are 887-993 MHz, 960-1163 MHz, 1299-1524 MHz, and 1630-1680 MHz, accounting for 74% of the band.

| Pointing | Coordinates | | MFS Image resolution (robust = −0.5) | RMTF FWHM (rad m ^{−2}) | RM Synthesis (smoothed cube) | | | | |
|-----------|-------------|-----------|--|--|--|--|--------------------------------|--------------------------------|------|
| | RA | DEC | | | median RM RMS off-source (μJy beam ^{−1}) | median per-chan background Q (μJy beam ^{−1}) | U (μJy beam ^{−1}) | V (μJy beam ^{−1}) | |
| XMMLSS_12 | 02 17 51.0 | −04 59 59 | 7.75'' × 6.81'' | −35.1° | 56.8 | 3.12 | 25.3 | 26.9 | 25.1 |
| XMMLSS_13 | 02 20 42.0 | −04 49 59 | 7.69'' × 6.73'' | −21.2° | 56.8 | 3.97 | 27.9 | 31.2 | 27.2 |
| XMMLSS_14 | 02 23 22.0 | −04 49 59 | 7.93'' × 6.90'' | −35.2° | 57.6 | 2.90 | 25.3 | 26.1 | 25.4 |
| COSMOS | 10 00 28.6 | +02 12 21 | 7.80'' × 7.22'' | −20.1° | 55.2 | 3.21 | 31.2 | 31.6 | 31.5 |

TABLE 6.2: MIGHTEE-POL image and cube properties for each pointing.

It is important to note that the residual on-axis leakage after calibration measures approximately 0.1%. However, at the upper end of the L-band, there is beam squint and squash that varies with frequency, resulting in off-axis frequency-dependent leakage (Asad et al., 2021; Sekhar et al., 2022). To mitigate the impact of strong leakage at the high-frequency range, I have limited the analysis of polarisation signals to frequencies below 1380 MHz. Below this threshold, the leakage remains below 0.2% within a 0.5° radius from the field center. See Table 1.1 for resulting frequency range, channel width and Faraday parameters.

6.2 MeerKAT Deep Field optimal wavelet selection

In Section 3.5 I have seen that depending on the data, Faraday depth signals might have different structures. i.e thin sources, thick sources or both. Again, to select the wavelet which best represents the signal. In order to simulate data for MeerKAT I will use the L-band frequency range and equations 3.32 and 3.33. Additionally, I will set S_{ν_0} to 0.055 and 0.066 Jy beam⁻¹ for scenarios 1 and 2, respectively and a spectral index of 0.7. For scenario 2 we have also set ϕ_{fg} to 40 rad m⁻². This is summarized on Table 6.3. Following steps from Section 3.5.1, we have set removal fraction to 0.3 and noise to 2.2804 and 2.38714 mJy beam⁻¹ in Stokes Q and U, respectively.

Given Equation 6.1 from Stil et al., 2014 I can get the polarisation percentage by drawing Gaussian random variables such that $a \sim \mathcal{N}(0.051, 0.004)$ and $b \sim \mathcal{N}(0.038, 0.007)$. Consequently, I also draw $S \sim \mathcal{U}_{[S_{\max}, 5\sigma_S]}$ as a uniform random variable where S_{\max} and σ_S are the maximum flux and rms noise in mJy on real Stokes I in at 1.4 GHz, respectively. The maximum flux is 34 mJy beam⁻¹ and the rms noise is 0.00504 mJy beam⁻¹.

$$\log \Pi_{0,\text{med}} = -a \log S_{1.4} + b \quad (6.1)$$

Finally, after multiplying the polarisation percentage by $S/100$ we set polarised intensity values for the simulated sources.

Results from Tables 6.4, 6.5, 6.6 and Figures 6.3 and 6.4 show that the optimal family according to the lowest AIC for scenario 1 is the delta wavelet. Note that, even thoughdb25 provides a better PSNR and superior RMSE, we have decided to choose the

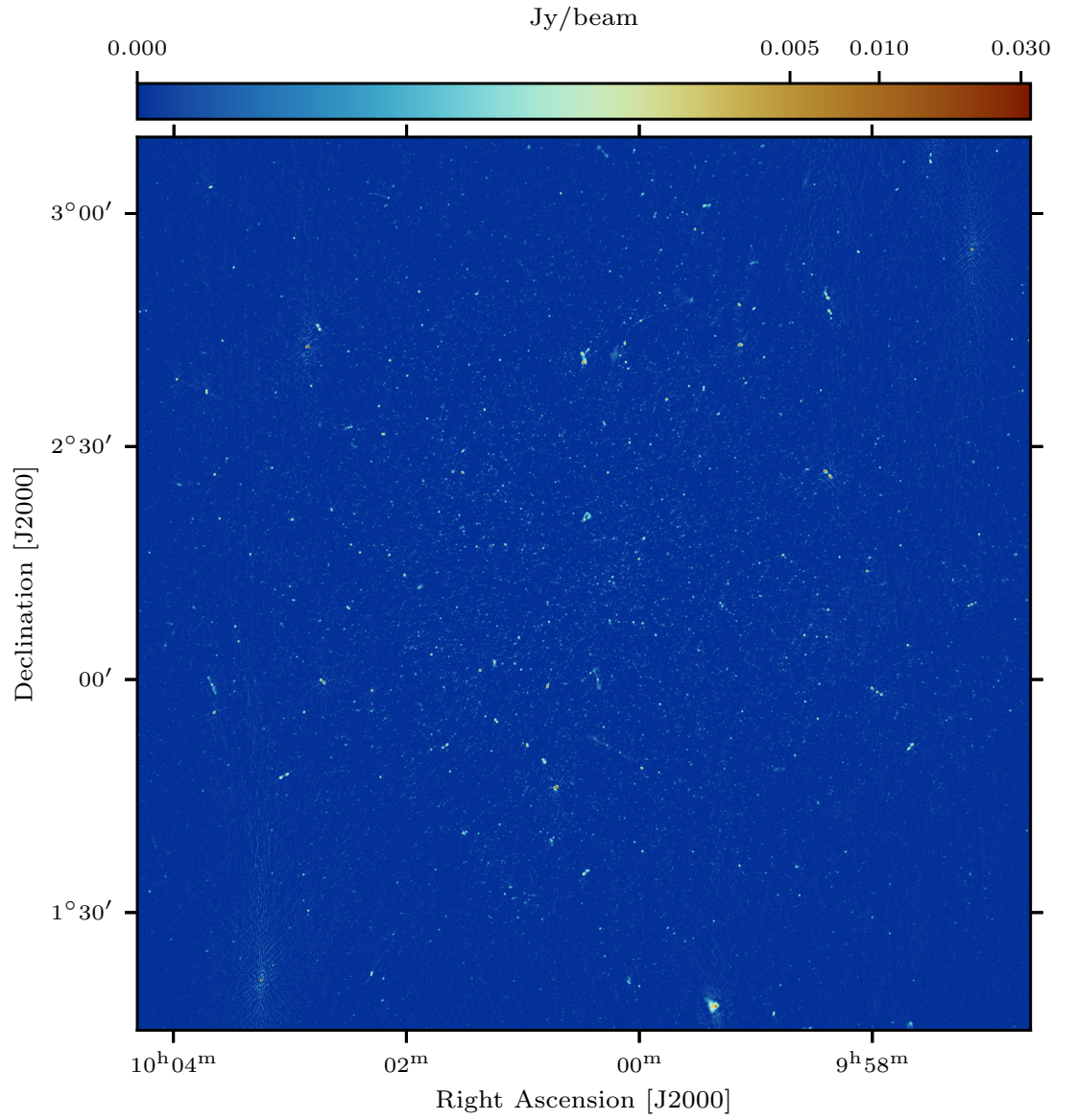


FIGURE 6.2: COSMOS MFS Stokes I continuum image at 1.28 GHz using Briggs weighting and robust -0.5 . The colorbar has a log scale and has been saturated to a minimum of 0.0 Jy beam^{-1} to show extended fainter emission.

| Scenario | ϕ_1 [rad m ⁻²] | ϕ_{fg} [rad m ⁻²] | ϕ_0 [rad m ⁻²] | S_{ν_0} [Jy/beam] |
|----------|------------------------------------|---------------------------------------|------------------------------------|--------------------------|
| 1 | -200 | - | - | 0.055 |
| 2 | - | 40 | 200 | 0.066 |

TABLE 6.3: MeerKAT L-band simulation details

| | Scenario 1 | Scenario 2 | Scenario 3 |
|-------------|------------------------------------|------------------------------------|------------------------------------|
| AIC | -16473.97 ± 121.79 | -16675.31 ± 69.21 | -16306.49 ± 112.43 |
| BIC | -15632.70 ± 379.94 | -16019.68 ± 196.20 | -15314.80 ± 267.24 |
| PSNR | 346.41 ± 103.08 | 108.16 ± 19.93 | 292.59 ± 93.70 |
| RMSE | $(248.38 \pm 4.76) \times 10^{-5}$ | $(237.06 \pm 4.22) \times 10^{-5}$ | $(258.40 \pm 7.41) \times 10^{-5}$ |

TABLE 6.4: AIC, BIC, PSNR and RMSE for delta function basis.

delta wavelet as optimal since it will help us to identify the RM at the maximum with greater precision."

6.3 Rotation Measure extraction on the MIGHTEE-POL survey

I conducted the RM synthesis using a $\Delta\phi = 0.4, \text{rad}, \text{m}^{-2}$ and constructed it over a Faraday depth range of $\pm 2000, \text{rad}, \text{m}^{-2}$. Faraday depth signals were reconstructed from the on-source catalog, which points to text files containing the polarised spectra of on-source sources. In order to avoid the large off-axis leakage at the high end of the band, and as mentioned above, I restricted RM synthesis to frequencies less than 1380 MHz. I also checked and filtered the catalog for possible sources on which the flux density fit failed and either the flux density was zero, or the spectral index error was too high. This was important due to the impact of the spectral index on the RMTF. For example, Figure 6.5 shows the RMTF for the wavelength-squared sampling of COSMOS for spectral indices -1.0, 0.0 and 1.0. On the bottom left, it shows the residuals between the RMTFs using $\alpha = -1.0$ and $\alpha = 0.0$. On the bottom right the same residual is calculated between RMTFs using $\alpha = 0.0$ and $\alpha = 1.0$. The residuals are not zero (peaks on the amplitudes are around 0.1). This demonstrates a difference between RMTFs, and there is an impact when using different spectral index when reconstructing Faraday depth spectra. Additionally, it is possible to see on the top left plot that sidelobes are thicker than those when using $\alpha = 0.0$ or $\alpha = 1.0$. Another example is shown in Figure 6.6, which depicts a RMTF of a fainter source with a fitted spectral index $\alpha = 110.46 \pm 61.65$. On the right, the RMTF for the same sampling, but this time forcing the spectral index to a value of -0.7. It is

| | Scenario 1 | | Scenario 2 | | Scenario 3 | |
|---------------------|------------------------------------|------------------------------------|------------------------------------|------------------------------------|------------------------------------|------------------------------------|
| | WT | UWT | WT | UWT | WT | UWT |
| Best wavelet family | haar | haar | haar | haar | haar | haar |
| AIC | -16392.37 ± 150.02 | -15199.08 ± 288.31 | -16659.79 ± 87.98 | -15628.69 ± 190.52 | -16203.82 ± 122.41 | -14312.71 ± 472.85 |
| BIC | -15815.51 ± 295.55 | -11501.69 ± 1000.41 | -16247.48 ± 147.86 | -12399.92 ± 601.51 | -15400.09 ± 259.50 | -8624.71 ± 1525.12 |
| PSNR | 158.44 ± 24.61 | 163.95 ± 27.82 | 81.15 ± 22.35 | 38.44 ± 3.65 | 153.38 ± 24.13 | 164.18 ± 22.40 |
| RMSE | $(265.23 \pm 9.78) \times 10^{-5}$ | $(265.42 \pm 5.50) \times 10^{-5}$ | $(246.46 \pm 6.50) \times 10^{-5}$ | $(242.67 \pm 5.32) \times 10^{-5}$ | $(275.03 \pm 8.60) \times 10^{-5}$ | $(277.85 \pm 9.23) \times 10^{-5}$ |

TABLE 6.5: AIC, BIC, PSNR and RMSE for discrete wavelets transforms (WT) and undecimated wavelet transforms (UWT) with the minimum AIC.

| | Scenario 1 | | Scenario 2 | | Scenario 3 | |
|---------------------|------------------------------------|------------------------------------|------------------------------------|------------------------------------|-------------------------------------|------------------------------------|
| Best wavelet family | D+WT db | D+UWT haar | D+WT haar | D+UWT haar | D+WT db | D+UWT haar |
| AIC | -16460.83 ± 147.871 | -15206.63 ± 315.86 | -16610.73 ± 105.32 | -15564.75 ± 333.21 | -16158.84 ± 182.93 | -14281.35 ± 377.99 |
| BIC | -15698.88 ± 351.33 | -11501.48 ± 1067.85 | -16055.69 ± 247.02 | -12147.92 ± 1097.16 | -14987.25 ± 446.89 | -8386.21 ± 1246.50 |
| PSNR | 443.34 ± 238.47 | 164.65 ± 27.46 | 76.93 ± 23.11 | 37.93 ± 4.21 | 384.76 ± 220.08 | 165.78 ± 21.49 |
| RMSE | $(252.35 \pm 8.38) \times 10^{-5}$ | $(264.43 \pm 5.82) \times 10^{-5}$ | $(245.97 \pm 5.81) \times 10^{-5}$ | $(242.01 \pm 5.87) \times 10^{-5}$ | $(265.89 \pm 10.41) \times 10^{-5}$ | $(273.11 \pm 7.28) \times 10^{-5}$ |

TABLE 6.6: AIC, BIC, PSNR and RMSE for delta basis function combined with discrete wavelets transforms (D+WT) and undecimated wavelet transforms (D+UWT) with the minimum AIC.

| | Scenario 1 | | Scenario 2 | | Scenario 3 | |
|---------------------|------------------------------------|------------------------------------|------------------------------------|------------------------------------|------------------------------------|------------------------------------|
| Best wavelet family | D+WT db25 | D+UWT haar | D+WT haar | D+UWT haar | D+WT db36 | D+UWT haar |
| AIC | -16565.94 ± 55.75 | -15206.63 ± 315.86 | -16610.73 ± 105.32 | -15564.75 ± 333.21 | -16276.35 ± 101.67 | -14281.35 ± 377.99 |
| BIC | -15936.84 ± 152.44 | -11501.48 ± 1067.85 | -16055.69 ± 247.02 | -12147.92 ± 1097.16 | -15218.28 ± 256.98 | -8386.21 ± 1246.50 |
| PSNR | 624.64 ± 21.42 | 164.65 ± 27.46 | 76.93 ± 23.11 | 37.93 ± 4.21 | 585.64 ± 36.65 | 165.78 ± 21.49 |
| RMSE | $(247.40 \pm 4.47) \times 10^{-5}$ | $(264.43 \pm 5.82) \times 10^{-5}$ | $(245.97 \pm 5.81) \times 10^{-5}$ | $(242.01 \pm 5.87) \times 10^{-5}$ | $(258.82 \pm 6.45) \times 10^{-5}$ | $(273.11 \pm 7.28) \times 10^{-5}$ |

TABLE 6.7: AIC, BIC, PSNR and RMSE for delta basis function combined with discrete wavelets transforms (D+WT) and undecimated wavelet transforms (D+UWT) with the minimum AIC.

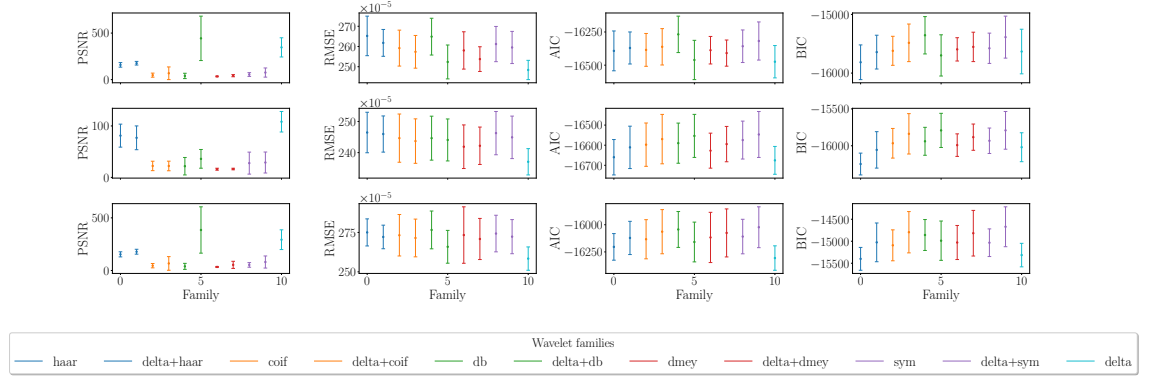


FIGURE 6.3: PSNR, RMSE, AIC and BIC using all discrete wavelet families for reconstruction of MeerKAT simulated data using the discrete wavelet transform. First row shows scenario 1, second row for scenario 2 and third row for scenario 3.

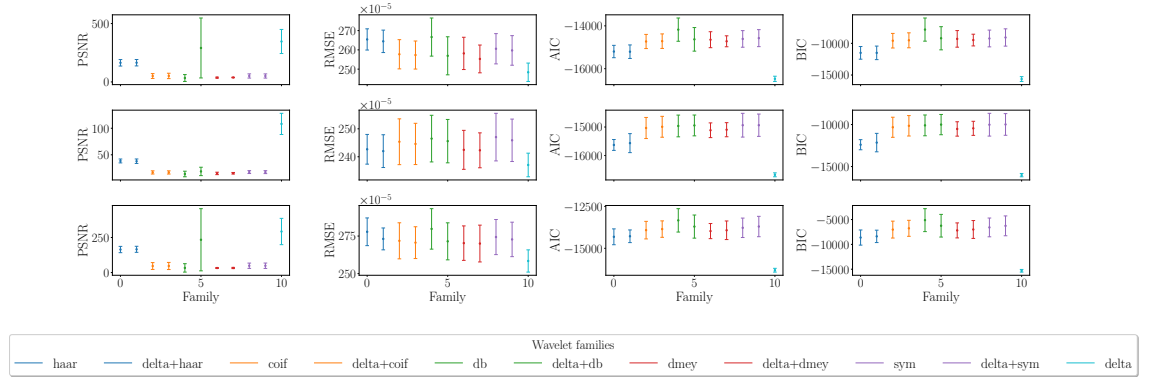


FIGURE 6.4: PSNR, RMSE, AIC and BIC using all wavelet families for reconstruction of MeerKAT simulated data using the undecimated wavelet transform. First row shows scenario 1, second row for scenario 2 and third row for scenario 3.

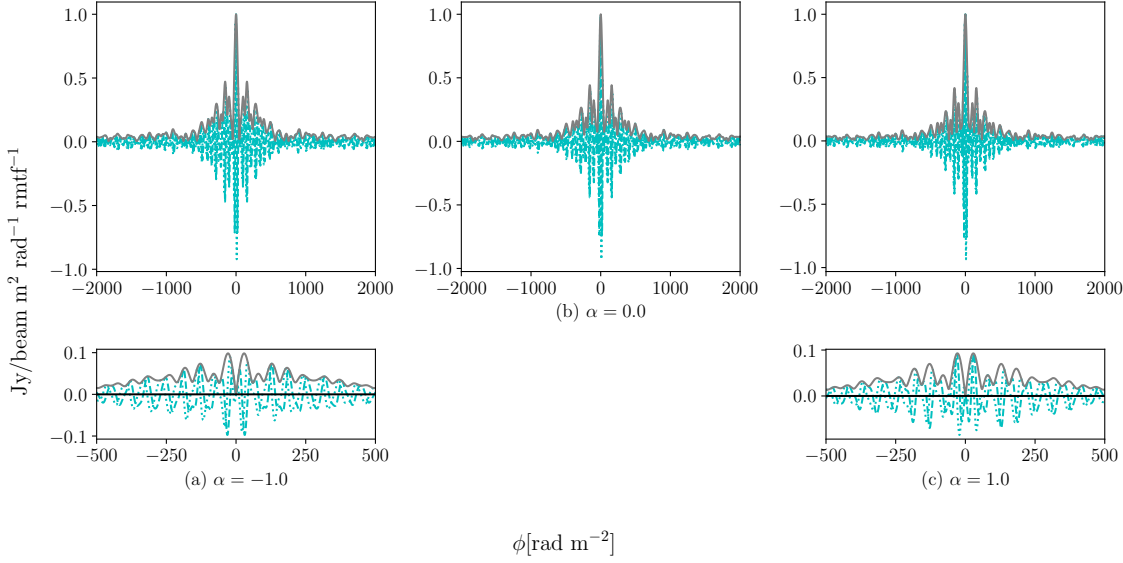


FIGURE 6.5: On the top, from left to right: RMTF for the COSMOS wavelength squared sampling using spectral indices -1.0, 0.0 and 1.0. On the bottom left: Residual between RMTFs using $\alpha = -1.0$ and $\alpha = 0.0$. On the bottom right: Residual between RMTFs using $\alpha = 0.0$ and $\alpha = 1.0$

clear, that the value of the spectral index is crucial for a good reconstruction of fainter signal. Therefore, for this kind of sources, I forced a spectral index equal to the mode of the distribution (see Figure 6.7) on the in-source catalog equal to -0.74. Additionally, after reconstructing Faraday depth, I corrected the maximum value and position of the RM using a quadratic interpolation.

6.3.1 COSMOS

To analyse the resulting polarised intensity from the reconstruction of the on-source sources using *cs-romer*, I will refer to Figure 6.8 which shows these values versus the peak flux density for each source. This displays the polarisation fraction of each source and indicates which sources should be categorised as polarised. Additionally, I have included polarised intensity values from both dirty and reconstructed Faraday spectra in order to compare them. For example, one of the first things one can notice is that most of the sources with polarisation fraction over 10% and over the 99.9 percentile threshold have moved on the reconstructed plot with respect to the dirty one. Firstly, various sources less than 1% polarised were moved below the 99.9 percentile. Secondly, sources that were over 10% polarised moved below the 10% polarised line. This is expected since we do not expect either sources with a polarisation over 10% or sources below 1% and above 99.9 percentile. Lastly, by looking at Figure 6.9 we can see that the reconstruction of Faraday depth spectra is able to correct outlier sources seen in the histogram from the dirty Faraday spectra (e.g. the source with a polarisation fraction of 4). Furthermore, reconstructions have corrected those sources with low polarisation fractions that were over the 99.9 percentile.

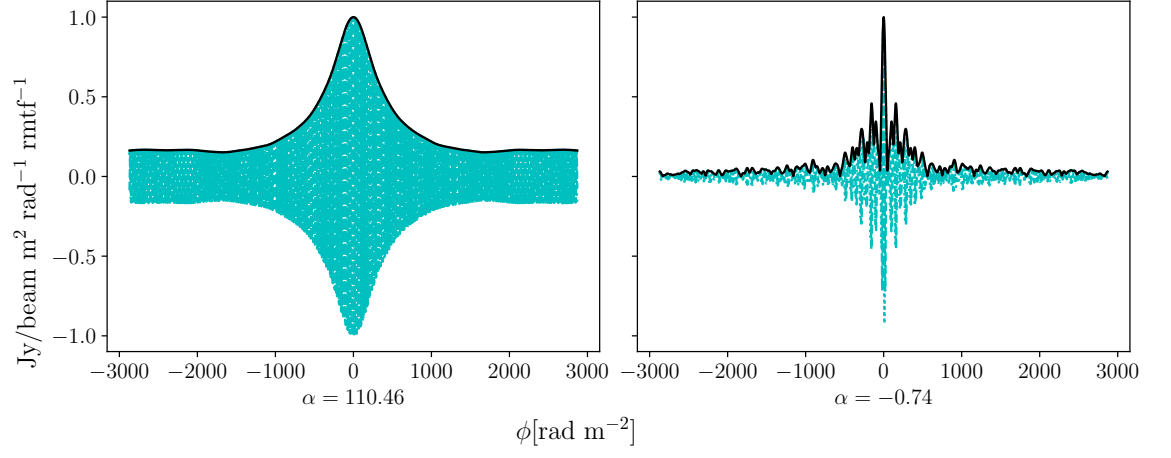


FIGURE 6.6: On the left: RMTF for one of the fainter sources of the in-source catalog. This source has a fitted $\alpha \sim 100$. On the right: RMTF for the same source and sampling but forcing the spectral index to a value of -0.74.

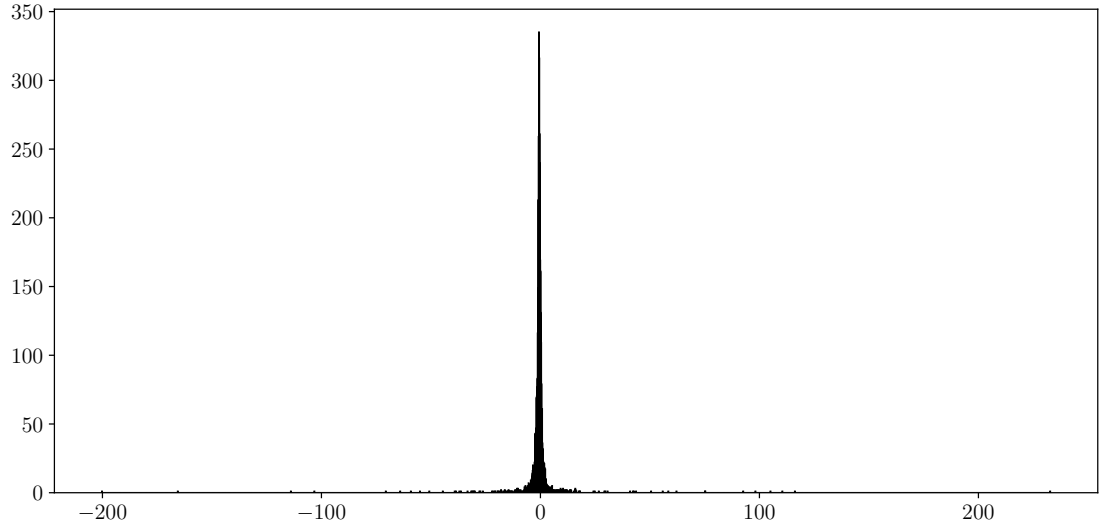


FIGURE 6.7: Spectral index distribution for COSMOS in-source sources. The mean of the distribution is -0.598, the standard deviation is 8.797 and the mode is -0.74.

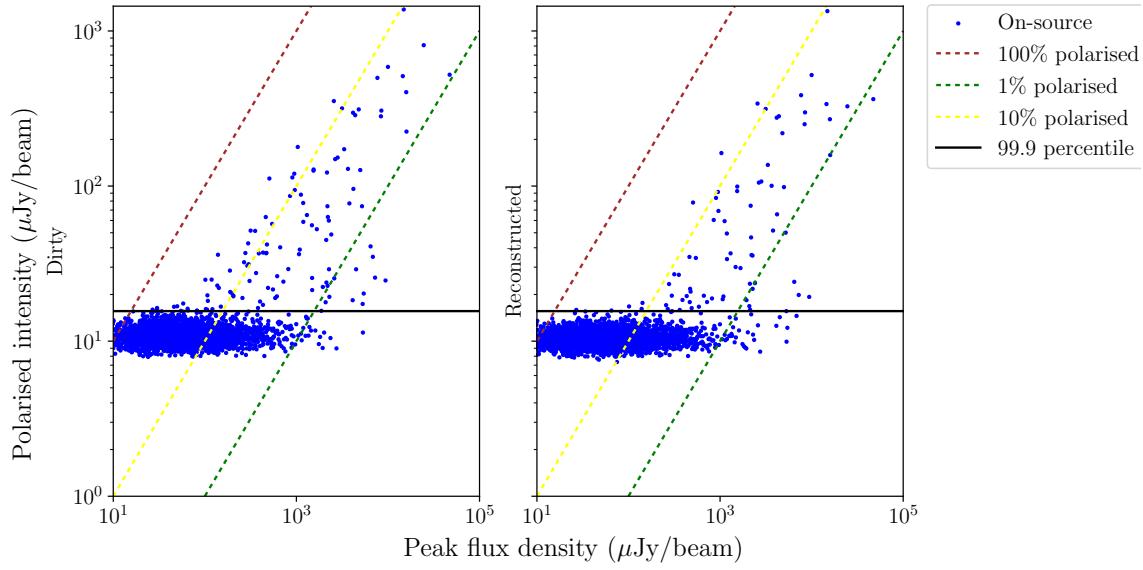


FIGURE 6.8: polarised intensity of the maximum of the RM synthesis spectra for the dirty (left) and reconstructed (right) on-source (blue dots) positions plotted against the peak total intensity for each source. This plot is for the COSMOS field. The diagonal dashed lines represent lines of constant fractional polarisation of 1, 10 and 100%. The horizontal black and green line represent respectively the 99.9 percentile and the median plus 4 sigma of the off-source spectral peaks.

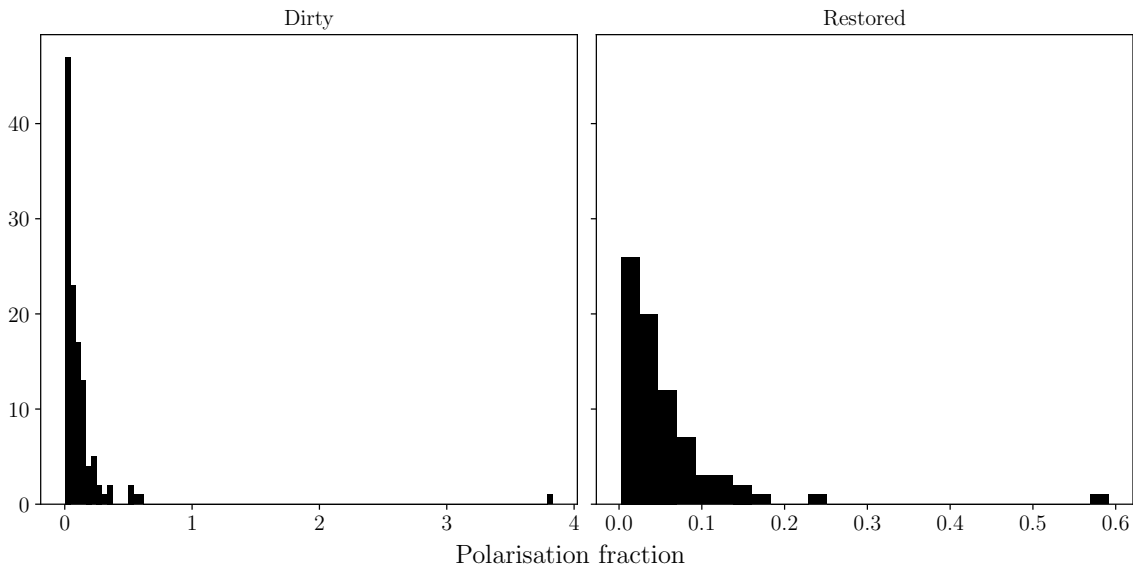


FIGURE 6.9: Histograms for dirty and reconstructed Faraday spectra for in-source sources with polarisation fractions above the 99.9 percentile.

Finally, this chapter has provided significant insights about polarisation and its utility in understanding temporal changes in magnetic fields in cosmic web filaments. Studies such as those by Carretti et al., 2022b and Kronberg et al., 2008 demonstrate that the RM is an effective tool for gaining insights into the magnetized space traversed by radiation. This data can be leveraged to track modifications in magnetic fields. Concurrently, alterations in polarisation fraction may indicate changes in depolarisation (Sokoloff et al., 1998) and in the magneto-ionic conditions at the origin of the radiation or in the intergalactic medium (Berger, A. et al., 2021).

In this chapter, I used RM synthesis and analysed polarised spectra from on-source sources from the COSMOS catalogue. To ensure the accuracy of my results, I meticulously examined the catalogue and eliminated any sources with flux density fits that had failed or that had significant spectral index errors. This was a crucial step since the spectral index can influence the RMTF, as illustrated by Figure 6.5. When determining the spectral index for fainter sources proved challenging, I assigned it to the mode of the distribution to enhance the reliability of the reconstructions.

Next, I employed the *cs-romer* framework to reconstruct on-source sources and analyze their polarised intensity. The polarised intensity of each source in relation to its peak flux density is demonstrated in Figure 6.8. This comparison assists in determining the polarisation fraction for each source. I observed significant differences when comparing the polarised intensity values from both the dirty and reconstructed Faraday spectra. For instance, sources with polarisation fractions exceeding 10% and those in the 99.9 percentile exhibited differing positions in the reconstructed plot as opposed to the dirty plot. This finding aligns with the presumption that extreme polarisation fractions surpassing certain thresholds are improbable.

Although I have reconstructed the Faraday depth spectra of extragalactic sources, the polarisation fraction is not fully described yet. Nonetheless, these findings guide us towards promising areas for future investigation. To replicate the outcomes in Carretti et al., 2022b using MIGHTEE-POL MeerKAT early science data, I need to delve deeper into the fluctuations of RM and polarisation fraction of extragalactic sources with redshift. More precise measurements will aid us in comprehending the origins and evolution of magnetic fields. Gauging the variations in the cosmic magnetic field across cosmic time can offer invaluable insights into its derivation from primordial fields and the potential role of field seeding and amplification by astrophysical sources (Carretti et al., 2022b; Akahori and Ryu, 2011; Vazza, F. et al., 2015; Subramanian, 2016; Vazza et al., 2017; O’Sullivan et al., 2020; Arámburo-García et al., 2021).

The suitability of cosmic web filaments for this research arises from their lesser processed state, which closely mirrors original conditions (Carretti et al., 2022b). Moreover, examining these filaments can also provide valuable insights into the extragalactic sources themselves, such as alterations in their physical conditions and environments (Kronberg et al., 2008; Berger, A. et al., 2021). This adds to our knowledge of the temporal evolution of magnetic fields.

In summary, the findings of this chapter enhance the precision of polarisation fraction measurements for extragalactic sources. The analysis of polarised intensity from the reconstruction of Faraday depth spectra yields valuable insights into the evolution of magnetic fields in cosmic web filaments. These results serve as a foundation for further investigations, particularly on the COSMOS and XMM-LSS fields. The accuracy of these measurements is of vital importance for understanding how magnetic fields originate and evolve in the universe. By deepening our understanding of these fundamental aspects, we edge closer to unravelling the mysteries of the origins and development of magnetic fields and their role in shaping the cosmos.

Chapter 7

Future work and conclusions

In this chapter I will discuss recommendations of future work, what is left to do and can we improve in the forthcoming research. Additionally, this chapter presents the final conclusions of this thesis.

7.1 Future work

Potential future improvements to the `cs-romer` framework could include the implementation of a more flexible optimization algorithm such as SDMM (Moolekamp and Melchior, 2018). This addition would allow the framework to further generalize the compressed sensing problem by adding several regularization or constraint functions. Furthermore, although `cs-romer` currently uses the `pywavelets` package to provide discrete and undecimated wavelets, it does not yet include the implementation of continuous wavelets. This enhancement would increase the software's flexibility, enabling users to either incorporate existing continuous wavelets or program their own wavelets to decompose and reconstruct Faraday depth signals. Additionally, while in this thesis I have implemented and adopted the error bound calculation from Carrillo et al., 2014; Pratley et al., 2017, the study of multiple regularizations and their parameters remains an open topic of research. Several studies about regularization parameter selection criteria have been conducted (see e.g. Hansen, 2000; Karl, 2005; Shi et al., 2018). Looking forward, it would be advantageous to implement an L-hypersurface criterion using the fixed-point optimization method from Belge et al., 2002. Since `cs-romer` has been implemented following the object-oriented programming paradigm, users should be able to include these enhancements in a straightforward manner. Given the context of next-generation telescopes and their data-rates, it is critical to incorporate big data and big computing technologies into the `cs-romer` framework. Technologies such as `dask` and `cupy` would not only allow handling large data cubes but also scale them out to clusters and process them using GPUs. An even more challenging and long-term project is the incorporation of RM Synthesis into an aperture synthesis software as in (see e.g. Bell, M.

R. and Enßlin, T. A., 2012). This would permit reconstructing a Faraday depth cube directly from Fourier space, thereby reducing the number of steps currently taken to obtain a Faraday depth cube.

Additionally, the process of time-frequency averaging plays a pivotal role in the pre-processing of radio-interferometric data, often implemented to decrease the volume of datasets, which can become unwieldy due to the vast amount of information generated by modern radio telescopes. However, this method can influence the resulting data in the wavelength-squared space and subsequently affect the reconstruction of Faraday depth spectra. Instead of applying a traditional frequency averaging, a more nuanced approach might involve averaging in the wavelength-squared space. This technique is reminiscent of baseline-dependent averaging (see e.g. Wijnholds et al., 2018; Atemkeng et al., 2018; Deng et al., 2022), respecting the distinct information contributed at each wavelength in a similar way that baseline-dependent averaging considers the unique contribution of each antenna pair. By adopting this wavelength-squared averaging approach, we can mitigate the potential adverse effects on the Faraday depth spectra reconstruction. This method would account for the specific characteristics of data in the wavelength-squared space, ensuring crucial astronomical information remains intact during the data preprocessing phase, all while maintaining the beneficial aspect of data volume reduction.

This work has also spurred new research questions regarding the use of the NUFFT. Just as in image synthesis, it remains unclear whether the application of gridding in λ^2 -space would prove beneficial when reconstructing Faraday depth structures from data. While gridding would decrease the volume of data, as multiple points would be summed into the same cell, it remains to be determined if gridding leads to reconstructions with improved evaluation metrics such as PSNR and RMSE.

Regarding the MeerKAT MIGHTEE-POL survey, considering that I was unable to calculate the 99% percentile threshold for COSMOS, the optimal approach to verify the accuracy of the polarisation detections would be to reproduce the results from the cubes using `cs-romer` and repeat this process for all the fields. In addition, future calibration of MeerKAT data will incorporate full-Stokes A-projection, which will necessitate a complete redo of the analysis from scratch. It is important to note that the data presented in this thesis are based on early science shared risk.

Even though I did not find any polarisation signal in the Abell 1314/IC708 eMERLIN dataset, there is still a need to process the other sources from project CY4234. Perhaps other sources may indeed contain polarisation signals, allowing for better estimations of the magnetic fields of those clusters. Now that I have the parallel-hand, cross-hand, and self-calibration pipelines to pre-process the datasets, this task has become realistically achievable.

7.2 Conclusions

In the course of this thesis, I have devised and implemented the object-oriented framework, *cs-romer*, aimed at reconstructing Faraday depth structures from radio polarimetric data via compressed sensing. This process also involves regularising an under-constrained optimisation problem. In parallel, I have introduced two additional object-oriented frameworks: *ocarina* and *snow*. These frameworks facilitate the calibration of cross-hand correlations for measurement sets from a circular feed, and the self-calibration of parallel-hands, respectively. Moreover, I have adapted the eMERLIN CASA pipeline to integrate with the modular version of CASA.

Throughout the progression of my thesis, I have implemented numerous features within the *cs-romer* framework. Initially, I ensured that the framework could simulate sources directly in frequency (data) space. In addition, I utilized the NUFFT to calculate the values of irregularly spaced λ^2 measurements from regularly spaced Faraday depth during reconstruction. Next, I incorporated a suite of filters for discrete and undecimated wavelet transforms into *cs-romer*, providing the option to combine them with a delta function basis. Furthermore, I integrated a prior that encourages sparsity in Faraday depth space or wavelet space, such as the L1-norm, into *cs-romer*. Additionally, I included convex regularisation functions like Total Variation (TV) and Total Squared Variation (TSV), providing the capability to smooth the reconstructed signal as necessary.

Other optional astrophysical features that I have implemented in this framework are the derotation of the Galactic Faraday rotation, which can be applied directly in wavelength-squared space using external measures of the Galactic foreground. In addition, I have developed the option to correct for the spectral dependency of the radio polarisation data. As it has been shown in Chapter 6, the spectral index has a big impact on the width of the sidelobes of the RMTE, and therefore, this needs to be used with discretion. Direction-dependent spectral index can be provided as a single scalar value or as a map resulting from an MFS deconvolution algorithm such as CASA's *tclean*.

In Chapter 3, I have also demonstrated the *cs-romer* framework for a variety of Faraday depth structures scenarios and under different observational configurations such as different instances of signal-to-noise and RFI flagging. The different simulated scenarios were used to compare different evaluation metrics and select the optimal wavelet basis that best represents the Faraday depth data for a given observational set-up. This selection also depends on the application and the scientific aims of the user. For example, we have seen in Chapter 6 that even though the Daubechies 25 wavelet gave a better PSNR and RMSE, we have chosen the delta wavelet since it helped us to find the RM at the peak with more precision.

Furthermore, in the concluding portion of the chapter, I have made a comparison between Faraday depth spectra reconstructions using the optimally chosen wavelet basis and the widely known RM-CLEAN method. This comparison not only serves as a validation for the efficacy of our proposed framework but also establishes it as a capable alternative to RM-CLEAN. The results from this comparison propose that our *cs-romer*

framework can indeed compete with RM-CLEAN, and thus, it introduces a promising prospect in the domain of Faraday depth spectra reconstruction.

I have demonstrated the *cs-romer* framework on real data from the JVLA telescope towards the low-mass galaxy cluster Abell 1314 in Chapter 4. By using the optimal basis function determined in Chapter 3, incorporating the de-rotation of the Galactic foreground and a direction-dependant spectral index map I was able to analyse Faraday depth spectra on individual galaxies within Abell 1314. These galaxies show a behaviour that deviates from what is expected for a Faraday-thin screen. This suggests the galaxies in this cluster, most noticeably IC 708, suffer a Faraday rotation that is dominated by local magneto-ionic structures rather than the large-scale intra-cluster medium.

Even though no significant polarisation signal was detected in Chapter 5, I have demonstrated the parallel-hand and cross-hand calibration using the modified CASA eMERLIN pipeline and the *ocarina* framework. Additionally, I have shown the importance of using a self-calibration framework such as *snow* when pre-processing a dataset, especially when the signal-to-noise ratio is low after parallel-hand calibration as in the eMERLIN Abell 1314 case. We have also shown that the framework was able to improve the PSNR of the dataset from 91.7 to 524.7.

In Chapter 6 I applied the *cs-romer* framework to real data from the MeerKAT telescope, specifically on the COSMOS field. I have analysed a catalog with in-source sources and compared the polarised intensity values using the dirty and reconstructed Faraday spectra. Reconstructed Faraday depth spectra values from the framework are able to correct for those outliers seen with the dirty. These outcomes lay the foundation for future investigations that concentrate on examining the behavior of the RM and polarisation fraction as a function of redshift within the COSMOS and XMM-LSS fields. The accuracy of these measurements is of crucial importance in comprehending the genesis and progression of magnetic fields in the universe.

Finally, the frameworks developed for this thesis work are a first step with respect to next-generation telescopes and the SKA. We have already seen that RM Synthesis is a much more under-constrained problem than image synthesis, and therefore, regularisation for Faraday depth spectra along with compressed-sensing are a must when analysing and studying magnetic fields using this technique on wide field and VLBI images. Looking to the future, the data-rates, angular and spectral resolution of next-generation telescopes, we aim to incorporate big data and big computing technologies into these frameworks to be able to process forthcoming datasets.

Bibliography

- A. Richard Thompson James M. Moran, George W. Swenson Jr. (2004a). *Interferometry and Synthesis in Radio Astronomy*. Weinheim: WILEY-VCH Verlag GmbH & Co. KGaA.
- (2004b). *Interferometry and Synthesis in Radio Astronomy*. Weinheim: WILEY-VCH Verlag GmbH & Co. KGaA.
- Akahori, Takuya and Dongsu Ryu (Aug. 2011). “FARADAY ROTATION MEASURE DUE TO THE INTERGALACTIC MAGNETIC FIELD. II. THE COSMOLOGICAL CONTRIBUTION”. In: *The Astrophysical Journal* 738.2, p. 134. DOI: [10.1088/0004-637X/738/2/134](https://doi.org/10.1088/0004-637X/738/2/134). URL: <https://dx.doi.org/10.1088/0004-637X/738/2/134>.
- Akiyama, Kazunori et al. (Mar. 2017a). “Imaging the Schwarzschild-radius-scale Structure of M87 with the Event Horizon Telescope Using Sparse Modeling”. In: *The Astrophysical Journal* 838.1, p. 1. DOI: [10.3847/1538-4357/aa6305](https://doi.org/10.3847/1538-4357/aa6305). URL: <https://dx.doi.org/10.3847/1538-4357/aa6305>.
- Akiyama, Kazunori et al. (Mar. 2017b). “Superresolution Full-polarimetric Imaging for Radio Interferometry with Sparse Modeling”. In: *The Astronomical Journal* 153.4, p. 159. DOI: [10.3847/1538-3881/aa6302](https://doi.org/10.3847/1538-3881/aa6302). URL: <https://doi.org/10.3847/1538-3881/aa6302>.
- Akiyama, Kazunori et al. (2018). *Faraday Tomography with Sparse Modeling*. arXiv: [1811.10610](https://arxiv.org/abs/1811.10610) [astro-ph.IM].
- Andrecut, M., J. M. Stil, and A. R. Taylor (Dec. 2011). “SPARSE FARADAY ROTATION MEASURE SYNTHESIS”. In: *The Astronomical Journal* 143.2, p. 33. DOI: [10.1088/0004-6256/143/2/33](https://doi.org/10.1088/0004-6256/143/2/33). URL: <https://doi.org/10.1088/0004-6256/143/2/33>.
- “Appendix E: Model Selection Criterion: AIC and BIC” (2014). In: *The Basics of Financial Econometrics*. John Wiley & Sons, Ltd, pp. 399–403. ISBN: 9781118856406. DOI: <https://doi.org/10.1002/9781118856406.app5>. eprint: <https://onlinelibrary.wiley.com/doi/pdf/10.1002/9781118856406.app5>. URL: <https://onlinelibrary.wiley.com/doi/abs/10.1002/9781118856406.app5>.
- Arnaud, K. A. (Jan. 1996). “XSPEC: The First Ten Years”. In: *Astronomical Data Analysis Software and Systems V*. Ed. by George H. Jacoby and Jeannette Barnes. Vol. 101. Astronomical Society of the Pacific Conference Series, p. 17.
- Arámburo-García, Andrés et al. (June 2021). “Magnetization of the intergalactic medium in the IllustrisTNG simulations: the importance of extended, outflow-driven bubbles”. In: *Monthly Notices of the Royal Astronomical Society* 505.4, pp. 5038–5057. ISSN: 0035-8711. DOI: [10.1093/mnras/stab1632](https://doi.org/10.1093/mnras/stab1632). eprint: <https://academic.oup.com/>

- [mnras/article-pdf/505/4/5038/38836682/stab1632.pdf](https://doi.org/10.1093/mnras/stab1632). URL: <https://doi.org/10.1093/mnras/stab1632>.
- Asad, K M B et al. (Jan. 2021). “Primary beam effects of radio astronomy antennas – II. Modelling MeerKAT L-band beams”. In: *Monthly Notices of the Royal Astronomical Society* 502.2, pp. 2970–2983. ISSN: 0035-8711. DOI: [10.1093/mnras/stab104](https://doi.org/10.1093/mnras/stab104). eprint: <https://academic.oup.com/mnras/article-pdf/502/2/2970/36276175/stab104.pdf>. URL: <https://doi.org/10.1093/mnras/stab104>.
- Atemkeng, M et al. (Mar. 2018). “Baseline-dependent sampling and windowing for radio interferometry: data compression, field-of-interest shaping, and outer field suppression”. In: *Monthly Notices of the Royal Astronomical Society* 477.4, pp. 4511–4523. ISSN: 0035-8711. DOI: [10.1093/mnras/sty668](https://doi.org/10.1093/mnras/sty668). eprint: <https://academic.oup.com/mnras/article-pdf/477/4/4511/24831946/sty668.pdf>. URL: <https://doi.org/10.1093/mnras/sty668>.
- Bajkova, A. T. (Nov. 2008). “Multi-frequency synthesis of VLBI images using a generalized maximum entropy method”. In: *Astronomy Reports* 52.12, p. 951. ISSN: 1562-6881. DOI: [10.1134/S1063772908120019](https://doi.org/10.1134/S1063772908120019). URL: <https://doi.org/10.1134/S1063772908120019>.
- Bajkova, Anisa T. and Alexander B. Pushkarev (2011). “Multifrequency synthesis algorithm based on the generalized maximum entropy method: application to 0954+658”. In: *Monthly Notices of the Royal Astronomical Society* 417.1, pp. 434–443. DOI: [10.1111/j.1365-2966.2011.19280.x](https://doi.org/10.1111/j.1365-2966.2011.19280.x). URL: <http://dx.doi.org/10.1111/j.1365-2966.2011.19280.x>.
- Bauer, Frank and Mark A. Lukas (2011). “Comparing parameter choice methods for regularization of ill-posed problems”. In: *Mathematics and Computers in Simulation* 81.9, pp. 1795–1841. ISSN: 0378-4754. DOI: <https://doi.org/10.1016/j.matcom.2011.01.016>. URL: <https://www.sciencedirect.com/science/article/pii/S0378475411000607>.
- Beck, A. and M. Teboulle (2009a). “A Fast Iterative Shrinkage-Thresholding Algorithm for Linear Inverse Problems”. In: *SIAM Journal on Imaging Sciences* 2.1, pp. 183–202. DOI: [10.1137/080716542](https://doi.org/10.1137/080716542). eprint: <https://doi.org/10.1137/080716542>. URL: <https://doi.org/10.1137/080716542>.
- Beck, Amir and Marc Teboulle (Nov. 2009b). “Fast Gradient-Based Algorithms for Constrained Total Variation Image Denoising and Deblurring Problems”. In: *IEEE Transactions on Image Processing* 18.11, pp. 2419–2434. ISSN: 1941-0042. DOI: [10.1109/TIP.2009.2028250](https://doi.org/10.1109/TIP.2009.2028250).
- Belge, Murat, Misha E Kilmer, and Eric L Miller (July 2002). “Efficient determination of multiple regularization parameters in a generalized L-curve framework”. In: *Inverse Problems* 18.4, pp. 1161–1183. DOI: [10.1088/0266-5611/18/4/314](https://doi.org/10.1088/0266-5611/18/4/314). URL: <https://doi.org/10.1088/0266-5611/18/4/314>.
- Bell, M. R. and Enßlin, T. A. (2012). “Faraday synthesis - The synergy of aperture and rotation measure synthesis”. In: *A&A* 540, A80. DOI: [10.1051/0004-6361/201118672](https://doi.org/10.1051/0004-6361/201118672). URL: <https://doi.org/10.1051/0004-6361/201118672>.

- Berger, A. et al. (2021). “Faint polarised sources in the Lockman Hole field at 1.4 GHz”. In: *A&A* 653, A155. DOI: [10.1051/0004-6361/202040009](https://doi.org/10.1051/0004-6361/202040009). URL: <https://doi.org/10.1051/0004-6361/202040009>.
- Blumensath, Thomas and Mike E. Davies (2009). “Iterative hard thresholding for compressed sensing”. In: *Applied and Computational Harmonic Analysis* 27.3, pp. 265–274. ISSN: 1063-5203. DOI: <https://doi.org/10.1016/j.acha.2009.04.002>. URL: <http://www.sciencedirect.com/science/article/pii/S1063520309000384>.
- Bonafede, A. et al. (July 2022). “The Coma Cluster at LOFAR Frequencies. II. The Halo, Relic, and a New Accretion Relic”. In: *The Astrophysical Journal* 933.2, p. 218. DOI: [10.3847/1538-4357/ac721d](https://doi.org/10.3847/1538-4357/ac721d). URL: <https://dx.doi.org/10.3847/1538-4357/ac721d>.
- Bonafede, A. et al. (2009). “Double relics in Abell 2345 and Abell 1240 - Spectral index and polarization analysis”. In: *A&A* 494.2, pp. 429–442. DOI: [10.1051/0004-6361:200810588](https://doi.org/10.1051/0004-6361:200810588). URL: <https://doi.org/10.1051/0004-6361:200810588>.
- Bonafede, A. et al. (2010). “The Coma cluster magnetic field from Faraday rotation measures”. In: *A&A* 513, A30. DOI: [10.1051/0004-6361/200913696](https://doi.org/10.1051/0004-6361/200913696). URL: <https://doi.org/10.1051/0004-6361/200913696>.
- Boyd, Stephen et al. (Jan. 2011). “Distributed Optimization and Statistical Learning via the Alternating Direction Method of Multipliers”. In: *Found. Trends Mach. Learn.* 3.1, pp. 1–122. ISSN: 1935-8237. DOI: [10.1561/22000000016](https://doi.org/10.1561/22000000016). URL: <http://dx.doi.org/10.1561/22000000016>.
- Brentjens, M. A. and de Bruyn, A. G. (2005). “Faraday rotation measure synthesis”. In: *A&A* 441.3, pp. 1217–1228. DOI: [10.1051/0004-6361:20052990](https://doi.org/10.1051/0004-6361:20052990). URL: <https://doi.org/10.1051/0004-6361:20052990>.
- Burke, Bernard F., Francis Graham-Smith, and Peter N. Wilkinson (2019). *An Introduction to Radio Astronomy*. 4th ed. Cambridge University Press. DOI: [10.1017/9781316987506](https://doi.org/10.1017/9781316987506).
- Burn, B. J. (July 1966). “On the Depolarization of Discrete Radio Sources by Faraday Dispersion”. In: *Monthly Notices of the Royal Astronomical Society* 133.1, pp. 67–83. ISSN: 0035-8711. DOI: [10.1093/mnras/133.1.67](https://doi.org/10.1093/mnras/133.1.67). eprint: <http://oup.prod.sis.lan/mnras/article-pdf/133/1/67/8078603/mnras133-0067.pdf>. URL: <https://dx.doi.org/10.1093/mnras/133.1.67>.
- Cai, T. T. and L. Wang (July 2011). “Orthogonal Matching Pursuit for Sparse Signal Recovery With Noise”. In: *IEEE Transactions on Information Theory* 57.7, pp. 4680–4688. ISSN: 0018-9448. DOI: [10.1109/TIT.2011.2146090](https://doi.org/10.1109/TIT.2011.2146090).
- Candes, E. J. and T. Tao (Dec. 2006). “Near-Optimal Signal Recovery From Random Projections: Universal Encoding Strategies?” In: *IEEE Transactions on Information Theory* 52.12, pp. 5406–5425. ISSN: 0018-9448. DOI: [10.1109/TIT.2006.885507](https://doi.org/10.1109/TIT.2006.885507).
- Candes, Emmanuel J. and Michael B. Wakin (2008). “An Introduction To Compressive Sampling”. In: *IEEE Signal Processing Magazine* 25.2, pp. 21–30. DOI: [10.1109/MSP.2007.914731](https://doi.org/10.1109/MSP.2007.914731).
- Cantwell, T. M. et al. (June 2020). “Low-frequency observations of the giant radio galaxy NGC 6251”. In: *Monthly Notices of the RAS* 495.1, pp. 143–159. DOI: [10.1093/mnras/staa1160](https://doi.org/10.1093/mnras/staa1160). arXiv: [2004.11104](https://arxiv.org/abs/2004.11104) [astro-ph.GA].

- Carretti, E et al. (Oct. 2022a). “Magnetic field evolution in cosmic filaments with LOFAR data”. In: *Monthly Notices of the Royal Astronomical Society* 518.2, pp. 2273–2286. ISSN: 0035-8711. DOI: [10.1093/mnras/stac2966](https://doi.org/10.1093/mnras/stac2966). eprint: <https://academic.oup.com/mnras/article-pdf/518/2/2273/47266691/stac2966.pdf>. URL: <https://doi.org/10.1093/mnras/stac2966>.
- Carretti, Ettore et al. (Feb. 2022b). “Magnetic field strength in cosmic web filaments”. In: *Monthly Notices of the Royal Astronomical Society* 512.1, pp. 945–959. ISSN: 0035-8711. DOI: [10.1093/mnras/stac384](https://doi.org/10.1093/mnras/stac384). eprint: <https://academic.oup.com/mnras/article-pdf/512/1/945/42947737/stac384.pdf>. URL: <https://doi.org/10.1093/mnras/stac384>.
- Carrillo, R. E., J. D. McEwen, and Y. Wiaux (Oct. 2012). “Sparsity Averaging Reweighted Analysis (SARA): a novel algorithm for radio-interferometric imaging”. In: *Monthly Notices of the Royal Astronomical Society* 426, pp. 1223–1234. DOI: [10.1111/j.1365-2966.2012.21605.x](https://doi.org/10.1111/j.1365-2966.2012.21605.x). arXiv: [1205.3123](https://arxiv.org/abs/1205.3123) [astro-ph.IM].
- (Apr. 2014). “PURIFY: a new approach to radio-interferometric imaging”. In: *Monthly Notices of the Royal Astronomical Society* 439, pp. 3591–3604. DOI: [10.1093/mnras/stu202](https://doi.org/10.1093/mnras/stu202). arXiv: [1307.4370](https://arxiv.org/abs/1307.4370) [astro-ph.IM].
- Carroll, Bradley W. and Dale A. Ostlie (2007). *An Introduction to Modern Astrophysics*. Ed. by San Francisco: Pearson Addison-Wesley. 2nd (International).
- Casadio, Carolina et al. (2017). “3 mm GMVA Observations of Total and Polarized Emission from Blazar and Radio Galaxy Core Regions”. In: *Galaxies* 5.4. ISSN: 2075-4434. DOI: [10.3390/galaxies5040067](https://doi.org/10.3390/galaxies5040067). URL: <https://www.mdpi.com/2075-4434/5/4/67>.
- Casassus, S. et al. (2015). “A compact concentration of large grains in the HD142527 protoplanetary dust trap”. In: *The Astrophysical Journal* 0.0, p. 10.
- Casassus, Simon et al. (2018). “An inner warp in the DoAr 44 T Tauri transition disk”. In: *Monthly Notices of the Royal Astronomical Society*, sty894. DOI: [10.1093/mnras/sty894](https://doi.org/10.1093/mnras/sty894).
- Chael, Andrew A. et al. (Apr. 2018). “Interferometric Imaging Directly with Closure Phases and Closure Amplitudes”. In: *The Astrophysical Journal* 857.1, p. 23. DOI: [10.3847/1538-4357/aab6a8](https://doi.org/10.3847/1538-4357/aab6a8). URL: <https://doi.org/10.3847/1538-4357/aab6a8>.
- Cieza, Lucas A. et al. (Dec. 2017). “ALMA Observations of Elias 2–24: A Protoplanetary Disk with Multiple Gaps in the Ophiuchus Molecular Cloud”. In: *The Astrophysical Journal Letters* 851.2, p. L23.
- Collaboration, The Event Horizon Telescope et al. (Mar. 2021). “First M87 Event Horizon Telescope Results. VII. Polarization of the Ring”. In: *The Astrophysical Journal Letters* 910.1, p. L12. DOI: [10.3847/2041-8213/abe71d](https://doi.org/10.3847/2041-8213/abe71d). URL: <https://dx.doi.org/10.3847/2041-8213/abe71d>.
- Conway, J. E., T. J. Cornwell, and P. N. Wilkinson (Oct. 1990). “Multi-Frequency Synthesis - a New Technique in Radio Interferometric Imaging”. In: *Monthly Notices of the Royal Astronomical Society* 246, p. 490.
- Cooray, Suchetha et al. (Nov. 2020). “An iterative reconstruction algorithm for Faraday tomography”. In: *Monthly Notices of the Royal Astronomical Society* 500.4, 5129–5141.

- ISSN: 1365-2966. DOI: [10.1093/mnras/staa3580](https://doi.org/10.1093/mnras/staa3580). URL: <http://dx.doi.org/10.1093/mnras/staa3580>.
- Cornwell, T. J. (Oct. 2008). "Multiscale CLEAN Deconvolution of Radio Synthesis Images". In: *IEEE Journal of Selected Topics in Signal Processing* 2.5, pp. 793–801. ISSN: 1932-4553. DOI: [10.1109/JSTSP.2008.2006388](https://doi.org/10.1109/JSTSP.2008.2006388).
- Cornwell, T. J. and K. F. Evans (Feb. 1985). "A simple maximum entropy deconvolution algorithm". In: *Astronomy and Astrophysics* 143, pp. 77–83.
- Cotton, W. D. (2012). "A new method for cross polarized delay calibration of radio interferometers". In: *Journal of Astronomical Instrumentation* 01.01, p. 1250001. DOI: [10.1142/S2251171712500018](https://doi.org/10.1142/S2251171712500018). eprint: <https://doi.org/10.1142/S2251171712500018>. URL: <https://doi.org/10.1142/S2251171712500018>.
- Cuciti, V. et al. (2021). "Radio halos in a mass-selected sample of 75 galaxy clusters - I. Sample selection and data analysis". In: *A&A* 647, A50. DOI: [10.1051/0004-6361/202039206](https://doi.org/10.1051/0004-6361/202039206). URL: <https://doi.org/10.1051/0004-6361/202039206>.
- Cárcamo, M. et al. (2018). "Multi-GPU maximum entropy image synthesis for radio astronomy". In: *Astronomy and Computing* 22, pp. 16–27. ISSN: 2213-1337. DOI: <https://doi.org/10.1016/j.ascom.2017.11.003>. URL: <http://www.sciencedirect.com/science/article/pii/S2213133717300094>.
- Daubechies, I. (1992). *Ten Lectures on Wavelets*. Society for Industrial and Applied Mathematics. DOI: [10.1137/1.9781611970104](https://doi.org/10.1137/1.9781611970104). eprint: <http://epubs.siam.org/doi/pdf/10.1137/1.9781611970104>. URL: <http://epubs.siam.org/doi/abs/10.1137/1.9781611970104>.
- Daubechies, I. et al. (1992). *Ten Lectures on Wavelets*. CBMS-NSF Regional Conference Series in Applied Mathematics. Society for Industrial and Applied Mathematics. ISBN: 9780898712742. URL: <https://books.google.cl/books?id=9t5SG06AiTOC>.
- Deng, Qing-Wen et al. (Mar. 2022). "Performance Evaluation of Baseline-dependent Averaging Based on Full-scale SKA1-LOW Simulation". In: *Research in Astronomy and Astrophysics* 22.4, p. 045014. DOI: [10.1088/1674-4527/ac56cd](https://doi.org/10.1088/1674-4527/ac56cd). URL: <https://dx.doi.org/10.1088/1674-4527/ac56cd>.
- Ding, Jie, Vahid Tarokh, and Yuhong Yang (2018). "Model Selection Techniques: An Overview". In: *IEEE Signal Processing Magazine* 35.6, pp. 16–34. DOI: [10.1109/MSP.2018.2867638](https://doi.org/10.1109/MSP.2018.2867638).
- Donoho, D. L. (Apr. 2006). "Compressed Sensing". In: *IEEE Trans. Inf. Theor.* 52.4, pp. 1289–1306. ISSN: 0018-9448. DOI: [10.1109/TIT.2006.871582](https://doi.org/10.1109/TIT.2006.871582). URL: <https://doi.org/10.1109/TIT.2006.871582>.
- Donoho, D. L. et al. (1992). "Maximum Entropy and the Nearly Black Object". In: *Journal of the Royal Statistical Society* 54.1.
- Elad, M. et al. (2007). "A wide-angle view at iterated shrinkage algorithms". In: *Wavelets XII*. Ed. by Dimitri Van De Ville, Vivek K. Goyal, and Manos Papadakis. Vol. 6701. International Society for Optics and Photonics. SPIE, p. 670102. DOI: [10.1117/12.741299](https://doi.org/10.1117/12.741299). URL: <https://doi.org/10.1117/12.741299>.
- Faraday, Michael (2012). *Experimental Researches in Electricity*. Vol. 3. Cambridge Library Collection - Physical Sciences. Cambridge University Press. DOI: [10.1017/CB09781139383165](https://doi.org/10.1017/CB09781139383165).

- Feretti, L. et al. (Oct. 1995). "The magnetic field in the Coma cluster". In: *A&A* 302, p. 680. DOI: [10.48550/arXiv.astro-ph/9504058](https://doi.org/10.48550/arXiv.astro-ph/9504058). URL: <https://doi.org/10.48550/arXiv.astro-ph/9504058>.
- Feretti, L. et al. (2001). "The giant radio halo in Abell 2163". In: *A&A* 373.1, pp. 106–112. DOI: [10.1051/0004-6361:20010581](https://doi.org/10.1051/0004-6361:20010581). URL: <https://doi.org/10.1051/0004-6361:20010581>.
- Fessler, J.A. and B.P. Sutton (2003). "Nonuniform fast Fourier transforms using min-max interpolation". In: *IEEE Transactions on Signal Processing* 51.2, pp. 560–574. DOI: [10.1109/TSP.2002.807005](https://doi.org/10.1109/TSP.2002.807005).
- Flatters, C. (Apr. 1987). "MERLIN polarization observations of the quasar 3C380". In: *Nature* 326.6114, pp. 683–684. ISSN: 1476-4687. DOI: [10.1038/326683a0](https://doi.org/10.1038/326683a0). URL: <https://doi.org/10.1038/326683a0>.
- Frick, P. et al. (Jan. 2010). "Wavelet-based Faraday rotation measure synthesis". In: *Monthly Notices of the Royal Astronomical Society: Letters* 401.1, pp. L24–L28. ISSN: 1745-3925. DOI: [10.1111/j.1745-3933.2009.00778.x](https://doi.org/10.1111/j.1745-3933.2009.00778.x). eprint: <https://academic.oup.com/mnrasl/article-pdf/401/1/L24/6140341/401-1-L24.pdf>. URL: <https://doi.org/10.1111/j.1745-3933.2009.00778.x>.
- Gabuzda, D. C. and V. A. Chernetskii (Mar. 2003). "Parsec-scale Faraday rotation distribution in the BL Lac object 1803+784". In: *Monthly Notices of the Royal Astronomical Society* 339.3, pp. 669–679. ISSN: 0035-8711. DOI: [10.1046/j.1365-8711.2003.06204.x](https://doi.org/10.1046/j.1365-8711.2003.06204.x). eprint: <https://academic.oup.com/mnras/article-pdf/339/3/669/2925041/339-3-669.pdf>. URL: <https://doi.org/10.1046/j.1365-8711.2003.06204.x>.
- Gaensler, B.M., R. Beck, and L. Feretti (2004). "The origin and evolution of cosmic magnetism". In: *New Astronomy Reviews* 48.11. Science with the Square Kilometre Array, pp. 1003–1012. ISSN: 1387-6473. DOI: <https://doi.org/10.1016/j.newar.2004.09.003>. URL: <https://www.sciencedirect.com/science/article/pii/S1387647304000910>.
- Garsden, H. et al. (Mar. 2015). "LOFAR sparse image reconstruction". In: *Astronomy & Astrophysics* 575, A90, A90. DOI: [10.1051/0004-6361/201424504](https://doi.org/10.1051/0004-6361/201424504). arXiv: [1406.7242](https://arxiv.org/abs/1406.7242) [astro-ph.IM].
- George, Samuel J., Jeroen M. Stil, and Ben W. Keller (2012). "Detection Thresholds and Bias Correction in Polarized Intensity". In: *Publications of the Astronomical Society of Australia* 29.3, 214–220. DOI: [10.1071/AS11027](https://doi.org/10.1071/AS11027).
- Golilarz, Noorbakhsh Amiri and Hasan Demirel (2017). "Image de-noising using undecimated wavelet transform (UWT) with soft thresholding technique". In: *2017 9th International Conference on Computational Intelligence and Communication Networks (CICN)*, pp. 16–19. DOI: [10.1109/CICN.2017.8319347](https://doi.org/10.1109/CICN.2017.8319347).
- Govoni, F. et al. (2001). "Radio galaxies and magnetic fields in A514". In: *A&A* 379.3, pp. 807–822. DOI: [10.1051/0004-6361:20011355](https://doi.org/10.1051/0004-6361:20011355). URL: <https://doi.org/10.1051/0004-6361:20011355>.
- Griffiths, David J. (2017). *Introduction to Electrodynamics*. 4th ed. Cambridge University Press. DOI: [10.1017/9781108333511](https://doi.org/10.1017/9781108333511).

- Haar, Alfred (Sept. 1910). "Zur Theorie der orthogonalen Funktionensysteme". In: *Mathematische Annalen* 69.3, pp. 331–371. ISSN: 1432-1807. DOI: [10.1007/BF01456326](https://doi.org/10.1007/BF01456326). URL: <https://doi.org/10.1007/BF01456326>.
- Hansen, Per Christian (2000). "The L-Curve and its Use in the Numerical Treatment of Inverse Problems". In: *Computational Inverse Problems in Electrocardiology*, ed. P. Johnston, *Advances in Computational Bioengineering*. WIT Press, pp. 119–142.
- Heald, G. (Apr. 2009). "The Faraday rotation measure synthesis technique". In: *Cosmic Magnetic Fields: From Planets, to Stars and Galaxies*. Ed. by K. G. Strassmeier, A. G. Kosovichev, and J. E. Beckman. Vol. 259. IAU Symposium, pp. 591–602. DOI: [10.1017/S1743921309031421](https://doi.org/10.1017/S1743921309031421).
- Heywood, I. and M. J. Jarvis et al. (2021). "MIGHTEE: total intensity radio continuum imaging and the COSMOS / XMM-LSS Early Science fields". English. In: *Monthly Notices of the Royal Astronomical Society* 509, 2150–2168. ISSN: 0035-8711.
- HI4PI Collaboration: et al. (2016). "HI4PI: a full-sky Hurvey based on EBHIS and GASS". In: *A&A* 594, A116. DOI: [10.1051/0004-6361/201629178](https://doi.org/10.1051/0004-6361/201629178). URL: <https://doi.org/10.1051/0004-6361/201629178>.
- Hogbom, J. A (1974). "Aperture Synthesis with a Non-Regular Distribution of Interferometer Baselines". In: *Astron. Astrophys. Suppl. Ser.* 15, pp. 417–426.
- Hovatta, Talvikki et al. (Sept. 2012). "MOJAVE: MONITORING OF JETS IN ACTIVE GALACTIC NUCLEI WITH VLBA EXPERIMENTS. VIII. FARADAY ROTATION IN PARSEC-SCALE AGN JETS". In: *The Astronomical Journal* 144.4, p. 105. DOI: [10.1088/0004-6256/144/4/105](https://doi.org/10.1088/0004-6256/144/4/105). URL: <https://dx.doi.org/10.1088/0004-6256/144/4/105>.
- Hurvich, Clifford M., Jeffrey S. Simonoff, and Chih-Ling Tsai (Jan. 2002). "Smoothing Parameter Selection in Nonparametric Regression Using an Improved Akaike Information Criterion". In: *Journal of the Royal Statistical Society Series B: Statistical Methodology* 60.2, pp. 271–293. ISSN: 1369-7412. DOI: [10.1111/1467-9868.00125](https://doi.org/10.1111/1467-9868.00125). eprint: https://academic.oup.com/jrsssb/article-pdf/60/2/271/49589041/jrsssb_60_2_271.pdf. URL: <https://doi.org/10.1111/1467-9868.00125>.
- Hurvich, Clifford M. and Chih-Ling Tsai (June 1989). "Regression and time series model selection in small samples". In: *Biometrika* 76.2, pp. 297–307. ISSN: 0006-3444. DOI: [10.1093/biomet/76.2.297](https://doi.org/10.1093/biomet/76.2.297). eprint: <https://academic.oup.com/biomet/article-pdf/76/2/297/737009/76-2-297.pdf>. URL: <https://doi.org/10.1093/biomet/76.2.297>.
- Hutschenreuter, S. et al. (Jan. 2022). "The Galactic Faraday rotation sky 2020". In: *Astronomy and Astrophysics* 657, A43, A43. DOI: [10.1051/0004-6361/202140486](https://doi.org/10.1051/0004-6361/202140486). arXiv: [2102.01709](https://arxiv.org/abs/2102.01709) [astro-ph.GA].
- Iacobelli, M., M. Haverkorn, and P. Katgert (Jan. 2013). "Rotation measure synthesis at the 2 m wavelength of the FAN region: unveiling screens and bubbles". In: *Astronomy and Astrophysics* 549, A56, A56. DOI: [10.1051/0004-6361/201220175](https://doi.org/10.1051/0004-6361/201220175). arXiv: [1210.6801](https://arxiv.org/abs/1210.6801) [astro-ph.GA].

- Ideguchi, Shinsuke et al. (Aug. 2014). "FARADAY DISPERSION FUNCTIONS OF GALAXIES". In: *The Astrophysical Journal* 792.1, p. 51. DOI: [10.1088/0004-637x/792/1/51](https://doi.org/10.1088/0004-637x/792/1/51). URL: <https://doi.org/10.1088/0004-637x/792/1/51>.
- Jackson, J. D. (2003). "Electrodynamics, Classical". In: *digital Encyclopedia of Applied Physics*. John Wiley & Sons, Ltd. ISBN: 9783527600434. DOI: <https://doi.org/10.1002/3527600434.eap109>. eprint: <https://onlinelibrary.wiley.com/doi/pdf/10.1002/3527600434.eap109>. URL: <https://onlinelibrary.wiley.com/doi/abs/10.1002/3527600434.eap109>.
- Jagannathan, P. et al. (Aug. 2017). "Direction-dependent Corrections in Polarimetric Radio Imaging. I. Characterizing the Effects of the Primary Beam on Full-Stokes Imaging". In: *Astronomical Journal* 154.2, 56, p. 56. DOI: [10.3847/1538-3881/aa77f8](https://doi.org/10.3847/1538-3881/aa77f8). arXiv: [1706.01501](https://arxiv.org/abs/1706.01501) [astro-ph.IM].
- Jarvis, Matt and Russ Taylor et al. (2016). "The MeerKAT International GHz Tiered Extragalactic Exploration (MIGHTEE) Survey". In: *Proceedings of Science MeerKAT Science: On the Pathway to the SKA*, Stellenbosch, 25-27 May 2016, p. 6. DOI: [10.22323/1.277.0006](https://doi.org/10.22323/1.277.0006).
- Kandus, Alejandra, Kerstin E. Kunze, and Christos G. Tsagas (2011). "Primordial magnetogenesis". In: *Physics Reports* 505.1, pp. 1–58. ISSN: 0370-1573. DOI: <https://doi.org/10.1016/j.physrep.2011.03.001>. URL: <https://www.sciencedirect.com/science/article/pii/S0370157311000536>.
- Karl, W.Clem (2005). "3.6 - Regularization in Image Restoration and Reconstruction". In: *Handbook of Image and Video Processing (Second Edition)*. Ed. by AL BOVIK. Second Edition. Communications, Networking and Multimedia. Burlington: Academic Press, pp. 183–V. ISBN: 978-0-12-119792-6. DOI: <https://doi.org/10.1016/B978-012119792-6/50075-9>. URL: <https://www.sciencedirect.com/science/article/pii/B9780121197926500759>.
- Knowles, K. et al. (2022). "The MeerKAT Galaxy Cluster Legacy Survey - I. Survey Overview and Highlights". In: *A&A* 657, A56. DOI: [10.1051/0004-6361/202141488](https://doi.org/10.1051/0004-6361/202141488). URL: <https://doi.org/10.1051/0004-6361/202141488>.
- Kowalski, Matthieu (2014). "Thresholding RULES and iterative shrinkage/thresholding algorithm: A convergence study". In: *2014 IEEE International Conference on Image Processing (ICIP)*, pp. 4151–4155. DOI: [10.1109/ICIP.2014.7025843](https://doi.org/10.1109/ICIP.2014.7025843).
- Krahmer, Felix, Christian Kruschel, and Michael Sandbichler (2017). "Total Variation Minimization in Compressed Sensing". In: *Compressed Sensing and its Applications: Second International MATHEON Conference 2015*. Ed. by Holger Boche et al. Cham: Springer International Publishing, pp. 333–358. ISBN: 978-3-319-69802-1. DOI: [10.1007/978-3-319-69802-1_11](https://doi.org/10.1007/978-3-319-69802-1_11). URL: https://doi.org/10.1007/978-3-319-69802-1_11.
- Kronberg, P. P. et al. (Mar. 2008). "A Global Probe of Cosmic Magnetic Fields to High Redshifts". In: *The Astrophysical Journal* 676.1, p. 70. DOI: [10.1086/527281](https://doi.org/10.1086/527281). URL: <https://dx.doi.org/10.1086/527281>.
- Kuramochi, Kazuki et al. (May 2018). "Superresolution Interferometric Imaging with Sparse Modeling Using Total Squared Variation: Application to Imaging the Black

- Hole Shadow". In: *The Astrophysical Journal* 858.1, p. 56. DOI: [10.3847/1538-4357/aab6b5](https://doi.org/10.3847/1538-4357/aab6b5). URL: <https://dx.doi.org/10.3847/1538-4357/aab6b5>.
- Lannes, A., E. Anterrieu, and P. Marechal (May 1997). "Clean and Wipe". In: *Astronomy and Astrophysics* 123, pp. 183–198.
- Ledlow, Michael J. et al. (Dec. 2003). "The X-Ray Properties of Nearby Abell Clusters from the ROSAT All-Sky Survey: The Sample and Correlations with Optical Properties". In: *The Astronomical Journal* 126.6, p. 2740. DOI: [10.1086/379670](https://doi.org/10.1086/379670). URL: <https://dx.doi.org/10.1086/379670>.
- Lee, Gregory R. et al. (2019). "PyWavelets: A Python package for wavelet analysis". In: *Journal of Open Source Software* 4.36, p. 1237. DOI: [10.21105/joss.01237](https://doi.org/10.21105/joss.01237). URL: <https://doi.org/10.21105/joss.01237>.
- Li, F., Cornwell, T. J., and de Hoog, F. (2011a). "The application of compressive sampling to radio astronomy - I. Deconvolution". In: *A&A* 528, A31. DOI: [10.1051/0004-6361/201015045](https://doi.org/10.1051/0004-6361/201015045). URL: <https://doi.org/10.1051/0004-6361/201015045>.
- Li, F. et al. (2011b). "The application of compressive sampling to radio astronomy - II. Faraday rotation measure synthesis". In: *A&A* 531, A126. DOI: [10.1051/0004-6361/201015890](https://doi.org/10.1051/0004-6361/201015890). URL: <https://doi.org/10.1051/0004-6361/201015890>.
- Lin, Jyh-Miin (2018). "Python Non-Uniform Fast Fourier Transform (PyNUFFT): An Accelerated Non-Cartesian MRI Package on a Heterogeneous Platform (CPU/GPU)". In: *Journal of Imaging* 4.3. ISSN: 2313-433X. DOI: [10.3390/jimaging4030051](https://doi.org/10.3390/jimaging4030051). URL: <https://www.mdpi.com/2313-433X/4/3/51>.
- Lin, Yen-Ting and Joseph J. Mohr (Dec. 2004). "K-band Properties of Galaxy Clusters and Groups: Brightest Cluster Galaxies and Intracluster Light". In: *Astrophysical Journal* 617.2, pp. 879–895. DOI: [10.1086/425412](https://doi.org/10.1086/425412). arXiv: [astro-ph/0408557](https://arxiv.org/abs/astro-ph/0408557) [astro-ph].
- Lüdke, E. et al. (Sept. 1998). "MERLIN polarization observations of compact steep-spectrum sources at 5 GHz". In: *Monthly Notices of the Royal Astronomical Society* 299.2, pp. 467–478. ISSN: 0035-8711. DOI: [10.1046/j.1365-8711.1998.01843.x](https://doi.org/10.1046/j.1365-8711.1998.01843.x). eprint: <https://academic.oup.com/mnras/article-pdf/299/2/467/3340326/299-2-467.pdf>. URL: <https://doi.org/10.1046/j.1365-8711.1998.01843.x>.
- Macquart, J. P. et al. (May 2012). "On the Reliability of Polarization Estimation Using Rotation Measure Synthesis". In: *Astrophysical Journal* 750.2, 139, p. 139. DOI: [10.1088/0004-637X/750/2/139](https://doi.org/10.1088/0004-637X/750/2/139). arXiv: [1203.2706](https://arxiv.org/abs/1203.2706) [astro-ph.IM].
- Mahdavi, Andisheh and Margaret J. Geller (June 2001). "The LX- σ Relation for Galaxies and Clusters of Galaxies". In: *The Astrophysical Journal* 554.2, p. L129. DOI: [10.1086/321710](https://doi.org/10.1086/321710). URL: <https://dx.doi.org/10.1086/321710>.
- Martin-Alvarez, Sergio et al. (Apr. 2021). "Unravelling the origin of magnetic fields in galaxies". In: *Monthly Notices of the Royal Astronomical Society* 504.2, pp. 2517–2534. ISSN: 0035-8711. DOI: [10.1093/mnras/stab968](https://doi.org/10.1093/mnras/stab968). eprint: <https://academic.oup.com/mnras/article-pdf/504/2/2517/39271006/stab968.pdf>. URL: <https://doi.org/10.1093/mnras/stab968>.
- McMullin, J. P. et al. (2007). "Astronomical Data Analysis Software and Systems XVI". In: *ASP Conf. Ser.* Ed. by R. A. Shaw, F. Hill, and D. J. Bell. 376. San Francisco, CA, p. 127.

- Mesarcik, Michael et al. (Sept. 2022). "Learning to detect radio frequency interference in radio astronomy without seeing it". In: *Monthly Notices of the Royal Astronomical Society* 516.4, pp. 5367–5378. ISSN: 0035-8711. DOI: [10.1093/mnras/stac2503](https://doi.org/10.1093/mnras/stac2503). eprint: <https://academic.oup.com/mnras/article-pdf/516/4/5367/46130168/stac2503.pdf>. URL: <https://doi.org/10.1093/mnras/stac2503>.
- Miyashita, Yoshimitsu, Shinsuke Ideguchi, and Keitaro Takahashi (Apr. 2016). "Performance test of RM CLEAN and its evaluation with chi-square value". In: *Publications of the Astronomical Society of Japan* 68.3. 44. ISSN: 0004-6264. DOI: [10.1093/pasj/psw039](https://doi.org/10.1093/pasj/psw039). eprint: <https://academic.oup.com/pasj/article-pdf/68/3/44/6848040/psw039.pdf>. URL: <https://doi.org/10.1093/pasj/psw039>.
- Moolekamp, Fred and Peter Melchior (Dec. 2018). "Block-simultaneous direction method of multipliers: a proximal primal-dual splitting algorithm for nonconvex problems with multiple constraints". In: *Optimization and Engineering* 19.4, pp. 871–885. ISSN: 1573-2924. DOI: [10.1007/s11081-018-9380-y](https://doi.org/10.1007/s11081-018-9380-y). URL: <https://doi.org/10.1007/s11081-018-9380-y>.
- Motter, J. C. and D. C. Gabuzda (Feb. 2017). "18–22 cm VLBA Faraday rotation studies of six AGN jets". In: *Monthly Notices of the Royal Astronomical Society* 467.3, pp. 2648–2663. ISSN: 0035-8711. DOI: [10.1093/mnras/stx256](https://doi.org/10.1093/mnras/stx256). eprint: <https://academic.oup.com/mnras/article-pdf/467/3/2648/10875265/stx256.pdf>. URL: <https://doi.org/10.1093/mnras/stx256>.
- Narayan, R. and R. Nityananda (1986). "Maximum entropy image restoration in astronomy". In: *Annual Review of Astronomy and Astrophysics* 24, pp. 127–170.
- Natarajan, B. (1995). "Sparse Approximate Solutions to Linear Systems". In: *SIAM Journal on Computing* 24.2, pp. 227–234. DOI: [10.1137/S0097539792240406](https://doi.org/10.1137/S0097539792240406). eprint: <https://doi.org/10.1137/S0097539792240406>. URL: <https://doi.org/10.1137/S0097539792240406>.
- Ndiritu, S. W. et al. (Apr. 2021). "Gaussian process modelling for improved resolution in Faraday depth reconstruction". In: *Monthly Notices of the RAS* 502.4, pp. 5839–5853. DOI: [10.1093/mnras/stab379](https://doi.org/10.1093/mnras/stab379). arXiv: [2101.07099](https://arxiv.org/abs/2101.07099) [astro-ph.IM].
- Nocedal, J. and S. Wright (2006). *Numerical Optimization*. Springer Series in Operations Research and Financial Engineering. Springer New York. ISBN: 9780387303031. URL: <https://www.springer.com/gb/book/9780387303031>.
- Offringa, A. R. and O. Smirnov (June 2017). "An optimized algorithm for multiscale wide-band deconvolution of radio astronomical images". In: *Monthly Notices of the Royal Astronomical Society* 471.1, pp. 301–316. ISSN: 0035-8711. DOI: [10.1093/mnras/stx1547](https://doi.org/10.1093/mnras/stx1547). eprint: <https://academic.oup.com/mnras/article-pdf/471/1/301/19371792/stx1547.pdf>. URL: <https://doi.org/10.1093/mnras/stx1547>.
- Offringa, A. R., van de Gronde, J. J., and Roerdink, J. B. T. M. (2012). "A morphological algorithm for improving radio-frequency interference detection". In: *A&A* 539, A95. DOI: [10.1051/0004-6361/201118497](https://doi.org/10.1051/0004-6361/201118497). URL: <https://doi.org/10.1051/0004-6361/201118497>.

- O'Sullivan, S P et al. (May 2020). "New constraints on the magnetization of the cosmic web using LOFAR Faraday rotation observations". In: *Monthly Notices of the Royal Astronomical Society* 495.3, pp. 2607–2619. ISSN: 0035-8711. DOI: [10.1093/mnras/staa1395](https://doi.org/10.1093/mnras/staa1395). eprint: <https://academic.oup.com/mnras/article-pdf/495/3/2607/33326753/staa1395.pdf>. URL: <https://doi.org/10.1093/mnras/staa1395>.
- Perley, R. A. and B. J. Butler (Jan. 2013). "AN ACCURATE FLUX DENSITY SCALE FROM 1 TO 50 GHz". In: *The Astrophysical Journal Supplement Series* 204.2, p. 19. DOI: [10.1088/0067-0049/204/2/19](https://doi.org/10.1088/0067-0049/204/2/19). URL: <https://dx.doi.org/10.1088/0067-0049/204/2/19>.
- (May 2017). "An Accurate Flux Density Scale from 50 MHz to 50 GHz". In: *The Astrophysical Journal Supplement Series* 230.1, p. 7. DOI: [10.3847/1538-4365/aa6df9](https://doi.org/10.3847/1538-4365/aa6df9). URL: <https://doi.org/10.3847/1538-4365/aa6df9>.
- Poon, Clarice (2015). "On the Role of Total Variation in Compressed Sensing". In: *SIAM Journal on Imaging Sciences* 8.1, pp. 682–720. DOI: [10.1137/140978569](https://doi.org/10.1137/140978569). eprint: <https://doi.org/10.1137/140978569>. URL: <https://doi.org/10.1137/140978569>.
- Popesso, P. et al. (2004). "RASS-SDSS Galaxy clusters survey* - I. The catalog and the correlation of X-ray and optical properties". In: *A&A* 423.2, pp. 449–467. DOI: [10.1051/0004-6361:20035818](https://doi.org/10.1051/0004-6361:20035818). URL: <https://doi.org/10.1051/0004-6361:20035818>.
- Pratley, Luke, Melanie Johnston-Hollitt, and Bryan M. Gaensler (Oct. 2020). "Removing non-physical structure in fitted Faraday rotated signals: non-parametric QU-fitting". In: *arXiv e-prints*, arXiv:2010.07932, arXiv:2010.07932. arXiv: [2010.07932](https://arxiv.org/abs/2010.07932) [astro-ph.IM].
- Pratley, Luke, Melanie Johnston-Hollitt, and Bryan M. Gaensler (2021). "Removing non-physical structure in fitted Faraday rotated signals: Non-parametric QU-fitting". In: *Publications of the Astronomical Society of Australia* 38, e060. DOI: [10.1017/pasa.2021.49](https://doi.org/10.1017/pasa.2021.49).
- Pratley, Luke et al. (Sept. 2017). "Robust sparse image reconstruction of radio interferometric observations with purify". In: *Monthly Notices of the Royal Astronomical Society* 473.1, pp. 1038–1058. ISSN: 0035-8711. DOI: [10.1093/mnras/stx2237](https://doi.org/10.1093/mnras/stx2237). eprint: <http://oup.prod.sis.lan/mnras/article-pdf/473/1/1038/21392037/stx2237.pdf>. URL: <https://doi.org/10.1093/mnras/stx2237>.
- Press, William H. et al. (2007). *Numerical Recipes 3rd Edition: The Art of Scientific Computing*. 3rd ed. New York, NY, USA: Cambridge University Press. ISBN: 0521880688, 9780521880688.
- Purcell, Edward M. and David J. Morin (2013). *Electricity and Magnetism*. 3rd ed. Cambridge University Press. DOI: [10.1017/CB09781139012973](https://doi.org/10.1017/CB09781139012973).
- Puy, G. et al. (Nov. 2009). "Spread spectrum for imaging techniques in radio interferometry". In: *Monthly Notices of the Royal Astronomical Society* 400.2, pp. 1029–1038. ISSN: 0035-8711. DOI: [10.1111/j.1365-2966.2009.15519.x](https://doi.org/10.1111/j.1365-2966.2009.15519.x). eprint: <http://oup.prod.sis.lan/mnras/article-pdf/400/2/1029/3344627/mnras0400-1029.pdf>. URL: <https://doi.org/10.1111/j.1365-2966.2009.15519.x>.

- Rau, U. and T. J. Cornwell (Aug. 2011). “A multi-scale multi-frequency deconvolution algorithm for synthesis imaging in radio interferometry”. In: *Astronomy and Astrophysics* 532, A71, A71. DOI: [10.1051/0004-6361/201117104](https://doi.org/10.1051/0004-6361/201117104). arXiv: [1106.2745](https://arxiv.org/abs/1106.2745) [astro-ph.IM].
- Reichert, A. et al. (n.d.). “Observational constraints on the redshift evolution of X-ray scaling relations of galaxy clusters out to $z \sim 1.5$ ”. In: ().
- Repetti, Audrey et al. (Aug. 2016). “Scalable splitting algorithms for big-data interferometric imaging in the SKA era”. In: *Monthly Notices of the Royal Astronomical Society* 462.4, pp. 4314–4335. ISSN: 0035-8711. DOI: [10.1093/mnras/stw1859](https://doi.org/10.1093/mnras/stw1859). eprint: <http://oup.prod.sis.lan/mnras/article-pdf/462/4/4314/18512115/stw1859.pdf>. URL: <https://doi.org/10.1093/mnras/stw1859>.
- Reynolds, C., T.V. Cawthorne, and D.C. Gabuzda (Nov. 2001). “Faraday rotation in the VLBI core of BL Lacertae”. In: *Monthly Notices of the Royal Astronomical Society* 327.4, pp. 1071–1080. ISSN: 0035-8711. DOI: [10.1046/j.1365-8711.2001.04816.x](https://doi.org/10.1046/j.1365-8711.2001.04816.x). eprint: <https://academic.oup.com/mnras/article-pdf/327/4/1071/3252984/327-4-1071.pdf>. URL: <https://doi.org/10.1046/j.1365-8711.2001.04816.x>.
- Rybicki, George B. and Alan P. Lightman (1985). *Radiative Processes in Astrophysics*. John Wiley & Sons, Ltd. ISBN: 9780471827597. DOI: <https://doi.org/10.1002/9783527618170>.
- Ryle, M. and A. Hewish (Mar. 1960). “The Synthesis of Large Radio Telescopes”. In: *Monthly Notices of the Royal Astronomical Society* 120.3, pp. 220–230. ISSN: 0035-8711. DOI: [10.1093/mnras/120.3.220](https://doi.org/10.1093/mnras/120.3.220). eprint: <https://academic.oup.com/mnras/article-pdf/120/3/220/8074735/mnras120-0220.pdf>. URL: <https://doi.org/10.1093/mnras/120.3.220>.
- Sabol, Edward J. and Steven L. Snowden (Apr. 2019). *sxrbg: ROSAT X-Ray Background Tool*. ascl: [1904.001](https://ascl.net/1904.001).
- Sault, R. J. and M. H. Wieringa (Dec. 1994). “Multi-frequency synthesis techniques in radio interferometric imaging.” In: *Astronomy and Astrophysics* 108, pp. 585–594.
- Scaife, A. M. M. (2020). “Big telescope, big data: towards exascale with the Square Kilometre Array”. In: *Philosophical Transactions of the Royal Society A: Mathematical, Physical and Engineering Sciences* 378.2166, p. 20190060. DOI: [10.1098/rsta.2019.0060](https://doi.org/10.1098/rsta.2019.0060). eprint: <https://royalsocietypublishing.org/doi/pdf/10.1098/rsta.2019.0060>. URL: <https://royalsocietypublishing.org/doi/abs/10.1098/rsta.2019.0060>.
- Schwarz, Ulrich J. (1978). “Mathematical-statistical description of iterative beam removing technique (Method CLEAN)”. In: *Astronomy and Astrophysics* 65, pp. 345–356.
- Sebastian, Biny, Dharam V. Lal, and A. Pramesh Rao (Sept. 2017). “Giant Metrewave Radio Telescope Observations of Head–Tail Radio Galaxies”. In: *The Astronomical Journal* 154.4, p. 169. DOI: [10.3847/1538-3881/aa88d0](https://doi.org/10.3847/1538-3881/aa88d0). URL: <https://dx.doi.org/10.3847/1538-3881/aa88d0>.
- Sekhar, Srikrishna et al. (Jan. 2022). “Direction-dependent Corrections in Polarimetric Radio Imaging. III. A-to-Z Solver—Modeling the Full Jones Antenna Aperture Illumination Pattern”. In: *The Astronomical Journal* 163.2, p. 87. DOI: [10.3847/1538-3881/ac41c4](https://doi.org/10.3847/1538-3881/ac41c4). URL: <https://dx.doi.org/10.3847/1538-3881/ac41c4>.

- Shi, Yue, Siow Yong Low, and Ka Fai Cedric Yiu (2018). "Hyper-parameterization of sparse reconstruction for speech enhancement". In: *Applied Acoustics* 138, pp. 72–79. ISSN: 0003-682X. DOI: <https://doi.org/10.1016/j.apacoust.2018.03.020>. URL: <https://www.sciencedirect.com/science/article/pii/S0003682X17309076>.
- Sokoloff, D. D. et al. (Aug. 1998). "Depolarization and Faraday effects in galaxies". In: *Monthly Notices of the Royal Astronomical Society* 299.1, pp. 189–206. ISSN: 0035-8711. DOI: [10.1046/j.1365-8711.1998.01782.x](https://doi.org/10.1046/j.1365-8711.1998.01782.x). eprint: <https://academic.oup.com/mnras/article-pdf/299/1/189/18540555/299-1-189.pdf>. URL: <https://doi.org/10.1046/j.1365-8711.1998.01782.x>.
- Srivastava, Shweta and Ashok K Singal (Feb. 2020). "GMRT observations of IC 711 – the longest head-tail radio galaxy known". In: *Monthly Notices of the Royal Astronomical Society* 493.3, pp. 3811–3824. ISSN: 0035-8711. DOI: [10.1093/mnras/staa520](https://doi.org/10.1093/mnras/staa520). eprint: <https://academic.oup.com/mnras/article-pdf/493/3/3811/32902941/staa520.pdf>. URL: <https://doi.org/10.1093/mnras/staa520>.
- Starck, Jean-Luc, Jalal Fadili, and Fionn Murtagh (2007). "The Undecimated Wavelet Decomposition and its Reconstruction". In: *IEEE Transactions on Image Processing* 16.2, pp. 297–309. DOI: [10.1109/TIP.2006.887733](https://doi.org/10.1109/TIP.2006.887733).
- Starck, Jean-Luc, Fionn Murtagh, and Mario Bertero (2011). "Starlet Transform in Astronomical Data Processing". In: *Handbook of Mathematical Methods in Imaging*. Ed. by Otmar Scherzer. New York, NY: Springer New York, pp. 1489–1531. ISBN: 978-0-387-92920-0. DOI: [10.1007/978-0-387-92920-0_34](https://doi.org/10.1007/978-0-387-92920-0_34). URL: http://dx.doi.org/10.1007/978-0-387-92920-0_34.
- Stil, J. M. et al. (May 2014). "Degree of polarization and source counts of faint radio sources from stacking polarized intensity". In: *The Astrophysical Journal* 787.2, p. 99. DOI: [10.1088/0004-637X/787/2/99](https://doi.org/10.1088/0004-637X/787/2/99). URL: <https://dx.doi.org/10.1088/0004-637X/787/2/99>.
- Stuardi, C. et al. (Apr. 2021). "The intracluster magnetic field in the double relic galaxy cluster Abell 2345". In: *Monthly Notices of the RAS* 502.2, pp. 2518–2535. DOI: [10.1093/mnras/stab218](https://doi.org/10.1093/mnras/stab218). arXiv: [2101.09302](https://arxiv.org/abs/2101.09302) [astro-ph.GA].
- Stuardi, C. et al. (2022). "Using the polarization properties of double radio relics to probe the turbulent compression scenario". In: *A&A* 666, A8. DOI: [10.1051/0004-6361/202244179](https://doi.org/10.1051/0004-6361/202244179). URL: <https://doi.org/10.1051/0004-6361/202244179>.
- Subramanian, Kandaswamy (May 2016). "The origin, evolution and signatures of primordial magnetic fields". In: *Reports on Progress in Physics* 79.7, p. 076901. DOI: [10.1088/0034-4885/79/7/076901](https://doi.org/10.1088/0034-4885/79/7/076901). URL: <https://dx.doi.org/10.1088/0034-4885/79/7/076901>.
- Taylor, G. B., C. L. Carilli, and R. A. Perley, eds. (1999). *Synthesis Imaging in Radio Astronomy II*. Vol. 180. Astronomical Society of the Pacific Conference Series. San Francisco: Astronomical Society of the Pacific. ISBN: 978-1583815168.
- Temlyakov, V. N. (2008). "Greedy approximation". In: *Acta Numerica* 17, 235–409. DOI: [10.1017/S0962492906380014](https://doi.org/10.1017/S0962492906380014).

- The CASA Team et al. (Oct. 2022). "CASA, the Common Astronomy Software Applications for Radio Astronomy". In: *Publications of the Astronomical Society of the Pacific* 134.1041, p. 114501. DOI: [10.1088/1538-3873/ac9642](https://doi.org/10.1088/1538-3873/ac9642). URL: <https://dx.doi.org/10.1088/1538-3873/ac9642>.
- The Event Horizon Telescope Collaboration et al. (Apr. 2019). "First M87 Event Horizon Telescope Results. IV. Imaging the Central Supermassive Black Hole". In: *The Astrophysical Journal Letters* 875.1, p. L4. DOI: [10.3847/2041-8213/ab0e85](https://doi.org/10.3847/2041-8213/ab0e85). URL: <https://dx.doi.org/10.3847/2041-8213/ab0e85>.
- Tibshirani, Robert (1996). "Regression Shrinkage and Selection Via the Lasso". In: *Journal of the Royal Statistical Society: Series B (Methodological)* 58.1, pp. 267–288. DOI: <https://doi.org/10.1111/j.2517-6161.1996.tb02080.x>. eprint: <https://rss.onlinelibrary.wiley.com/doi/pdf/10.1111/j.2517-6161.1996.tb02080.x>. URL: <https://rss.onlinelibrary.wiley.com/doi/abs/10.1111/j.2517-6161.1996.tb02080.x>.
- Vacca, Valentina et al. (July 2022). "Puzzling large-scale polarization in the galaxy cluster Abell 523". In: *Monthly Notices of the Royal Astronomical Society* 514.4, pp. 4969–4981. ISSN: 0035-8711. DOI: [10.1093/mnras/stac1421](https://doi.org/10.1093/mnras/stac1421). eprint: <https://academic.oup.com/mnras/article-pdf/514/4/4969/44589989/stac1421.pdf>. URL: <https://doi.org/10.1093/mnras/stac1421>.
- Vallee, J. P. and A. S. Wilson (Feb. 1976). "Head-tail radio sources in the cluster of galaxies Abell 1314". In: *Nature* 259.5543, pp. 451–454. DOI: [10.1038/259451a0](https://doi.org/10.1038/259451a0).
- Van Eck, C. L. et al. (June 2018). "Polarized point sources in the LOFAR Two-meter Sky Survey: A preliminary catalog". In: *Astronomy and Astrophysics* 613, A58, A58. DOI: [10.1051/0004-6361/201732228](https://doi.org/10.1051/0004-6361/201732228). arXiv: [1801.04467](https://arxiv.org/abs/1801.04467) [astro-ph.GA].
- Vazza, F et al. (Oct. 2017). "Simulations of extragalactic magnetic fields and of their observables". In: *Classical and Quantum Gravity* 34.23, p. 234001. DOI: [10.1088/1361-6382/aa8e60](https://doi.org/10.1088/1361-6382/aa8e60). URL: <https://dx.doi.org/10.1088/1361-6382/aa8e60>.
- Vazza, F. et al. (2015). "Forecasts for the detection of the magnetised cosmic web from cosmological simulations". In: *A&A* 580, A119. DOI: [10.1051/0004-6361/201526228](https://doi.org/10.1051/0004-6361/201526228). URL: <https://doi.org/10.1051/0004-6361/201526228>.
- Wenger, Stephan et al. (Oct. 2010). "SparseRI: A Compressed Sensing Framework for Aperture Synthesis Imaging in Radio Astronomy". In: *Publications of the Astronomical Society of the Pacific (PASP)* 122.897, pp. 1367–1374.
- Wiaux, Y. et al. (May 2009). "Compressed sensing imaging techniques for radio interferometry". In: *Monthly Notices of the Royal Astronomical Society* 395, pp. 1733–1742. DOI: [10.1111/j.1365-2966.2009.14665.x](https://doi.org/10.1111/j.1365-2966.2009.14665.x). arXiv: [0812.4933](https://arxiv.org/abs/0812.4933).
- Widrow, Lawrence M. (July 2002). "Origin of galactic and extragalactic magnetic fields". In: *Rev. Mod. Phys.* 74 (3), pp. 775–823. DOI: [10.1103/RevModPhys.74.775](https://doi.org/10.1103/RevModPhys.74.775). URL: <https://link.aps.org/doi/10.1103/RevModPhys.74.775>.
- Wijnholds, S J, A G Willis, and S Salvini (Feb. 2018). "Baseline-dependent averaging in radio interferometry". In: *Monthly Notices of the Royal Astronomical Society* 476.2, pp. 2029–2039. ISSN: 0035-8711. DOI: [10.1093/mnras/sty360](https://doi.org/10.1093/mnras/sty360). eprint: <https://arxiv.org/abs/1709.01511>.

academic.oup.com/mnras/article-pdf/476/2/2029/24309145/sty360.pdf.
URL: <https://doi.org/10.1093/mnras/sty360>.

Wilber, A. et al. (2019). “Evolutionary phases of merging clusters as seen by LOFAR”. In: *A&A* 622, A25. DOI: [10.1051/0004-6361/201833884](https://doi.org/10.1051/0004-6361/201833884). URL: <https://doi.org/10.1051/0004-6361/201833884>.

Yang, J. and Y. Zhang (2011). “Alternating Direction Algorithms for ℓ_1 -Problems in Compressive Sensing”. In: *SIAM Journal on Scientific Computing* 33.1, pp. 250–278. DOI: [10.1137/090777761](https://doi.org/10.1137/090777761). eprint: <https://doi.org/10.1137/090777761>. URL: <https://doi.org/10.1137/090777761>.

Zangwill, Andrew (2012). *Modern Electrodynamics*. Cambridge University Press. DOI: [10.1017/CB09781139034777](https://doi.org/10.1017/CB09781139034777).